Multi-parameter imaging of lipid bilayers and cell membranes using time- and polarisation-resolved fluorescence microscopy

Le Marois, Alix Marie

Awarding institution:
King's College London

Multi-parameter imaging of lipid bilayers and cell membranes using time- and polarisation-resolved fluorescence microscopy

Alix Marie Isabelle LE MAROIS

A thesis submitted in partial fulfilment of the requirements for the degree of

Doctor of Philosophy in Physics

King's College London

Department of Physics

King's College London

2018

Supervised by Prof. Klaus SUHLING and Dr. Dylan OWEN

A Mamie-Claire.

Abstract

This thesis presents the development and application of multi-dimensional fluorescence imaging based on confocal microscopy and time-correlated single photon counting (TCSPC) instrumentation, to reveal the relationship between microenvironment and order parameters of lipid bilayers, which are the fundamental entities of cell membranes. The objective is to use all the information available from the fluorescence signal - emission wavelength, lifetime and polarisation - to independently interrogate several biophysical properties of biomembranes, simultaneously.

The photophysical characterisation of membrane dye laurdan was carried out using fluorescence spectroscopy, and this showed that its emission wavelength and fluorescence lifetime report on different characteristics of its environment, namely, hydration and polarity. Time-resolved anisotropy measurements were used to report on two membrane order parameters related to the hindered rotational diffusion of the fluorophore in the bilayer. An experimental and analytical framework was implemented in order to measure and quantify these four parameters, on the same field of view. This method was then applied to the extensive characterisation of the relationship between these membrane properties in artificial bilayers, and showed distinct dependence of membrane microenvironment and order to temperature and to membrane chemistry, i.e. the degree of saturation and cholesterol content. This approach also proved informative in resolving the dynamics of domain mixing in ternary lipid mixtures. Applied to the membranes of live cells, simultaneous imaging of membrane micro-environments and order parameters showed that while plasma and internal membranes display different membrane polarity and order parameter values, linked to their different chemical composition, the relationship between these parameters is preserved throughout the cell. The role of cholesterol in the preservation of these parameters was investigated, showing that cholesterol strongly determines membrane hydration and polarity, while the order parameters are less sensitive to modulation of cholesterol content. Interpretation of spectral and lifetime information allowed discrimination between the effect of cholesterol on membrane hydration and polarity. Cell-derived plasma membrane vesicles were also characterised as a system to study lipid bilayers with compositions more faithful to that of the cell membrane, and results suggest that the lipid content of such vesicles is strongly determined by the modalities of their formation.

Lastly, strategies to improve the analysis of multi-dimensional time-resolved fluorescence image data were explored. A novel processing routine based on principal component analysis was created, allowing sensitive detection of lifetime contrast in photon-limited TCSPC images, and the potential to analyse time-resolved anisotropy data in a pixel-wise fashion was also demonstrated.

Author Declaration

All the work presented here is my own; significant contributions were made by collaborators for the following elements:

- The examples cited in section 1.7. of Chapter 1 are the result of collaborative work, with the main collaborators cited when relevant.
- The work on the optical system described in Chapter 1 is a collaborative effort of our laboratory, in particular Dr. Liisa Hirvonen and Yurema Teijeiro-Gonzalez contributed to beam shaping and optical design.
- The analysis procedures presented in Chapter 4 are the results of a collaboration with Prof. Rainer Heintzmann, from whom the idea originated.

Acknowledgements

My gratitude to Prof. Klaus Suhling for providing me with the opportunity to work in his team, introducing me to so many interesting and passionate people, some of whom have become collaborators and friends, and for trusting me to develop and implement my own ideas. Dr Dylan Owen has been of great help and guidance as a second supervisor, many thanks to him. Thank you to Dr. James Levitt for his kindness and useful tips, especially at the beginning! Thanks to Dr. Liisa Hirvonen for her advice and collaboration, I have always admired your talent. Thanks to the technical, teaching and administrative staff of the department: Bill, Sam, Julian, John, Christina, Rowena, Bonnie, Meghan, Paul, James, Dr Eva Phillippaki, who ensure that we work in a productive and safe environment. Thanks to Julia Kilpatrick for babysitting all of us with such dedication, we miss you! My time at King's would not have been so enjoyable without the friends I have made here: Pooya, Krys, Marco^2, Gianmarco, Marcello, Dan, Alena, Yurema, Emilie, Fedor, Andreas, Leo, Mary, Soraya, Diane, Juliette, David, Mike, George, Lorenzo, Thomas^3, Chandni et al... A special thank you and my gratitude to Juliette, with whom I discovered the physical and psychological feats I was capable of through marathon running!

I would also like to thank my collaborators, from whom I have learnt so much: Prof. Rainer Heintzmann, Dr. Alex Ivetic, Prof. Gerard Marriott, Dr. Alex Hoepker, Dr. Arun Shivalingam, Dr. Elnaz Naghini, Dr. Thomas Gensch, Dr Wolfgang Becker, Dr Nell Yu. Thank you to Dr. Simon Ameer-Beg and Prof. Maddy Parsons for their time, enthusiasm and faith in me. I am grateful to my thesis examiners, Prof. Tony Magee and Dr. Alessandro Esposito, for thorough evaluation of this work and helpful comments.

Thanks to my dearest friend Claire for her constant support and continued friendship, and to my family who doesn't understand my work but certainly understands, and encourages, my passion! Thank you to my father for always feeding my enthusiasm, and to my mother for pushing me to apply for this project; without you I would be in a different place altogether. Thank you to Shyam for his affection and for supporting me, in the French and English sense of the term!

Publications

Research articles

- **Le Marois, A.**, Labouesse, S., Suhling, K., Heintzmann, R., Noise-Corrected Principal Component Analysis of fluorescence lifetime imaging data (2016). Journal of Biophotonics 10, 1124-1133, 2017. doi:10.1002/jbio.201600160

- Hirvonen, L.M., Becker, W., Milnes, J., Conneely, T., Smietana, S., **Le Marois, A.**, Jagutzki, O., Suhling, K. Picosecond wide-field time-correlated single photon counting fluorescence microscopy with a delay line anode detector (2016). Applied Physics Letters 109, 071101. doi:10.1063/1.4961054.

- Yaghini, E., Turner, H.D., **Le Marois, A.**, Suhling, K., Naasani, I., MacRobert, A.J., In Vivo Biodistribution Studies and Ex Vivo Lymph Node Imaging Using Heavy Metal-Free Quantum Dots, Biomaterials (2016). 104, 182-191, doi :10.1016/j.biomaterials.2016.07.014.

- Shivalingam, A., Angeles Izquierdo, M., **Le Marois, A.**, Vysniauskas, A., Suhling, K., Kuimova, M., and Vilar, R. The Interactions between a small molecule and G-quadruplexes are visualized by fluorescence lifetime imaging microscopy, Nature Communications (2015) 6:8178, doi: 10.1038/ncomms9178.

- Hoepker, A.C., Wang, A., **Le Marois, A.**, Suhling, K., Yan, Y., Marriott, G. Genetically encoded sensors of protein hydrodynamics and molecular proximity, Proceedings of the National Academy of Sciences (2015). E2569–E2574. doi:10.1073/pnas.1424021112.

- Ulusoy, M., Walter, J., Lavrentieva, A., Kretschmer, I., Sandiford, L., **Le Marois, A.**, Bongartz R., Aliuos, P., Suhling, K., Stahl, F., Green, M., Scheper T., One-pot aqueous synthesis of highly strained CdTe/CdS/ZnS nanocrystals and their interactions with cells, RSC Advances (2015). 5:7485-7494, doi:10.1039/c4ra13386b.

Book Chapters and Conference proceedings

- **Le Marois, A.**, and Suhling, K. Quantitative live cell FLIM imaging in three dimensions. Advances in Experimental Medicine and Biology, Multi-Parametric Live Cell Microscopy of 3D Tissue Models (2017). doi: 10.1007/978-3-319-67358-5.

- Suhling, K., Hirvonen, L.M., Becker, W., Smietana, S., Netz, H., Milnes, J., Conneely, T., **Le Marois, A.**, Jagutzki, O., Wide-field TCSPC-based fluorescence lifetime imaging (FLIM) microscopy. In: Proc. SPIE 9858, Advanced Photon Counting Techniques X, 98580J (2016). doi:10.1117/12.2227198.

- Roth, D., Nasir M.E., Krasavin, A., Ginzburg, P., Dickson, W., **Le Marois, A**., Suhling, K., Richards, D., Podolskiy, V.A., Zayats, A., Spontaneous emission and non-radiative processes inside a hyperbolic metamaterial. In: Proc. SPIE 9920, Active Photonic Materials VIII, 99201A (2016). doi:10.1117/12.2237735.

- **Le Marois, A.**, Owen, D.M., Suhling, K., 2015. Investigating cell membrane structure and dynamics with TCSPC-FLIM. In: Proc. SPIE 9329, Multiphoton Microscopy in the Biomedical Sciences XV, 932938 (2015). doi:10.1117/12.2178563.

- Suhling, K., Hirvonen, L.M., Levitt, J.A., Chung, P.-H., Tregidgo, C., **Le Marois, A.**, Rusakov, D.A., Zheng, K., Ameer-Beg, S., Poland, S., Coelho, S., Henderson, R., Krstajic, N., Fluorescence lifetime imaging (FLIM): Basic concepts and some recent developments. Medical Photonics, Fluorescence lifetime measurements in the biomedical sciences 27, 3–40 (2015). doi:10.1016/ j.medpho.2014.12.001.

- Suhling, K., Hirvonen, L.M., Levitt, J.A., Chung, P.-H., Tregidgo, C., **Le Marois, A.**, Rusakov, D.A., Zheng, K., Ameer-Beg, S., Poland, S., Coelho, S., Fluorescence Lifetime Imaging (FLIM): Basic Concepts and Recent Applications, in W. Becker, Advanced Time-Correlated Single Photon Counting Applications, Springer Series in Chemical Physics 111 (2015).

Conference presentations

Le Marois, A., Owen, D.M., Heintzmann, R., and Suhling, K.: Fluorescence lifetime and polarization imaging of environmentally-sensitive dyes for multi-parameter analysis of lipid bilayers and cell membranes.

Presented at:

- 11th FLIM Workshop – Berlin, Germany (short talk and poster), July 2017.

- FluoroFest Workshop – Glasgow, UK (short talk and poster), April 2017.

- Focus on Microscopy – Bordeaux, France (poster), April 2017.

- Frontiers in Imaging – Janelia Farm, VA., USA (poster), April 2017.

Le Marois, A., Labouesse, S., Suhling, K. and Heintzmann, R.: Noise-Corrected Principal Component Analysis of Fluorescence Lifetime Imaging Data.

Presented at:

- Mathematical methods in biology - King's College London (poster), November 2017.

- Quantitative Bio-Imaging – Delft, Netherlands (poster), January 2016.

Le Marois, A., Ivetic, A., Owen, D.M., and Suhling, K.: Time-Resolved Fluorescence Anisotropy Imaging and Cell Membrane Dynamics.

Presented at:

- 12th Annual Advanced Imaging Methods Workshop (AIM) – Berkeley, CA., USA (poster), January 2015.
- Photonics West – San Francisco, CA., USA (poster), January 2015.

Contents

1 Fluorescence lifetime, polarisation and microscopy **27**

1.1 Fluorescence is a light-matter interaction 29

1.1.1 Modalities of light absorption 29

1.1.2 Modalities of fluorescence emission 31

1.1.3 The fluorescence emission spectrum 32

1.1.4 Fluorophores in biological imaging 33

1.2 Fluorescence lifetime 34

1.3 Polarisation of light and fluorescence 36

1.3.1 Polarisation is the description of the electric field vector orientation 36

1.3.2 Fluorescence is a polarisation-specific process 37

1.3.3 Theory of fluorescence polarisation decay 39

1.3.3.1 Case of a uniform distribution of fluorophores rotating freely. . . . 40

1.3.3.2 Case of membranes: non-uniform fluorophore distribution with hindered rotation ("wobble-in-cone" model) 41

1.3.4 Steady-state anisotropy 44

1.4 Time-resolved fluorescence microscopy 45

1.4.1 Time-correlated single photon counting (TCSPC) 45

1.4.2 Time-Gated FLIM 48

1.4.3 Frequency domain FLIM 49

1.4.4 FLIM and microscopy 50

1.4.4.1 Confocal microscopy and FLIM 50

1.4.5 Alternatives to confocal-TCSPC for FLIM 51

1.4.5.1 Two-photon FLIM 51

1.4.5.2 Choice of time-resolved imaging instrumentation 53

1.4.6 Note on microscope resolution 53

1.5 Time-and polarisation-resolved fluorescence microscopy in the laboratory 55

1.5.1 The laboratory setup 55

1.5.2 Optimisation of the optical system and calibrations . . . 56
1.5.2.1 On the excitation side . . . 56
1.5.2.2 On the detection side . . . 59
1.5.2.3 Measuring the optical resolution of the microscope . . . 63
1.6 Overview of existing analysis methods for FLIM and TR-FAIM . . . 65
1.6.1 Pixel-wise fitting approaches of fluorescence intensity decays . . . 65
1.6.1.1 The Non-Linear Least Squares method . . . 65
1.6.1.2 The Maximum Likelihood Estimation Method . . . 66
1.6.2 Global fitting approaches . . . 67
1.6.3 Method of moments . . . 68
1.6.4 The phasor approach to FLIM . . . 68
1.6.5 Analysis of time-resolved fluorescence anisotropy data . . . 71
1.6.5.1 Position of the problem . . . 71
1.6.5.2 Method 1 : "brute-force" - exponential decay fitting of time-resolved anisotropy . . . 72
1.6.5.3 Method 2 : "Trying to be smart" - fitting the polarisation-resolved intensity decays to extract the anisotropy parameters. . . . 74
1.6.6 Rationale on the adopted data processing strategy in this work . . . 75
1.7 Examples of applications of fluorescence lifetime and polarisation measurements . . . 77
1.7.1 Detection of Förster Resonance Energy Transfer (FRET) with FLIM . . . 77
1.7.2 Detection of molecular micro-environments using FLIM . . . 79
1.7.3 Applications of time-resolved anisotropy analysis . . . 81
1.7.3.1 Detection of rotational correlation times . . . 81
1.7.3.2 Detection of homo-FRET . . . 82

2 Multi-dimensional microscopy of model membranes 86

2.1 Introduction . . . 86
2.1.1 Cell membranes and artificial models . . . 86
2.1.1.1 Structure and biological importance of cell membranes. . . . 86
2.1.1.2 Model membranes for biophysical studies . . . 88
2.1.1.3 Phase behaviour of lipid bilayers . . . 89
2.1.1.4 Models for the lateral organisation of the cell membrane . . . 90
2.1.2 Methods to study membrane biophysics . . . 93
2.1.2.1 Quantifying diffusion in cell membranes . . . 93
2.1.2.2 Probing membrane micro-environments . . . 95
2.1.3 Hypothesis and research questions . . . 98

2.2 Methods . . . 99
2.2.1 Sample preparation . . . 99
2.2.1.1 Giant Unilamellar Vesicles . . . 99
2.2.1.2 Sample Immobilisation . . . 100
2.2.2 Choice of fluorescent membrane dyes . . . 102
2.2.3 Temperature Control . . . 103
2.2.3.1 Construction of a temperature-controlled heated stage sample chamber . . . 103
2.2.3.2 Validation of the accuracy of the temperature readings . . . 104
2.2.4 Time-Resolved Fluorescence microscopy . . . 106
2.2.5 Spectroscopy . . . 106
2.2.6 Data processing . . . 107
2.2.6.1 Time-resolved anisotropy . . . 107
2.2.6.2 Intensity decays . . . 107
2.2.6.3 Statistical analysis . . . 110
2.3 Results . . . 110
2.3.1 Photophysical characterisation of di-4-ANEPPDHQ and laurdan. . . . 110
2.3.1.1 Is di-4-ANEPPDHQ a molecular rotor? . . . 110
2.3.1.2 Preliminary results in GUVs with Di-4-ANEPPDHQ . . . 114
2.3.1.3 Relationship between spectral emission and fluorescence lifetime of laurdan . . . 115
2.3.2 Correlating membrane polarity and order parameters in homogeneous lipid mixtures . . . 123
2.3.2.1 DOPC . . . 123
2.3.2.2 POPC . . . 126
2.3.2.3 DPPC . . . 129
2.3.3 The effect of cholesterol on the relationship between membrane hydration and membrane order . . . 132
2.3.3.1 DOPC and cholesterol . . . 132
2.3.3.2 DPPC and Cholesterol . . . 135
2.3.4 Phase-separating lipid mixtures . . . 138
2.4 Conclusions and outlook . . . 145

3 Multi-dimensional microscopy of cell membranes 152

3.1 General methods . . . 153
3.1.1 Cell culture and staining . . . 153

3.1.2 Cell-Derived Vesicles . . . 153
3.1.3 Imaging . . . 155
3.1.4 Data analysis . . . 155
3.1.4.1 ROI selection . . . 155
3.1.4.2 Phasor analysis . . . 156
3.2 Correlating micro-environments and order parameters in HeLa cell membranes . . 158
3.2.1 Experiments on live cells . . . 158
3.2.1.1 Relationship between membrane polarity and order parameters in live cell membranes . . . 158
3.2.2 Characterisation of cell-derived vesicles as a model system to study membrane microenvironments and order parameters . . . 162
3.2.2.1 Studying the effect of vesiculating agent concentration on the characteristics of GPMV membranes . . . 163
3.2.2.2 Membrane microenvironment and order parameters in GPMVs . . 165
3.2.2.3 Comparison of laurdan fluorescence in GPMVs and live cells . . . 168
3.2.3 Effect of the actin cytoskeleton on membrane microenvironments and order parameters . . . 170
3.3 Investigating the dynamics of cholesterol in cell membranes . . . 173
3.3.1 Experiments on live cells . . . 175
3.3.1.1 Plasma membranes . . . 175
3.3.1.2 Internal membranes . . . 179
3.3.2 Experiments on cell-derived vesicles . . . 180
3.4 Conclusions and discussion . . . 181

4 NC-PCA for time-resolved imaging data 184

4.1 Application of PCA to TCSPC-FLIM . . . 186
4.1.1 Searching for a performance metric adapted to global analysis methods . . 187
4.1.2 The noise problem . . . 191
4.1.3 Validation of NC-PCA on simulated data . . . 198
4.1.3.1 Comparison between NC-PCA and phasor analysis . . . 198
4.1.3.2 Visual examples . . . 199
4.1.3.3 Parameter sweep . . . 199
4.1.3.4 Simulating a FRET situation . . . 203
4.1.3.5 Testing for the robustness of NC-PCA to experimental conditions 204
4.1.4 Application of NC-PCA to experimental data . . . 206
4.1.4.1 Detection of fine lifetime variations at an interface . . . 206

4.1.4.2 Detection of membrane microenvironments and effect of cholesterol depletion using NC-PCA on HeLa cells stained with di-4-ANEPPDHQ 208
4.1.5 NC-PCA for de-noising 211
4.2 NC-PCA and time-resolved anisotropy data 212
4.2.1 Adaptation of NC-PCA to TR-FAIM 212
4.2.2 Assessing NC-PCA performance as a function of decay parameters θ, r_0, r_∞, I_0 and τ 216
4.2.3 Application of NC-PCA on experimental time-resolved anisotropy and intensity data 217
4.2.3.1 Case of free rotation: resolving lifetime and rotational correlation time changes in water-glycerol mixtures. 217
4.2.3.2 Application of NC-PCA to TR-FAIM of di-4-ANEPPDHQ in model membranes 220

5 Conclusions and future directions **225**

Bibliography **237**

List of Figures

1.1 Some examples of organic fluorescent dyes. 29
1.2 The Franck-Condon model explains modalities of photon absorption and emission. 30
1.3 Jablonski-Perrin diagram 32
1.4 Excitation and emission spectra of di-4-ANEPPDHQ in a glycerol-water solution . 33
1.5 The polarisation state of light. 37
1.6 Representation of incident polarised light on a sample of randomly distributed fluorophores 38
1.7 Example of polarisation-resolved intensity (left) and corresponding anisotropy (right) decays of fluorescein in glycerol. 41
1.8 Schematic representation of a fluorophore inserted in a lipid bilayer. 41
1.9 Domains of existence of membrane fluorophores according to the hard-cone model, and Gaussian model. 43
1.10 Basic principle of Time-Correlated Single Photon Counting (TCSPC). 45
1.11 Typical detector trace of fluorescence photons with pulsed laser excitation. 46
1.12 Classic TCSPC architecture. 47
1.13 Basic principle of time-gated fluorescence detection. 48
1.14 Basic principle of frequency-domain determination of fluorescence lifetimes. 50
1.15 Optical sectioning in the confocal microscope. 51
1.16 The laboratory setup. 55
1.17 Optical diagram of laser beam shaping elements used for the 467 nm diode laser. . 57
1.18 Optical diagram of the beam shaping elements used for the 357 nm diode laser. . 57
1.19 Diagram of the optical configuration of the excitation paths. 58
1.20 Pulse shape of 467nm laser as a function of operating power. 59
1.21 G factor measurement using the tail-matching method. 60
1.22 G factor as a function of the pinhole size. 60
1.23 Relationship between CFD threshold, gain and count rate for time-resolved detectors. 62

1.24 Calibration curves obtained for the two HPM 100-40 detectors. 62
1.25 Imaging of fluorescent nanoparticles to measure the microscope point spread function. 63
1.26 Analysis of TCSPC data using exponential fitting. The χ^2_{red} shown here corresponds to the NLLS estimate. 65
1.27 Phasor analysis of a HeLa cell stained with membrane dye di-4-ANEPPDHQ. . . . 70
1.28 Phasor analysis of fluorescence species in live tissue samples. 70
1.29 Contour plot of the measurement uncertainty on anisotropy as a function of polarisation-resolved intensities. 72
1.30 Example of an anisotropy decay fitted to a single exponential model. 73
1.31 Results of weighted and unweighted fits on simulated time-resolved anisotropy data. 74
1.32 Recovered lifetime and anisotropy parameters from simulated noisy dataset. 75
1.33 Simulated FRET efficiencies (E) as a function of the distance separating the two fluorophores. 78
1.34 Measurement of FRET between LUMP and Venus. 79
1.35 Detection of G-quadruplexes using FLIM of DAOTA-M2. 80
1.36 FLIM of U2OS cells stained with DAOTA-M2 upon Pyridostatin displacement. . . 81
1.37 Schematic representation of two interacting GFP-like fluorophores. 82
1.38 Homo-FRET imaging of l-selectin clustering during leukocyte transmigration. . . 84

2.1 Chemical structure of membrane lipids 87
2.2 Phase diagrams of ternary lipid mixtures with unsaturated lipid (DOPC), saturated lipid (DPPC) and Cholesterol. 90
2.3 Chemical structures of laurdan and di-4-ANEPPDHQ. 96
2.4 Order parameters of lipid bilayers resolved by Haluska et al using fluorescence polarisation of TMA-DPH. 97
2.5 The electroformation system. 100
2.6 x-z sections of GUVs (DOPC/DPPC/Chol 2:2:1) stained with di-4-ANEPPDHQ, containing 1% molar biotinylated lipids and tethered on an avidin-coated coverslip. 101
2.7 Reconstituted volume of a GUV (DOPC) stained with di-4-ANEPPDHQ and embedded in a 0.25% w/v agarose gel. 102
2.8 Design of a temperature-controlled heated slide chamber system. 104
2.9 Emission spectrum of laurdan in DPPC vesicles as a function of temperature. . . 104
2.10 GP of laurdan in DPPC at different temperatures. 105
2.11 GP of laurdan in DPPC as a function of temperature. 106
2.12 Comparison of fitting results for simulated intensity decays computed directly or as the sum of two polarisation-resolved intensity decays 108

2.13 Illustration of the data obtained from the time-resolved experiments. 109
2.14 Examples of fits for intensity decay and corresponding anisotropy decay of laurdan in lipid bilayers 109
2.15 Picture of methanol-glycerol mixtures containing 5 μM di-4-ANEPPDHQ on a UV lamp. The label indicates the glycerol content. 111
2.16 emission spectroscopy of di-4-ANEPPDHQ in methanol-glycerol mixtures. 112
2.17 Intensity decay analysis of di-4-ANEPPDHQ in methanol-glycerol mixtures. 113
2.18 Time- and polarisation-resolved fluorescence analysis of di-4-ANEPPDHQ in different lipid mixtures. 114
2.19 Solvatochromicity of laurdan. 118
2.20 Intensity decays of laurdan acquired in various solvents. 119
2.21 Graphs showing the relationships between laurdan lifetime and solvent dielectric constant. 120
2.22 Relationship between the average lifetime in the blue and green detection channels, and the dipolar moment or dielectric constant. 121
2.23 Plots of average lifetimes in the blue and green channels as a function the maximum emission wavelength. 122
2.24 Boxplots showing average lifetime, rotational correlation time and order parameter of laurdan in DOPC as a function of temperature. 123
2.25 Examples of intensity and anisotropy decays of laurdan in DOPC at 25 and 50^{o}C. 124
2.26 Relationship between laurdan lifetime and order parameters in DOPC. 125
2.27 Laurdan GP analysis of DOPC vesicles. 125
2.28 Relationship between and lifetime and order parameters for DOPC and POPC. . . 126
2.29 Representative normalised intensity and anisotropy decays for DOPC and POPC at 25^{o}C. 127
2.30 GP of laurdan in POPC as a function of temperature. 128
2.31 GP against lifetime and anisotropy parameters. 128
2.32 Boxplots for lifetime, anisotropy and GP parameters for laurdan in DPPC as a function of temperature. 130
2.33 Plots of lifetime against anisotropy parameters for DPPC compared to DOPC. . . 131
2.34 Representative intensity and anisotropy decays of laurdan in DOPC and DPPC at 25^{o}C and 50^{o}C. 131
2.35 Plots of lifetime against anisotropy parameters in DOPC GUVs containing 0%, 30% or 50% cholesterol (mol%) 133

2.36 Examples of intensity and normalised anisotropy decays of laurdan in DOPC:Chol 5:5 vesicles at 22, 37 and 50^{o}C 134
2.37 GP values for DOPC:Chol 7:3 and 5:5 134
2.38 Plots of lifetime against anisotropy parameters for DPPC and DPPC:Chol 9:1. . . 135
2.39 Plots of lifetime against anisotropy parameters for DPPC and DPPC:Chol 7:3. . . 136
2.40 Laurdan GP analysis of DPPC:Chol 9:1 vesicles as a function of temperature. . . . 137
2.41 Laurdan GP analysis of DPPC:Chol 7:3 vesicles as a function of temperature. . . . 138
2.42 Example of series of images acquired for phase-separated GUV composed of DPPC:DOPC:Chol 2:2:1 at 25^{o}C. 139
2.43 ROI selection on images of phase-separated GUVs. 140
2.44 GP images of DPPC:DOPC:Chol 2:2:1 vesicles at varying temperatures. 140
2.45 Boxplots of lifetime, anisotropy parameter and GP values as a function of temperature for DPPC:DOPC:Chol vesicles. 141
2.46 Relationship between lifetime and static order parameters in single and double-phase GUVs. 142
2.47 Correlation between lifetime and GP values in phase-separating mixtures. 142
2.48 Analysis of the composition of the Lo-Ld domains using the results from homogeneous lipid bilayers. 143
2.49 Evolution of GP values in the Ld (A) and Lo (B) domains between 25 and 30^{o}C. . 144
2.50 Proposed model of Lo-Ld domain mixing in ternary lipid mixtures. 145
2.51 Lifetime parameters of laurdan in solution as a function of maximum emission wavelength. 148
2.52 Lifetime parameters of laurdan in solution as a function of solvent dipole moment. 149
2.53 Lifetime parameters of laurdan in solution as a function of solvent dielectric constant. 150
2.54 Summary of fit parameters for laurdan intensity decays in various solvents. 151

3.1 Brightfield images of HeLa cells after 1h incubation with vesiculation agents for GPMV extraction. 154
3.2 Confocal intensity image of GPMVs extracted from HeLa cells and stained with laurdan. Scale bar = 10 μm. 155
3.3 ROI selection for the analysis of cell membranes. 156
3.4 Illustration of the phasor analysis method. 157
3.5 Effect of the weighting procedure in phasor fitting. 158
3.6 Representative normalised intensity and anisotropy decays of laurdan in HeLa cell membranes at 25 and 37^{o}C. 159

3.7 Boxplots of membrane polarity and order parameters in plasma membranes of HeLa cells at different temperatures. 159
3.8 Boxplots of membrane polarity and order parameters in internal membranes of HeLa cells at different temperatures. 160
3.9 Correlation between polarity and order parameters in HeLa cell membranes. 161
3.10 GP analysis of HeLa cell membranes as a function of temperature. 162
3.11 Domains at low temperature in GPMVs. 163
3.12 Effect of vesiculating agent concentration on laurdan lifetime in GPMVs. 164
3.13 Effect of vesiculating agent concentration on laurdan GP in GPMVs. 165
3.14 Boxplots showing the values of order parameters and for two concentrations in vesiculating agents. 166
3.15 Boxplots showing the temperature evolution of lifetime, anisotropy and GP parameters in GPMVs 167
3.16 Examples of intensity and anisotropy decays as a function of temperature in GPMVs. 168
3.17 GP analysis of GPMVs. 168
3.18 Correlation between lifetime and order parameters and in GPMVs. 169
3.19 Images of HeLa cells stained with laurdan and treated with Cytochalasin D (right) compared to untreated cells (left). Scale bar is 50 μm. 171
3.20 Lifetime analysis of laurdan upon cytoskeleton disruption. 171
3.22 Boxplots showing the order parameters in plasma and internal membranes of HeLa cells treated with Cytochalasin D. 172
3.21 GP of laurdan upon cytoskeleton disruption. 172
3.23 Effect of cholesterol depletion on laurdan lifetime in cell membranes. 175
3.24 Phasor clouds of plasma membrane pixels in control and cholesterol-depleted cells, at 25^{o}C. 176
3.25 Phasor histograms of control and cholesterol-depleted cells. 176
3.26 GP images of HeLa cells upon cholesterol depletion. 177
3.27 GP histograms of HeLa cell membranes upon cholesterol depletion at varying temperatures. Data is from one of the datasets used for lifetime analysis. 177
3.28 Effect of cholesterol depletion on rotational correlation time of laurdan in cell membranes. 178
3.29 Effect of cholesterol depletion on static order parameter of laurdan in cell membranes. 178
3.30 Lifetime analaysis in GPMVs of cholesterol-depleted cells. 180
3.31 GP analysis in GPMVs from cholesterol-depleted cells - samples are the same as in Fig. 3.30. 181

4.1 Hyperspectral Raman microscopy image of a HeLa cell imaged using PCA. 185
4.2 Multi-component HeLa cell images used for PCA-FLIM simulations. 188
4.3 Example of the determination of goodness of fit for 2-component simulated data. . 189
4.4 Eigenvalues and alpha metrics on a three-component simulation. 190
4.5 Determination of the lower threshold for image autocorrelation metric α. 191
4.6 PCA score images from three-component simulated image (τ_1=1.5 ns, τ_2= 3 ns, τ_3= 6 ns, 1000 photons per pixel on average). 191
4.7 Variance-scaled PCA score images from three-component simulated image (τ_1=1.5 ns, τ_2= 3 ns, τ_3= 6 ns, 1000 photons per pixel on average). 192
4.8 Poisson noise-scaled PCA score images from three-component simulated image (τ_1=1.5 ns, τ_2= 3 ns, τ_3= 6 ns, 1000 photons per pixel on average). 193
4.9 Effect of photon-counting variances on PCA using a simple simulation of 2 correlated bins. 194
4.10 Evaluation of PCA performances on two bins for varying average bin intensities. . 195
4.11 Visual representation of the NC-PCA procedure. 198
4.12 Examples of NC-PCA results for simulated FLIM images containing one, two or three fluorescence decay components. 199
4.13 FLIM image parameter sweep: each simulation is represented by a point in the parameter space. 200
4.14 Comparison of and metrics on 2-component simulated data with varying intensities and lifetime values. 201
4.15 Contour plots showing the minimum intensity necessary for the accurate number of decay components to be detected in two-component simulated data for varying lifetime combinations. 202
4.16 Contour plot showing the minimum intensity necessary for the accurate number of decay components to be detected in three-component simulated data for varying lifetime combinations. 202
4.17 Comparison of NC-PCA with minimal fraction of donor and phasor methods on a simulated FLIM FRET dataset. 204
4.18 Effect of non-fluorescent background offset on NC-PCA results. 205
4.19 Phasor clouds for 0 (left), 1 (centre) and 5 (right) counts per bin, on the same data as in Figure 4.18. 205
4.20 Effect of the IRF width on NC-PCA results for simulated 2-component data. . . . 206
4.21 NC-PCA results on a fluorescent bead in glycerol. 207
4.22 Phasor analysis of the FLIM image of a fluorescent microbead in glycerol. 208

4.23 HeLa cells stained with di-4-ANEPPDHQ and analyzed with NC-PCA. 209
4.24 Comparison of NC-PCA and phasor projections on FLIM images of HeLa cells stained with di-4-ANEPPDHQ. 210
4.25 The effect of cholesterol depletion on cell plasma membranes. 211
4.26 Illustration of NC-PCA based filtering. 212
4.27 Simulation of simple anisotropy image data for validation of PCA method and noise correction. 213
4.28 PCA results with 3 different scalings applied to simulated anisotropy image data. . 214
4.29 Testing the effect of intensity parameters on NC-PCA of anisotropy data. 215
4.30 Minimum intensities necessary to resolve two anisotropy decay components in an image as a function of θ. 216
4.31 Fluorescein in 60:40 and 80:20 glycerol:water mixtures. 218
4.32 NC-PCA on anisotropy data of fluorescein in water-glycerol mixtures. 219
4.33 NC-PCA results on the intensity decays of fluorescein in glycerol. 219
4.34 2-D histograms displaying contrast in the data according to anisotropy and lifetime. 220
4.35 NC-PCA on time-resolved anisotropy image of a SM-Chol 7:3 vesicle stained with di-4-ANEPPDHQ. 221
4.36 Analysis of pixel values for intensity, steady-state anisotropy and NC-PCA anisotropy results. 222

List of Tables

1.1 A brief comparison of scanning and wide-field techniques 51

1.2 Table showing the simulated parameters to compare the effect of weighting on fitting accuracy. 74

2.1 Artificial membrane models: sizes, preparation methods and applications. 88

2.2 Viscosity of water-glycerol mixtures at 22^{o}C. 111

2.3 Solvents used to study the lifetime-emission wavelength relationship of laurdan. . 117

2.4 Summary of parameters for the linear fit between τ_{av} and θ for DOPC. 124

2.5 Summary of parameters for the linear fit between τ_{av} and θ for POPC. 126

2.6 Summary of the variation in parameters over the temperature range investigated. . 132

2.7 Summary of the linear fit results and ranges of variation for parameters in DOPC-Chol GUVs. 133

2.8 Summary of parameters for the linear fit between τ_{av} and θ for DPPC:Chol 7:3. . 136

2.9 Ranges of variation of the bilayer parameters for DPPC and DPPC:Chol 7:3. . . . 137

3.1 Ranges of variation between 25 and 37^{o}C for the parameters in HeLa cells. 160

3.2 Linear fit parameters for GPMVs. 169

3.3 Cholesterol depletion experiments in the literature. 174

5.1 Summary of figures subject to copyright in this thesis. License to re-use was obtained for print and electronic formats. 234

List of abbreviations and acronyms

ADC: Analog to Digital Converter

AFM: Atomic Force Microscopy

BODIPY: Boron-Dipyrromethene

BP: Bandpass

CFD: Constant Fraction Discriminator

DAPI: 4',6-diamidino-2-phenylindole

DCVJ: 9-(2,2-Dicyanovinyl)julolidine

di-4-ANEPPDHQ: 2-di-butylaminonaphthylethylpyridinium propyl-2-hydroxy-3-dimethyl-hydroxyethyl quaternary ammonium cation

DiO: 3,3'-Dihexadecyloxacarbocyanine Perchlorate

DMEM: Dulbecco's Modified Eagle's Medium

DMSO: Dimethyl Sulfoxide

DNA: Desoxyribonucleic Acid

DOPC: di-Oleyl-Phosphatidylcholine

DOPE: di-Oleyl-Phosphatidylethanolamine

DPPC: di-Palmitoyl-Phosphatidylcholine

DTT: Dithiothreitol

EM: Electron Microscopy

FBS: Fetal Bovine Serum

FCS: Fluorescence Correlation Spectroscopy

FLIM: Fluorescence Lifetime Imaging Microscopy

FP: Fluorescent Protein

FRAP: Fluorescence Recovery after Photobleaching

FRET: Förster Resonance Energy Transfer

FWHM: Full Width at Half Maximum

Ga-AsP: Gallium Arsenide Phosphide

GFP: Green Fluorescent Protein

GOI: Gated Optical Intensifier

GP: Generalised Polarisation

GPMV: Giant Plasma Membrane Vesicle

GUV/LUV/SUV: Giant/Large/Small Unilamellar Vesicle

HeLa: Henrietta Lacks (cell line)

HEPES: 4-(2-hydroxyethyl)-1-piperazineethanesulfonic acid

HOMO: Highest Occupied Molecular Orbital

IRF: Instrument Response Function

IR: Infrared

LAURDAN: Lauryl dimethylaminonaphthalene

LDL: Low Density Lipoprotein

Ld: Liquid-disordered

Lo: Liquid-ordered

LSCM: Laser-Scanning Confocal Microscopy

LUMO: Lowest Unoccupied Molecular Orbital

LUMP: Lumazine-associated Protein

mβcd: methyl-β-cyclodextrin

MLE: Maximum Likelihood Estimator

NA: Numerical Aperture

NADH: Nicotinamide Adenine Dinucleotide

NLLS: Non-Linear Least-Squares

PALM: Photoactivation Localisation Microscopy

PCA: Principal Component Analysis

PBS: Phosphate Buffered Saline

PFA: Paraformaldehyde

PM546: Pyrromethene 546

PMT: Photomultiplier Tube

POPC: 1-Palmitoyl-2-Oleyl-Phosphatidylcholine

PSF: Point-Spread Function

RFP: Red Fluorescent Protein

ROI: Region of Interest

SIM: Structured Illumination Microscopy

SLB: Supported Lipid Bilayer

SPIM: Selective Plane Illumination Microscopy

STED: Stimulated Emission Depletion

STORM: Stochastic Optical Reconstruction Microscopy

SVD: Singular Value Decomposition

TAC: Time to Amplitude Converter

TCSPC: Time-Correlated Single Photon Counting

TDM: Transition Dipole Moment

Ti:Sapphire: Titanium:Sapphire

TIRF: Total Internal Reflection Fluorescence

TPE: Two-photon Excitation

TTS: Transit Time Spread

TR-FAIM: Time-Resolved Fluorescence Anisotropy

U-2 OS Human Bone Osteosarcoma cell line

UV: Ultraviolet

Organisation of this thesis

In the first chapter, the basic principles of fluorescence, microscopy and TCSPC are presented, and time-resolved data analysis methods are compared and discussed. In particular, a theoretical and analytical framework enabling the quantification of membrane order parameters from time-resolved fluorescence anisotropy data is established.

In the second chapter, current knowledge about the biophysical behaviour of lipid bilayers and cell membranes is summarised, and the environmental sensitivity of fluorescence membrane dyes laurdan and di-4-ANEPPDHQ is investigated with comparison to existing work from the literature, to inform on the relationship between fluorescence emission wavelength, lifetime and membrane micro-environments. Using these dyes, the relationship between the chemical nature and the physical properties of artificial membrane models is then quantified by measuring all the parameters available from the fluorescence signal - emission wavelength, excited-state lifetime, and fluorescence polarisation - on the same field of view.

In the third chapter, this method is extended to cellular membranes in cell-derived vesicles and live cells, where the roles of cholesterol and actin cytoskeleton on membrane microenvironment and order parameters are interrogated.

In the fourth chapter, strategies for the combined analysis of lifetime and polarisation-resolved images are explored, and a novel image processing method based on Principal Component Analysis is developed, with an emphasis on optimal reduction of photon-counting noise.

Chapter 1

Theory, measurement and analysis of fluorescence lifetime and polarisation microscopy

In this chapter, the photophysical mechanisms of light absorption and fluorescence emission necessary to understand fluorescence lifetime and polarisation are detailed. Then, implementation of a time-and polarisation resolved fluorescence imaging setup is described. Lastly, different methods to analyse time-resolved intensity and polarisation data are discussed and compared.

Why fluorescence to image biological systems?

Research in the life sciences seeks to understand the behaviour of biological systems at all levels. Our field of investigation has expanded over the years, integrating individual organisms in entire ecosystems on one side, and analyzing their function at cellular, subcellular and even molecular scales on the other. It logically follows that the variety, evolution and level of technical advancement of methods and instruments developed to solve biological questions is commensurate with the complexity of life. These techniques draw from mathematics, statistics, chemistry, physics and engineering. As the constitutive unit of organisms, cells are a primordial object of study for biology. Indeed, relevant biological phenomena and symptoms in most pathological states can be investigated through the observation of cell viability, migration, gene expression, structure or biochemistry. Cell cultures are used as model systems because direct, non-destructive measurements on pluricellular organisms still remain a technological challenge, though techniques such as light-sheet microscopy or high-resolution mesoscopy offer promising results. With this in mind,

high-resolution techniques allowing the visualisation of cellular function appear particularly attractive. Non-optical microscopy techniques such as Electron Microscopy (EM) and Atomic Force Microscopy (AFM) offer resolution at a molecular scale, giving information on the finest levels of organisation of living matter. In the case of EM, an electron-beam is directed to the sample, and the scattering of electrons on its features generates contrast. The wavelength of the electrons is such that the smallest structures that can be resolved are sub-nanometric. However, the technical requirements of EM (the sample must be usually coated with conductive layers or cut into thin sections, and imaged in a vacuum) make it wholly incompatible with live-cell imaging. AFM can be used to interrogate the properties of single molecules and the organisation of molecular assemblies. Because they rely on the physical interaction between the sample and the tip of a microscopic probe scanning the sample, AFM is nowadays limited to surface studies or ex-vivo experiments.

Yielding a maximal resolution of up to a few hundreds of nanometers (before the introduction of super-resolution microscopy, as will be discussed further) and being compatible with live cells, optical microscopy has risen as a technique of choice for imaging such systems. However, most cellular samples are thin and transparent, so historically the initial issue was the generation of contrast in the image. Simple methods include colored or absorbing dyes such as eosin staining, which are still used in histochemical studies [1]. Polarisation and phase-based transmitted-light optical designs, such as Phase Contrast or Differential Interference Contrast, have advanced the field considerably (with the Nobel Prize awarded to Zernike in 1953 for the invention of phase contrast [2, 3]). Nowadays, the most widespread technique is the introduction of fluorescent dyes in the sample and the collection of emitted fluorescence. The specificity and tunability of fluorescent molecules, the possibility of multiplexing and functional imaging have made fluorescence microscopy increasingly popular over the past few decades. Methods allowing the improvement of spatial resolution include scanning confocal microscopy, two-photon excitation and near-field techniques such as Total Internal Reflection Fluorescence (TIRF). More recently, localisation microscopy has achieved lateral resolutions well below the Abbe diffraction limit [4], launching optical imaging in the realm of nanoscopy. Being inherently multiparametric, the photophysical effect of fluorescence in itself can be used in many ways to inform about a biological sample. Indeed, spectrum, intensity, excited-state lifetime, and polarisation, can be measured [5]. In this work, it was attempted to utilise the full scope of information provided by fluorescence to achieve multi-parametric imaging of lipid bilayers and cell membranes.

1.1 Fluorescence is a light-matter interaction

1.1.1 Modalities of light absorption

Fluorescence is a type of light-matter interaction which arises from the creation of electronically excited states in a molecule upon absorption of a photon. In most cases of fluorescence we are concerned with, the energy of the absorbed photon corresponds to a quantised $\pi \rightarrow \pi^*$ orbital transition in the molecule, the electron of the Highest Occupied Molecular Orbital (HOMO) being promoted to a singlet state (the spin of the electron is conserved) in the Lowest Unoccupied Molecular Orbital (LUMO) [6]. The energy of the $\pi \rightarrow \pi^*$ transition is lowered by the presence of conjugated π systems, so it logically follows that fluorophores usually contain such features. The larger the conjugated system, the lower the transition energy, and therefore the longer the fluorescence excitation and emission wavelengths. As an example, some fluorophores of relevance to this project are shown in Fig.1.1 below.

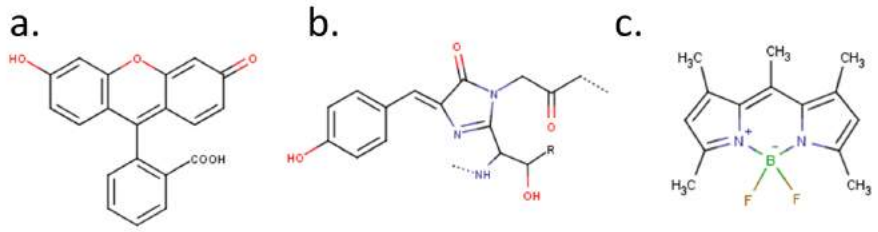

Figure 1.1: Some examples of organic fluorescent dyes. a: Fluorescein ; b: fluorophore of the Green Fluorescent Protein ; c: PM546 - the fluorophore of fluorescent molecular rotor BODIPY.

The probability of a transition occurring between electronic states is linked to the strength of the interaction between this molecule and the electric field of the excitation. This can be understood by considering the fluorescent molecule and the incident radiation as a charged particle in an electric field. In this situation, the interaction energy is given by the general scalar product:

$$E = -\overrightarrow{\mu}.\overrightarrow{\epsilon} \tag{1.1}$$

Where the vectors $\overrightarrow{\mu}$ and $\overrightarrow{\epsilon}$ are the dipole moment of the system and the electric field vector, respectively [7]. The dipole moment is a summation of the products of individual charges by their position vectors, for all charges in the system. Calculating an expectation value for the dipole moment logically involves the use of the wave-functions ψ (related to the probability density functions of electronic positions) of the system integrated over all directions of space:

$$\langle \overrightarrow{\mu} \rangle = \int\int\int \psi^{tr} \mu \psi dx dy dz \tag{1.2}$$

Our interest resides in the study of the electronic transition. The interaction energy in the case of a transition is hence given by using the transition dipole moment $\overrightarrow{\mu_T}$, the calculation of which requires the wavefunctions of the initial and final states ψ_i and ψ_f :

$$\langle \mu_T \rangle = \iiint \psi_f^{tr} \, \mu \, \psi_i \; dxdydz \tag{1.3}$$

And accordingly adapting 1.1, we now have: $E_T = -\overrightarrow{\mu_T}.\overrightarrow{\epsilon}$. The transition dipole moment (TDM) is therefore a vectorial proportionality factor between the transition interaction energy and the electric field vector. The probability of transition is proportional to E_T^2 (in the same way the probability density function for electronic positions is proportional to ψ^2), hence it is proportional to $cos^2\alpha$, with α, the angle between $\overrightarrow{\epsilon}$ and $\overrightarrow{\mu_T}$ (by definition of the scalar product). It is interesting to know this, because the direction of the electric field vector in the case of a propagating electromagnetic wave is also known as its polarisation. Now considering the excitation process in a dynamic way, absorption of a photon very rapidly deforms the electronic cloud of the molecule [8]. The nuclei are affected by this deformation and are hence not at equilibrium position, which leads them to vibrationally transfer energy to their surroundings. To understand this, let us schematically consider a two-atom molecule described by a Morse potential (Fig.1.2).

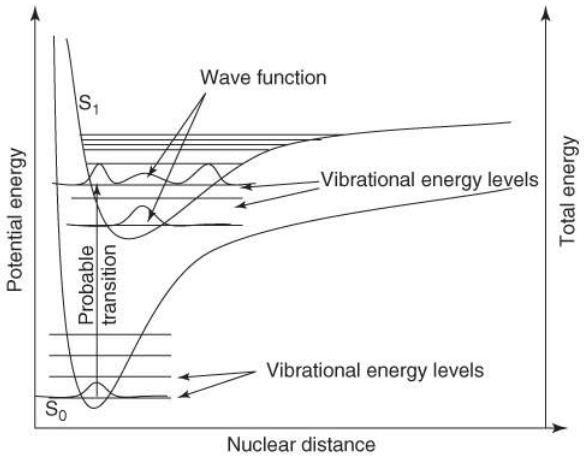

Figure 1.2: The Franck-Condon model explains modalities of photon absorption and emission. The excited state leads to a shifted electronic potential, and the probability of the transition depends on the overlap spatial between the wavefunctions in ground- and excited-state. Reproduced from ref. [8] with permission from Wiley VCH.

Because the electronic clouds of the atoms are larger in the excited state, the equilibrium configuration is situated at a larger internuclear distance, as shown by the displacement to the right of the potential curve in S1. However, photons are absorbed at a rate much faster than would allow nuclei to move to that position. The probability of excitation to a certain vibrational level of S1 then depends on the overlap between nuclear vibrational orbitals in the ground and excited states, at matching nuclear distances [6] (so-called "vertical absorption"). Each of these

orbitals corresponds to quantised vibrational energy levels. First shown in the 1920s by Franck, this semi-classical explanation is qualified as the Franck-Condon principle and can be visualised as shown on Fig. 1.2 on the left [8, 9, 10].

As a summary, fluorescence absorption depends on the polarisation of the excitation light, and consists in the promotion of the molecule in an electronically excited singlet state. In practical terms, light absorption can be measured using a spectrophotometer. What is measured is the absorbance, which corresponds to the loss in light intensity as it travels through a sample:

$$A_\lambda = log\left(\frac{I_\lambda}{I_\lambda^0}\right) = -log(T) \tag{1.4}$$

Where I_λ^0 and I_λ are the light intensities before and after travelling through the sample, and T is the transmittance. The absorbance is linked to the molar extinction coefficient ϵ_λ and to the concentration of the sample c through Beer-Lambert's law:

$$A_\lambda = l\,\epsilon_\lambda c \tag{1.5}$$

Where l is the path length (i.e., cuvette thickness).

1.1.2 Modalities of fluorescence emission

As further formalised by Kasha in 1950 [11], nuclear relaxation to the vibrational ground state v_0 of S1 occurs typically within 10 picoseconds, which is orders of magnitude shorter than the excited state lifetime. The de-excitation pathways from (S1, v_0) back to S0, include, among others, the emission of a photon. Hence, the fluorescence photon is always emitted from this level of lower vibrational energy. This is a capital feature of fluorescence: the emission is always of lower energy, hence longer wavelengths, than the absorbed radiation; the distance between absorption and emission wavelengths is qualified as the Stokes' shift [6]. The Frank-Condon principle also applies to radiative de-excitation, as seen in 1.2 above. The molecule relaxes radiatively from (S1, v_0) to the most overlapping nuclear vibrational orbital in S0, and thereafter relaxes non-radiatively to the vibrational ground state (S0, v_0). The symmetry between vibrational levels in S0 and S1 explains the symmetry in the absorption and emission spectra of the molecule. Electronic transitions involved in photoluminescence can be helpfully represented with Jablonski-Perrin diagrams, summarising the possible de-excitation pathways upon creation of the excited state. An example of such a diagram is shown in Fig. 1.3 below [8].

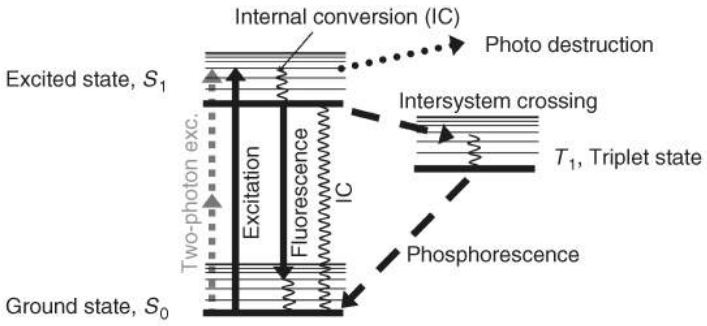

Figure 1.3: Jablonski-Perrin diagram showing the possible pathways for photon absorption (on the left), fluorescence emission (middle), as well as the occurrences of inter-system crossing, internal relaxation and phosphorescence. Reproduced from ref. [8] with permission from Wiley VCH.

While the absorption and emission processes in themselves can be considered instantaneous, the lifetime of the excited state is typically of a few nanoseconds. Fluorescence spectroscopy and imaging rely on the detection of photons spontaneously emitted from S1, as seen in the previous paragraphs. However, many other non-radiative de-excitation pathways compete with fluorescence, and the probability of each of them is kinetically determined. One can hence define the quantum yield Γ of a fluorophore as the ratio between the number of emitted photons over the number of absorbed photons, which is also the ratio of the radiative rate k_r over the sum of the rates of all possible relaxation pathways, $k_r + k_{nr}$:

$$\Gamma = \frac{k_r}{k_r + k_{nr}} \tag{1.6}$$

Non-radiative decay pathways include internal conversion, such as twisting, as occurs in molecular rotors [12], electron transfer (e.g., in chlorophylls), molecular collisions, quenching by metal surfaces [13] or solutes [14, 15], and Förster Resonance Energy Transfer (FRET), the modality of which will be described later in this section.

1.1.3 The fluorescence emission spectrum

As mentioned above, fluorescence is characterised by a shift between the excitation and emission wavelength, the Stokes' shift. Because of the many possible transitions from vibrational levels of S0 to S1 (and conversely, from the vibrational ground state of S1 to S0), and the existence of additional rotational levels, fluorescence at ambient temperatures is characterised by a distribution of absorption and emission wavelengths rather than single lines, which is further broadened by various solvent effects. These distributions are the absorption and fluorescence emission spectra, as illustrated in Fig. 1.4. The likeness in vibrational levels between S0 and S1 explains the mirror symmetry of the absorption and emission spectra. The emission wavelength of a fluorophore is determined by structural elements such as the size of a delocalised system, and also, in some cases, by

the environment of the fluorophore. Indeed, dipole-dipole interactions between the fluorophore and the medium can modify the energy level of the excited state; this effect is called solvatochromism and can be used for sensing purposes. An example of solvatochromism will be shown in more detail in Chap. 2.

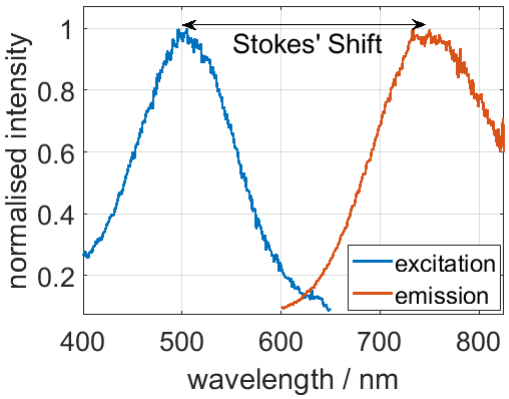

Figure 1.4: Excitation and emission spectra of di-4-ANEPPDHQ in a glycerol-water solution. Emission was recorded for a 488 nm excitation, and excitation for a 750 nm emission. The Stokes' shift is highlighted by the double arrow. Note that the excitation spectrum corresponds to the fluorescence intensity collected at a set emission wavelength, and is therefore not equivalent to the absorption spectrum.

1.1.4 Fluorophores in biological imaging

Several types of fluorescent molecules are available for spectroscopy and microscopy in the biological sciences:

- Organic fluorophores can be synthesized to have an affinity for specific biological environments such as subcellular organelles. Examples include lipophilic dyes to stain cell membranes such as the DiO family [16], or nucleic acid dyes which intercalate in the groove of the DNA double helix such as DAPI. Another possible way of targeting organic fluorophores to specific compartments is by attaching them to antibodies directed against a particular epitope. This is the principle of immunofluorescence, and has been used extensively in combination with confocal microscopy as well as localisation microscopy. The advantages of organic fluorophores include their high quantum yield, small size, their tunability and versatility.

- Genetically-encoded fluorescent proteins have greatly advanced the field of fluorescence imaging, since the discovery of wtGFP in the jellyfish Aquaeora victoria and its refinement into the GFP family by the 2008 Nobel Prize in Chemistry Laureates R. Tsien, O. Shimomura and M. Chalfie [17]. Genes of proteins of interest can be fused to to the gene of a fluorescent

protein, and this genetic construct inserted into cells in the form of a plasmid, using transfection techniques. The cell then expresses a fluorescently-tagged version of the protein. FPs have been extended to cover the full visible spectrum, and photoactivatable FPs have also been developed for super-resolution imaging purposes.

- Techniques intermediate between exogenous labeling and genetically-encoded fluorescent proteins include the HALO-Tag system [18], whereby a genetically-encoded modified dehalogenase enzyme binds a halogenoalkane substrate, itself tagged with an organic fluorophore. Another such example are the FlAsH/ReAsH biarsenical reagents, which become fluorescent when bound to a tetracysteine residue which can be added to a recombinant protein of interest [19].

- In some cases, endogenous fluorophores, i.e., fluorescent molecules produced by the biological sample itself, can be informative. For example, metabolic cofactor NADH is fluorescent, and its fluorescence signal changes between its bound or unbound state, which can be used to reveal orientation towards glycolytic or oxidative pathways [20, 21].

1.2 Fluorescence lifetime

The fluorescence lifetime describes the characteristic time that a fluorophore stays in the excited state before emission of the fluorescence photon, and it is considered an intrinsic property of the molecule, related to its spectral properties through the Strickler-Berg equation [22]:

$$k_r = \frac{1}{\tau_0} = 2.88.10^{-9} n^2 \frac{\int I(\nu) d\,\nu}{\int I(\nu)\nu^{-3} s\,\nu} \int \frac{\epsilon(\nu)}{\nu} d\nu \tag{1.7}$$

Where τ_0 is the natural lifetime, ϵ is the molar extinction coefficient and ν the wavenumber. Interestingly, k_r also depends on the refractive index of the medium, n^2, with higher refractive indices linked to shorter lifetimes.

To understand fluorescence lifetimes and how to measure them, the dynamics of population decay from the excited state to the ground state and the corresponding fluorescence intensity can be solved using a kinetic model [6]: let $[N^*]$ be the number of molecules of a sample in the excited state after an infinitely short pulse, and I the fluorescence intensity. The evolution of $[N^*]$ depends on the decay rates k_r and k_{nr}, and fluorescence intensity is proportional to the radiative rate constant k_r.

$$\begin{cases} \frac{d[N^*](t)}{dt} = -(k_r + k_{nr})[N^*](t) \\ I(t) \propto k_r[N^*](t) \end{cases} \tag{1.8}$$

Therefore:

$$\begin{cases} [N^*](t) = [N^*]_0 e^{-t/\tau} \\ I(t) = A e^{-t/\tau} \\ \tau = \frac{1}{k_r + k_{nr}} \end{cases} \tag{1.9}$$

Where τ is the excited-state lifetime of the molecule and includes the radiative and non-radiative components of the decay to the ground state. $[N^*]_0$ is the number of molecules in the excited state at t=0, and A is the initial intensity, which is determined by $[N^*]_0$ and k_r. This consideration brings us to some essential points concerning fluorescence lifetime. The most obvious one is that the evolution of intensity emanating from a population of fluorophores after a delta excitation is an exponential decay function, the exponential factor being linked to the decay rate.

If the population of fluorophores or micro-environments in the sample are heterogeneous, it is likely that sub-populations of fluorophores will exhibit different lifetimes; hence the intensity decay dynamics of the population will be a linear combination of several fluorescence exponentials:

$$I(t) = \sum_i \alpha_i e^{-t/\tau_i} \tag{1.10}$$

Where where α_i are the amplitudes of the respective decay times, τ_i. These lifetime parameters can therefore be recovered by fitting time-resolved intensity decay curves to exponential model functions (see section 7). The corollary is that the shape of the decay is determined by the exponential factor, and is therefore independent of initial intensity. This is of great interest in biological samples, where the concentration of fluorescent dyes or proteins cannot be readily controlled. Nevertheless, this would be of no use if the decay rates were invariant. As mentioned earlier, both the radiative and non-radiative de-excitation pathways are influenced by the properties of the local environment. Some parameters such as temperature or dioxygen will affect most fluorescent molecules in the same manner: elevated temperatures increase probability of molecular vibrations and collisions and hence increase the non-radiative decay rate. Dioxygen also quenches fluorescence through a collisional process. On the other hand, fluorophores can be tuned to display measurable shifts in decay rates according to relevant changes in their surroundings. An overview of the various parameters that have been measured through fluorescence lifetime measurements can be found in reference [14].

In conclusion, the interest of fluorescence lifetimes in spectroscopy and microscopy therefore relies on this property being concentration-independent (in concentration ranges low enough to avoid concentration quenching effects) and environmentally-sensitive. Section 6 of this chapter will mention technological solutions for the measurement of fluorescence lifetimes, and section

7 provides a few examples of how fluorescence lifetime measurements can be used for biological applications. It is worth noting that the photo-physical reason for the environmental sensitivity of fluorophores is not always understood or trivial to investigate [23], especially since it can be linked to changes in both non-radiative and radiative decay rates.

1.3 Polarisation of light and fluorescence

Unlike those of the cuttlefish [24], human eyes are not sensitive to polarisation, making it one of the properties of light less known to the public. However, many phenomena in nature are polarisation-specific, and processes such as reflection on an interface can have complex behaviours when analysed in terms of light polarisation. These aspects have been applied in microscopy, notably to obtain information on the structure of the sample at a molecular scale. The use of polarisation microscopy in conjunction with time-resolved instrumentation constitutes one important technical aspect of this work. In this section, I present the basic principle of polarisation, its exploitation in the field of fluorescence microscopy, and the instruments relevant to the implementation of polarisation-resolved microscopy.

1.3.1 Polarisation is the description of the electric field vector orientation

The polarisation of an electromagnetic wave is used to describe the evolution of the direction of its electric field vector, $\overrightarrow{E}$, as it propagates. The magnitude of this vector oscillates with a periodicity corresponding to the wavelength λ; however, the direction of this vector, while always perpendicular to the direction of the wave propagation, is not necessarily invariant (see Fig.1.5.a).

$\overrightarrow{E}$ can be, at every moment in space and time, decomposed into three spatial components in an orthogonal basis: $\overrightarrow{E_x}$, $\overrightarrow{E_y}$ and $\overrightarrow{E_z}$. Since the basis is orthogonal, we can orient one component, say $\overrightarrow{E_z}$, in the direction of the wave propagation. This leaves us with two necessary components to accurately describe the polarisation of the wave (Fig.1.5.b), both oscillating with the same frequency. The phase difference between these two components determines the polarisation state of the wave.

If $\overrightarrow{E_x}$ and $\overrightarrow{E_y}$ oscillate in phase, i.e., their maximal and minimal amplitudes coincide in time, the orientation of the field vector $\overrightarrow{E}$ is time-independent, and the polarisation is linear as shown in Fig.1.5.c).

If $\overrightarrow{E_x}$ and $\overrightarrow{E_y}$ oscillate with a phase difference of $\frac{\pi}{2}$, i.e., the maximum amplitude of one component corresponds to the minimum amplitude of the other, the possible directions of $\overrightarrow{E}$ describe a full circle as the distance of one wavelength is covered while the amplitude remains constant, and

the polarisation is circular. Any intermediate phase difference will result in elliptical polarisation, which is effectively the general case for any type of polarisation (see Fig.1.5.d). Note that unpolarised light does not exist physically speaking, but is often used to qualify the mixture of waves with different polarisations.

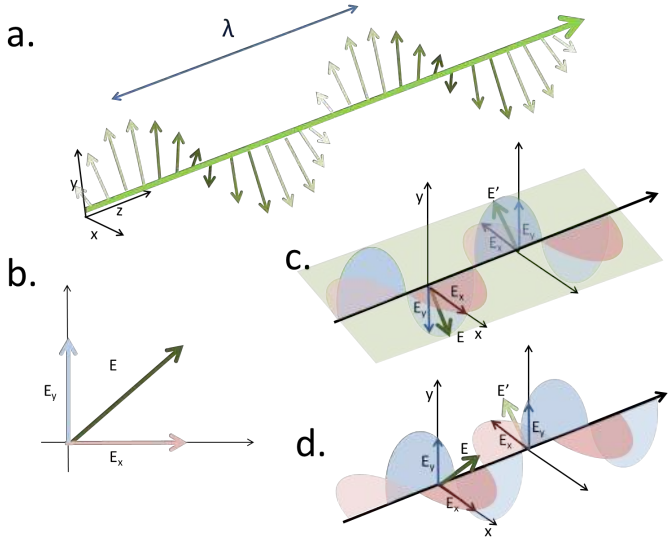

Figure 1.5: The polarisation state of light. a.: $\overrightarrow{E}$ (small green arrows) is always orthogonal to the direction of the propagation of the wave (thick green arrow). This represents an arbitrarily polarised wave, with the $\overrightarrow{E}$ oscillating in (dark arrows) and out (light arrows) of the plane of the image. b.: At any point in space and time, $\overrightarrow{E}$ can be decomposed into $\overrightarrow{E_x}$ and $\overrightarrow{E_y}$. c.: $\overrightarrow{E_x}$ (red) and $\overrightarrow{E_y}$ (blue) are in phase, and $\overrightarrow{E}$ can always be contained in an imaginary plane (in green): this wave is linearly polarised. d.: $\overrightarrow{E_x}$ (red) and $\overrightarrow{E_y}$ (blue) are out of phase; the direction of $\overrightarrow{E}$ varies periodically, describing an elliptical polarisation.

1.3.2 Fluorescence is a polarisation-specific process

The use of linearly polarised light as an excitation source in fluorescence leads to photoselection of the sample, meaning that the probability of each individual molecule to be excited depends on the orientation of its absorption TDM with respect to the electric vector in the sample plane, as seen in the previous section. additionally, considering the fluorescence emission to be a transition from a molecular state with strong dipolar strength to a weaker one, it is easy to understand that the resulting electromagnetic wave is polarised in the direction of the emission transition dipole moment [25]. This means that fluorescence polarisation is directly linked to the orientational distribution of the emitting fluorophores. The question here is to understand and formalise the nature of this relationship. Let us consider a population of randomly oriented fluorophores under polarised excitation, as described in Figure 1.6 below [6]:

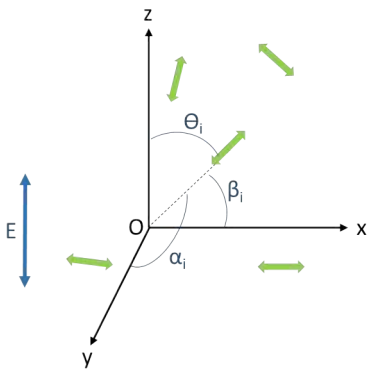

Figure 1.6: Representation of incident polarised light on a sample of randomly distributed fluorophores

The excitation light is along the Oz axis, and the fluorophores are represented by their emission transition dipole moments. $I_{\parallel}(t)$ is the sum of all emission components along Oz, and $I_{\perp}(t)$ along Ox or Oy, depending on which is the detected direction. A measure of fluorescence polarisation in space and time is the fluorescence anisotropy r:

$$r(t) = \frac{I_{\parallel}(t) - I_{\perp}(t)}{I_{\parallel}(t) + 2I_{\perp}(t)} \tag{1.11}$$

Ox and Oy are equivalent with respect to the excitation light and there is a symmetry about Oz, so essentially the result should depend only on the orientation with respect to Oz, represented by the angle θ. Mathematically speaking, r can take values between -0.5 and 1. Now, fluorescence intensity along each axis is proportional to the square of the component of the transition dipole moment along this axis, for each emitting fluorophore i (let us assume the emission TDMs have equal strength μ). Hence, for a population of fluorophores we have [6]:

$$\begin{cases} I_z(t) = I_{\parallel}(t) \propto \mu \overline{cos^2\theta(t)} \\ I_x(t) = I_y(t) = I_{\perp}(t) \propto \mu \overline{cos^2\alpha(t)} \end{cases} \tag{1.12}$$

With $\overline{cos^2\alpha}$ and $\overline{cos^2\theta}$ the average values of the cosines between the TDMs and axes Ox and Oz, respectively. Importantly, it can also be noted that $cos^2\alpha_i + cos^2\beta_i + cos^2\theta_i = 1$ for any fluorophore$i$ at all times, so the equality holds also for the average values. Because of the symmetry along Oz, we can further write: $cos^2\alpha_i = cos^2\beta_i$ and therefore $cos^2\theta_i = 1 - 2cos^2\alpha_i$. Using these two elements, we can express anisotropy as a function of $\theta(t)$ only:

$$\begin{cases} r(t) = \frac{\overline{cos^2\theta(t)} - \overline{cos^2\alpha(t)}}{\overline{cos^2\theta(t)} + 2\overline{cos^2\alpha(t)}} = \overline{cos^2\theta(t)} - \overline{cos^2\alpha(t)} \\ \leftrightarrow r(t) = \frac{3\overline{cos^2\theta(t)} - 1}{2} = \langle P_2(cos(\theta(t))) \rangle \end{cases} \tag{1.13}$$

Where P_2 is the second-degree Legendre Polynomial [26].

1.3.3 Theory of fluorescence polarisation decay

"*Nature laughs at the difficulties of integration.*"

Pierre-Simon de Laplace

The question now resides in solving the value of $\overline{cos^2\theta(t)}$, that is, the average cosine of the emitting TDMs with respect to the excitation polarisation.

Let us firstly establish the general expression of anisotropy as a function of the distribution of fluorophores, and consider a few useful specific cases. This section is based on the understanding of founding article by Kinosita et al. [26]; the same formalism is used here with some simplifications.

The fluorophores are distributed with probability density function $W(\theta)$; each fluorophore has the ability to move position, but $W(\theta)$ in itself is stationary. At time 0, the excitation selects a sub-population proportionally to $cos^2\theta_0$, after which the fluorophores have the probability $G_{\theta_0}(\theta_t)$ to rotate in new position θ_t at time t, point at which their contribution to the fluorescence anisotropy is given by $P_2(cos\theta_t)$. This is the result of the previous section. Integration over all possible orientations θ_0 and θ_t yields the following expression:

$$r(t) = \int\int 3cos^2\theta_0 W(\theta) G_{\theta_0}(\theta_t) P_2(cos\theta_t) d\theta_0 d\theta_t \tag{1.14}$$

The factor of 3 ensures unit excitation. Since $W(\theta)$ is a stationary function, the conditional probability function $G_{\theta_0}(\theta_t)$ is equivalent to the probability of a certain displacement $p(w_{\theta,t})$ occuring within time t, with $w_{\theta,t} = \theta_t - \theta_0$.

We therefore obtain $\theta_t = \theta_0 + w_{\theta,t}$ and $cos(\theta_t) = cos(\theta_0)cos(w_{\theta,t}) - sin(\theta_0)sin(w_{\theta,t})$. Given this result, the addition theorem of the Legendre polynomials [27] also allows us to write: $P_2(cos\theta_t) = P_2(cos\theta_0)P_2(cos\, w_{\theta,t})$. Ulterior terms depend on azimuthal angles α, which we have seen in the previous section, disappear due to the symmetry of the problem. Eq. 1.14 then becomes:

$$r(t) = \int 3\, cos^2\theta_0 W(\theta) P_2(cos\theta_0) d\theta_0 \int P_2(cos\, w_{\theta,t}) p(w_{\theta,t}) d\theta \tag{1.15}$$

The first integral term only depends on the initial distribution of θ_0, so can be written as an initial term r_0:

$$\begin{aligned} &= r_0 \int P_2(cos\, w_{\theta,t}) p(w_{\theta,t}) d\theta \\ &= r_0 \langle P_2(cos\, w_{\theta,t}) \rangle \end{aligned} \tag{1.16}$$

It is now clear that the evolution of anisotropy after a pulse excitation is determined by an initial term r_0, which depends on initial sample configuration, and a dynamic term, $\langle P_2(cos\, w_{\theta,t}) \rangle$, which describes the temporal evolution of fluorophore distribution. These two terms are discussed

in the following paragraphs.

1.3.3.1 Case of a uniform distribution of fluorophores rotating freely.

Initial anisotropy term r_0. The first integral term from Eq. 1.15, which we have condensed in r_0, represents the initial contribution to anisotropy determined by the distribution $W(\theta_0)$. If the fluorophores are uniformly distributed in space, we can write (using the probability of finding a fluorophore in a surface of infinitesimal area $sin\theta d\phi d\theta$) [6]:

$$W(\theta)\, d\theta = \frac{1}{2}\, sin\theta\, d\theta \tag{1.17}$$

The first term of Eq. 1.15 can now be calculated using Eq. 1.17 :

$$r_0 = \frac{3}{4}\int_0^{\pi} (3cos^4\theta_0 - cos^2\theta_0)\, sin\theta_0 d\theta_0 \tag{1.18}$$

This calculation yields a value of $r_0 = 2/5$. In practice, while isotropy is a reasonable hypothesis in many samples, the absorption and emission transition dipole moments are rarely perfectly collinear, and the microscope introduces a number of depolarising artifacts, yielding a more realistic value for r_0 between 0.2 and 0.39, depending on the NA of the objective [28].

Dynamic anisotropy term. The dynamic integral term of Eq. 1.15, $\langle P_2(cos\, w_{\theta,t})\rangle$, represents the evolution of the distribution of the photoselected fluorophores, and depends essentially on the law determining the angular displacement $w_{\theta,t}$. It is interesting to note that this expression also can be used to correct the anisotropy of fluorophores with nonparallel TDMs, by including this phenomenon as an additional term contributing to an angular displacement of the emission from the absorption. Here again, several possible scenarios arise. In the case of free rotation, the law of $w_{\theta,t}$ is given by Brownian motion [6]:

$$\frac{\partial w_{\theta,t}}{\partial t} = D_r \nabla^2 w_{\theta,t} \tag{1.19}$$

D_r being the diffusion coefficient. Resolution of this differential equation in spherical coordinates yields a single exponential function:

$$r(t) = r_o e^{-6D_r t} \tag{1.20}$$

In the case of free rotation, the anisotropy hence decays exponentially from the initial value r_0, at a rate determined by diffusion. One can then use the Einstein-Stokes equation to extract the dynamic viscosity, assuming a spherical molecule:

$$\eta = \frac{k_B T}{6 D_r V} \tag{1.21}$$

Where k_B is the Boltzmann constant, T the absolute temperature and V the hydrodynamic volume of the molecule.

If the molecule is non-spherical, then the model becomes more complex, with Eq. 1.20 becoming multi-exponential: the molecule rotates along several axes, each of which contributes to the depolarisation at a different rate [29]. As a summary, Fig. 1.7 shows the polarisation-resolved intensity decays of fluorescein in glycerol and the resulting anisotropy decay, fitted to a mono-exponential decay curve ($\tau_c = 6.75 \pm 0.08$ ns).

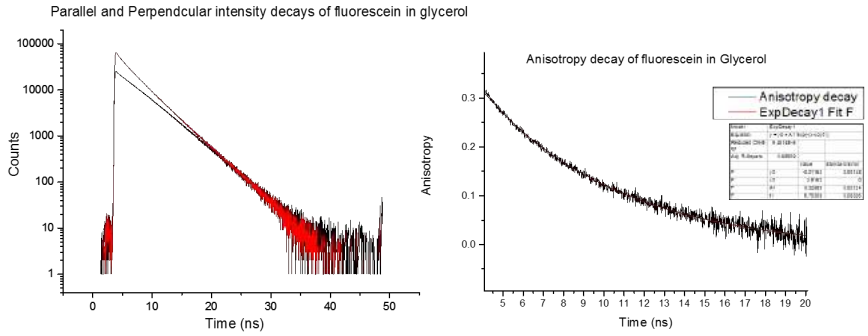

Figure 1.7: Example of polarisation-resolved intensity (left) and corresponding anisotropy (right) decays of fluorescein in glycerol.

1.3.3.2 Case of membranes: non-uniform fluorophore distribution with hindered rotation ("wobble-in-cone" model)

Initial anisotropy term r_0. Fluorophores may have a distribution restricted by their environment, for example in membranes, as shown schematically in Fig. 1.8.

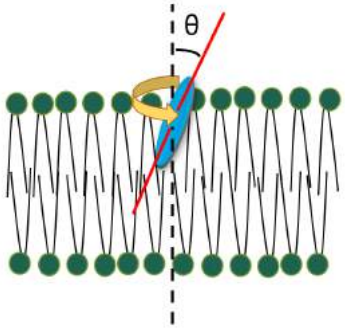

Figure 1.8: Schematic representation of a fluorophore (in blue) inserted in a lipid bilayer. The yellow arrow indicated rotational diffusion of the fluorophore; θ is the angle between the fluorophore TDM (along the red line) and the membrane normal n (dashed black line).

Several models exist to describe this type of restricted distribution and motion in lipid bilayers.

We will mention two of them here; note that it is now useful to use θ as the angular displacement from the normal to the membrane.

1. In the "rigid cone" uniform distribution, the fluorophore lives in a cone with half-angle θ_c, with a uniform probability distribution function within the cone, and null probability outside. This case produces a result close to Eq. 1.18, r_0 depending on the critical angle θ_c and ranging between -0.5 and 1, depending on the angular freedom and the orientation between the excitation and $\theta = 0$:

$$\begin{cases} W(\theta)d\theta = k(\theta_c)sin\theta d\theta & for\, \theta \in [0\, \theta_c] \\ W(\theta) = 0 & elsewhere \end{cases} \tag{1.22}$$

   In the case of ordered environments such as membranes, we understand that the anisotropy may be much greater than the usual maximum of 0.4; and orthogonal excitation and molecular arrangements can even yield negative values.

2. Another, possibly more realistic model dictates that the position of fluorophores is determined by their diffusion within a potential $V(\theta)$ on a unit sphere. In this case, the distribution can be written as:

$$W(\theta) = b\, e^{-V(\theta)/k_B T} \tag{1.23}$$

With b a constant, k_B the Boltzmann constant and T the absolute temperature. Conveniently, this model can be reconciled with a Gaussian distribution, where the fluorophore can occupy any position within a half-sphere, with a normal probability distribution following θ:

$$W(\theta) = c\, e^{q^2 cos^2 \theta/2} \tag{1.24}$$

With c a constant and q describing the spread of the distribution.

Both models are visualised schematically on Fig. 1.9 below.

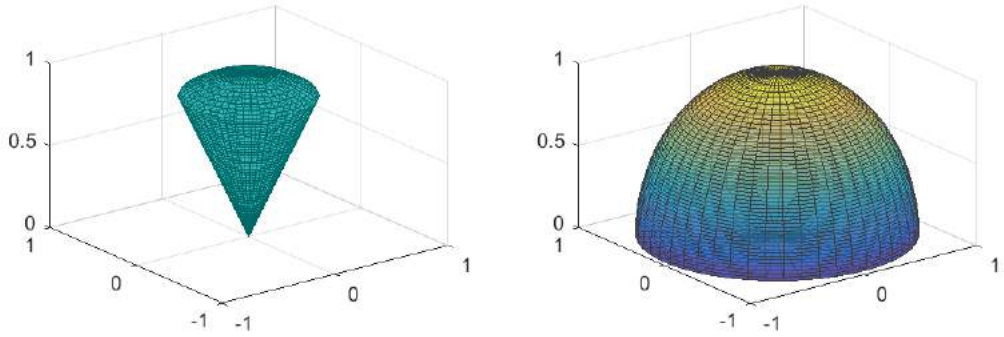

Figure 1.9: Domains of existence of membrane fluorophores according to the hard-cone model (left), and Gaussian model (right). The colours indicate the probability of the angular positions (high probability in yellow, low in purple). The spatial coordinates are arbitrary.

Dynamic anisotropy term If the rotation is hindered by environments such as lipid bilayers, the model of fluorophore diffusion within a potential can be used to solve the dynamic anisotropy term, as exposed in Eq. 1.23. The differential equation corresponding to the law of $w_{\theta,t}$ becomes:

$$\frac{\partial w_{\theta,\phi,t}}{\partial t} = D_r\left(\frac{1}{sin\theta}\frac{\delta^2}{\delta\theta^2}sin\theta + \frac{\delta^2}{\delta\phi^2}\frac{1}{sin^2\theta}\right) w_{\theta,\phi,t} \tag{1.25}$$

ϕ is the azimuthal angle with respect to the membrane normal n. One can see the similarity with free rotational motion as written in Eq. 1.19, in this case with symmetry along ϕ and dependence on polar angle θ. Kinosita et al give the following solution to this differential equation:

$$r(t) = r_0 \sum_i^{\infty} A_i e^{-D_r t/\sigma_i} \tag{1.26}$$

Where A_i and σ_i are functions of θ_c. This is not useful, since this represents an infinity of parameters which cannot be resolved by fitting of experimental data. The following simplification is proposed by Kinosita et al. by comparing their model to experimental data:

$$r(t) = r_0\left(A_\infty + (1 - A_\infty)e^{-D_r t/\langle\sigma\rangle}\right) \tag{1.27}$$

Where $A_\infty = \frac{r_\infty}{r_0}$, fully determined by θ_c. The term$\langle\sigma\rangle = \sum A_i\sigma_i$ contains all the information determined by θ_c in the dynamic anisotropy term. By letting $\tau_c = \frac{\langle\sigma\rangle}{D_r}$ and replacing A_∞ by its value $\frac{r_\infty}{r_0}$, we obtain the well-known relation for the decay of anisotropy in membranes:

$$r(t) = (r_0 - r_\infty)\, e^{-t/\tau_c} + r_\infty \tag{1.28}$$

While this is a relatively simple equation and is widely used in the anisotropy community, this paragraph has allowed us to understand the complexity underlying the decay of polarisation in membranes. It is also interesting and important to remember that this result is an approximation

of the exact solution for Eq. 1.25.

Order parameters. In conclusion, two membrane order parameters were adapted from this theoretical basis and used throughout this work:

- The static order parameter $\Delta = \frac{r_0 - r_\infty}{r_0} = 1 - A_\infty$. This parameter is fully determined by θ_c and represents the extent of rotational motion. In the case of fully aligned and immobile fluorophores, there is no decay of anisotropy, $r_\infty = r_0$ and $\Delta = 0$. In the opposite limiting scenario, if the fluorophore population is fully randomised at long times after the excitation, then $r_\infty = 0$, and $\Delta = 1$.
- The dynamic order parameter $\tau_c = \frac{\langle\sigma\rangle}{D_r}$. This exponential decay term represents the rate of rotational motion, and interestingly, depends on the diffusion coefficient D_r as well as the maximum cone angle θ_c (through $\langle\sigma\rangle$).

1.3.4 Steady-state anisotropy

Steady-state anisotropy is instrumentally easier to compute, since it does not require time-resolved equipment. On a time-resolved setup, it can also be obtained through integration of the polarisation-resolved channels:

$$\begin{aligned} r_{ss} &= \frac{\int I_\parallel(t) - G I_\perp(t)\, dt}{\int I_\parallel(t) + 2G I_\perp(t)\, dt} \\ &= \frac{\int r(t) I(t) dt}{\int I(t) dt} \end{aligned} \tag{1.29}$$

Though information about r_0 and decay rate are lost, steady state anisotropy still reports on the ordering of a sample with a single value, and is relevant in imaging contexts where the photon capital is too low to obtain reliable anisotropy decays. By assuming $I(t) = Ae^{-t/\tau}$ (single exponential decay), and using $r(t) = (r_0 - r_\infty)e^{-t/\tau_c} + r_\infty$, one obtains after integration:

$$r_{ss} = \frac{r_0 - r_\infty}{1 + \tau/\tau_c} + r_\infty \tag{1.30}$$

This is termed the Perrin equation, by which steady-state anisotropy is related to the rotational correlation time τ_c, the fluorescence lifetime τ and the anisotropy limiting values r_0 and r_∞. When fixed samples are investigated, the dynamic depolarisation is removed, and steady-state anisotropy reports directly on r_0 (save the instrumental depolarisation), and so is used in spectroscopy to inform on the orientation of absorption and emission TDMs, for example [30]. Some examples of applications of time-resolved and steady-state anisotropy in biological imaging are summarised in section 7.

1.4 Time-resolved fluorescence microscopy

The idea of time-resolved fluorescence imaging is the creation of images, the contrast of which is determined by fluorescence lifetime or anisotropy parameters. As seen above, these parameters determine the shape of the fluorescence emission in time after a modulated excitation, so the aim is to obtain a time-resolved intensity signal in each pixel of the image. This paragraph will focus on the technological solutions to measure fluorescence lifetimes, which can be done in the frequency domain and the time domain. Important elements of microscopy will also be laid out. The emphasis is made on time-correlated single photon counting (TCSPC), since it is the method employed in our laboratory, but alternatives are also presented.

1.4.1 Time-correlated single photon counting (TCSPC)

In time-correlated single photon counting, single fluorescence photons are detected after a pulsed excitation of fixed repetition rate, and their arrival time is measured within the excitation cycle. After many, many cycles, what is in effect obtained is an integrated distribution histogram of photon arrival times during the experiment, as shown in Figure 1.10. This arrival time histogram directly reflects the exponential decay of a population of fluorophores from the excited to the ground state, and the lifetime parameters can be recovered through exponential fitting techniques, as will be presented in Section 1.6. Ideally, the repetition rate of the experiment is set so that the full exponential decay can be sampled. Most fluorophores in biological imaging have fluorescence lifetimes between 0.1 and 10 ns, which places usual excitation frequencies in the range of 10-100 MHz.

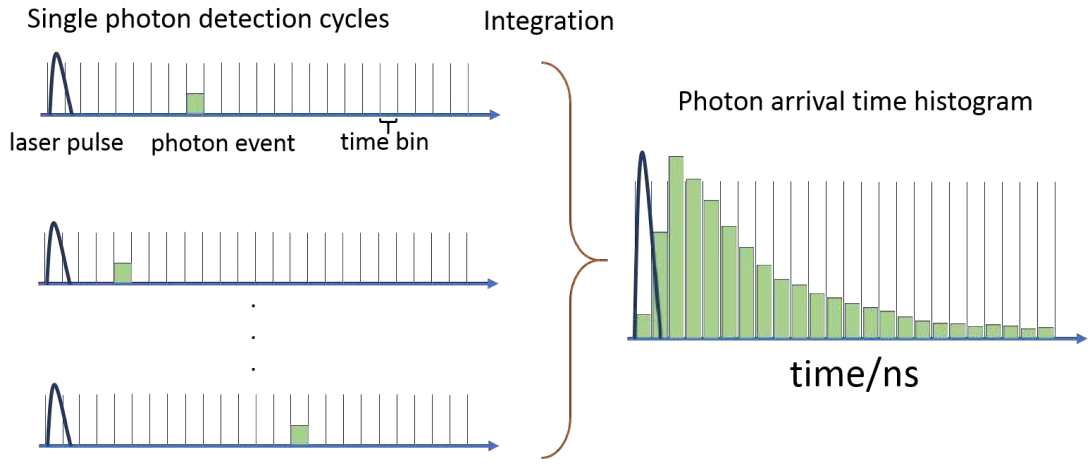

Figure 1.10: Basic principle of Time-Correlated Single Photon Counting (TCSPC): The time elapsed between the photon and a laser pulse is converted into a digital time address (left), and the integration of many single photon detection cycles constitutes an arrival time histogram of fluorescence photons (right).

TCSPC is achieved by using detectors in photon counting mode: the detector output is a train

of short, nanosecond-wide pulses of varying amplitudes (photon-counting detectors have a high amplitude jitter), as shown in Fig. 1.11. Arrival times are attributed to each detection event by processing the detector signal through several electronic building blocks.

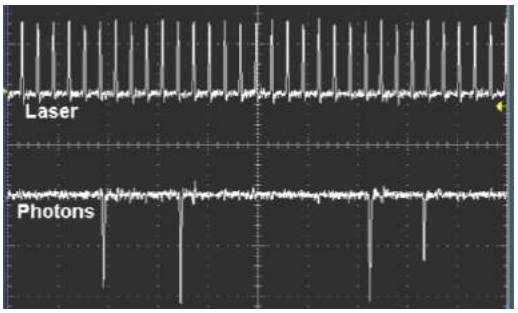

Figure 1.11: Typical detector trace (below) of fluorescence photons with pulsed laser excitation (above), from [31]. Note the reduced number of photon pulses (4) compared to the number of laser pulses (32). This is typical of a TCSPC experiment, to avoid counting loss.

In the Becker & Hickl TCSPC architecture used in this work, each photon pulse triggers a Constant Fraction Discriminator (CFD), which minimises the time-jitter from the amplitude jitter of the detector pulses. A second CFD (SYNC) is triggered by the excitation pulse. The two CFD signals trigger the START and STOP signals of a Time to Amplitude Converter (TAC). In short, the start signal comes from the detector CFD and triggers a linear ramp voltage sweep until the SYNC CFD triggers the STOP signal of the TAC. Because the TAC is launched at the detection of a photon and not at the beginning of each excitation cycle, the TAC operation rate is effectively the count rate, which is lower than the excitation rate, hence this is a big advantage in high repetition rate experiments [32]. The output voltage is now a function of photon arrival time with respect to the following laser pulse. This signal is then transformed into a time-address in the memory, which consists of a chosen number of time channels. This is done by the Analog to Digital Converter (ADC). This system architecture (represented schematically in Fig. 1.12) is slightly more complex than other possible methods which convert the CFD signal into a digital signal directly, as proposed by the PicoQuant TCSPC architecture. However, the time resolution rendered by the TAC-ADC architecture is an order of magnitude higher, in the order of a picosecond compared to fully digital methods.

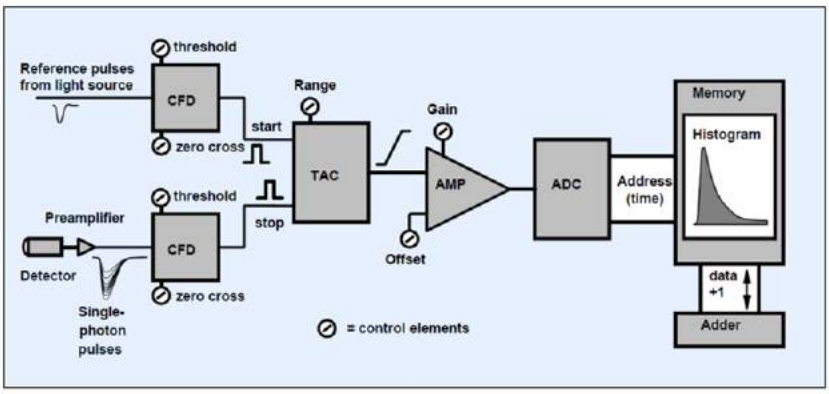

Figure 1.12: Classic TCSPC architecture, from ref. [31]

One may be tempted to question the necessity of single photon detection, given that thousands of them are required to resolve an exponential decay curve, and that it would be conceptually more efficient to collect many photons at once. The first element is that single photon counting mode uses the advantage of digital processing, where only the timing of the detected signal is used, rather than its amplitude. This yields high resolution of photon arrival times, which is limited by the transit time spread (TTS) of the detector. The TTS relates to the variability in time between the absorption of a photon at the photocathode and the emission of an electronic pulse at the anode [31, 29]. As an example, the reported TTS of the detectors used in this work is of 120 ps [33, 34]. Single photon detection also presents the advantage of high dynamic ranges and well-defined Poisson-distributed statistics linked to shot noise. The second element is purely instrumental: photon-counting detectors have a dead time which often exceeds the observation window. Physically, any photon arriving after the detected photon and within the detector dead-time will not be registered, so in effect single photons are detected in each excitation cycle. This is qualified as "counting loss" or the "photon pile-up" effect, and is undesirable; in practice, the experiment is set such that the likelihood of several photons arriving in the same time window is negligible, by adjusting the count rate of the detected photons to be much lower than the laser repetition rate. As a rule of thumb, the target count rate should be around 1% of the repetition rate (1 photon detection for 100 laser pulses) [35]. While this may sound wasteful of excitation cycles, in biological samples under investigation, it is rare that an excessive count rate should be a problem. Moreover, when operated in such a manner, the counting efficiency of TCSPC is near-ideal; indeed, very few emitted photons are lost (not detected) [36, 35].

Ultimately, the high time resolution and sensitivity of TCSPC yields accurate and precise resolution of fluorescence lifetimes. However, detector dead times still contribute to the overall slow acquisition rates of this technique. Therefore, recent technical efforts aim to overcome this issue, for example by distributing the emitted photons onto several detectors [37, 38], or by developing

new detector architectures with shorter dead times [36]. Alternatives to TCSPC such as Time-Gated FLIM and frequency-domain FLIM present the advantage of shorter acquisition times, as detailed hereafter.

1.4.2 Time-Gated FLIM

In time-gated systems, series of fluorescence images are collected at increasing delays after a short excitation pulse (Fig. 1.13). Several technical implementations of Time-Gated FLIM have been developed and adapted to different microscope systems. The lifetime information is obtained by direct analysis of the intensity decays similarly to TCSPC [39, 40], or from the intensity ratios between these time gates [41].

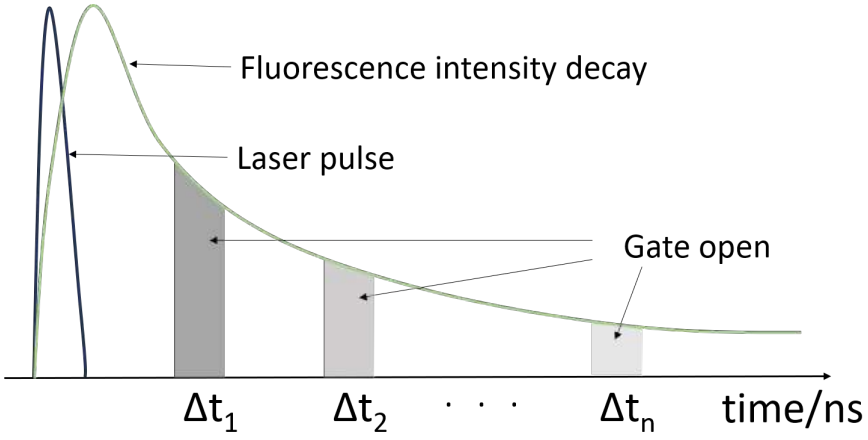

Figure 1.13: Basic principle of time-gated fluorescence detection.

One possibility for time-gated FLIM is to gate the detector, through the use of Gated Optical Intensifiers (GOI) in front of a camera to sample the fluorescence decay is sampled at increasing times, in all pixels simultaneously. This was for example implemented in the group of Prof. Paul French (Imperial College London) [42]. Elsewhere, this architecture was coupled with fluorescence anisotropy imaging by Devauges et al. to detect homo-FRET in live cells [43]. Optical sectioning techniques such as TIRF [43], structured illumination [39, 44, 45], multi-focal scanning [46], and spinning disk [47] microscopes have been developed in combination with this architecture. Though detector time-gating is less efficient than TCSPC since many fluorescence photons are discarded by the gate [48, 49], one advantage of such systems compared is their speed and compatibility with wide-field imaging. The wide-field detection allows much faster frame rates than achievable with scanning microscopes, and limits photodamage since the sample is illuminated with a homogeneous field of light (such as achieved by Köhler illumination) rather than a focused beam.

Another possibility for time-gated FLIM was for example implemented in the group of Prof. Hans Gerritsen [49, 41], whereby the output from a photon counting detector itself is divided

into time gates using a series of counters which are sequentially enabled and disables using programmable delay lines synchronized with the lased pulses. This type of system has the same excellent photon counting efficiency as TCSPC [38], and has been coupled with confocal and two-photon microscope systems. Anisotropy imaging was further implemented with two such Lifetime Modules (LiMos), which enabled the quantification of cluster sizes in homo-FRET experiments [50, 51].

1.4.3 Frequency domain FLIM

Frequency domain fluorescence lifetime imaging, the excitation is modulated in time, and the fluorescence lifetime is derived from the phase and amplitude modulation between the excitation and fluorescence signals [48, 23], as shown in Fig. 1.14. The excitation can be pulsed, similarly to time-domain measurements, or sine-modulated. Usually, both the phase and intensity demodulation signals are measured for varying excitation modulation frequencies, and used together to extract the fluorescence lifetime from the phase and modulation lifetimes, τ_ϕ and τ_m:

$$\begin{cases} \tau_\phi = \omega^{-1} tan\phi \\ \tau_m = \frac{1}{\omega}\sqrt{(\frac{1}{m^2} - 1} \end{cases} \tag{1.31}$$

Frequency-domain FLIM is often coupled with wide-field microscopy [52], though it can been used with scanning systems as well [53, 54]. Time-resolved anisotropy was also measured in the frequency domain by Clayton et al [55], where homo-FRET of GFP was detected in *E.coli* bacteria.

Frequency-domain systems allow for fast acquisition of FLIM data, and are hence compatible with imaging of biological processes. However, the resolution of complex decay profiles such as multi-exponentials and incomplete decays can be difficult using frequency-domain methods. Analysis of Frequency-domain FLIM is performed by fitting curves of phase and amplitude modulation values at different excitation modulation frequencies, or by using Fourier-domain analysis such as the phasor transformation [56], as will be presented in section 1.6.

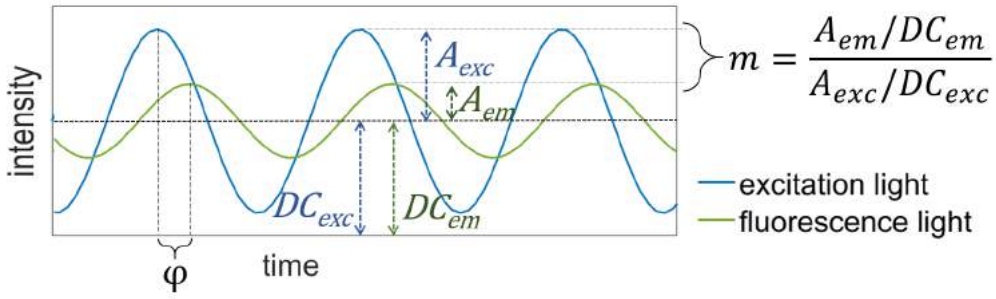

Figure 1.14: Basic principle of frequency-domain determination of fluorescence lifetimes.

1.4.4 FLIM and microscopy

The time resolution of the TCSPC system, as shown in the previous section, is in the order of picoseconds. Detectors which can achieve this are time-resolved Photomultiplier Tubes (PMTs), or in the case of our current setup, hybrid Ga-AsP detectors [34], as well as Single-Photon Avalanche Photodiodes [57, 58, 59] and cameras with a delay line anode architecture [60, 61]. PMTs and hybrid Ga-AsP detectors have no spatial resolution, so it follows that the use of these detectors in an imaging context requires scanning of the excitation beam over the field of view and pixel-wise reconstruction of the image. To this effect, the TCSPC technique can be coupled to a Laser-Scanning Confocal Microscope (LSCM) system.

1.4.4.1 Confocal microscopy and FLIM

In scanning microscopy, the laser is focused on the sample to a diffraction-limited volume, and scanned by a system of galvanometric mirrors over the desired area. Fluorescence is then collected through the objective lens and separated from the excitation beam by a dichroic mirror. The particularity of a confocal microscope is the presence of a pinhole in front of the detector in a plane optically conjugated with the sample plane, as seen in Fig.1.15. This allows dramatic improvement of the axial resolution, by physically obstructing out-of focus fluorescence emanating from z-planes above and below the image plane.

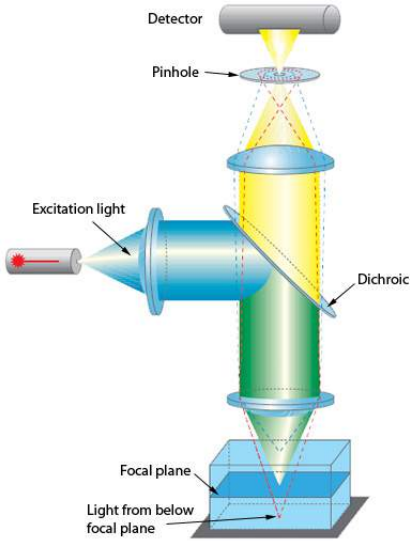

Figure 1.15: Optical sectioning in the confocal microscope: light coming from above and below the sample plane (blue and red dashed lines, respectively) is blocked from the detector by the detection pinhole. Image from ref. [62].

The optical sectioning provided by confocal microscopes has made them attractive instruments in the life sciences, and their use is widespread. However, scanning over the field of view takes time, and this makes confocal imaging much slower than camera-based, wide-field microscopy. For these reasons, it is difficult to image highly dynamic phenomena (>1 Hz) with confocal microscopes.

At the moment, TCSPC is overwhelmingly used with confocal microscopes for imaging purposes, though work is underway in our laboratory to develop wide-field TCSPC techniques, using various wide-field detectors [63, 64]. This would allow access of TCSPC-FLIM to the imaging techniques associated with wide-field microscopy. A brief comparison of wide-field and confocal microscopy is summarised in the Table 1.1 below:

Table 1.1: A brief comparison of scanning and wide-field techniques

	Scanning	Wide-Field
Speed of acquisition	-	+
Time Resolution	~10 ps	ms (without time gating)
Axial resolution	+	-
Lateral resolution improvements	LSCM, STED	PALM, STORM, SIM
Associated techniques	FCS, TCSPC, FRAP	TIRF, SPIM, SIM

1.4.5 Alternatives to confocal-TCSPC for FLIM

1.4.5.1 Two-photon FLIM

Since longer wavelengths are less prone to scattering due to weaker interactions with the small features of the sample, using excitation sources in the long wavelength range can improve penetration into the sample. To this effect, multi-photon microscopy is an attractive option for 3D live

cell and tissue imaging. A fluorescent molecule can be promoted to the excited state by absorbing one photon of wavelength λ (single photon absorption), or two simultaneous (less energetic) photons of wavelengths λ_1 and λ_2, such that $\lambda_1^{-1} + \lambda_2^{-1} = \lambda^{-1}$ [65, 66]. The fluorescence photon is then emitted following the same process in both cases (the fluorescent molecule retains no memory of its excitation process [11]. In practice, two-photon excitation is achieved by focusing the light of very short (femtosecond) laser pulses through a microscope objective. Because the likelihood of absorption is linked to the strength of the electric field vector (Eq. 1.1), two-photon excitation (TPE) can only be achieved at the focal point of the microscope objective where the electric field density is highest, hence naturally limiting fluorescence to the focal point without the need for a pinhole. Photobleaching is also reduced since the periphery of the focal point is not excited. Thanks to this remarkable phenomenon theorised by Maria Göppert-Mayer in the early XXth century [67], excitation light with near-IR wavelengths (>700 nm), which travel deeper into the sample and cause less photodamage can be used. Because multiphoton microscopy requires pulsed laser sources, it is also ideally combined with TCSPC-FLIM. Two-photon FLIM is now a widespread microscopy technique, notably to image samples in three dimensions. FLIM of autofluorescence is often carried out with multiphoton excitation, since endogenous fluorophores such as NADH usually have UV excitation bands and lifetimes below 3-4ns, compatible with the fixed high repetition rate of Ti:Sapphire lasers (around 80 MHz). More interestingly, the dynamic range of fluorescence anisotropy with 2-photon excitation is higher, since the absorption cross-section of the fluorophores is narrower: for an isotropic sample and parallel TDMs, $r_o^{TPE} > 0.4$. So why doesn't everybody use two-photon microscopes? The downsides of two-photon excitation include:

- Achieving high energy density at the focal point requires high-power, femtosecond-pulsed source such as Titanium-Sapphire lasers, which can be prohibitive in cost (>100k$).
- Titanium-Sapphire lasers are tunable in emission wavelength but the repetition rate is usually fixed to around 80 MHz. The observation period for a fluorescence decay is hence then around 12.5ns, which is too short to observe the full decay of long-lived species. However, this can be amended using pulse pickers.
- The requirement of TPE for high energy density at the focal volume may elicit nonlinear photodamage in the sample. In live cell or tissue imaging, experimental design must therefore balance the advantage of reduced photobleaching and higher penetration depth with photodamage, for example by adapting pulse width or the number of scans over a field of view [68].

1.4.5.2 Choice of time-resolved imaging instrumentation

In the previous sections, several technical implementations of FLIM and tr-FAIM have been presented. Quantification of fluorescence depolarisation is possible using TCSPC [69], time-gated and frequency-domain architectures [51, 50, 43, 70, 69]. In this work, the objective is to resolve membrane order parameters from anisotropy decays as presented in section 1.3.3, which requires high time resolution. However, the model membrane systems under investigation do not strictly require fast image acquisition rates as long as the samples can be immobilised. Moreover, the fluorescence membrane dyes used in this work have complex photophysical behaviours and exhibit multi-exponential fluorescence decays. Therefore, TCSPC was chosen as the time-resolved fluorescence detection technique yielding a sufficiently high time resolution for the straightforward measurement and analysis of anisotropy decays, as well as the accurate determination of fluorescence lifetime parameters.

1.4.6 Note on microscope resolution

Regardless of the technological pathway used, resolution (i.e., the size of the smallest features which it is possible to distinguish) in optical imaging is limited by the diffraction of light as it interacts with structures on the order of its wavelength. All diffraction orders contain information (light) about the emitters, hence it is desirable to collect as many of them as possible to create the image. However, the collection is made by an objective lens of finite diameter. The widest angle emanating from the focal plane from which the objective can collect light is given by its Numerical Aperture (NA), defined by the following equation:

$$NA = nsin\beta \tag{1.32}$$

With n the refractive index of the medium, and β the aperture angle of the objective. For this reason, the image of a single emitter by an optical system is not a single point, but rather a three-dimensional diffraction pattern (analytically, the optical transfer function), which is experimentally qualified as the Point-Spread Function (PSF). In terms of intensity, this image can be described by an Airy function. The lateral and axial resolutions of the system can then be defined in terms of separation between two Airy functions. There are several possible formulations of the resolution; the most popular one originated from Lord Rayleigh, suggesting that two objects separated by a distance equal to the radius of the Airy disk can be resolved, giving a maximal lateral resolution for the confocal microscope of:

$$d_l = \frac{0.4\lambda}{NA} \tag{1.33}$$

With λ the excitation wavelength. With similar methods the axial resolution of a system can also be calculated for a confocal microscope:

$$d_a = \frac{0.88\lambda}{n - \sqrt{n^2 - NA^2}} \tag{1.34}$$

From this it is evident that the lateral resolution is always higher than the axial resolution. Also, resolution is an analytical value which can be theoretically calculated for any microscopic setup if the numerical aperture, the refractive index of the immersion medium and the excitation wavelength are known. For instance, the theoretical value using an excitation wavelength of 467 nm and a numerical aperture of 1.2 with water immersion ($n = 1.33$), yields a lateral resolution of 156 nm, and an axial resolution of 538 nm.

This means that in the case of confocal microscopy used here, features smaller than these dimensions cannot be resolved. Recently, fluorescence imaging methods circumventing the optical diffraction limit have pushed fluorescence in the field of nanoscopy. These methods rely on the spatio-temporal isolation of fluorophore point-spread functions, through chemical methods (use of photo-activatable fluorophores in PALM, or of reducing buffers to provoke stochastic blinking of the fluorophores in STORM) or physical methods (the localised depletion of the excited state in STED) [71, 72, 73].

1.5 Time-and polarisation-resolved fluorescence microscopy in the laboratory

1.5.1 The laboratory setup

The laboratory system is a confocal TCSPC-FLIM microscope with polarisation resolution, enabling Time-Resolved Fluorescence Anisotropy Imaging. The lasers used in this work were picosecond pulsed diode lasers (Hamamatsu 467 nm and Horiba DDL series). The excitation beam is linearly polarised and coupled in free space (to avoid depolarisation through optical fibres) into a Leica TCS SP2 confocal microscope. On the detection side, steady-state confocal microscopy is performed with two photomultiplier tubes present in the the confocal microscope, enabling 2-colour imaging. For time-and polarisation-resolved microscopy, the fluorescence emission is instead separated into two orthogonal linear polarised components by a polarising beamsplitter (Linos Optics). The two components are detected by two Ga-AsP hybrid photon-counting detectors (HPM 100-40, Becker & Hickl), each individually connected to a TCSPC module (SPC 150, Becker & Hickl). Fig. 1.16 below is a schematic representation of the confocal polarisation-resolved FLIM setup currently used in the laboratory [69].

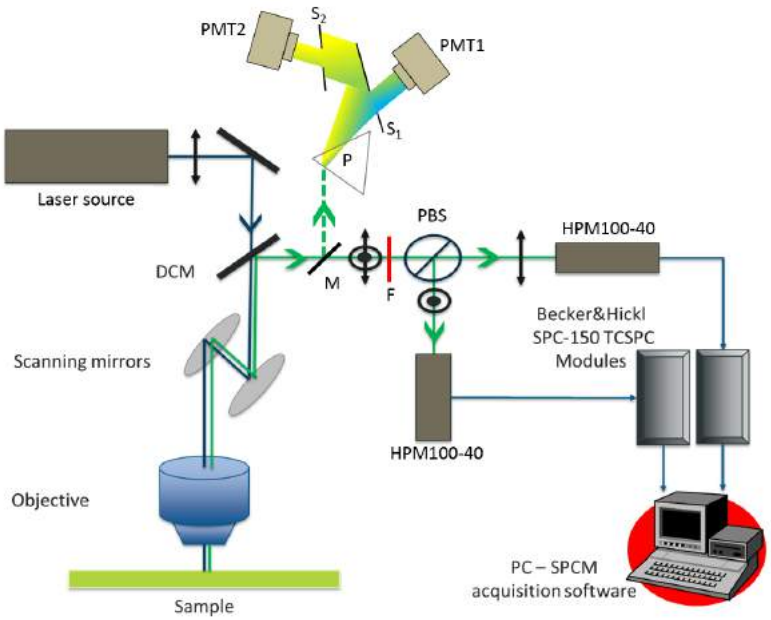

Figure 1.16: The laboratory setup. Throughout this work, diode lasers of different excitation wavelengths (e.g. 375, 467 and 440 nm) were used. DCM: Dichroic Mirror. M: Software-operated mirror. Light path above M (green dashed line) shows the steady-state 2-colour imaging capability using PMT1 and PMT2 from the Leica confocal microscope. P: Prism, S_1 and S_2 are slits of adjustable width with reflective surfaces. Path on the right of M (full green line) shows the home-built polarisation-resolved FLIM capacity using two Ga-AsP HPM 100-40 hybrid detectors (Becker&Hickl) and two SPC-150 PCI boards (also from Becker&Hickl). F: emission filter (transmission band cited when relevant). PBS: Polarising beamsplitter.

1.5.2 Optimisation of the optical system and calibrations

1.5.2.1 On the excitation side

Beam shaping. For confocal microscopy, an optimised beam profile is collimated and has the dimensions of the input coupling aperture when entering the microscope scan head (in our case, 5 mm). Diode lasers rarely have an ideal beam profile when they exit the laser head, i.e., they may be divergent or convergent, non-circular, and with local defects. The beam must therefore be shaped before coupling to the microscope. The modifications brought to each of the lasers used in this project are described here.

The Hamamatsu 467 nm diode laser was adjusted for divergence and beam size using a collimation lens and a beam expander. The optical diagram is presented in Fig. 1.17 below. The beam was firstly collimated to a diameter of approximately 1 cm using an adjustable convex lens built into the output of the laser head ($\mathcal{L}_1$) - note that on Fig. 1.17, $\mathcal{L}_1$ is shown some distance away from the laser head for clarity, and to underline the strong divergence of the beam at the direct output of the laser. This collimated beam was then reduced to a size of 5 mm diameter using the $\mathcal{L}_2 - \mathcal{L}_3$ lens assembly: $\mathcal{L}_2$ converges the beam rays to its front focal point, which is made to coincide with the back focal point of lens $\mathcal{L}_3$, with $f_3 < f_2$. The beam exiting this assembly is therefore collimated, and reduced in size to $x = 5$mm, which is the size of the input port of the confocal scanhead. The beam is thereafter spectrally filtered using a 485/50 BP filter ($\mathcal{F}$), and the polarisation cleaned up using a linear polariser ($\mathcal{LP}$). Spatial filtering was also envisaged to improve the beam profile. Indeed, the collimated beam was not of Gaussian profile; instead, it presented concentric rings, in the shape of an interference pattern. By placing a pinhole $\mathcal{P}$ at the point where the beam converges in the beam expander, the central part of the beam can be selected for re-expansion only, producing a more Gaussian profile. This provides a better-defined excitation volume when the beam is converged by the objective, and ultimately, a better resolution. However, this was at the cost of a strong drop in intensity. Increasing the laser power is possible to compensate for this, but for this specific model, led to a temporal broadening of the laser pulse and a distortion of the fluorescence in its initial moments. It was determined that the gain in resolution was too low in view of the reduced intensity of the beam, and spatial filtering was not used.

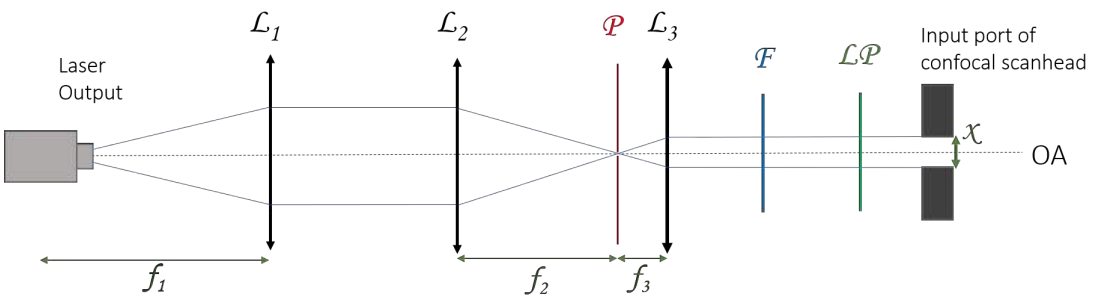

Figure 1.17: Optical diagram of laser beam shaping elements used for the 467 nm diode laser. Convex lenses $\mathcal{L}_1$, $\mathcal{L}_2$ and $\mathcal{L}_3$ have back focal lengths f_1, f_2 and f_3, respectively, with $f_2 = 100\,mm$ and $f_3 = 25\,mm$. $\mathcal{L}_1$ was integrated with the laser head, and its focal length was approx. 5 cm. $\mathcal{P}$ is the pinhole used for spatial filtering of the beam. $\mathcal{F}$ is a 485/50 excitation filter. $\mathcal{LP}$ is a linear polariser. OA: Optical Axis

The Horiba 375 nm DDL diode laser was much less divergent than the 467 nm laser, and the diameter was also smaller at the output. A beam expander assembly was therefore not required, and the beam was solely collimated using a 50 cm focal length UV-coated plano-convex lens, and polarised using the linear polariser as above. The optical diagram is presented below in Fig. 1.18.

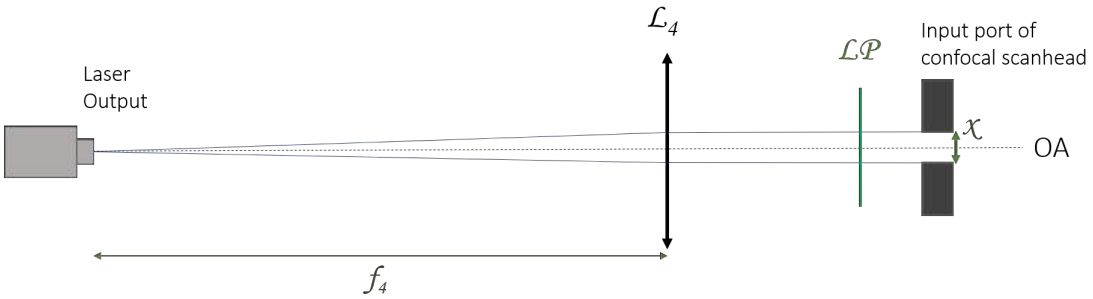

Figure 1.18: Optical diagram of the beam shaping elements used for the 375 nm diode laser. Convex lens $\mathcal{L}_4$ has a back focal length of f_4=50 cm.

Alternating between excitation wavelengths. To add versatility to the system and allow for different users and applications, it is useful to have several laser lines easily coupled into the scanhead without the need for systematic re-alignment and modifications in the beam paths. Flip mirrors and reflection filters were therefore used to alternate the coupling of different lasers into the microscope. The configuration of the excitation paths is shown in Fig. 1.19. Note that the dichromatic mirror within the scanhead needed to be changed manually between experiments with different wavelengths. Experiments with 467 nm excitation required a dichroic with a 485 nm, while the ones with 375 nm excitation were performed with a cutoff at 405 nm.

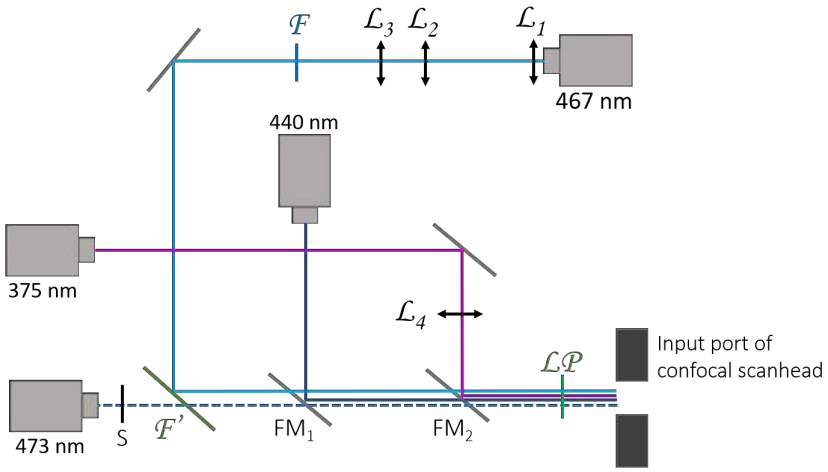

Figure 1.19: Diagram of the optical configuration of the excitation paths. The 473 nm laser and shutter S constitute a FRAP module, not used in the experiments described here. Aside from the optical elements already shown in Figs. 1.17 and 1.18, $\mathcal{F}'$ is a reflection filter with a cut-off between 467 and 473 nm, hence transmitting the FRAP beam but reflecting the 467 nm laser beam. M1 and M2 are mirrors, and FM1 and FM2 are two flip mirrors.

The temporal instrument response function. The measurement of fluorescence lifetime parameters, as explained above, is done by detecting single photons after an excitation pulse. In an ideal world, the pulse and the transit time of the detector signal are infinitely short. Of course in reality neither of these assumptions are exact, and the measured decay curve I_m is the convolution of the "pure" exponential decay function I_p with the Instrument Response Function (IRF), representing the combination of excitation and detection responses of finite widths, as shown in Eq. 1.35

$$I_m(t) = \int_0^\infty IRF(\tau).I_p(t-\tau)d\tau \tag{1.35}$$

The true decay parameters are contained in I_p, so in essence any fitting procedure should take into account the distortion of the decay curve by the instrument response. Knowing the IRF allows extraction of decay parameters with better accuracy through fitting methods taking the response function into account, such as the iterative reconvolution method. The ideal IRF is as short as possible. The IRF can be measured using a mirror or scattering sample, reflecting back the excitation light through the detection beampath – however it is not ideal since the dichroic mirror and emission filters are designed to block out this wavelength. Another possibility is then to use a fluorescent sample, the lifetime of which is shorter than the IRF. To this effect, fluorescein quenched by an iodide salt can be used, or a molecular rotor such as DCVJ with a picosecond lifetime in low viscosity solvents such as methanol. The shape of the IRF depends on the operating gain of the detectors as well as the laser power, as can be seen in the IRF profiles below (Fig. 1.20). The 467 nm laser suffers from afterpulsing at high powers: the pulse shape shows secondary peaks

and an overall longer pulse widths, as also highlighted by the plot of pulse width against laser power, in Fig.1.20. D. – for better accuracy it is therefore preferable to keep the laser power at a minimal value, for a FHWM of 155 ps.

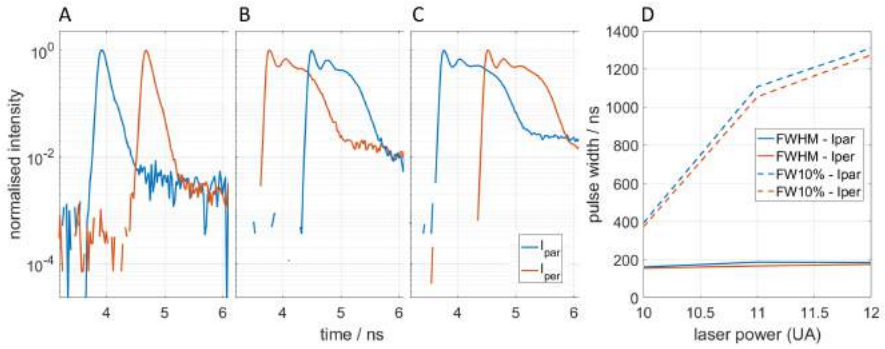

Figure 1.20: Pulse shape of 467nm laser as a function of operating power: low (A - 10 Arbitrary Units), intermediate (B - 11 AU) and high (C - 12 AU) laser powers. D: Full width at 50% (FWHM - full lines) and 10% (FW10% - dashed lines) of the laser pulse maximum as a function of laser power.

The 375 nm laser did not show power-dependent pulse broadening, and the FWHM was calculated at 320 ps.

1.5.2.2 On the detection side

The G factor Anisotropy measurements are achieved using two separate detectors, which may have different detection efficiencies. This will affect the detected intensities and hence the final anisotropy value. The anisotropy operation therefore incorporates a correction factor, called the G factor. Its name originates from "Grating", due to the gratings used in spectroscopy originally.

$$r = \frac{I_{\parallel} - G\, I_{\perp}}{I_{\parallel} + 2\, G\, I_{\perp}} \tag{1.36}$$

In microscopy, the G factor can be obtained by measuring the polarisation-resolved fluorescence decays of a dye in a low-viscosity solvent [69]. In such a sample, at short times after the excitation pulse (a few nanoseconds), the excited dye population has fully randomised its orientations, and there should be no difference between the two polarisation detection channels. Computing the ratio between the two channels is known as tail matching, and yields the G factor. This method is illustrated in Fig. 1.21:

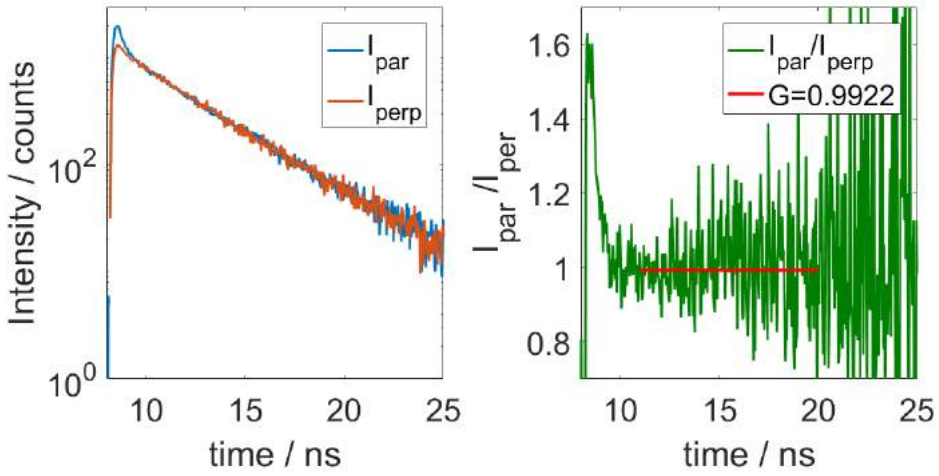

Figure 1.21: G factor measurement using the tail-matching method. Left: polarisation-resolved transients of fluorescein in 10:90 v/v% glycerol:water (375 nm excitation). Right: G factor transient $I_{\parallel}/I_{\perp}$ (in green), with the tail value (average $I_{\parallel}/I_{\perp}$ after decay of the fluorescence anisotropy, in red) yielding the G factor.

Ideally, G=1, indicating equal detection efficiency in both detectors. In practice, G factor values between 0.9 and 1.1 are acceptable. It is crucial to measure the G factor in the measurement conditions: detector gains, confocal pinhole aperture, laser alignment, etc. As an example, the G factor value as a function of the pinhole size is shown in Fig. 1.22. The increase in G factor values as the pinhole size is increased (a 10% increase over the range investigated) shows a slight misalignment of the polarising beamsplitter and/or of the emission pinhole. Since perfect beamsplitter alignment can be difficult to reach, the G factor can simply be measured at all the pinhole sizes used during the experiment.

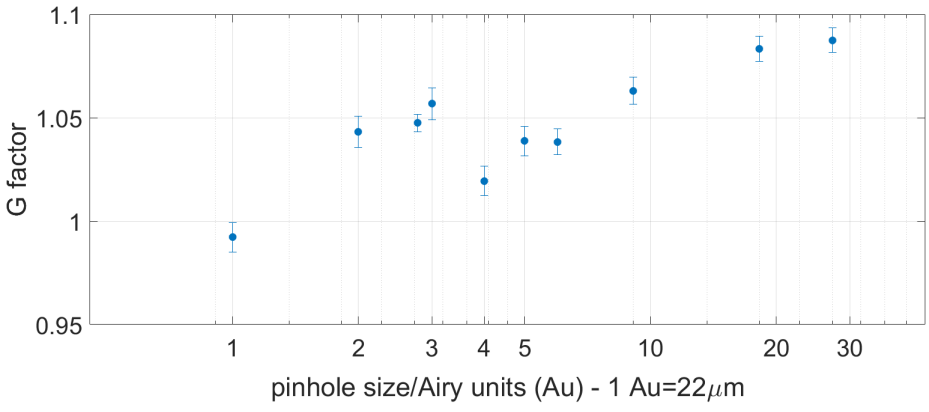

Figure 1.22: G factor as a function of the pinhole size. The error bars represent the standard deviation of the G factor estimate (from the mean of the tail values in the G factor transient) at each measurement.

The depolarisation factor. High aperture objectives such as the one used in these experiments distort the linear polarisation of the excitation beam, and create non-negligible Ey and Ez com-

ponents to an initially linearly polarised Ex radiation [28, 74, 31]. This effect leads to a reduced photoselection effect, and to a decrease in the dynamic range of the anisotropy values as visible by lower initial anisotropy values than expected.

Experimentally, the effect of objective aperture on anisotropy values can be quantified by measuring r_0^{meas}, the fundamental anisotropy of a dye of known r_0^{the}, through the objective. The difference between r_0^{the} and r_0^{meas} can be used to compute a depolarisation factor x_{na}. Further, x_{na} can be introduced as a correction term in the anisotropy equation, as proposed by Devauges et al [43, 75]:

$$r_{corr} = \frac{I_{\parallel} - G\, I_{\perp}}{I_{\parallel} + 2\, G\, x_{na}\, I_{\perp}} \tag{1.37}$$

In practice, this was not implemented in our analysis, since the same 63x, 1.2NA water immersion lens was used throughout all the experiments. The depolarisation effect was the same for all samples, and did not affect the data interpretation. As an indication, for such an objective, numerical calculations from refs. [76, 28] indicate Ey components of approx 1.5% of that of Ex, while the magnitude of the Ez components can reach 30% of Ex.

TCSPC module settings. Initially, the TCSPC system was composed of a single SPC 830 card (Becker & Hickl), into which signal from the two detectors was fed through a router. The image size and ADC resolution were therefore limited to the maximum data rate and on-board storage allowed by this particular model. To increase spatial and temporal resolutions of the TCSPC system, this architecture was replaced by two SPC 150 cards, one for each detector. One preliminary task to ensure the accuracy of time-domain FLIM measurements is to calibrate the parameters of the SPC-150 cards to their ideal working values. The parameters of interest here are the CFD threshold and operating detector gains. The underlying theory is that additionally to photon pulses, the detectors give out electronic noise and pulses from dynodes, at low amplitude but very high frequencies. This type of signal must not be detected as fluorescence photons. On the other hand, the detectors have a considerable amplitude jitter, so the threshold should be set so as tolerate the amplitude distribution of photon signals. This amplitude distribution depends on the detector gain. This is shown in Fig. 1.23 below on the left-hand side graph.

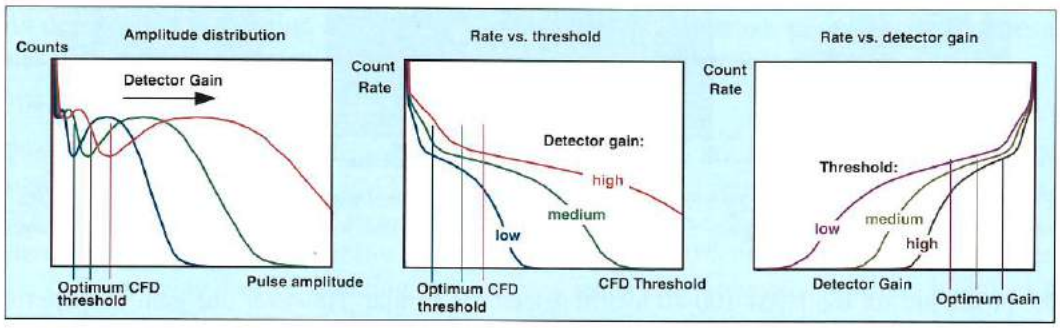

Figure 1.23: Relationship between CFD threshold, gain and count rate for time-resolved detectors. From ref. [31]

It should be noted that for the hybrid detectors, there is no noise from the dynodes (intermediate bump on the left hand graph), so there should be a smooth transition between the electronic noise and the photon amplitude distribution. As a strategy for the experimental determination of the optimal parameters, the CFD threshold and the gain were adjusted while the detectors were illuminated with background light, to recreate the curves as seen above for both detectors. The results are shown in the graphs below (Fig. 1.24). In the case of hybrid detectors, the count rate as a function of the gain for a set threshold is highly nonlinear, which means that the plateau is very flat until reaching detector instability ("overload"). Detector overload was reached at a gain of 90%, so the measurements were stopped at a gain of 88%. For both detectors a reasonable CFD threshold is set to -10mV, for a range of possible operating gains of 80 to 88%.

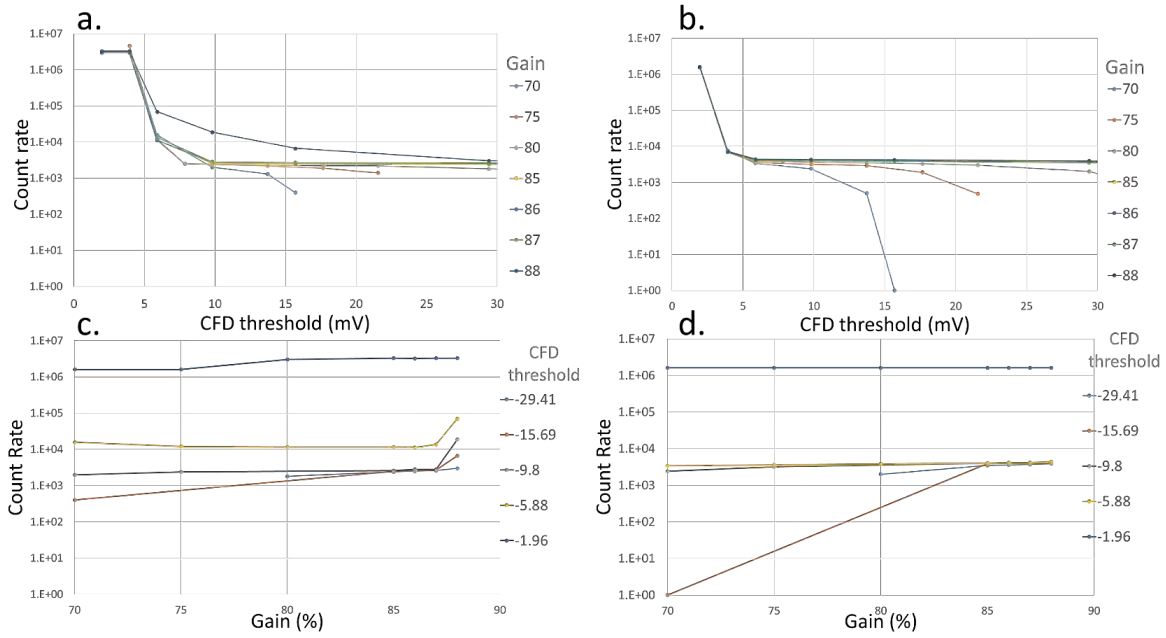

Figure 1.24: Calibration curves obtained for the two HPM 100-40 detectors. a. and b. : Count Rate as a function of the CFD threshold for different detector gains. c. and d.: Count Rate as a function of the detector Gain for different CFD thresholds.

1.5.2.3 Measuring the optical resolution of the microscope

Measuring the size and shape of the PSF of a system and deducing its actual resolution gives an idea of the ideality of the setup and can be used to detect misalignments or defects in the microscope optics. To measure the PSF of a microscope system, a sample containing point emitters has to be created; a good object for this is fluorescent nanoparticles of around 100 nm in diameter. They are more convenient than individual fluorophores because of their low photobleaching and high intensity, and it is also straightforward to immobilise them on a coverslip. To measure the resolution of the confocal FLIM system, Green PS-Speck microbeads from Invitrogen® were used. The confocal PMT gain and offsets were adjusted to yield maximum sensitivity to low intensity signal. Once individual particles were found, a z-series of 40 x-y frames over a depth of 4.4μm was made, the pixel size being 38 nm. The lateral resolution is determined by selecting the frame at which the image was the smallest, brightest spot, and extracting the intensity profile from it (Fig. 1.25).

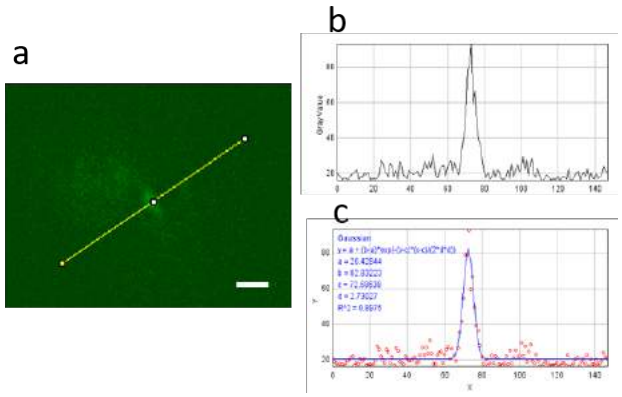

Figure 1.25: Imaging of fluorescent nanoparticles to measure the microscope point spread function. a.: Image of a single nanoparticle. The intensity profile of the yellow line is shown in b., and a gaussian fit performed in c. Scale bar is 1μm.

The peak could then be fit to a Gaussian function $G(x) = ae^{-(x-x_0/\sigma\sqrt{2})^2}$, with x_0 the position of the maximum and σ the width of the function. The FWHM of the Gaussian yields the experimental value for the resolution of the system and can be deduced from the standard deviation σ as follows:

$$FWHM = 2\sigma\sqrt{2ln2} \tag{1.38}$$

The results are presented in the following figure for one selected nano-bead. The FWHM was found to be 244.3 nm in this instance using Eq. 1.38, which is larger than the expected value calculated in section 1.4.6. This may be due to a low fill factor of the microscope objective, causing an effective NA lower than the theoretical one, or to the non-ideal profile of the laser beam. Nonetheless, this value is in the range of what is usually obtained as the lateral resolution

for conventional microscopy, and was deemed reasonable for the pursuit of our experiments.

1.6 Overview of existing analysis methods for FLIM and TR-FAIM

Fluorescence intensity and anisotropy decay data are multi-parametric, have a signal-dependent noise distribution and are usually limited in quality by photon capital. There are therefore several possible methods for extracting information from time-resolved imaging data and there is no consensus on which method is ultimately superior to the others [77]. Moreover, the field of FLIM and TR-FAIM data analysis is constantly evolving, and new approaches are regularly developed. in this chapter, an overview of existing methods is given along and their strengths and limitations are discussed.

1.6.1 Pixel-wise fitting approaches of fluorescence intensity decays

The most widespread methods for the analysis of FLIM data involve extracting the decay parameters in each pixel by fitting their decays individually. The intensity decay obtained by TCSPC is fitted directly using exponential decay models, as shown in Fig. 1.26. A "pure" fluorescence decay $B+\sum_i \alpha_i e^{-t/\tau_i}$, where B is the background offset, α_i the amplitudes of the respective decay times τ_i, is convolved with the instrument response factor $IRF(t)$, in blue. The model function is therefore a convolution of the IRF with a multi-exponential decay function. The IRF is measured experimentally by scattering some laser light onto the detectors, or by using quenched fluorescence, or can also be inferred from the shape of the rising edge of the decay if not available. Several fitting possibilities exist to estimate the lifetime parameters from the decay data.

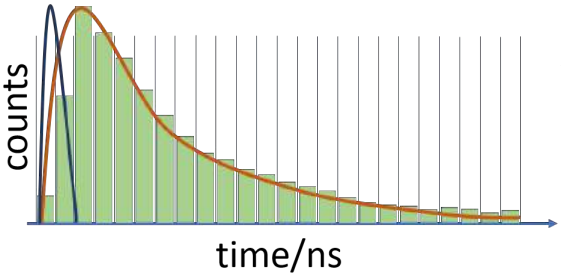

$$I_f(t) = IRF(t) \otimes \left(B + \sum_i \alpha_i e^{-t/\tau_i} \right)$$

$$\chi_r^2 = \frac{1}{\nu} \sum_t \frac{(I_m(t) - I_f(t))^2}{I_m(t)}$$

Figure 1.26: Analysis of TCSPC data using exponential fitting. The χ^2_{red} shown here corresponds to the NLLS estimate.

1.6.1.1 The Non-Linear Least Squares method

The Non-Linear Least Squares (NLLS) fitting method is the most popular method to estimate lifetime parameters, due to its simplicity and omnipresence in data analysis software. The goodness of fit, χ^2_{red} (reduced Chi-squared), is related to this distance:

$$\chi^2_{red} = \frac{1}{n-(2P+1)} \sum_{k=1}^{n} \frac{(I_k - \mu_k \otimes IRF(t))^2}{W_k} \tag{1.39}$$

Where I_k is the intensity measured in the time bin k, $\otimes$ represents the convolution integral operation, and the constant factor $n-(2P+1)$ represents the number of degrees of freedom in the data with P the number of fit parameters. W_k is a weighting factor: in intensity decays with Poisson-distributed noise the estimate for the variance is equal to the signal, so in our case $W_k = I_k$. For the same reasons, if the difference between the data and the fit is solely due to random errors, its estimate is the standard deviation $\sqrt{I_k}$. Each data point hence contributes to χ^2_{red} by a factor of 1; since the number of degrees of freedom is roughly equal to the number of datapoints for a large number of time bins, a good fit yields a value for χ^2_{red} close to 1 [23].

1.6.1.2 The Maximum Likelihood Estimation Method

Although the NLLS method is widespread and routinely used for decay fitting, it is not mathematically optimised for Poisson-distributed data. Indeed, the goodness of fit χ^2_{red} is based on the Maximum Likelihood Estimator (MLE) for Gaussian-distributed variables. Therefore, the correct method for Poisson variables should be based on the MLE of a Poisson variable. It was indeed proven that the NLLS method produces a biased estimator [78, 79, 80]. When the photon count is high, the discrepancy is mitigated since in these cases the Poisson distribution converges towards normality. However, for low intensity situations, which are always present at the end of intensity decays and in general in photon-limited data, there is significant deviation between Poisson and Gaussian distributions.

The likelihood function for a set of independent Poisson variables is given by the combined probability to measure intensities $\{I_k\}$ when the expected values are $\{\mu_k\}$ [81, 79]:

$$\mathcal{L}_\mu(I) = \prod_k \frac{e^{-\mu_k} \mu_k^{I_k}}{I_k!} \tag{1.40}$$

The likelihood is usually linearised using a logarithmic transformation and constant positive terms removed so that the following negative log-likelihood function is minimised:

$$-ln\mathcal{L}_\mu(I) = \sum_k \mu_k - I_k ln(\mu_k) \tag{1.41}$$

Several studies on simulated data have shown more accurate recovery of the decay parameters with Poisson-MLE compared to the NLLS method [82, 78, 81]. The commercial fitting software SPCImage [31] uses nonlinear Least Squares routines to estimate parameters and is hence liable to biased estimations in low intensity images. Non-commercial software such as TRI2 or FLIMfit offer the possibility of maximum Likelihood estimations. Other methods to resolve lifetime parameters

include the Bayesian fitting approach [82, 83], which has shown excellent performance in improving the accuracy of lifetime estimates in low intensity situations.

1.6.2 Global fitting approaches

In the event of low photon counts, pixel-wise fitting methods may become unreliable, with high uncertainties associated with each parameter estimation [84]. In such cases, it can be interesting to reduce the number of parameters to estimate [85]. For example, in a FLIM image containing 2 decay components, the lifetimes can be fixed using the average value from the lifetime estimates of all pixels, or fixed using prior information. The two remaining parameters are then the component abundances, to be determined in a pixel-wise fashion. This is particularly useful for FRET applications where the abundance of the short decay component informs on the fraction of interacting donor. Warren et al. [40] have developed another fitting approach to determine lifetime and amplitude parameters sequentially, using partitioned variable projection or separable nonlinear least-squares [86]. Firstly, the least-squares fitting problem for each pixel i is used :

$$r_i(\alpha, \tau) = \sqrt{\sum_k (I_{ki} - \mu_{ki})^2} \tag{1.42}$$

Which can be written in matrix form for the entire image, with I containing the observed data while the model is written as a product of matrices $\lambda(\tau)$ containing the exponential terms, and A containing the amplitudes:

$$R(\alpha, \tau) = \|I - \lambda(\tau).A\| \tag{1.43}$$

Since the objective is a minimised value of $R(\alpha, \tau)$, the minimisation problem can be written as : $I = \lambda(\tau)A \implies A = \lambda(\tau)^+ I$.

Where $\lambda(\tau)^+$ is the Moore-Penrose pseudo-inverse matrix of $\lambda(\tau)$. The minimisation problem is now reduced to the parameters contained in λ:

$$argmin(R(\alpha, \tau)) = argmin(I - \lambda(\tau)\lambda(\tau)^+ I) \tag{1.44}$$

Once the parameter matrix $\lambda(\tau)$ has been determined using Eq. 1.44, Eq. 1.43 can be used to recover parameters in A. This routine was helpfully implemented as an open access software platform, FLIMfit.

1.6.3 Method of moments

A very simple technique to analyse FLIM data which does not rely on fitting is to use the mean arrival time of the photons in each pixel:

$$\langle\tau\rangle = \frac{\int_0^T t.I(t)dt}{\int_0^T I(t)dt} \tag{1.45}$$

This technique provides a quick analysis and is useful to show simple contrast in images on the basis of photon arrival time and is used especially when photon capital is low. It has been used to estimate FRET efficiency in the case of interacting fluorophores [87]. This technique, though not widespread, is explained briefly here because it is used as a comparative for the global analysis method proposed in this work. The minimal fraction of interacting donor is calculated on the basis that in the case of FRET, the fluorescence intensity can be written as:

$$I(t) = (1 - f_{et})\, e^{-t/\tau_r} + f_{et}\, e^{-t/\tau_{et}} \tag{1.46}$$

Where f_{et} is the fraction of interacting donor, τ_r the lifetime of the donor in the absence of FRET, and τ_{et} its lifetime in the presence of FRET. Using the expression of $I(t)$ from Eq. 1.46 in Eq. 1.45, the fraction of interacting donor can be expressed as a function of τ_{et}/τ_r from the measured $\langle\tau\rangle$:

$$f_{et} = \frac{1 - \langle\tau\rangle/\tau_r}{1 - (\langle\tau\rangle/\tau_r - (\tau_{et}/\tau_r)^2 + \langle\tau\rangle/\tau_r \times \tau_{et}/\tau_r)} \tag{1.47}$$

The minima of the function $f_{et}(\tau_{et}/\tau_r, \langle\tau\rangle/\tau_r)$ for τ_{et}/τ_r represent the minimum fraction of donor in each pixel, and are obtained mathematically for $\tau_{et} = \langle\tau\rangle/2$. The minimal fraction of donor is then obtained:

$$mf_d = \frac{1 - \langle\tau\rangle/\tau_r}{(\langle\tau\rangle/2 \times \tau_r - 1)^2} \tag{1.48}$$

Analysing data in this fashion does not require knowledge of τ_{et}, and provides a non-fitting based quantitative approach to the extent of FRET in the sample. However, it provides no information on the number of independent decay species in the image and on decay characteristics.

1.6.4 The phasor approach to FLIM

Other possible analysis methods involve projection of the fluorecence decay data onto a space of reduced dimensionality. Indeed, time resolved data is an array of observations (pixels) with as many variables as there are time bins. Projection methods allow visual representation of the data, without requiring a specific mathematical model. Pixels with different decay profiles will appear

at different coordinates in the subspace, hence providing observable contrast in the image. The phasor approach to FLIM is such a technique, and was first proposed by Digman et al. in the laboratory of Prof. Gratton [56]. This method was first employed for frequency-domain FLIM, where the fluorescence intensity is sampled and analysed with modulated excitation intensity and detection gain [23]. The fluorescence decay is never observed and other techniques must be used to recover the decay parameters. Phasor-FLIM was subsequently adapted to TCSPC measurements, proving attractive especially in the case of low-level fluorescence [88], enabling rapid identification of regions in the image according to decay characteristics [89]. To obtain the phasor coordinates for each pixel, the following operation is applied to the decay $I_k(t)$ in each pixel k:

$$F_k(\omega) = \frac{\int_0^\infty I(t)\, e^{i\omega t} dt}{\int_0^\infty I(t)\, dt} \tag{1.49}$$

With ω the modulation frequency - for TCSPC data, any frequency can be used. The frequency of the average decay yields maximum spread to the data at hand. $F_k(\omega)$ is a hence a couple of Fourier coefficients, projecting the time-domain data onto a space determined by frequency of the fluorescence decay.

For a mono-exponential decay with lifetime τ, integration of Eq. 1.49 yields:

$$F_k(\omega) = \frac{\int_0^\infty e^{t(\omega\tau - 1/\tau)} dt}{\int_0^\infty e^{-t/\tau} dt} = \frac{1 + \tau i\omega}{1 + (\tau\omega)^2} \tag{1.50}$$

The real and imaginary parts of $F_k(\omega)$ are $Re(F_k) = 1/1+(\tau\omega)^2$ and $Im(F_k) = \tau\omega/1+(\tau\omega)^2$; and when plotted against one another these values lie on a semi-circle of radius one and centre (1/2,0), for any τ and ω:

$$(Re(F_k) - \frac{1}{2})^2 + Im(F_k)^2 = \frac{1}{4} \tag{1.51}$$

Due to the linearity of the transform in Eq. 1.50, multi-exponential decays lie inside the circle, on the cord connecting the two pure single-exponential species on the circle. The position on this cord depends on the relative amplitudes of the two components. Using this method, single exponential and multi-exponential decays can be discriminated, and the distribution of the abundances between two fluorescence species can be monitored. If the pure decay species are known, they can be used as fixed parameters; otherwise they can be determined (as shown in Fig. 1.27) by fitting the cloud of points to a straight line.

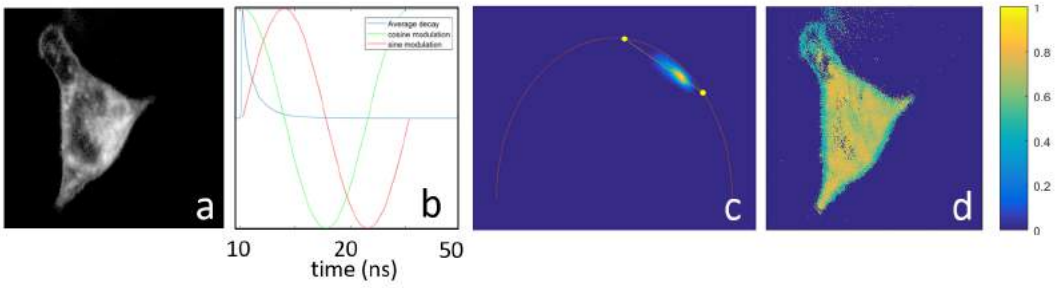

Figure 1.27: Phasor analysis of a HeLa cell stained with membrane dye di-4-ANEPPDHQ. The decay in each pixel from the image (a) is transformed according to Eq.1.49 using an appropriate modulation frequency (b) and appears as one data point on the phasor cloud, here shown as a 2-D histogram (c). By fitting the data cloud to a straight line, the pure (conjectured) mono-exponential components are retrieved as intersections between the line and the universal circle, and a phasor image based on the projection of each pixel on this line is computed, where the value of each pixel is related to the position of its orthogonal projection on the straight line (d).

The presence of fluorophores in a complex sample can be identified from their position on a phasor plot, after having created a map using the pure fluorophores as a reference. Stringari et al. [88] have mapped the phasor signature of several endogenous fluorophores such as collagen, retinol, NADH (free and bound) (Fig. 1.28. A). Their presence can then be mapped in a sample (panel B) from the location of the pixel coordinates on the phasor (C).

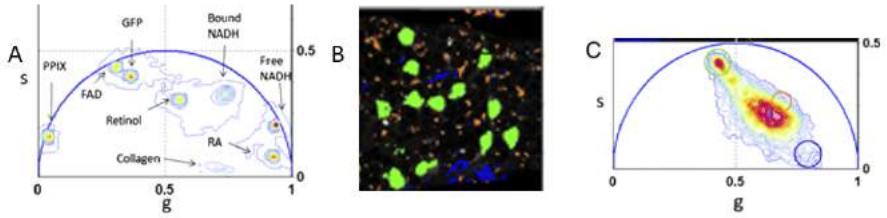

Figure 1.28: Phasor analysis of fluorescence species in live tissue samples. The phasor region of pure fluorophores in solution is mapped (A), and the species a tissue sample (B) are identified from the location of the pixel coordinates on the phasor (C). From ref. [88] - No permission required for non-commercial re-use from PNAS.

Despite its advantages, phasor analysis is heavily dependent on the exponentiality of the data: any deviation from a pure mixture of exponentials such a wide IRF, non-fluorescent background or incomplete decays displaces the clouds of points in phasor space. This is not a problem for visual representation of decays in phasor space but will complicate quantitative analysis, such as comparison of lifetimes and determination of the number of decay components. Moreover, presence of 3 or more distinct decay species may be difficult to resolve due to the two-dimensional character of the phasor space, hence offering an under-determined projection.

1.6.5 Analysis of time-resolved fluorescence anisotropy data

1.6.5.1 Position of the problem

As seen in the previous section, time-resolved anisotropy consists of exponential decays, with or without a constant offset depending on whether the rotation is hindered or free. Several difficulties arise in the analysis of TR-FAIM data:

- The analytical probability distribution law of each data point in the transient is not known: indeed, while the polarisation-resolved intensity decays from which anisotropy is derived are both described with Poisson-distributed variables, subtracting and dividing such variables does not yield a Poisson-distributed variable. To the best of my knowledge, there is no analytical expression of the noise distribution of anisotropy data, which makes the establishment of an accurate maximum likelihood estimator impossible.

- The uncertainty associated with an anisotropy measurement is potentially high: the value is calculated using standard propagation of errors on the measurements of $I_{\parallel}$, $I_{\perp}$, and G, as also shown by Lidke et al. in [90]. Assuming there is no uncertainty in G and that G=1, we obtain:

$$\delta(r) = 3\frac{\sqrt{I_{\parallel}^2 I_{\perp} + I_{\perp}^2 I_{\parallel}}}{(I_{\parallel} + 2I_{\perp})^2} \tag{1.52}$$

Using this equation, the uncertainty associated with each anisotropy value as a function of $I_{\perp}$ and $I_{\parallel}$, can then be represented, as shown in Fig. 1.29. This illustrates that for low intensities, the error on the anisotropy value can be as much as 0.15, which is on the order of magnitude of the final anisotropy value (usually between 0 and 0.4). For these reasons, the photon capital is critical for anisotropy measurements in order to limit the associated uncertainty, but it is not always possible to achieve sufficient intensities. It also means that the tail values in anisotropy decays, which are computed from the tail values of the intensity decays themselves, are extremely noisy.

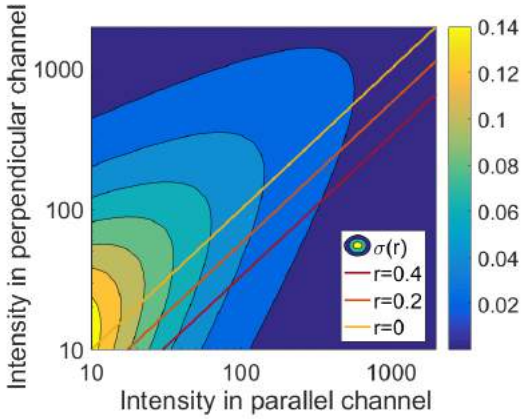

Figure 1.29: Contour plot of the measurement uncertainty $\delta(r)$ as a function of polarisation-resolved intensity $I_{\parallel}$and $I_{\perp}$. Isolines showing the values $r = 0.4$, $r = 0.2$ and $r = 0$ are also displayed.

In the following sections, several methods for the analysis of TR-FAIM data are proposed. Only methods that allow the presence of r_{∞} are discussed, though others exist such as use of the Perrin equation [91] or the maximum entropy method [92].

1.6.5.2 Method 1 : "brute-force" - exponential decay fitting of time-resolved anisotropy

This method consists in quite simply fitting the anisotropy decay to a single- or double-exponential model using a non-linear least square fit, to obtain r_0, θ and r_{∞} parameters. This provides reliable information when the intensity decays used to derive the anisotropy transient have high peak intensity. This can be done for example when spatial resolution is not important (e.g. solution measurements), and one single decay is computed for the entire field of view (see an example of fitted anisotropy decay Fig. 1.30). Reliable determination of the parameters is compromised when the intensities are low, or when the rate of anisotropy decay is large compared to the fluorescence lifetime. In these cases, the fluorescence intensity has already decayed significantly before any substantial depolarisation has taken place. This is typically the case for GFP, which has a lifetime below 2.5 ns, but is a bulky molecule with slow rotational motion. For these reasons, pixel-wise anisotropy decay fitting is difficult in imaging configurations.

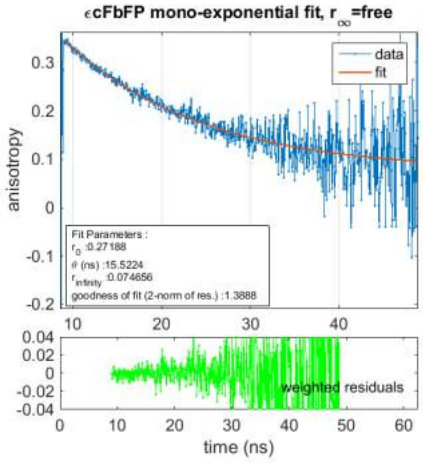

Figure 1.30: Example of an anisotropy decay fitted to a single exponential model. The sample is a fluorescent LOV-domain protein (ϵcFbFP) produced by group members of collaborator Thomas Gensch (Julich).

To improve the quality of the fits, a weighted fitting procedure was tested, using Eq. 1.52 to compute the weight for each data point. The performance of weighted and unweighted fits was then assessed using simulated anisotropy data. To simulate anisotropy decays, the intensity decays are expressed as a function of the anisotropy decays and the total intensity (using the anisotropy equation and $I_{tot} = I_{\parallel} + 2I_{\perp}$), as also shown by Kapusta et al [93]:

$$\begin{cases} I_{\parallel} = \frac{1+2r}{3} I_{tot} \\ I_{\perp} = \frac{1-r}{3} I_{tot} \end{cases} \tag{1.53}$$

If one can assume that $I_{tot}(t)$ and $r(t)$ follow mono-exponential models:

$$\begin{cases} I(t) = Ae^{-t/\tau} \\ r(t) = (r_0 - r_\infty)e^{-t/\theta} + r_\infty \end{cases} \tag{1.54}$$

Then Eqs. 1.53 and 1.54 can be combined to yield:

$$\begin{cases} I_{\parallel} = \frac{A}{3}((1+2r_\infty)e^{-t/\tau} + 2(r_0 - r_\infty)\, e^{-t(\tau+\theta)/\tau\theta}) \\ I_{\perp} = \frac{A}{3}((1-r_\infty)e^{-t/\tau} - (r_0 - r_\infty)\, e^{-t(\tau+\theta)/\tau\theta}) \end{cases} \tag{1.55}$$

This system of equations was adapted from [93] to include a non-zero r_∞ term. Using this formalism, the two polarisation-resolved decays were simulated using pre-determined intensity, lifetime and anisotropy decay parameters, as described in Eq. 1.55. The IRF was simulated using a Gaussian function with a FWHM of 240 ps, and convolved to the exponential decays. Poisson noise was then added to each of them, and the anisotropy decay computed using the anisotropy equation. The parameters chosen for this simulation are shown in Table 1.2. Ten thousand decays

were computed in this way, applying random Poisson noise independently on each individual repeat of the noise-free decays. The noisy decays were then fitted using weighted or unweighted routines.

Parameter Name	Value
A	10^3
τ	5 ns
θ	3 ns
r_0	0.3
r_∞	0.1

Table 1.2: Table showing the simulated parameters to compare the effect of weighting on fitting accuracy.

Results show that weighted fits result in more accurate recovery of the true parameters compared to an unweighted fit. Indeed, the recovered parameters are closer to the true simulated parameter, and have lower bias, as shown in Fig.1.31. The residual bias in the parameters obtained through weighted fitting may be linked to the NLLS routine (as opposed to MLE), and/or the the presence of the IRF.

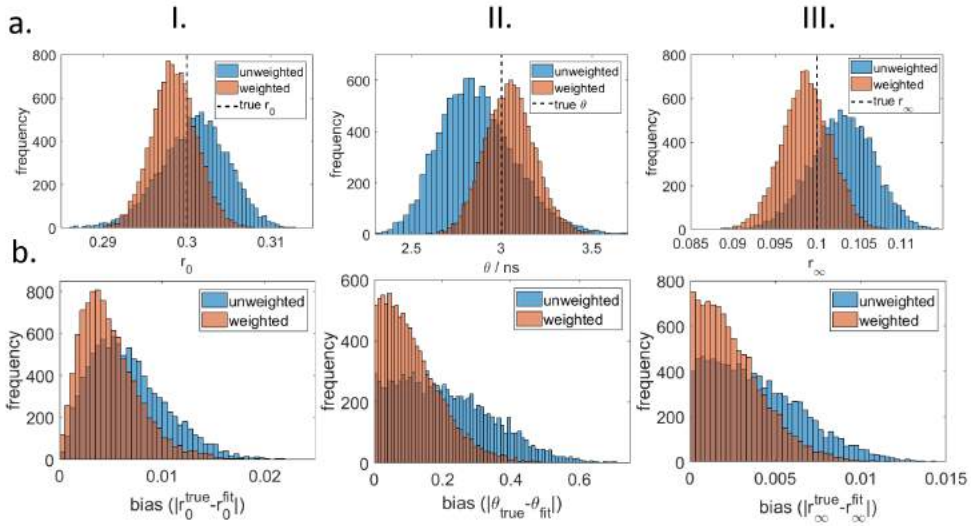

Figure 1.31: Results of weighted and unweighted fits on simulated time-resolved anisotropy data. a.: histograms showing the frequencies of the recovered parameters (I. : r_0, II.: θ, III. : r_∞) for 10^3 repeats of noisy anisotropy decays using the parameters shown in Table. 1.2. b.: histograms showing the corresponding modulus of the bias for each parameter.

1.6.5.3 Method 2 : "Trying to be smart" - fitting the polarisation-resolved intensity decays to extract the anisotropy parameters.

This method consists in using the polarised intensity decays rather than the anisotropy decay to extract anisotropy decay parameters. The polarisation-resolved transients $I_\parallel$ and $I_\perp$ are fitted

individually (usually, only $I_{\parallel}$ may be used, since the intensity is expected to be higher). The value for τ can be determined using fitting of I_{tot} [94]. Through this method, r_0, r_∞ and θ can be determined from the fit parameters as shown in Eq. 1.55, taking advantage of the fact that the polarised intensity decays have a Poisson noise distribution and can be fitted in the same way as classical intensity decays. Fig. 1.32 shows the recovered values for a simulated dataset with input parameters $A = 5000$, $\tau = 3,5$ ns, $r_0 = 0.385$, $r_\infty = 0.15$ and $\theta = 6$ ns. Direct anisotropy fitting (unweighted) and indirect, intensity transient-based fittings are compared. Results show that using the polarisation-resolved transients to determine the lifetime and subsequently the anisotropy parameters results in more accurate recovery of parameter values, especially for the rotational correlation time θ.

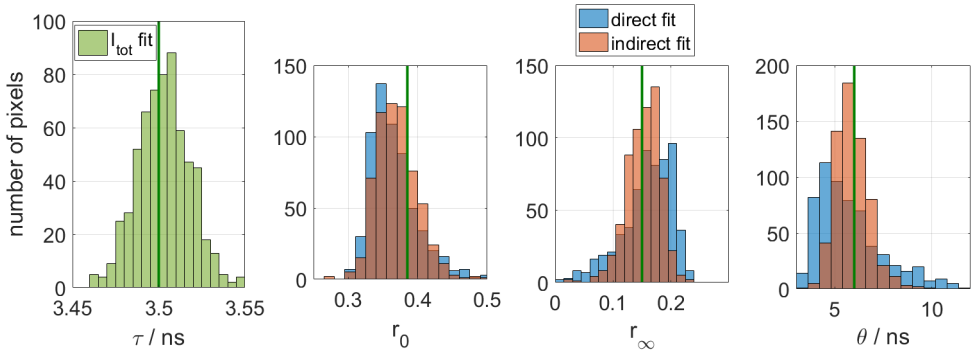

Figure 1.32: Recovered lifetime and anisotropy parameters from simulated noisy dataset. The performance of direct anisotropy decay fitting (blue histograms) is compared to that of indirect parameter determination through fitting of the total intensity decay I_{tot} (green histogram) and the polarisation-resolved intensity decay $I_{\parallel}$ (orange histograms). The green vertical lines indicate input parameter values.

This alternative method allows extraction of anisotropy parameters with lower signal to noise ratios than direct fitting. However, it still relies on the assumption that the total intensity decay and the anisotropy decay are mono-exponential. While this may be easy to verify for intensity, this is less so the case for the anisotropy. Moreover, if the intensity decay is multi-exponential, the model quickly becomes more complex, with each polarisation-resolved intensity decay being described by 4 exponential components. In this case, the intensities required to resolve this number of parameters accurately become very high and in practice, hardly achievable unless some parameters are fixed. For these reasons, the direct fit method is still used in the anisotropy community, and will be used to analyse anisotropy decays throughout this report.

1.6.6 Rationale on the adopted data processing strategy in this work

As seen from this section, a variety of methods exist to analyse time-resolved fluorescence decay and image data. Some of these methods have been developed as proprietary or open-access software. Because the objective of this work was to combine spectral, lifetime and anisotropy analysis from

the same samples, it is more convenient to be able to analyse all types of data in the same platform, to avoid the necessity for multiple file format conversions, data import, export and pre-processing steps. Therefore, most analysis routines, including single decay fitting, image processing (binning, ROI selection, background correction, etc.), phasor analysis, and confocal image analysis were performed using home-written routines in Matlab, using the bioformats toolbox to import .spc and .tif image formats. This may be perceived as redundant and time consuming, since such routines already exist elsewhere (SPCImage, TRI2, ImageJ, Origin). However, it was considered that the gain in performing all analysis steps on a single platform and storing data under a single format was largely worth the time allocated to implementing such routines in the first place. Moreover, there is no current existing software for the streamlined processing of polarisation-resolved images to obtain intensity and anisotropy images, taking into account the G factor, the time shift between the two images and different backgrounds. The detail of the relevant analysis procedures will be given in the Methods sections of the corresponding Chapters.

1.7 Examples of applications of fluorescence lifetime and polarisation measurements

In this section, applications of fluorescence lifetime and polarisation illustrate the possible uses of these techniques. When possible, they were extracted from collaborative work carried out during this PhD, though not directly related to the present project.

1.7.1 Detection of Förster Resonance Energy Transfer (FRET) with FLIM

"*We need super-duper resolution*"

Steven S. Vogel, AIM Conference, Berkeley, 2015

In view of the arsenal of advanced and powerful techniques available to investigate biophysical processes, it is always important to understand the relevance of one particular method, as well as its limits. This is even more so the case in the rapidly evolving discipline of fluorescence imaging, with the recent invention and popularisation of super-resolution and single molecule localisation microscopy [4, 95]. FRET is possibly the best example of a photophysical phenomenon occuring below the highest resolution currently offered by these techniques, and detectable with diffraction-limited systems. Indeed, FRET occurs when fluorophores are within a ∼10-nanometre distance of each other [96], hence being a method of choice to monitor oligomerisation events, as well as protein-protein interactions.

FRET is a near-field, non-radiative process occurring when two fluorophores are in close proximity (<10 nm), initially theorised by Theodor Förster in the mid-20th century [97, 98]. FRET depends on the extent of spectral overlap between the emission band of a donor fluorophore and the absorption band of an acceptor fluorophore, as well as on the relative orientation of the emission and absorption transition dipole moments of these molecules. The likelihood of FRET decreases with the 6th power of inter-fluorophore distance, and is therefore an attractive method to detect and quantify protein-protein interactions at the nanoscale using diffraction-limited instrumentation such as spectrometers and microscopes. FRET competes with radiative decay on the donor side, and consequently decreases the excited state lifetime of the donor (Eq. 1.9) by increasing the strength of k_{nr}. The rate of energy transfer, k_{et} can be written as:

$$k_{et} = \frac{1}{\tau_{donor}} \left(\frac{R_0}{R} \right)^6 \tag{1.56}$$

Where τ_{donor} is the fluorescence lifetime of the donor in the absence of the acceptor, R is the distance between the two fluorophores, and R_0 is the Förster radius, determined as the distance for

which photon emission and energy transfer are both equally likely. R_0 encompasses the important parameters on which the rate of energy transfer depends:

$$R_0 = \sqrt[6]{\frac{9000 \mid \kappa \mid^2 \hbar c^2 ln10^2}{8\pi^3 \mathcal{N_A}^2 n^2 R^6} J(E_0)} \tag{1.57}$$

$J(E_0)$ is an expression the spectral overlap integral in energy scale, and $|\kappa|^2$ is a measure of the average relative orientation of the two interacting fluorophores. Here all the important dependencies of the probability of energy transfer can be seen, including the $\frac{1}{R^6}$ proportionality factor, mutual orientation, and the overlap integral.

FRET efficiency represents the number of photons absorbed by the donor and transferred to the acceptor, and can be calculated using fluorescence lifetimes:

$$E = 1 - \frac{\tau_{donor-acceptor}}{\tau_{donor}} \tag{1.58}$$

Where $\tau_{donor-acceptor}$ is the lifetime of the donor in presence of the acceptor. The effect of the Forster radius on FRET efficiency is illustrated in the simulation in Fig. 1.33.

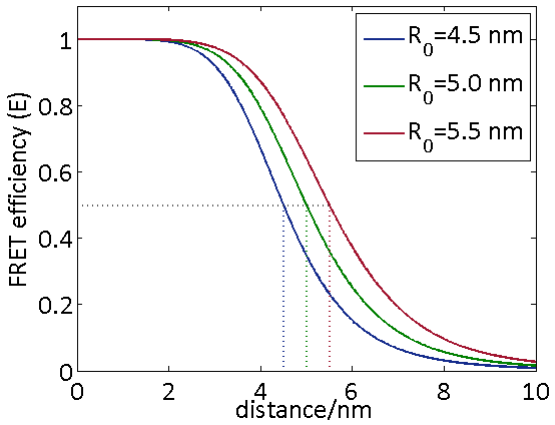

Figure 1.33: Simulated FRET efficiencies (E) as a function of the distance separating the two fluorophores. The effect of the Förster radius, inherent to the pair of fluorophores considered, is shown.

Popular donor-acceptor pairs include fluorescent protein couples with appropriate spectral properties, such as GFP-RFP or Cerulean-Venus. FRET-based biosensors have been developed to show changes in FRET efficiency upon a variety of biomolecular phenomena such as phosphorylation, allosteric changes, etc.

In collaboration with Prof. Gerard Marriott from UC Berkeley, we measured FRET in a new protein pair, based on a long lifetime donor (lumazine-associated protein, or LUMP, which has a lifetime of up to 13.6 ns), coupled to a Venus acceptor [30]. LUMP is produced by *Photobacterium leiognathi*, which lives symbiotically in the light organ of the ponyfish. It emits cyan fluorescence

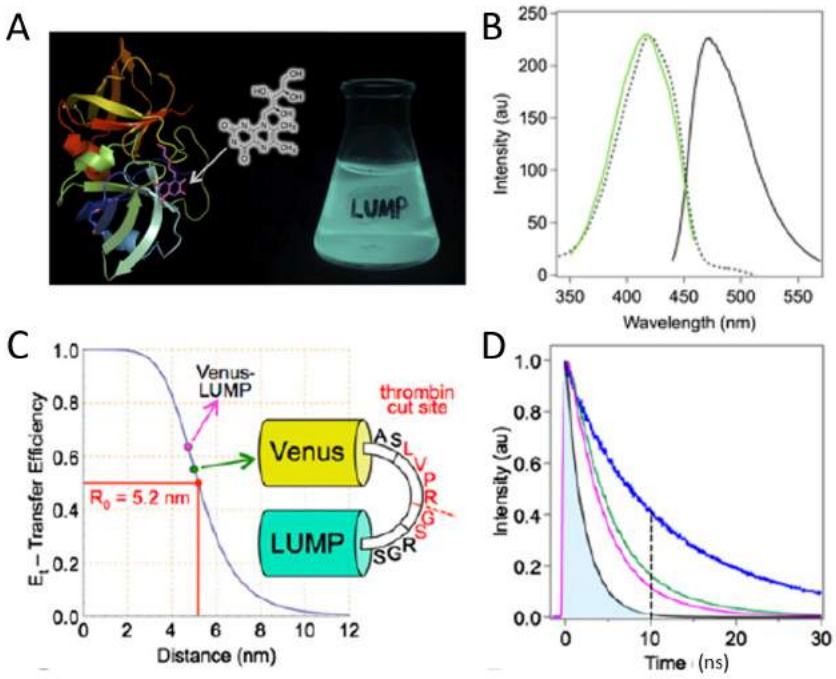

Figure 1.34: Measurement of FRET between LUMP and Venus. A. : FRET efficiency as a function of inter-fluorophore distance for LUMP-Venus. Details for the calculation of R_0 are available in the original publication ref. [30]. The FRET efficiency of LUMP-Venus with a 2 amino-acid linker is shown in pink, while the diagram shows another possible construct, containing a thrombin cutting site in the linker, which can be used to follow catalytic activity. B. Intensity decays of LUMP (blue, $\tau_{av} = 13.6$ns), LUMP-tcs-Venus (green, $\tau_{av} = 6.7$ns), and LUMP-Venus (pink, $\tau_{av} = 5.2$ns). Black: simulated intensity decay of CFP, with a lifetime of 2.2 ns. Figure adapted from ref. [30].

(Fig. 1.34.A-B) and is smaller than GFP-derived fluorescent proteins (see structure in Fig. 1.34.A, 20 kDa for LUMP compared to 28 kDa for CFP), hence decreasing inter-fluorophore distance and increasing FRET efficiency, while its long lifetime of 13.6 ns increases the dynamic range of FRET measurements. The lifetime of LUMP when linked to Venus with a short amino-acid linker (Fig. 1.34.C-D) was of 5.2 ns, yielding a FRET efficiency of 62% using Eq. 1.58. A similar, optimised, construct with CFP Venus yields a maximal FRET efficiency of 31% [99], hence showing the interest of a light-weight, long lifetime donor fluorophore for FRET experiments.

1.7.2 Detection of molecular micro-environments using FLIM

As shown in Section 2, the lifetime of organic fluorophores can be influenced by environmental factors. Fluorophores can therefore be synthesized to be made sensitive to physical parameters or chemical microenvironments of interest. In collaboration with the groups of Drs Ramon Vilar and Marina Kuimova from Imperial College London, we used FLIM of a synthetic fluorophore to detect the presence of non-canonical DNA structures called G quadruplexes in live cells. G-quadruplexes are formed by the assembly of Guanine residues in tetrads which then are stacked up on one another,

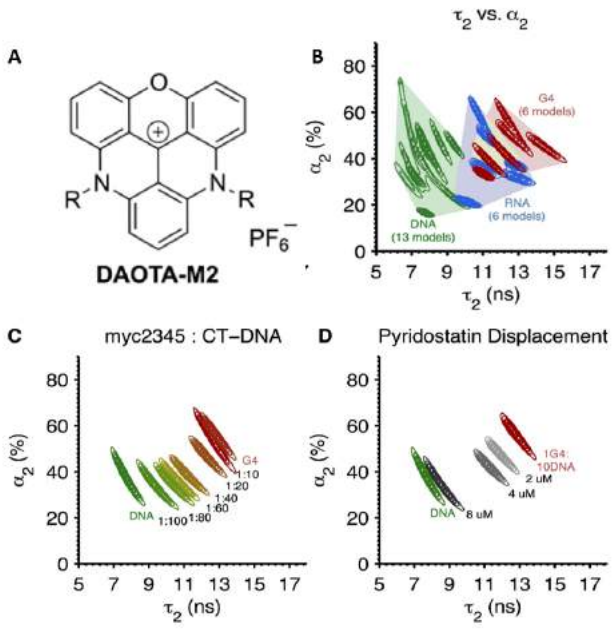

Figure 1.35: Detection of G-quadruplexes using FLIM of DAOTA-M2. A: Structure of DAOTA-M2. B: α_2 vs τ_2 contour plot showing the fluorescence lifetime signature of DAOTA-M2 in DNA (green), RNA (blue), and G-quadruplexes (red). The RNA-G-quadruplex region is shown in light orange. The number of nucleic acid models tested for each type is given. C. Same plot showing the lifetime signatures for duplex DNA-G-quadruplex mixtures. D. Same plot showing the displacement of DAOTA M2 from G-quadruplexes in a duplex DNA-G-quadruplex mixture with pyridostatin, a G-quadruplex ligand. The concentrations of pyridostatin are indicated for each contour. Figure adapted from ref. [100].

breaking the double-helix structure of genomic DNA. Their existence has been shown in vitro but their presence in live cells has remained elusive, and the development of small molecular probes offered a possibility for the detection in live cells using imaging methods. Our colleagues have developed a fluorescent compound, DAOTA-M2, which has a planar structure with a positively charged central carbonium ion (Fig. 1.35.A). This design binds to nucleic acids in vitro, probably by intercalating in the negatively charged DNA grooves. The lifetime of DAOTA-M2 when bound to G-quadruplexes was overall longer than in canonical double-stranded DNA (dsDNA) and RNA structures *in vitro*, as shown by a surface plot of lifetime parameters τ_2 against α_2 of the compound in solution with dsDNA, RNA and G-quadruplex models (Fig. 1.35.B). Titration assays showed that G-quadruplexes were detectable at 1% content in a dsDNA-G-quadruplex mixture through this lifetime shift (Fig. 1.35.C). This effect could be due to enhanced stabilisation of the excited state in these structures [100]. When a dsDNA-G-quadruplex mixture of 10:1 was treated with non-fluorescent G-quadruplex ligand Pyridostatin, DAOTA-M2 lifetime signature shifted towards the dsDNA signature (Fig. 1.35.D), suggesting the specificity of DAOTA-M2 lifetime to type of DNA structure.

Furthermore, DAOTA-M2 was shown to stain nucleic acids in live Human Bone Osteosarcoma

(U2OS) cells, and similarly to the *vitro* assay, a shift towards lower lifetimes was observed when cells were treated with pyridostatin (Fig. 1.36). These results suggest that G-quadruplexes are present in live cells, and that compounds such as DAOTA-M2 can be used to detect them *in vivo*.

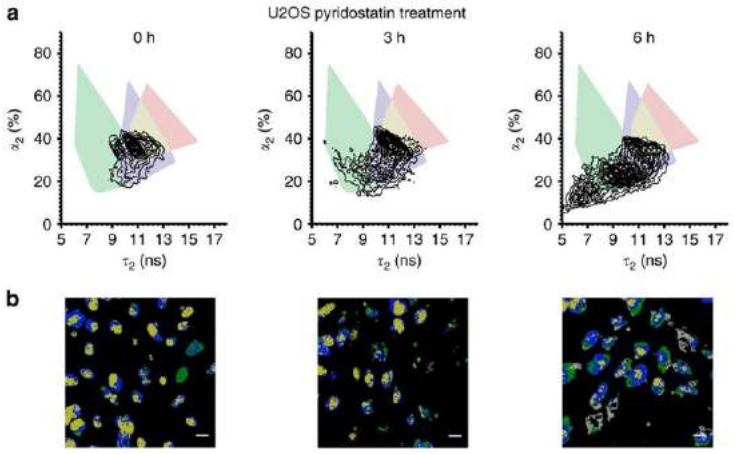

Figure 1.36: FLIM of U2OS cells stained with DAOTA-M2 upon Pyridostatin displacement for 0, 3 or 6h. a. α_2 vs τ_2 contour plot showing the fluorescence lifetime signature of DAOTA-M2 in U2OS cells as a surface plot over the DNA, RNA and G-Quadruplex domains as shown in Fig. 1.35. B (same colours). b. Images of DAOTA-M2 fluorescence in cells, colour-coded according to the position in the α_2 - τ_2 space of each pixel value. Images correspond to plots in a.

1.7.3 Applications of time-resolved anisotropy analysis

1.7.3.1 Detection of rotational correlation times

As seen in the previous section, time-resolved anisotropy can be used to report on the size and viscosity of a medium, through the Einstein-Stokes equation (Eq. 1.21). For example, Vishwasrao et al. [101] have used time-resolved anisotropy profiles of NADH autofluorescence as a signature of the bound or free state of the NADH molecule of live hippocampal tissue. This has allowed them to probe the evolution of NADH bound and unbound species upon transitioning from hypoxic to normoxic conditions.

In another recent study, Zheng et al. [70] have mapped and quantified the diffusivity of a small fluorescent molecule, AlexaFluor350, in the extracellular environment of hippocampal brain slices. The dynamics of molecular diffusion were investigated in interstitial and intracellular compartments, revealing slower overall motion in the tissue than in free medium, as well as differential diffusion in the cellular soma and in the dendrites. Furthermore, imaging the extracellular area of giant synaptic clefts formed onto CA3 pyramidal cells revealed that diffusion within the synaptic area was slower than in non-synaptic extracellular space.

While the principle and implementation of time-resolved anisotropy setups are well documented, the difficulty of obtaining good enough signal-to-noise ratios to accurately extract anisotropy parameters has precluded the more widespread use of this technique in imaging configurations.

Steady-state anisotropy is less informative but easier to achieve, and therefore enjoys more popularity.

1.7.3.2 Detection of homo-FRET

As seen in the previous section, fluorophores in close proximity can transfer excitation energy non-radiatively one to another. Historically, FRET was described analogically to coupled harmonic oscillators by François and Jacques Perrin in the twenties, and applied to electronic coupling with the appropriate energetic treatment and distance dependence by Theodor Förster in the late forties [98, 97]. Actually, the possibility of proximity-related energy transfer was postulated by Förster after the observation of concentration depolarisation in fixed fluorescent samples, which could not be only explained by reabsorption. Whilst the original publications by Förster describe the effect of energy migration on fluorescence polarisation, a formalism linking resonant energy transfer and the measure of time-resolved fluorescence depolarisation was first established in 1979 by Tanaka & Mataga [102].

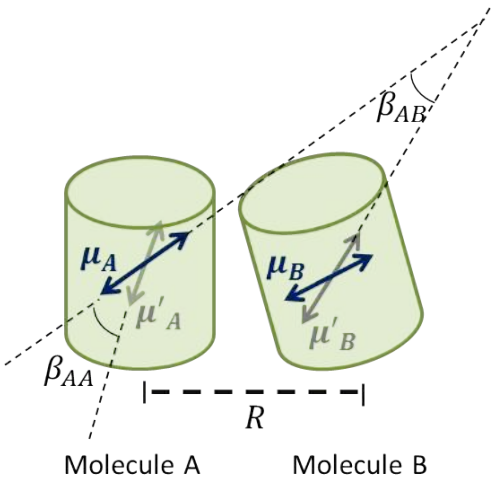

Figure 1.37: Schematic representation of two interacting GFP-like fluorophores. R is the distance between the two molecules, μ' and μ are the absorption and emission transition dipole moments for each molecule, respectively. In this section we assume that $\mu' = \mu$. β_{ij} are the angles between the emission transition dipole moment of molecule i and the absorption transition dipole moment of molecule j.

For a static interacting dimer (as shown in Fig. 1.37), the anisotropy of a population of interacting fluorophores can be written as Eq. 1.59:

$$\begin{cases} r(t) = r_\infty + (r_0 - r_\infty)\, e^{-2k_{et}t} \\ r_\infty = \frac{1}{10}(1 + 3\overline{cos^2\beta}) \\ r_0 = \frac{2}{5} \end{cases} \tag{1.59}$$

Where k_{et} is the rate of energy transfer, as defined in Eq. 1.56, with $\overline{cos^2\beta}$ the average value of

$cos^2\beta$ in the sample. r_∞ is the residual anisotropy, which subsists after all depolarizing processes have taken place. It is interesting to see that the time evolution of r(t) takes the same form as that of a hindered rotor, while here the depolarisation is due to energy transfer. The parameters r_∞ and k_{et} inform on the interacting system at hand:

- k_{et} gives the separating distance R between the two fluorophores, after R_0 and τ have been determined.
- The residual anisotropy r_∞ is determined by the angular distribution of β. If the dipoles of the interacting molecules are randomly oriented with respect to each other, we have $\overline{cos^2\beta} = 1/2$ and equation 1.59 can be simplified to (1.60):

$$r(t) = \frac{1}{4} + \frac{3}{20}e^{-2\rho t} \tag{1.60}$$

  So, in the case of an interacting dimer system, we obtain a residual anisotropy of 1/4. In the absence of interaction, the limiting anisotropy is equivalent to the initial value since no depolarisation occurs, and we obtain $r_\infty = r_0 = \frac{2}{5}$. The presence of energy transfer can hence be detected in motionless samples by the decay of the fluorescence anisotropy to a limiting value lower than that of non-interacting monomers. Here the case of a dimer was exposed, but this theory can be extended to the scenario of larger oligomerisation states. In this case, the residual anisotropy is even lower.

Though the use of homo-FRET is not as widespread as its photophysical cousin hetero-FRET, possibly due to higher instrumental and analytical requirements, homo-FRET is a powerful tool for biophysics since it requires only one fluorophore, end hence simplifies the imaging by eliminating possible bleed-through and ensures 100% of the signal from interacting fluorophores is captured (against 50% in the case of hetero-FRET, where the donor-donor and acceptor-acceptor interactions are lost). Moreover, the molecular biology is also unburdened from multiple cloning necessary for hetero-FRET [103].

In collaboration with Dr. Aleksandar Ivetic from King's College London, we used homo-FRET imaging to detect the clustering behaviour of a membrane protein, l-selectin, during leukocyte transmigration. Transmigration is the sequence of events by which a white blood cell leaves the blood stream and squeezes through the vascular endothelium to progress towards the site of an inflammation in the tissue. Endothelial cells are bound by tight junctions, and therefore the molecular processes necessary for leukocytes to efficiently transmigrate involve many different proteins. L-selectin is one such protein, and is involved in cell surface adhesion during the 'tethering and rolling' process in the initial stages of transmigration [104]. Our data shows lower anisotropy values in the protruding areas of the cell (Fig. 1.38), suggesting that l-selectin clusters increasingly in

these regions, which is corroborated by similar published studies using hetero-FRET of l-selectin [105]. The homogeneity of GFP lifetimes across the cell demonstrate that homo-FRET does not affect this parameter (central panel).

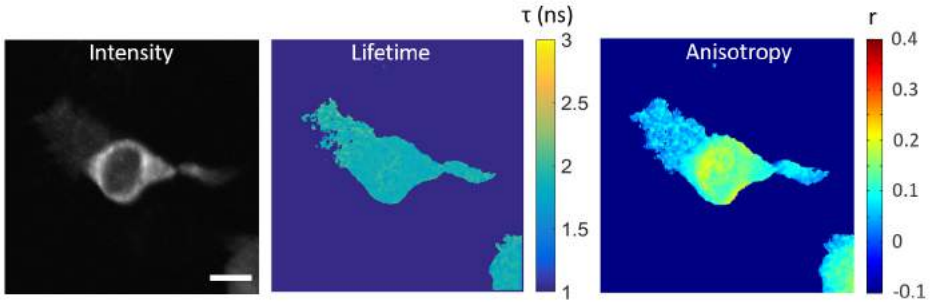

Figure 1.38: Homo-FRET imaging of l-selectin clustering during leukocyte transmigration. Left: Confocal intensity image. Centre: Lifetime map (a single exponential decay model was used with a convolution sum filter of kernel 3-by-3 pixels, to obtain a minimum of 100 photons in the maximum bin) - colorbar values are in nanoseconds. Right: steady-state anisotropy image. Scale bar is 10 μm.

Homo FRET has been used by Joao Sarmento et al. to quantify Ca^{2+}-dependent PIP2 clustering in membranes [106], and by Bader et al. to quantify the clustering behaviour of membrane protein EGFR using a time-gated system [50, 51, 107]. Other applications include the development of biosensors based on homo-FRET. For example, Cameron et al [108] have developed a fluorescent biosensor of NADP+ based on homo-FRET, and use steady-state 1-photon or 2-photon anisotropy to map $NADP^+$ localisation in live cells and the interplay between $NADP^+$ depletion and hydrogen peroxide generation.

Conclusions

This chapter has introduced the concepts of fluorescence, fluorescence lifetime and polarisation, as well as their use in imaging experiments. The theory of time-resolved fluorescence depolarisation in membranes was summarised two membrane order parameters were established, to be used in the following chapters. The polarisation-resolved TCSPC-confocal FLIM microscope used in the laboratory has also been described, as well as the calibrations carried out to ensure the good quality of the acquired data. Methods to analyse FLIM and TR-FAIM data were introduced as well, and their respective advantages and limitations discussed. In particular, different strategies for the analysis of time-resolved anisotropy were explored and compared, with the introduction of a weighted fitting routine. Lastly, applications of FLIM and TR-FAIM were shown from the body of collaborative work carried out in our laboratory, some of which has led to publications, highlighting the versatility of these two techniques. The next chapter makes use of these concepts to develop

a method for multi-dimensional fluorescence imaging of lipid bilayers and cell membranes. Some biological background relevant to the experiments at hand will firstly be reviewed.

Chapter 2

Linking the chemical nature of lipid bilayers to their physical properties using multi-dimensional fluorescence of environmentally-sensitive dyes

2.1 Introduction

2.1.1 Cell membranes and artificial models

2.1.1.1 Structure and biological importance of cell membranes.

All living cells are limited by a membrane, which acts as a selective barrier through which cells exchange, sense and communicate with their environment. Membranes are structurally composed of lipid bilayers, which are characterized by a large variety of lipids. The chemical nature of these bilayers varies depending on cell types, organisms, and physiological states, and at any given point, the cell membrane is composed of hundreds of different types of lipid molecules, which can be divided in categories according to their chemical nature [109]:

- The bulk of the lipid bilayer is composed of glycerophospholipids, or phospholipids: a glycerol molecule is linked to two fatty acids on the sn1 and sn2 positions via ester bonds. The acyl chains of the fatty acids vary in length and degree of saturation, and may be different from one another in the same molecule. Unsaturations in the *cis* configuration (Fig. 2.1. A) create elbows in the acyl chains and decrease the melting temperature of such lipids, while fully saturated chains increase the level of hydrophobic interactions and create more packed

structures with higher melting temperatures. The third position of the glycerol molecule is phosphorylated, and usually linked to a polar headgroup, which also varies in chemical nature: the most common headgroups include choline (PC) and ethanolamine (PE). Less common phospholipids such as phosphatidylinositides (PI) and phosphatidylserine (PS) are present in small quantities in the membrane, but have important roles in signalling.

- Sphingolipids are derivatives of lipid sphingosine; in the most common sphingolipid, sphingomyelin, sphingosine is acylated and presents a phospho-choline group (Fig. 2.1.B). Less abundant sphingolipids include cerebrosides and gangliosides.

- Sterols (cholesterol in mammalian cells) are present at up to 50% molar in membranes and play a crucial role in regulating the fluidity of the membrane (Fig. 2.1.C). The turnover of cholesterol in cellular membranes is high, with plasma membranes continuously losing and receiving cholesterol to and from the extracellular medium via Low Density Lipoprotein (LDL)-mediated transport [110].

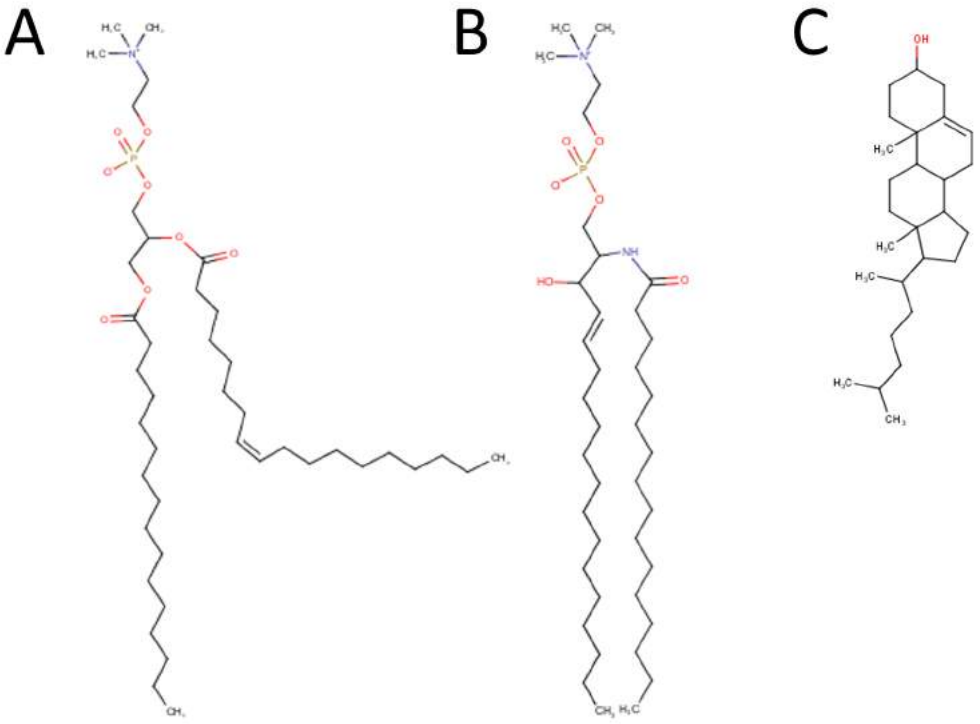

Figure 2.1: Chemical structure of membrane lipids. A. 1-Palmitoyl-2-Oleyl-phosphatidylcholine (POPC). B. An example of sphingomyelin. C. Cholesterol.

- The bilayer leaflet is also home to membrane proteins, which can be either intrinsic (presence of at least one transmembrane domain) or associated to the membrane via a lipid linker. Membrane proteins play crucial roles in reception of extracellular signals, ion and solute

trafficking, cell-cell and cell matrix interactions, and as such are the main functional elements of the membrane. Membrane proteins also mediate the mechanical coupling of the membrane to the cytoskeleton [111]. In particular, a network of actin filaments, the submembrane actin cortex, is crucial in maintaining cell shape and mechano-transduction, and is also involved in the lateral distribution and diffusion of membrane components, as will be further discussed.

Membrane leaflets are also asymmetric, with some lipids residing preferentially or exclusively in one leaflet or the other: for example, PE and PS tend to be more abundant in the inner leaflet, while GPI-associated proteins are specific to the outer leaflet [112]. The mechanisms by which cells adapt their membrane lipid composition to the environment are not yet fully elucidated, and the reasons for this chemical diversity are also still unclear. What is clear however, is that cells allocate significant resources for the production of a large variety of lipids [113]. In eukaryotic cells, subcellular organelles are also delimited by membranes, with specific compositions. The plasma membrane is enriched in sphingomyelins and cholesterol, which is thought to confer it additional stability. Studies have shown that plasma membrane organisation is cell-cycle and cell-type dependent [114, 115]. There is therefore interest in pushing our understanding of the physical properties of lipid bilayers in physiologically relevant compositions and conditions.

2.1.1.2 Model membranes for biophysical studies

Artificial membranes Understanding the physical behaviour of cell membranes has been greatly helped by the use of artificial lipid bilayers, which mimic the cell membrane while enabling full control of its chemical composition. Artificial bilayers can be created in the form of spheres, or unilamellar vesicles, with varying sizes (See Table 2.1). Another possibility is the formation of Supported Lipid Bilayers (SLBs), which are planar membranes on a flat surface such as glass or mica. Giant Unilamellar Vesicles (GUVs) and SLBs both have dimensions compatible with optical microscopy, and for this reason have been extensively used to study membrane biophysics.

Type	Size	Preparation	Applications	Refs.
Small Unilamellar Vesicles (SUVs)	10 - 100 nm	Sonication, Extrusion	Spectroscopy, Drug delivery, in vivo imaging	[116, 117, 118]
Large Unilamellar Vesicles (LUVs)	0.1 - 1 μm	Sonication, Extrusion	Spectroscopy, Optical microscopy	[119, 120]
Giant Unilamellar Vesicles (GUVs)	1 - 100 μm	Electroformation, Sonication	Optical microscopy	[91, 121, 122, 120]
Supported Lipid Bilayers (SLBs)	∞	Vesicle Deposition, Langmuir-Blodgett trough, Spin Coating.	Optical microscopy, AFM	[123, 124, 125, 126, 127, 128]

Table 2.1: Artificial membrane models: sizes, preparation methods and applications.

A popular method to prepare GUVs is the electroformation method, initially devised by Angelova et al [129], in which lipid films are deposited on conductive surfaces assembled to form a capacitor chamber in aqueous buffer. This chamber is then subjected to AC current with a low frequency (i.e. 10 Hz); this will cause the charged polar heads of the lipids to oscillate with the current, and eventually detach from the surface and form spheres suspended in the aqueous buffer. SLBs can be created by the vesicle deposition technique, where sub-micron sized vesicles fuse with a hydrophilic surface, break, spread and coalesce, to form continuous bilayers on the surface. For their ease of formation and their spherical shape, which is closer to the configuration of a cell (compared to a planar surface), GUVs were chosen as the model system to study lipid bilayers in this project.

Cell-derived vesicles Levental and colleagues have implemented a method to extract lipids from the membranes of live cells in adherent cultures in the form of micron-sized vesicles, named Giant Plasma Membrane Vesicles (or GPMVs) [130, 131]. Vesiculation agents such as Dithiothreitol (DTT) are used in combination with crosslinking compound Paraformaldehyde (PFA) to trigger vesicle production from cells. GPMVs have been shown to be free of actin cortex [132]. GPMVs offer an interesting advantage over artificial systems since they include the full diversity of cellular lipids as well as membrane proteins, while offering a simplified geometry and a theoretically pure plasma membrane fragment [133]. However, it is also likely that the vesiculating and crosslinking agents necessary for their formation affect the lateral organisation of membrane components. GPMVs will be characterised as a system to study membrane microenvironments and order parameters in the next chapter.

2.1.1.3 Phase behaviour of lipid bilayers

Lipids transition from a solid state to a liquid state, at a temperature defined by the number of unsaturations and the length of the acyl chains. Bilayers composed of a single type of lipid are in the gel phase (S, for solid) below the transition temperature, and in the liquid phase, Ld, above this temperature. In mixtures of two types of lipids, solid-liquid phase separation occurs at temperatures between the phase transitions of the two lipids, which means that the bilayer is composed of separate domains in the gel and liquid phases, respectively.

Furthermore, a "liquid-ordered" phase emerges from the association of cholesterol with phospholipids and sphingolipids. The Lo phase is intermediate in its physical properties between the Ld and S phases - the impact of cholesterol on the physical properties of lipid bilayers and the characterisation of the Lo phase have been the object of extensive research, and is presented in more detail in the next section.

Mixtures of cholesterol with saturated and unsaturated lipids also present phase-dependent domain formation. A Lo domain composed mainly of saturated lipids and cholesterol segregates from a Ld domain, composed mainly of unsaturated lipids. Using fluorescence microscopy, phase diagrams of domain formation have been established for such mixtures [134, 91], as shown in Fig. 2.2 below.

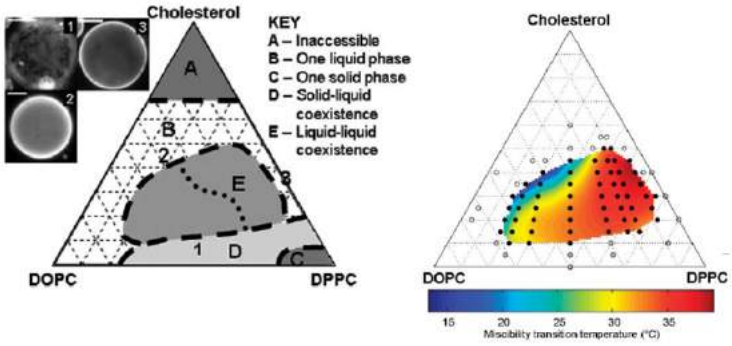

Figure 2.2: Phase diagrams of ternary lipid mixtures with unsaturated lipid (DOPC), saturated lipid (DPPC) and Cholesterol. The apices of the triangle represent pure compositions of the corresponding lipid. The diagram on the left shows the phase of each lipid composition. The diagram on the right shows the temperature below which Lo and Ld phases segregate into two distinct domains. Figure adapted from ref. [134] with permission from Elsevier.

While none of this is astonishing from a physical point of view, what is interesting is that in physiologically relevant proportions, the transition temperature for Ld-Lo domain coexistence of biological lipids is within the temperature range relevant to biology. For example, a DOPC:DPPC:Chol 2:2:1 bilayer contains segregated domains below 34^{o}C. For this reason, it has been postulated that the same phenomenon of Ld-Lo phase coexistence may occur in vivo, and there is growing evidence that the lateral organisation of cell membranes is dynamic and heterogeneous at the nanoscale. Understanding the basis of this lateral organisation is the object of active research, as introduced in the following section.

2.1.1.4 Models for the lateral organisation of the cell membrane

While micron-scale phase separation occurs in model systems as shown above, this is not observed in live cells under physiological conditions, so a simple phase partition model does not capture the full picture of lateral membrane organisation. The large variety of lipid molecules, the presence of membrane proteins and the interactions with the cytoskeleton may all contribute to controlling the lateral organisation of cell membranes. Since the introduction of the "fluid mosaic" model by Singer and Nicholson in 1972 [135], several models have been proposed to represent the lateral organisation of cell membranes. These models aim to encompass some of the fundamental properties of lipid bilayers, such as phase separation, protein diffusion and clustering, interactions with the actin

cortex, etc., and they are not necessarily mutually exclusive [136]. Here, the main characteristics of several such models relevant to this project are summarised, and some examples of experimental studies are given in which these particular models prove especially useful.

- **The lipid raft hypothesis**

Heterogeneity in biomembranes has been known since the 1970s, with the experimental observation of detergent-resistant membrane fractions and of membrane protein clusters. In their seminal paper, Simons and Ikonen introduce the notion of nanoscopic membrane domains enriched in saturated lipids (in particular, sphingomyelin) and cholesterol, and coin the term "lipid rafts", which would support the clustering of membrane proteins involved in signalling processes [110]. Since then, the lipid raft hypothesis has been strengthened by the observation of detergent-resistant membrane fractions [137], hindered lateral diffusion of lipids and proteins in model bilayers and live cells, and the fact that some lipids tend to self-aggregate. However, if lipid rafts do exist, the current consensus is that their size is below the optical resolution, and that they are highly dynamic. Therefore, direct observation of such structures in live cells remains challenging, and their existence, controversial, with different methods yielding contradicting results (see for example refs. [138, 139]). Different membrane proteins have been shown to segregate into different phase-separated domains of cell-derived vesicles, suggesting that nanoscale lipid domains may contribute to membrane clustering [133, 131, 130].

The lipid raft hypothesis offers attractive insight to understand phenomena involving biomembranes, such as viral melting. Viral melting proteins are thought to be associated with lipid rafts, which is supported by the observation that viral melting is inhibited by removal of cholesterol from viral and cell membranes. Remarkably, Yang and colleagues [119] recently showed that the HIV melting peptide gp41 targets Lo-Ld domain boundaries preferentially, and that these edges were necessary for full melting of HIV melting protein liposomes.

It follows from this type of observation that since viral melting occurs in vivo, Lo-Ld boundaries must occur in live cells (though in spatio-temporal scales very different to the ones showed here), possibly in the form of lipid rafts. The lipid raft model can be further consolidated by incorporation of the interactions between the bilayer and the underlying actin cortex.

- **The "picket fence" model**

Networks of actin filaments below the cell membrane, qualified as the submembrane actin cortex, interact directly with the bilayer through actin-binding membrane protein complexes such as members of the ERM (Ezrin-Radixin-Moesin) family. This network affects the lateral organisation of molecules for example by restricting the diffusion of lipids and proteins [111, 140], hence the notion of a "picket fence" model. The bilayer plane would therefore be composed of "pools" of

free molecules surrounded by fences of actin-associated proteins, and their long-range diffusion would be dependent on their ability to pass through these fences. This model has been particularly useful to explain the diffusion barriers present in cell membranes [141, 142]. Honigmann and coworkers [125] provided a compelling experimental observation of the effect of interactions with an actin meshwork on size of lipid domains in a supported lipid bilayer, and on the lateral diffusion of lipids, using STED microscopy and Fluorescence Correlation Spectroscopy. Binding of a SLB containing DOPC, DPPC and Cholesterol to actin fibers significantly increases the phase transition temperature, meaning that separate domains are stable at higher temperatures than in actin-free SLBs. The size of the domains in the presence of actin is also smaller and clearly below 100 nm, and their shape correlates with the organisation of the actin fibers. The actin fibers acted as diffusion barriers, while diffusion along the axis of the fibers was facilitated.

This study was carried out using a simplified, artificial system, with an actin cortex-membrane pinning which is different from the membrane protein-mediated mechanism observed in cells. However, these results strengthen the hypothesis that sub-resolution lipid domains exist in the cell membrane, with the shape, size and diffusion of these domains strongly determined by interactions with the submembrane actin cortex.

- **The shell model**

The shell model proposes that the membrane is organised in entities, such as nanoclusters, nanodomains and microdomains, of different spatial scales included in one another, and that these entities have different spatio-temporal dynamics [143]. This model is supported by experimental evidence of lateral heterogeneity at many different scales in cell membranes, such as the T-Cell immunological synapse. Indeed, membrane condensation has been observed at the micron scale in such systems [144], additionally to clustering events at the nanoscale [138].

- **The mattress model**

This model, introduced by Mouritsen in 1984 [145], provides a theoretical basis for the interaction between membrane proteins and lipids. The thickness of the bilayer varies locally to accommodate the presence of hydrophobic transmembrane α helices, to avoid the unfavorable exposure of such structures to the extra- or intra-cellular aqueous environment. This would then contribute to the nature of the lipid content around membrane proteins, and clusters thereof.

In the first part of this work, the objective is to describe the diffusion behaviour and microenvironment of membrane lipids as a bulk phase, beyond the notion of any model of membrane organisation. The results will therefore inform on the role of lipid chemistry itself on the collective properties (membrane order, polarity, hydration), of a lipid bilayer. In the second part of this work, these properties will be quantified in a phase-separating lipid mixture, which will provide

further understanding of the properties of lipid domains in the framework of the lipid raft hypothesis. Lastly, the extension of this investigation to live cells and cell-derived membranes (in Chapter 3) will interrogate the role of the cytoskeleton and cholesterol in membrane order and microenvironment, with the aim to understand the relevance of the more integrative models of lateral membrane organisation mentioned above (picket-fence, shell, mattress models) to explain such physical and chemical properties of lipid bilayers in biological contexts.

2.1.2 Methods to study membrane biophysics

Though the examples from the literature presented above all show results produced using fluorescence microscopy, other techniques exist to study the physical properties of cell membranes. Nuclear Magnetic Resonance and Mass Spectroscopies can identify the chemical composition of lipid samples by detecting spectroscopic signatures of different lipid molecules [146, 147, 148]. Such methods provide valuable information to understand the basis and evolution of large variety of lipids present in membranes, which is qualified as the "lipidome".

X-ray and neutron scattering can be used to measure lattice parameters and packing of hydrocarbon chains since lipid bilayers are essentially liquid crystalline structures [149]. These methods can resolve characteristics of lipid bilayers very precisely, however they offer no spatial resolution, and are often not compatible with live cell samples. On the other hand, Atomic Force Microscopy can be used in imaging mode, and its sensitivity goes down to the single atom and tenths of nanometres [150], therefore can be used to resolve nanoscopic lipid domains through small differences in bilayer thickness between the Lo, Ld and Gel phases [123, 115], which are impossible to resolve using optical techniques. AFM can also be used to quantify mechanical properties of the membrane such as stiffness.

Fluorescence microscopy, in spite of its lower spatial resolution abilities compared to AFM, offers many advantages as cited in the introduction. Here, the emphasis is made on the ability of fluorescence techniques to resolve functional, as well as structural, information, in lipid bilayers and cell membranes. Dynamic mechanisms such as diffusion processes, as well as the chemical characteristics of membrane environments can be probed using fluorescence microscopy, and this, in a manner compatible with live cell imaging, which sets it apart from other methods.

2.1.2.1 Quantifying diffusion in cell membranes

- **With Fluorescence Recovery After Photobleaching (FRAP),** the increase in fluorescence intensity is measured after a region in the sample is bleached. From the fluorescence recovery curves after the bleaching step, the lateral diffusion coefficient of the fluorophore is extracted. Mobile and immobile fractions of the membrane can also be derived from the in-

tensity after return to a steady state intensity. Using FRAP, Hao and colleagues have shown a decrease in the lateral mobility of lipids upon cholesterol depletion [151], while Goodwin et al. used FRAP to quantify the lateral diffusion of membrane-associated protein Ras in ref. [152].

- **Fluorescence Correlation Spectroscopy** measures intensity fluctuations in a small detection volume (diffraction-limited spot, or in the case of STED-FCS, even smaller) which contains only a few fluorescent molecules at any given point. An auto-correlation curve is computed from this intensity time course, and the characteristic time of this autocorrelation curve represents how long a fluorophore stays in the detection volume on average, and yields a diffusion parameter. Interestingly, FCS can be combined with TCSPC measurements, and fluorescence lifetimes and diffusion times are simultaneously obtained. In ref. [124], differences in diffusion times as domains of a phase-separated lipid bilayer were obtained using FCS, and lateral diffusion in the Ld phase was 6 to 10 times as rapid as in the Lo phase, depending on the dye used. FCS has been combined with STED, and by tuning the power of the depletion beam, the size of the detection volume can be controlled, to extract information about the diffusion properties as a function of the distance, hence evidencing phenomena such as hindered lateral diffusion, which would suggest that pools of fluorophores stay for long times in nanoscopic domains [153]. FCS has also been used to study lateral diffusion in coexisting Lo-Ld domains, showing that removal of cholesterol leads to a transition towards S-Ld domains [154]. In an imaging framework, image correlation methods such as Spatio-Temporal Image Correlation Spectroscopy (STICS), are also based resolving the dynamics of intensity fluctuations, and can resolve intensity and directionality of diffusion processes in membranes [155].

- **Fluorescence Anisotropy** measures the rate and extent of rotational diffusion by quantifying the depolarisation which occurs in a photo-selected population of fluorophores between absorption and emission, as explained in the introduction. Anisotropy can be measured in a time-resolved manner after a pulse excitation to resolve two order parameters θ and Δ, or in a steady-state fashion, where r_{ss} is linked to the fluorescence lifetime and order parameters via the Perrin equation. Possibly the first anisotropy imaging experiments in membranes were performed by Axelrod [156], who demonstrated the ordering of carbocyanine dye DiI in red blood cell ghosts. Anisotropy of GFP-tagged membrane proteins was first described by Rocheleau, in ref [157], showing that proteins are also aligned to the membrane normal, confirming the theory by Kinosita et al [26]. Note that other methods based on fluorescence polarisation exist to resolve order parameters in membranes, such as linear dichroism [158], which quantifies the angular distribution of a membrane dye using knowledge of its transition

dipole moment and of the sample geometry. This is an attractive method since it does not require time-resolved instrumentation; however, since the observed quantities depend on the local orientation of the membrane, effects of angular distribution and sample geometry are combined, and assumptions must be made about one to extract information about the other.

It is interesting to note that these three types of methods can be used to resolve diffusion processes in membranes; each of them is linked to a different spatial scale: FRAP quantifies lateral diffusion on the scale of several microns, while FCS and STICS do so within diffraction-limited volumes [155]. Lastly, anisotropy measures rotational diffusion, which occurs on the scale of the molecules themselves - though in conventional microscopy, the signal obtained is the sum of tens, if not hundreds of molecules. diffusion coefficients participate in the notion of membrane order, so these different techniques report on the ordering of the membrane at varying scales. Some developments have combined some of these methods to measure diffusion at different spatial scales, simultaneously: Machan et al have compared the information provided by FRAP and FCS on lipid bilayers [159], while simultaneous FRAP, FAIM and FLIM was recently implemented in our laboratory, though has not yet been applied to lipid bilayers [160].

2.1.2.2 Probing membrane micro-environments

Environmentally-sensitive membrane dyes The fluorescence intensity, emission wavelength and lifetime of membrane fluorophores can be made sensitive to relevant properties of the membrane. Membrane dyes sensitive to membrane charge , viscosity or hydration [16, 161, 162, 163, 164] have been synthesised and used for imaging purposes. Relevant to this experiment, fluorescent lipid analogues laurdan and di-4-ANEPPDHQ are solvatochromic dyes, where the relaxation of water molecules in proximity of the fluorophore decreases the energy of the excited state, and causes longer emission wavelengths. It follows that in bilayers which allow more water molecules and more diffusional freedom of these molecules, the spectrum of such dyes will be red-shifted.

Laurdan and members of the same chemical family have been extensively characterised since the 90's and used in spectroscopic contexts in the laboratory of Prof. Gratton [165, 166, 167], who proposed a quantification of this solvatochromic effect with two spectral windows using the generalised polarisation ratio:

$$GP = \frac{I_{blue} - I_{red}}{I_{blue} + I_{red}} \tag{2.1}$$

In environments with low hydration, the intensity of laurdan fluorescence and of di-4-ANEPPDHQ is relatively stronger in the blue emission band than in the red, yielding high GP values. In highly polar environments, the GP values are low. Parasassi et. al measured the GP of laurdan in various

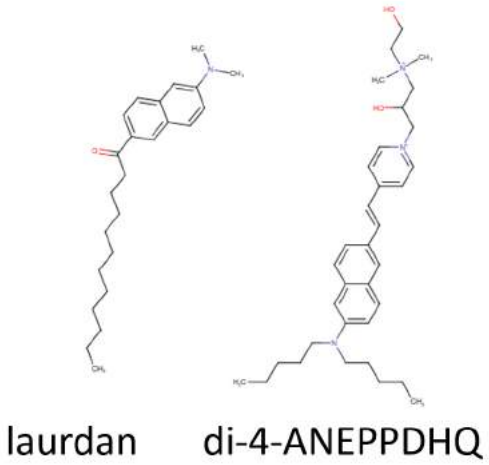

Figure 2.3: Chemical structures of laurdan and di-4-ANEPPDHQ.

solvents, and have found it to be related to the dielectric constant of the medium [165]. The spectral windows for I_{blue} and I_{red} should be chosen according to the dye and excitation wavelength. GP imaging has since been used extensively to identify changes in lipid hydration in bilayers and cell membranes [168, 169, 91, 170, 171, 172]. For example, Gaus and co-workers used GP of laurdan to show the condensation of the T-Cell plasma membrane upon formation of an immunological synapse in contact with an antigen-presenting cell [144].

Many other fluorescent probes exist and are used for a variety of applications, a detailed review can be found in ref. [16].

Simultaneous quantification of membrane micro-environments and diffusion properties
As seen from the paragraphs above, fluorescence can be used to acquire functional information on membranes such as diffusion processes, and membrane micro-environment. The purpose of this project is to acquire both types of information simultaneously, using multi-dimensional microscopy. Previous studies have used different approaches to achieve this. For example, Haluska and colleagues [173] used a combined fluorescence lifetime and polarisation imaging approach in GUVs stained with TMA-DPH, to resolve the order parameters and rotational regimes as a function of cholesterol content in homogeneous and phase-separated bilayers (Fig. 2.4). The order parameters are resolved from angular intensity profiles in the GUVs. Their results suggest that the rotational model ("hard cone model" or "diffusion in a potential model") differs depending on the phase, while the order parameters are affected differently by cholesterol in bilayers composed of unsaturated or saturated lipids. In unsaturated bilayers, order parameters increase linearly with cholesterol content, while saturated bilayers show little evolution of these order parameters with cholesterol

content. The fluorescence lifetime of TMA-DPH is assumed to report on membrane viscosity, and increases with cholesterol content with the same sensitivity in both saturated and unsaturated bilayers. Another interesting finding is that in DOPC-Sm-Chol ternary lipid mixtures showing phase separation, the order parameters of each phase are different to those of binary mixtures of either DOPC-Chol or SM-Chol with the same proportion of cholesterol. This suggests that the domains in phase-separated bilayers are composed of the three types of lipids composing the mixture, in different proportions.

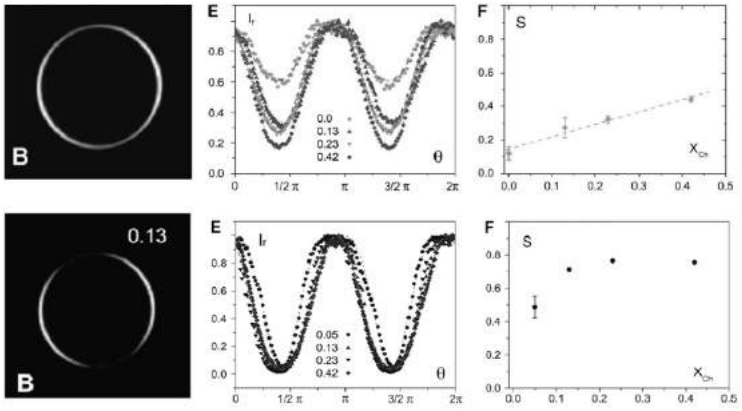

Figure 2.4: Order parameters of lipid bilayers resolved by Haluska et al using fluorescence polarisation of TMA-DPH. Upper row: DOPC-Chol. Lower row: DPPC-Chol. B: Images of GUVs composed of DOPC and DPPC containing 13 mol% Chol. Note the visible extinction at the poles of the DPPC-Chol vesicle, indicating that the dye is highly aligned with the membrane lipids. E: Angular intensity profiles of GUVs with varying cholesterol contents. F: Order parameter S derived from curves shown in E., as a function of cholesterol content. Figure adapted from ref. [173], with permission of Elsevier.

Other studies have proposed independent quantification of various bilayer parameters such as hydration, polarity, or cholesterol content, using spectrally-resolved fluorescence lifetime measurements [169]. However, the photophysical behavior of laurdan is complex and the specificity of laurdan lifetime to such properties, as well as the true independence of the measured quantities, is difficult to ascertain. Sanchez et al. [174] have combined GP with intensity fluctuation analysis to correlate membrane hydration and lateral diffusion in cell membranes to image microdomains . Steady-state anisotropy measurements of laurdan have been carried out in refs. [175, 91], and correlated with GP information. However, the dependence of steady-state anisotropy values on fluorescence lifetimes, due to the Perrin equation, creates an interdependence between the obtained quantities. This prompts the present idea to develop a method similar to that of Haluska et al [173], encompassing the spectral, lifetime and polarisation information of fluorescence, to achieve simultaneous and independent probing of membrane microenvironments and membrane order.

2.1.3 Hypothesis and research questions

The multiplication of fluorescence methods and probes to study biomembranes has led to a commensurate variety of terms to describe membrane behaviour: membrane polarity, fluidity, order, viscosity, packing, hydration, charge, etc. Frequently, changes in the fluorescence signal of solvatochromic probes are interpreted as changes in membrane order, when what is in effect measured is changes in dipolar relaxation at the immediate proximity of the fluorophore. Certainly, correlations exist between such properties, but often, one single property is sensed and used as a proxy to qualify the general state of the membrane as "ordered" or "disordered". This of course has been extremely useful in resolving general principles of phase behavior in lipid bilayers and explaining membrane function in cells including the lipid raft hypothesis, but by itself is a simplification of the system. Indeed, some studies point towards the fact these parameters evolve differently from one another with membrane composition [120, 91, 173, 169, 176]. Moreover, from a chemical point of view, the binary Ld/Lo phase partition model is only an incomplete way of describing lipid bilayers, and there is no consensus as to which lipid mixtures are most representative of Ld or Lo phases.

Taken together, these considerations mean that the terms "ordered" or "disordered" may encompass diverse and possibly heterogeneous compositions and physio-chemical properties in biological contexts. The hypothesis governing the work in this chapter is that the relationship between membrane order and microenvironment depends on the chemical nature of the membrane, as well as its phase state. With this in mind, answers to the following research questions will be sought:

- What microenvironmental properties are reported by commonly-used solvatochromic membrane dyes?
- Can membrane order parameters and microenvironment be independently measured using a single fluorescence probe?
- How are membrane microenvironment and membrane order related, and how does membrane chemistry and phase behaviour affect this relationship?
- Can the measurement of these properties inform on the chemical nature of a lipid bilayer?

Using time- and polarisation-resolved fluorescence microscopy of environmentally sensitive membrane dyes laurdan and di-4-ANEPPDHQ along with their spectral information, membrane microenvironment and membrane order parameters are probed simultaneously and independently. The fluorescence lifetime and spectral emission of the dyes are used to report on membrane hydration and polarity, while time-resolved anisotropy provides two order parameters indicating membrane fluidity and packing, as explained in the introduction. The novelty of this approach lies in the truly

independent but simultaneous measurement of these parameters, and unambiguous determination of order parameters using time-resolved anisotropy. Using this method, correlations between these parameters as a function of temperature and chemical composition of the lipid bilayer can be established. In this chapter, this method will be introduced and used on artificial membranes (Giant Unilamellar Vesicles, or GUVs) to establish the relationship between these membrane properties in simplified systems. Temperature control is used as a simple way to provoke changes in the physical behaviour of the bilayers, to understand how membrane microenvironment and order parameters evolve together. In the next chapter, this method will be extended to cell-derived plasma membrane vesicles (Giant Plasma Membrane Vesicles, or GPMVs) and live cells.

2.2 Methods

2.2.1 Sample preparation

2.2.1.1 Giant Unilamellar Vesicles

Lipids were purchased from Avanti Polar Lipids and stored at -20^{o}C. GUVs were created using the electro-formation method, as established by Angelova et al [129]. Desired lipid mixtures were created in 100 μL chloroform, to a final concentration of 10 mg/mL lipids. Laurdan was added from a 3.4 mM, 2:1 chloroform:methanol stock solution, so that the molar dye-to-lipid ratio was around 1%. Adding the dye directly into the lipid mixture before formation of the vesicles (as opposed to after) enabled control of its concentration and ensured homogeneous distribution of the dye in the bilayers, while limiting background fluorescence in the sample during imaging. 6 µL of the lipid mixtures were then spread onto the conductive sides of two Indium-Tin-Oxide coated slides (Sigma, 8-12 Ohm/cm^2), to form a circular film of around 1 cm^2. The film was then dried under nitrogen flow to eliminate traces of solvent, and a 2-cm diameter, 1-mm thick nitrile O-ring was coated in a thin layer of vacuum grease and applied to one of the ITO-coated slides, to form a chamber around the film. The chamber was filled with 200 mM sucrose buffer and closed with the second slide, and was connected to a generator delivering a 10 Hz, 2.5V sine-wave signal. For lipid mixtures containing DPPC or cholesterol, electro-formation was carried out at 50^{o}C. Vesicles were left to form for between 3 and 12 hours and their formation could be monitored using bright-field microscopy, with a low-magnification objective. An image of this home-built electroformation system is shown in Fig. 2.5.

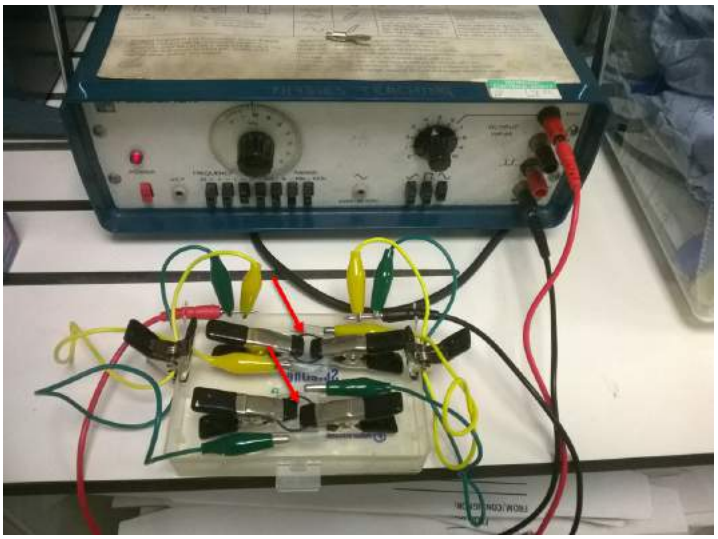

Figure 2.5: The electroformation system. The sample chambers are indicated by the red arrows; the nitrile O-ring is visible between the clips. This system enabled two samples to be created simultaneously.

2.2.1.2 Sample Immobilisation

Time-resolved microscopy requires acquisition times of several seconds or minutes, so the vesicles needed to be immobilised in the sample chamber. Two techniques were envisaged:

Immobilisation using avidin-biotin binding. The avidin protein presents 4 binding sites to its ligand biotin, and the dissociation constant is 10^{-15}M [177], making this binding process one of the strongest in biology. Vesicles can be tethered to the surface of a coverslip using the avidin-biotin binding couple by coating coverslips with avidin and using biotinylated lipids (available commercially). In practice, coverslips are coated by incubation with a 1 mg/mL aqueous solution of avidin. GUVs are prepared as explained above, incorporating 1% molar of biotinylated lipids in the chloroform mixture. Biotin-DOPE (di-oleyl-phosphoethanolamine) or biotin-DPPE (di-palmitoyl-phosphoethanolamine) were used, the former in lipid mixtures containing a majority of unsaturated chains, the latter in mixtures containing a majority of saturated chains in phase-separating mixtures, 0.5% molar of each were introduced, so that each phase contained biotinylated lipids. After electroformation, the vesicle suspension is diluted to 1/5 and the vesicles are left to settle for ca. 1 hour. It was then possible to observe tethered vesicles, with a portion of the bilayer flat against the coverslip, as visible in Fig. 2.6.

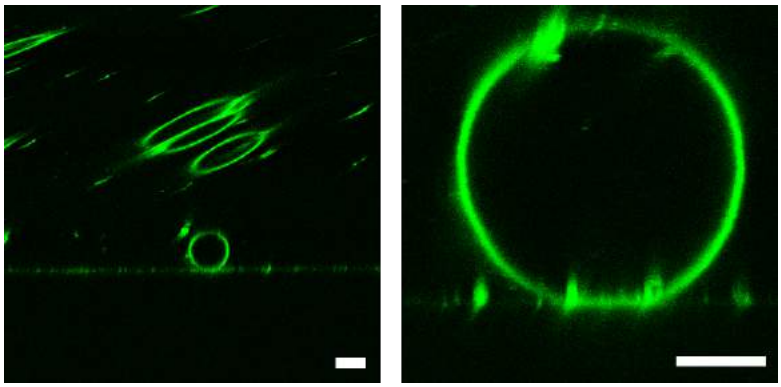

Figure 2.6: x-z sections of GUVs (DOPC/DPPC/Chol 2:2:1) stained with di-4-ANEPPDHQ, containing 1% molar biotinylated lipids and tethered on an avidin-coated coverslip. On the left-hand image, untethered vesicles above the coverslip moved in solution during the acquisition, and appear strongly distorted compared to the tethered ones. Scale bar = 10 μm.

However, avidin-biotin tethering presented some disadvantages: it has been shown by Joao Sarmento and colleagues that the tethering provoked rearrangements of phase-separated lipid domains [178]. Moreover, during long experiments, it was observed that the tethered portion tended to grow wider, as small motions of the vesicles exposed more and more bilayer to the coverslip, eventually strongly deforming the vesicles. This was especially the case at higher temperatures, where the vesicles initially in the ordered phase became more fluid, and the membrane more deformable. Less disruptive immobilisation techniques were therefore sought.

Immobilisation in an agarose gel. The idea of immobilising vesicles in agarose came from light-sheet microscopy, where samples are embedded in a polymer gel for imaging. Lira et al [122] had the same idea and published this method in 2016, helpfully showing that GUVs can be immobilised in low concentration matrices, and that this does not affect the micro-scale diffusion of the lipids (as evidenced by FCS). Agarose is inexpensive, forms gels at low concentrations (below 0.5% w/v in water), and agarose gels have the same refractive index as water, so the optical characteristics of the sample are not distorted.

In practice, a 0.3% w/v low melting point agarose solution is constituted in the GUV electroformation buffer. After electroformation, this solution is heated until boiling, and cooled until just above gelling temperature (42°C for this specific agarose). The GUV suspension is diluted to 1/5 in the molten agarose, and rapidly inserted into an imaging chamber. This enabled reliable immobilisation of the GUVs for the entire duration of the experiment. Fig. 2.7 shows a 3-dimensional image of a GUV in agarose.

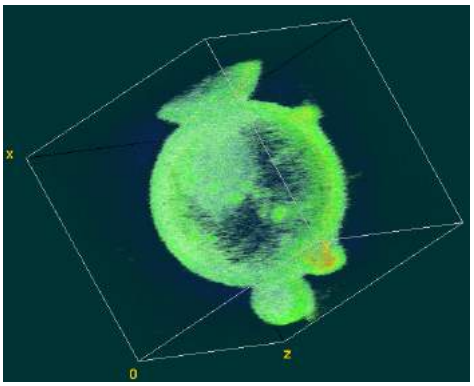

Figure 2.7: Reconstituted volume of a GUV (DOPC) stained with di-4-ANEPPDHQ and embedded in a 0.25% w/v agarose gel. 20 xy sections were taken with a spacing of 1.38 μm; the volume dimensions (white cube) are 34 μm in x and y, and 26 μm in z. Image was created in ImageJ volume viewer.

2.2.2 Choice of fluorescent membrane dyes

As stated previously, many types of membrane dyes exist to probe membrane micro-environments. Apart from the usual preference for bright and photostable dyes, more specific properties are needed for this project. In this study, the fluorescence lifetime, emission wavelength and polarisation are measured, so ideally the dye should fulfill the following criteria:

- The emission wavelength and lifetime should report on membrane micro-environment properties such as membrane hydration, polarity, or charge. They should not report on membrane viscosity, since this will be probed by fluorescence polarisation. At best, emission wavelength and lifetime should report on slightly different properties of the membrane, such that measuring both will provide more information on the system at hand.
- The absorption and emission transition dipole moments of the dye should be close to colinear, to provide a higher dynamic range of anisotropy values, and should be aligned with the long axis of the molecule, such that the rotational diffusion of the dye agrees with the "wobble in cone" model described previously.
- The fluorescence lifetime should be long enough to capture the dynamics of rotational diffusion (at least 2 ns), but short enough that the acquisition times are not unreasonably prolonged.

Fulfilling these requirements, commercially-available fluorescent lipid analogues laurdan and di-4-ANEPPDHQ appear well suited for this project. In particular, laurdan environmental sensitivity has been well characterised, and its long lifetimes (3-6 ns) are ideal to probe rotational dynamics in membranes. One downside is its poor photostability. Di-4-ANEPPDHQ is more photostable, but has shorter lifetimes (1.8-3.5 ns) and is less well characterised. Experiments with both dyes will therefore be carried out.

Another attractive candidate was DPH, which has a long lifetime of 5-10 ns and was previously used for lifetime and anisotropy studies [179, 120]. However, DPH is fully hydrophobic, and previous work suggests that it can intercalate between the two bilayer leaflets, which causes an altogether different rotational regime and environmental sensing [179]. A derivative of DPH, TMA-DPH, has a hydrophilic moiety, which causes it to be aligned with the lipid chains and to be anchored to the interface of the bilayer, similarly to laurdan or di-4-ANEPPDHQ, and was used by Haluska et al. in GUVs [173]. However, TMA-DPH emission wavelength was not reported to be sensitive to the environment.

2.2.3 Temperature Control

2.2.3.1 Construction of a temperature-controlled heated stage sample chamber

Given the strong temperature sensitivity of the physical properties of lipid bilayers, it is interesting to study the evolution of membrane hydration and order parameters as a function of temperature. To this effect, a microscope heating system was assembled using Indium-Tin Oxide (ITO) microscope slides. A $\sim$ 1mm hole was drilled in the centre of the ITO-coated slide using a diamond drill bit into which the end of a K-type thermocouple was fitted. The two electrodes were created using silver paint and strips of copper tape, $\sim$1.5 cm from the centre (see Fig. 2.8).

To mount the samples, a 1.5 cm diameter nitrile O-ring was coated with a thin layer of vacuum grease and placed on the non-coated side of the heating slide. 350 μL of sample suspension was pipetted in the chamber formed by the O-ring, and a 22-by-22 mm coverslip was placed on the top, while avoiding the formation of air bubbles in the chamber. The thermocouple hole was sealed on the conductive side with a small amount of vacuum grease.

The chamber slide was then placed on the microscope stage, and the copper strips were connected to a programmable DC generator. The thermocouple was connected to a digital thermometer (RS instruments) with a precision of +/- 0.1^{o}C. The sample temperature was found to be proportional to the DC voltage, as shown in Fig. 2.8. For immersion objectives, an objective heater was used, to decrease the temperature gradient between the objective and the sample.

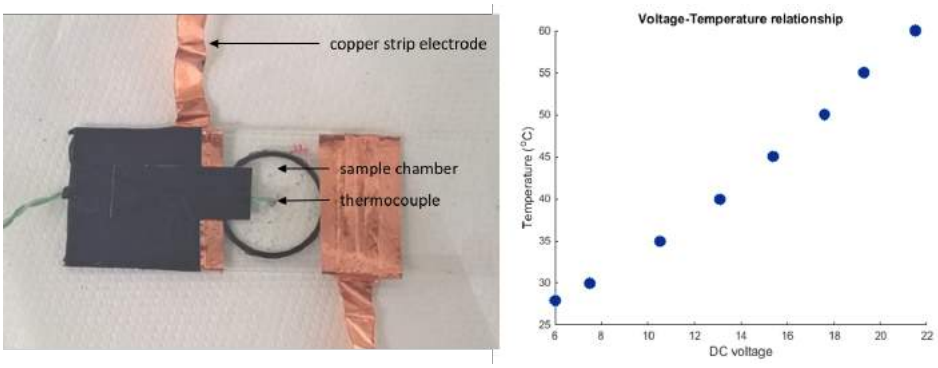

Figure 2.8: Design of a temperature-controlled heated slide chamber system. Left: photograph of the device. Right: Temperature in the sample chamber (filled with DI water) as a function of the DC voltage. Note that the proportionality factor between temperature and DC voltage depended on the slide used (4 such systems were built).

2.2.3.2 Validation of the accuracy of the temperature readings

The accuracy of the proposed temperature-controlled system was assessed by measuring the Generalised Polarisation of laurdan in DPPC vesicles. DPPC has a transition temperature at 41^{o}C and a sharp drop in GP values at this temperature is well documented [91]. The idea is to verify that this transition occurs at the expected temperature in our system.

Firstly, the two spectral windows for GP detection were determined by measuring the emission spectrum of DPPC-laurdan vesicles as a function of temperature, as shown in Fig. 2.9. Two emission bands corresponding to the solid and liquid phases were clearly visible, and the spectral windows were chosen to match with the transition: the short wavelength window between 410 and 465 nm, and the long-wavelength window between 465 and 520 nm.

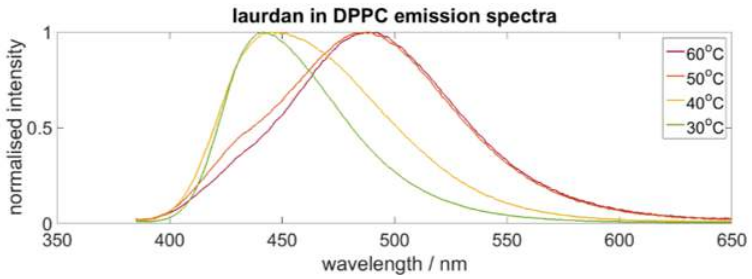

Figure 2.9: Emission spectrum of laurdan in DPPC vesicles as a function of temperature.

To measure generalised polarisation with the confocal microscope, the PMTs must firstly be calibrated to account for the difference in detection efficiency at different wavelengths and gain values. A fluorescent blue slide from Chroma (CAT number 92001) was chosen as the calibration sample; its GP was found to be $GP_{ref} = 0.530 \pm 3.10^{-4}$ from its emission spectrum using the spectral windows stated above. The slide was then imaged on the confocal microscope, one PMT for each spectral window, at the range of gains used during experiments (between 400 and 650 V). GP images and average GP values, GP_{meas}, were calculated for each gain, and a calibration factor

G_X was determined for each gain X using Eq. 2.2, as described in ref. [172]:

$$G_X = \frac{GP_{ref} - GP_{ref}GP_{meas} - GP_{meas} - 1}{GP_{meas} - GP_{ref}GP_{meas} - GP_{ref} - 1} \tag{2.2}$$

DPPC vesicles stained with laurdan were prepared as described above, and GP images were acquired for a range of temperatures between 27 and 51^{o}C, with 4 vesicles imaged per temperature. Examples of GP images and histograms are shown in Fig. 2.10.

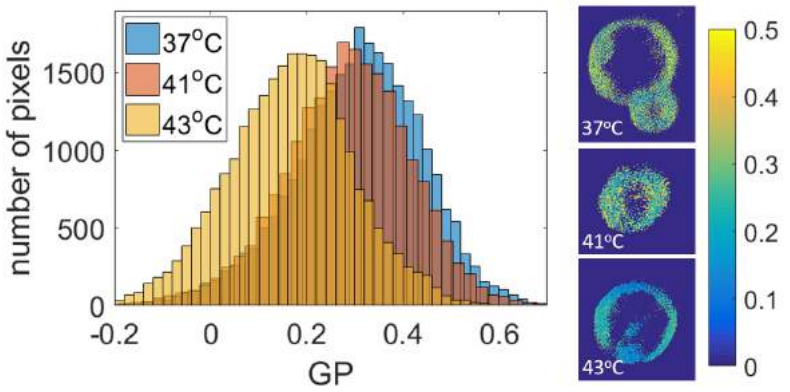

2.10

Figure 2.10: GP of laurdan in DPPC. Left: histograms of GP pixel values at different temperatures; histograms were computed from all 4 images for each temperature. Right: Exampled of GP images (top: 37^{o}C, middle: 41^{o}C, bottom: 43^{o}C).

The average GP value over each image was calculated, and these values were then averaged for each temperature. The evolution of GP with temperature is shown in Fig. 2.11. A decrease in GP values is visible from 41^{o}C. The data becomes more noisy at higher temperatures, possibly due to higher heterogeneity in the sample (some vesicles may have transitioned from the gel phase to the liquid phase before others). Therefore, a 2-point moving average of the data points was calculated, and the slope of this curve was computed, yielding a maximum negative slope at $T = 41.3^oC$, in agreement with previous studies [91] and suppliers (Avanti Polar Lipids : 41°C [180]). To avoid variability in the data, it is possible to wait longer between measurements when the temperature is increased, to ensure that the phase transition has occurred homogeneously across the sample.

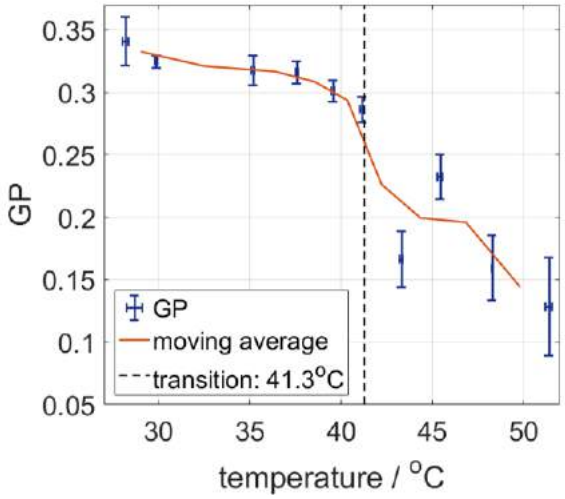

Figure 2.11: GP of laurdan in DPPC as a function of temperature. The error bars correspond to 1 standard deviation (4 datapoints for each temperature). The transition temperature calculated from the maximum negative slope value of the moving average (orange curve) is shown (dashed black line).

These results validated that the temperature in the home-built chamber slide was accurately measured and controlled, and this system was therefore used for the remainder of the experiments.

2.2.4 Time-Resolved Fluorescence microscopy

Time-and polarisation-resolved data was obtained by exciting the sample with a pulsed diode laser (Horiba DDL 375 nm for laurdan, Hamamatsu PL50 467 nm for di-4-ANEPPDHQ), on the setup described in the previous chapter. For single-phase GUVs and GPMVs, where no bilayer heterogeneity was expected at scales above the diffraction limit of the microscope, data was acquired in "single" mode, to create single polarisation-resolved intensity decays $I_{\parallel}$ and $I_{\perp}$ (with 1024 time bins) for each individual vesicle. Unless otherwise stated, all decays presented correspond to photons accumulated over the entire field of view. This provided smaller file sizes and easier analysis. Typical intensities ranged from 2000 to 10000 photons in the maximum bin (peak) for each vesicle. For GUVs displaying phase separation, in which bilayer heterogeneity was observable in the micron range, data was acquired in "FIFO Image" mode (with an image size of 512 pixels and 256 time bins). Vesicles were imaged for approximately 120 seconds.

2.2.5 Spectroscopy

Emission spectra were measured using quartz cuvettes from Starna scientific with a Horiba Fluoromax-4 emission spectrometer. Excitation wavelengths are stated where relevant, and excitation and emission slit widths were 1 or 2 nm. Absorption spectra were recorded in Quartz cuvettes in a Hitachi HI-400 spectrophotometer, with 1 nm slit widths.

2.2.6 Data processing

2.2.6.1 Time-resolved anisotropy

The polarisation-resolved decays $I_{\parallel}$ and $I_{\perp}$ were corrected for background and shift, and the anisotropy decay $r(t)$ was computed according to Eq. 1.11. Anisotropy decays were fitted according to model of hindered rotation presented in Eq. 1.28 using home-written weighted nonlinear least squares routines in Matlab (using the inbuilt lsqnonlin function). The weights $\delta(r)$ were calculated from the propagation of the Poissonian error associated with the polarisation-resolved intensities at each time point (assuming no error on the value of G), as also shown in ref. [181] and given in Eq. 1.52.

The dynamic and static order parameters τ_c and Δ were extracted from these fits as presented in paragraph 1.3.3.2. The notation τ_c for the rate of rotational diffusion is replaced with the more usual notation θ, to avoid confusion with fluorescence lifetime τ.

Note that the static order parameter Δ depends on the absolute values of r_0 and r_∞, which themselves depend on the local orientation of the fluorophores. For randomly distributed fluorophores, it is expected that the range of variation of Δ is between 0 and 1. For non-random distributions, this range can be different. In particular, highly ordered environments such as membranes can lead to fluorophores locally having very high or very low (negative) anisotropies. This does not affect the rate at which they diffuse rotationally so θ is unaffected, but this in practice leads to the dependence of Δ on the local orientation of the population of fluorophores. GUVs are spherically symmetric, so while the orientation of fluorophores is locally nonrandom, the information from a full circular section of the GUV yields a situation where all orientations are represented in equal proportion, and reproduces the results from a random distribution of fluorophores. In non-homogeneous bilayers, each domain is not present over the full section of a GUV and so the distribution of fluorophores within the domain is non-random, which leads to complications with parameter Δ, such as values crossing 0 and yielding non-representative 100% depolarisation situations. In such cases, a non-normalised version of this parameter is preferred, i.e, $\Delta' = r_0 - r_\infty$.

2.2.6.2 Intensity decays

The polarisation-resolved decays $I_{\parallel}$ and $I_{\perp}$ were corrected for the shift, and the total intensity decay $I_{tot}(t) = I_{\parallel} + 2GI_{\perp}$ was computed. Intensity decays were then fitted to a bi-exponential decay model using home-written weighted non-linear least squares routines:

$$I_{tot}(t) = A_1 e^{-t/\tau_1} + A_2 e^{-t/\tau_2} + B \tag{2.3}$$

Goodness of fit was assessed by the χ^2_{red} value, and visual inspection of the decay residuals.

It was found that for intensity decays obtained through addition of polarisation-resolved decays, fitting procedures yielded χ^2_{red} values slightly higher than for classical FLIM experiments (between 1.5 and 2.5, whereas $\chi^2_{red} \approx 1$ for good fits of fluorescence decays). This phenomenon was recapitulated in simulations: fitting results on simulated data of intensity decays either computed directly or from the addition of parallel and perpendicular decays with the same input parameters showed significantly higher χ^2_{red} in the latter case, while the lifetime parameter resolution was only slightly affected (Fig. 2.12.D). This observation in simulated data suggests that these higher χ^2_{red} values are likely linked to a statistical effect related to the addition of two decays, rather than an instrumental artifact such as the presence of a shift between the two channels, or depolarisation through the objective. In practice, fits were judged acceptable with values of χ^2_{red} between 1 and 2. Intensity decays acquired directly without polarisation resolution had χ^2_{red} values between 1 and 1.5.

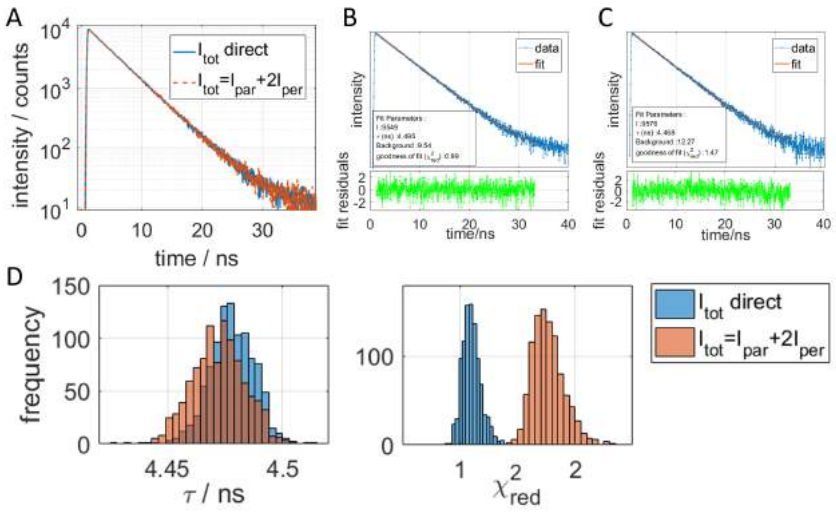

Figure 2.12: Comparison of fitting results for simulated intensity decays computed directly or as the sum of two polarisation-resolved intensity decays. A. Example of simulated decays with a single lifetime component: $I(t) = Ae^{-t/\tau} + b$. Input parameters were A=10000 photons, $\tau_0 = 4.5$ns, b=10 photons. B-C. Mono-exponential fits of decays shown in A; B: I_{tot} simulated directly, C: I_{tot} is the result of the sum of I_{par} and I_{per} simulated data. D. Histograms of fitting results for direct and polarisation-resolved-derived intensity decays with the same parameters as those shown in A and B. Poisson noise was randomly generated for each of the 1000 iterations. Note the deviation of fitting results from the true lifetime parameter τ_0, even in the case of directly-simulated decays: median recovered lifetime is 4.47 ns - 0.67% lower than the input value 4.5 ns. This is linked to the bias of Least-Squares fitting in the case of Poisson-distributed data, as mentioned in Chapter 1.

From the lifetime parameters τ_1 and τ_2 and amplitudes A_1 and A_2, the average lifetime τ_{av} was calculated:

$$\tau_{av} = \frac{(\tau_1^2 A_1 + \tau_2^2 A_2)}{(\tau_1 I_1 + \tau_2 I_2)} \tag{2.4}$$

The principle of using polarisation- resolved intensity decays to compute total intensity and anisotropy decays and their associated parameters is illustrated in Fig. 2.13.

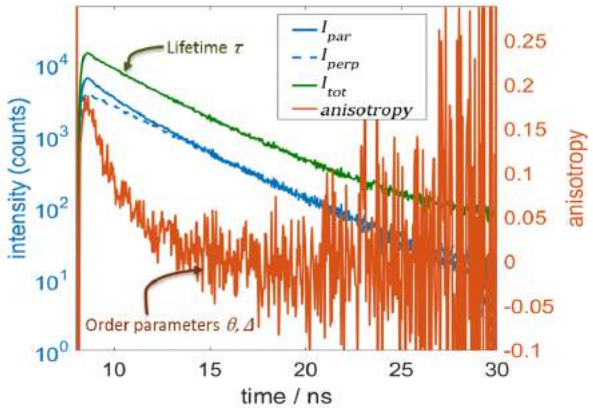

Figure 2.13: Illustration of the data obtained from the time-resolved experiments: the polarisation-resolved decays (in blue) are added together to yield I_{tot} (in green) from which is extracted the fluorescence lifetime τ_{av}. The anisotropy decay (orange) is also computed from the polarisation-resolved decays, to yield order parameters θ and Δ. Data is for a DOPC vesicle.

Examples of fitting results of intensity and corresponding anisotropy decays are shown in Fig. 2.14. Bi-exponential models were well adapted to all intensity datasets. For anisotropy data, mono-exponential models were sufficient in most cases. However, in Ld phase data with high signal-to-noise ratios, structure in the residuals can be observed (as shown here for POPC), and would indicate several rotational modes of laurdan in such bilayers, requiring multi-exponential models. However, for simplicity, and because it was difficult to achieve consistent distributions of the fit parameters when using bi-exponential fits, a mono-exponential model was kept for all GUVs.

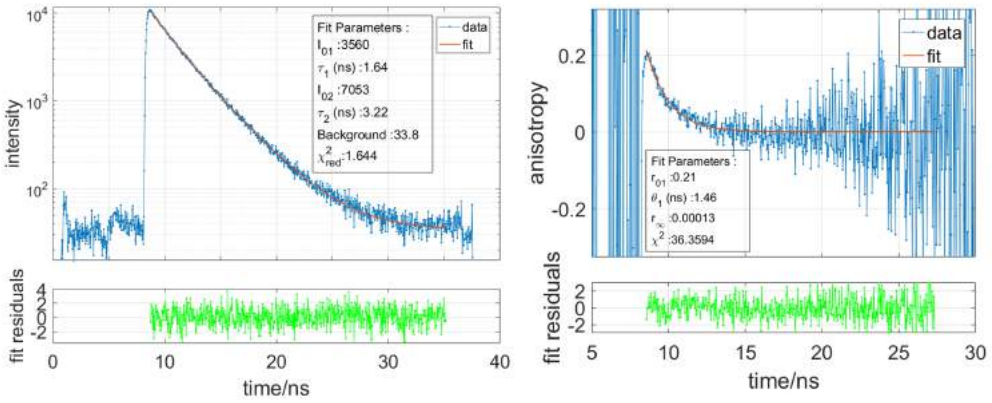

Figure 2.14: Examples of fits for intensity decay (left) and corresponding anisotropy decay (right) of laurdan in lipid bilayers (in this case, POPC at 50^{o}C). The fit parameters are indicated in the insets.

2.2.6.3 Statistical analysis

The lifetime and anisotropy parameter results are given as average values over the number of repeat measurements, and the range of reported uncertainties correspond to one standard deviation, unless otherwise stated. Repeat measurements are stated with N the number of independent experiments, and n the number of repeat measurements. Linear regressions and Student's t-test were performed using "fitlm" and "ttest2" functions in Matlab.

2.3 Results

2.3.1 Photophysical characterisation of di-4-ANEPPDHQ and laurdan.

2.3.1.1 Is di-4-ANEPPDHQ a molecular rotor?

From observing the structure of di-4-ANEPPDHQ, it is possible that some intramolecular twisting may take place. If this affects the fluorescence emission of the dye, this would place it in the family of fluorescent molecular rotors, which are compounds that relax from S1 to S0 through intramolecular twisting. This path competes with radiative decay, and is hindered in viscous environments, and therefore, fluorescence quantum yield and lifetimes of molecular rotors increase with viscosity. In particular, the lifetime of molecular rotors τ and the quantum yield Φ are related to viscosity following the Förster-Hoffman equations [182]:

$$\begin{cases} \tau = \frac{z\eta^{\alpha}}{k_0} \\ \Phi = z\eta^{\alpha} \end{cases} \tag{2.5}$$

With k_0 the radiative rate constant, and z and x constants with $0 < \alpha < 1$. More precisely, the theory from Förster & Hoffman predicts $\alpha = 2/3$. This can be rearranged to obtain a linear relationship between τ and η:

$$\begin{cases} log\tau = log(z/k_0) + \alpha log(\eta) \\ log\Phi = log(z) + \alpha log(\eta) \end{cases} \tag{2.6}$$

Molecular rotors are therefore used for viscosity mapping, and they have been developed to probe the microviscosity of cell cytoplasm, membranes, lipid droplets, and mitochondria [183, 161]. If di-4-ANEPPDHQ is such a molecule, this would therefore mean that it senses viscosity. This would be undesirable, since we need the fluorescence lifetime to report on membrane hydration, while membrane viscosity is reported by the order parameters derived from the anisotropy. It was therefore investigated whether di-4-ANEPPDHQ exhibits a rotor behaviour.

Ideally, this question would be addressed in membrane environments; however, it is difficult

glycerol - %volume	viscosity of methanol - glycerol mixture at 22^{o}C / cp
0	0.6
20	2.7
40	12.5
60	56.9
80	259.3
95	982

Table 2.2: Viscosity of water-glycerol mixtures at 22^{o}C. Values from the doctoral thesis of Dr. Pei-Chung - viscosity at 95% was obtained from linear extrapolation between 90 and 100% glycerol.

to control membrane viscosity while maintaining a constant membrane or polarity, so the experiments were firstly carried out in aqueous solution. A series of methanol-glycerol and methanol mixtures was made, from 0% to 95% glycerol (v/v%), with viscosities indicated in Table 2.2. Di-4-ANEPPDHQ was diluted to 5μM in these mixtures, and absorption and emission spectra as well as intensity decays were measured.

Emission spectroscopy analysis. Emission spectra were measured with 510 nm excitation, which corresponded to the absorption maximum (Fig. 2.16.A). Small variations in absorbance were likely caused by variations in dye concentration - therefore the emission spectra were scaled by a factor of A^X_{510}/A^{ref}_{510} , where A^X_{510} is the baseline-corrected absorbance value of sample X at 510 nm. The pure methanol sample was chosen as the reference value, A^{ref}_{510}. Fluorescence intensities increase strongly with glycerol content, as visible in Fig. 2.16 and visualised in the samples under UV illumination (Fig 2.15). The relationship between $log(\eta)$ and $log(I_{max})$ is linear, with a gradient of $m = 0.254 \pm 0.009$ ($R^2_{adj} = 0.99$, $p_{value} = 1.10^{-5}$, see Fig. 2.16.D). Under the assumption that the fluorescence intensity is proportional to the quantum yield, and that the measured absorbance values are in the linear regime of the spectrophotometer, (both reasonable hypotheses), the gradient of this fit corresponds to α from Eq. 2.6.

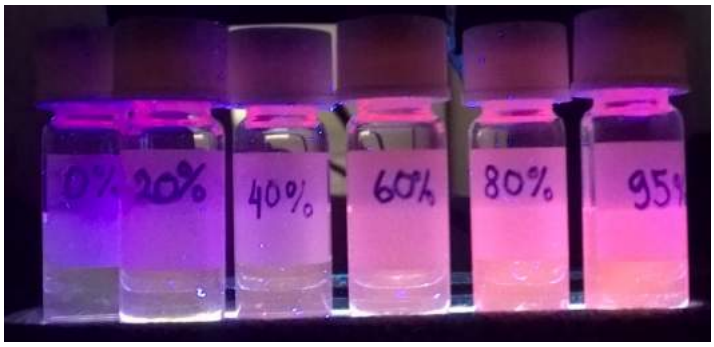

Figure 2.15: Picture of methanol-glycerol mixtures containing 5 μM di-4-ANEPPDHQ on a UV lamp. The label indicates the glycerol content.

A small shift in the emission maximum towards shorter wavelengths at higher viscosities (743 nm in pure methanol against 724 nm in 95% glycerol) is also noticeable. This shift is in the opposite

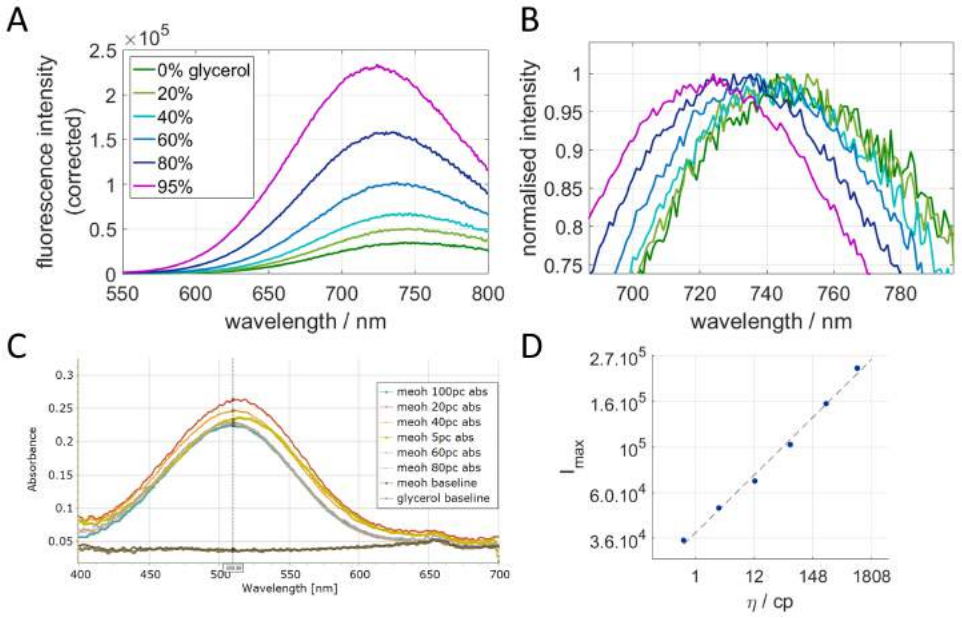

Figure 2.16: Emission spectroscopy of di-4-ANEPPDHQ in methanol-glycerol mixtures. A.: Emission spectra as a function of glycerol content. B. Spectra are normalised to highlight the red-shift in the emission maximum. C. Absorption spectra of the samples. D. Plot of $log(I_{max})$ as a function of $log(\eta)$. The linear fit is shown as the dashed line, the gradient is 0.25. Data is the result of two spectra per sample, which were averaged.

direction of the solvatochromic effect expected in the case of di-4-ANEPPDHQ and its sensitivity to solvent polarity: indeed, the dielectric constant of glycerol is higher than that of pure methanol ($\epsilon_{methanol} = 31.01$ and $\epsilon_{glycerol} = 42.5$ at 22^{o}C), so unlikely to be due to changes in the polarity of the medium.

Lifetime analysis. Fluorescence intensity decays were collected by exciting the samples in coverslip-bottomed 8-well plates on the setup described earlier, with 467 nm excitation and a 500LP emission filter. The decays were clearly multi-exponential, and were fitted to triple-exponential models. In particular, a long decay component (>2 ns) was present and especially visible in the low viscosity samples, as evident from the "crossing" of the decay curves between 5 and 7 ns. This long lifetime component was absent in the pure solvents and from imaging plates, and no contamination was detected in the absorption spectra, so this was not due to background fluorescence. However, dried samples of di-4-ANEPPDHQ yielded bright fluorescence with a long lifetime of 2.4 ns, and so it is possible that this long decay component could be linked to aggregated dye in the sample or immobilised on the coverslip. The fact that its magnitude was greater in low viscosity solvents can be explained by the lower overall intensity of these samples, and hence a greater relative contribution from the bright dye particles. The magnitude of this component was minimised by imaging at high z-planes and by reducing the pinhole size, though it was not possible to suppress it altogether. The short decay components however, seemed to increase with viscosity, going from

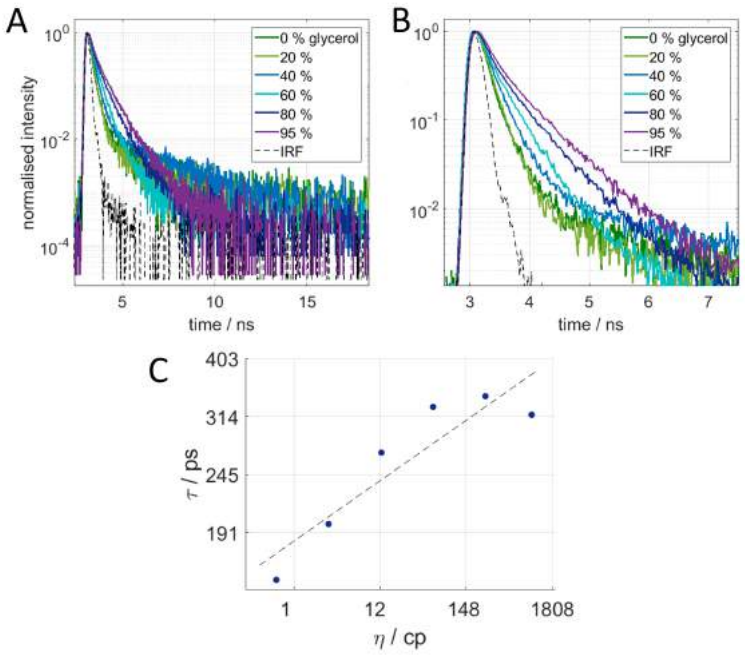

Figure 2.17: Intensity decay analysis of di-4-ANEPPDHQ in methanol-glycerol mixtures. Upper-right: the initial moments of the decays are shown. Below: lot of $log\,\eta$ against $log\,\tau_{av}$ - with linear fit.

155 ps in pure methanol to 317 ps in 95% glycerol, as also visible on the initial moments of the decay (Fig. 2.17, right). Plotting $log\,\eta$ against $log\,\tau_{av}$ yielded a linear relationship with $R^2_{adj} = 0.79$ and $p_{value} = 0.011$, as visible in Fig. 2.17, which verifies Eq. 2.6, with $m' = 0.10 \pm 0.02$. Lower τ_{av} values than expected by this relationship at higher viscosities are likely due to the decreased contribution of immobilised or aggregated dye, as explained above.

Conclusions The gradient of linear fits, m and m', should both reflect α but are clearly not equivalent and lower than the theoretical value of $^2/_3$; emission intensity showed higher dependence on medium viscosity than fluorescence lifetimes. Therefore the lifetime and emission spectroscopy analyses appear inconsistent in showing the relationship between di-4-ANEPPDHQ fluorescence and viscosity. One should note that the lifetime analysis was complicated by the complex nature of the intensity profiles of di-4-ANEPPDHQ in solution. Taken together, these observations point towards di-4-ANEPPDHQ fluorescence being sensitive to viscosity, though not displaying a stereotypical rotor behaviour, and the sensitivity is more modest than that of traditional rotors such as BODIPY C-12. Other parameters which could explain the differences in lifetime and intensity are perhaps the differences in solvent polarity, which di-4-ANEPPDHQ is sensitive to through a solvatochromic effect, with the fluorescence emission being red-shifted in environments of increased polarity.

The absence of a positive shift in wavelengths with glycerol content suggests that the variation

in solvent polarity in this experiment is not within a range in which di-4-ANEPPDHQ emission wavelength is very sensitive to, and that the main variation in environmental parameters susceptible to affect di-4-ANEPPDHQ fluorescence is the solvent viscosity.

It should be noted however, that the lifetimes and emission wavelengths of di-4-ANEPPDHQ in water-glycerol environments are very different to those in lipid bilayers: the short lifetime components of di-4-ANEPPDHQ intensity decays constitute up to 99% amplitudes; such short components are not observed in lipid bilayers (see next paragraph, Fig. 2.18). The emission bands of di-4-ANEPPDHQ in solutions are also at much longer wavelengths than in lipid bilayers (maxima at 750 nm in methanol:glycerol against 550 to 650 in bilayers [172, 121]).

It was concluded that while di-4-ANEPPDHQ shows signs of intramolecular twisting in solution, the fluorescence signature of this dye in solution is not consistent with observations in bilayers, which we can assume present much larger hindrance against rotational motion and lower solvent polarity in general. It is therefore unlikely that the contrast in di-4-ANEPPDHQ lifetime observed in bilayers should be due to the sensitivity of the dye to membrane viscosity.

2.3.1.2 Preliminary results in GUVs with Di-4-ANEPPDHQ

Di-4-ANEPPDHQ presents several advantages over laurdan: it is water-soluble, photostable and excitable with blue lasers, more readily available than their UV counterparts. The first experiments were therefore carried out with di-4-ANEPPDHQ. As a preliminary experiment, GUVs composed of DOPC, DPPC and Sphingomyelin (SM):Chol 7:3 were prepared, to represent the Ld, S and Lo phases, respectively. Time-and polarisation-resolved data was acquired at room temperature; lifetime and anisotropy parameters are presented in Fig. 2.18.

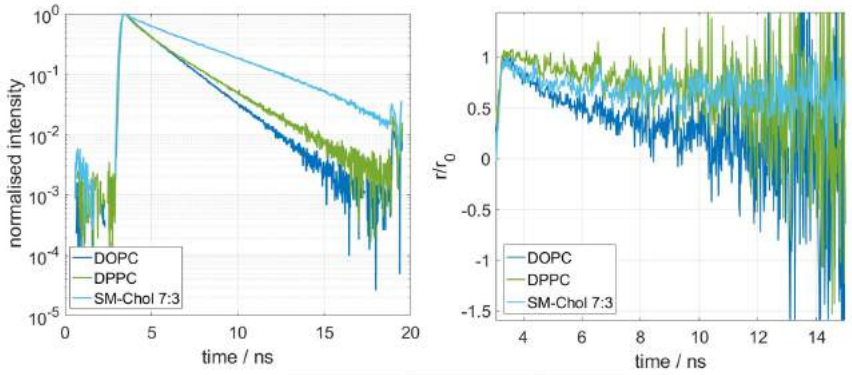

	τ (ns)	Θ (ns)	Δ (%)
DOPC	2.04±0.09	3.4±0.4	83±12
DPPC	2±0.2	3±1	54±13
SM:Chol 7:3	3.92±0.05	1.9±0.2	19±4

Figure 2.18: Time- and polarisation-resolved fluorescence analysis of di-4-ANEPPDHQ in different lipid mixtures. Left: Normalised intensity decays. Right: normalised anisotropy decays. Data is representative of N=2 independent experiments, with a total of 6 measurements for DOPC and 5 for DPPC and SM:Chol. Below: summary of fluorescence parameters. Reported values are the average parameter value $\pm\sigma/2$.

The first clear observation is that the lifetime of the S (gel phase), represented by DPPC, is intermediate between the Ld phase and the Lo phase, but closer to that of the Ld phase, suggesting greater hydration of the gel phase. The second order parameter, Δ, is also higher in DPPC than in SM:Chol, signifying greater rotational freedom. This is unexpected, since it contradicts the commonly accepted facts that the gel phase is tightly packed and in general more similar to a Lo phase than the Ld phase, which has been observed using laurdan lifetime and GP information.

One possible explanation for these results is that di-4-ANEPPDHQ localises differently in bilayers in the tightly packed gel phase, and therefore senses a different environment. For example, if the dye molecule is only partially inserted in the bilayer, one could imagine that the fluorophore is exposed to more water molecules, and that the molecule rotated more freely at the interface between the bilayer and the aqueous medium. Since di-4-ANEPPDHQ molecules are significantly larger than laurdan, this is not an unreasonable hypothesis. There is no evidence of work having been carried out in the gel phase with this dye that could be used as a comparative, and neither have any simulations investigated the behaviour of di-4-ANEPPDHQ in different types of membranes, unlike laurdan and other membrane dyes [184, 161]. Indeed, the environmental sensitivity of di-4-ANEPPDHQ was characterised by Owen and colleagues [185, 138] in DOPC and SM-Chol vesicles as well as in live cells. Carrying out MD simulations of di-4-ANEPPDHQ in different lipid environments, similarly to what has already been done for laurdan, would provide useful insight on the behaviour of this relatively new dye in saturated bilayers. For now, di-4-ANEPPDHQ was not used any further for this investigation since its behaviour in the gel phase contradicts current knowledge.

2.3.1.3 Relationship between spectral emission and fluorescence lifetime of laurdan

The sensitivity of the emission wavelength of the laurdan molecule to its immediate environment has been the object of extensive research. In ref. [165], Parasassi et al. relate the spectral emission of laurdan as quantified by GP to the dielectric constant of the solvent, and use this as a scale to obtain the polarity of a bilayer. Molecular dynamics simulations carried out by Jurkiewicz et al [184] have also related laurdan emission wavelength to its position in the bilayer: laurdan emission is longer when the probe is closer to the bilayer interface, and shorter when it is inserted deeper in the bilayer. The sensitivity of its fluorescence lifetime is however less straightforward to explain. Mazeres et al. [175] have measured the emission lifetime of laurdan in various solvents and find little evolution of the lifetime with solvent polarity, but their measurements were made on a spectrometer at a single wavelength, and so may not have captured the fact that laurdan fluorescence emission wavelength is time-dependent, with the emission maximum shifting to longer wavelengths at longer times after excitation. This is due to dipolar relaxation effects: the longer the molecule remains in

the excited state, the longer the solvent molecules have to re-orientate, and decrease the transition energy. It follows that the information extracted from intensity decays depends on the wavelength at which it is detected. In ref. [169], Golfetto and and colleagues postulate that lifetimes in the short wavelength range of the laurdan emission spectrum corresponds to a measure of solvent polarity, while lifetimes in the long wavelength range report on dipolar relaxation effects. While this is an attractive theory, a correlation between solvent polarity laurdan emission wavelength and emission lifetimes has never been systematically carried out. The idea here is to reproduce the experiment from Parasassi et al. [165] and Mazeres et al. [175], while including lifetime measurements, and relating spectral emission to fluorescence lifetime of laurdan.

What is solvent polarity? The polarity of a medium in itself is not a chemically or physically obvious property to define, since it depends on intrinsic properties of the molecules in the medium, molecular interactions within the medium, as well as such interactions between the molecules of the medium and those of the solute (in our case, the dye).

Several properties contribute to the notion of solvent polarity:

- The dielectric constant, or relative permittivity, relates to how a medium shields an electric field. To some extent it is a measure of its polarisability: polarisable molecules such as water have high dielectric constants and therefore a high capacity to rearrange in presence of an electric field.

- The dipole moment is a measure of the partial charge carried by a molecule. Molecules containing bonds between atoms of different electronegativities such as water will present large dipole moments; molecules containing only C-C and C-H bonds, such as toluene, have low dipole moments.

- Proticity indicates whether the solvent molecules can be involved in hydrogen bonding with a solute, linked to the presence of hydrogen atoms bound to electronegative atoms such as oxygen.

It is therefore clear that no single metric can represent solvent polarity. Overall, a more cautious definition of solvent polarity can be given as its general solvation capacity, encompassing all possible interactions between solutes and the solvent, as helpfully reminded by Reichardt [186]. Empirical scales of solvent polarity can then be introduced, based on the absorption properties of well-characterised solvatochromic dyes, which have the advantage of accounting for solute-solvent effects, as opposed to absolute scales such as dielectric constants or dipole moments. One such scale of "relative polarity" was proposed and refined by Reichardt and based on the absorption energy E_T of a pyridinium N-phenolate betaine dye family. These dyes were chosen for their strong

solvatochromicity and solubility in most solvents. E_T is defined as:

$$E_T = hc\nu_{\tilde{max}}\mathcal{N}_A \tag{2.7}$$

Where h is the Planck constant, c the speed of light and $\nu_{\tilde{max}}$ the wavenumber of the $S_0 \longrightarrow S_1$ transition at the absorption maximum. Such a value can be normalised to a range between to solvents; Tetramethysilane (TMS) and water were chosen as extreme nonpolar and polar solvents, yielding a normalised value E_T^N:

$$E_T^N = \frac{E_T(solvent) - E_T(TMS)}{E_T(water) - E_T(TMS)} \tag{2.8}$$

Laurdan emission spectra and lifetimes were therefore measured in a range of solvents, with the objective of understanding the relationship between the these different definitions of solvent polarity and the spectroscopic characteristics of laurdan. The solvents used, along with their dielectric constant, dipole moment, solvent class and relative polarity of the solvents are presented in Table 2.3 below:

Solvent	Dielectric constant ϵ	Dipole moment μ (D)	Relative polarity E_T^N	Solvent class
Toluene	2.4	0.36	0.099	non-polar, aprotic
Chloroform	4.8	1.0	0.259	non-polar, aprotic
Acetone	21	2.85	0.355	polar, aprotic
Dimethyl Sulfoxide	46.7	3.9	0.444	polar, aprotic
Isopropanol	19	1.66	0.546	polar, protic
Ethanol	24	1.7	0.654	polar, protic
Methanol	33	1.6	0.762	polar, protic

Table 2.3: Solvents used to study the lifetime-emission wavelength relationship of laurdan. Values were from ref. [187]

Laurdan spectral emission and solvent polarity The emission spectra of laurdan in these solvents are shown below in Fig. 2.19; the solvatochromic effect is clear from the continuous shift in the emission maximum. The ordering of the emission bands is in agreement with the results of Parasassi and colleagues [165]. When the emission maximum λ_{max} is plotted against indicators of solvent polarity, it appears that the metric most correlated with emission wavelength λ_{max} is the relative polarity E_T^N, with a clear linear relationship between the two ($R^2_{adj} = 0.995$, p-value of the model: $4.2.10^{-7}$). The dielectric constant and dipole moments also show positive trends, though linearity cannot be confirmed ($R^2_{adj} = 0.31$, p-value of the model: 0.11, and $R^2_{adj} = -0.1$, p-value of the model: 0.5, respectively). It is interesting to see that in these two cases, the polar protic

solvents (isopropanol, ethanol and methanol) significantly deviate from the linear trend constituted by the other solvents, with emission wavelengths anomalously higher than their dipole moments and dielectric constants would predict; this may be due to their ability to form hydrogen bonds with the laurdan molecule, further lowering the energy of the excited state. This also underlines the limitations of the use of mono-parametric quantities to define solvent polarity. In any case, these results validate the current assumptions on the environmental sensitivity of laurdan emission wavelength, and establish the relative polarity metric, E_T^N, as a more appropriate measure of solvent polarity when it comes to laurdan fluorescence. This differs from the conclusion from Parasassi et al [165], who have related laurdan emission wavelengths to the dielectric constant of the medium and is in line with the observation of anomalously low GP in protic solvents by Mazeres et al. [175]. The present data suggests that the dielectric constant only partially explains the solvatochromicity of laurdan. One possible criticism of E_T^N values is that they are empirical, and being based on the emission of a small family of dyes, their generalisation to all solutes is not necessarily justified. However, the high degree of correlation between emission wavelength and relative polarity values found here, for a dye chemically very different from the one by which it was established, suggests that the E_T^N metric is versatile enough to quantify the solvation ability of solvents for a variety of solutes.

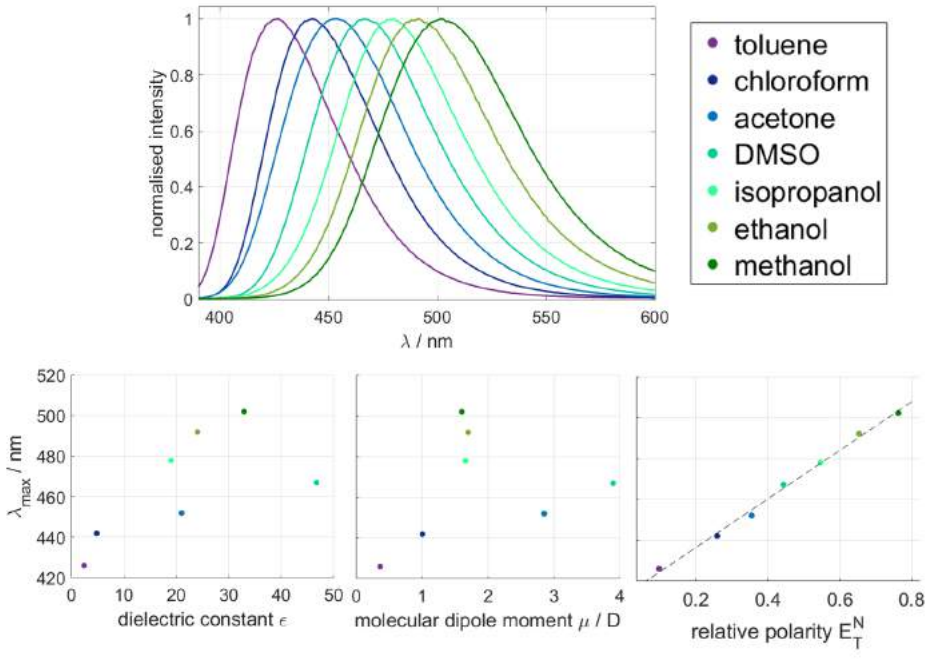

Figure 2.19: Solvatochromicity of laurdan. Above: emission spectra of laurdan in the solvents from table 1, when excited at 375 nm. Curves are the average of two spectra. Below: Emission maximum λ_{max} as a function of the dielectric constant ϵ (left), the molecular dipole moment of the solvent μ (centre), and the relative polarity E_T^N metric (right). Differences between the two spectra were negligible and therefore errors for λ_{max} are not displayed. The linear relationship between λ_{max} and E_T^N is evidenced by the black dashed line.

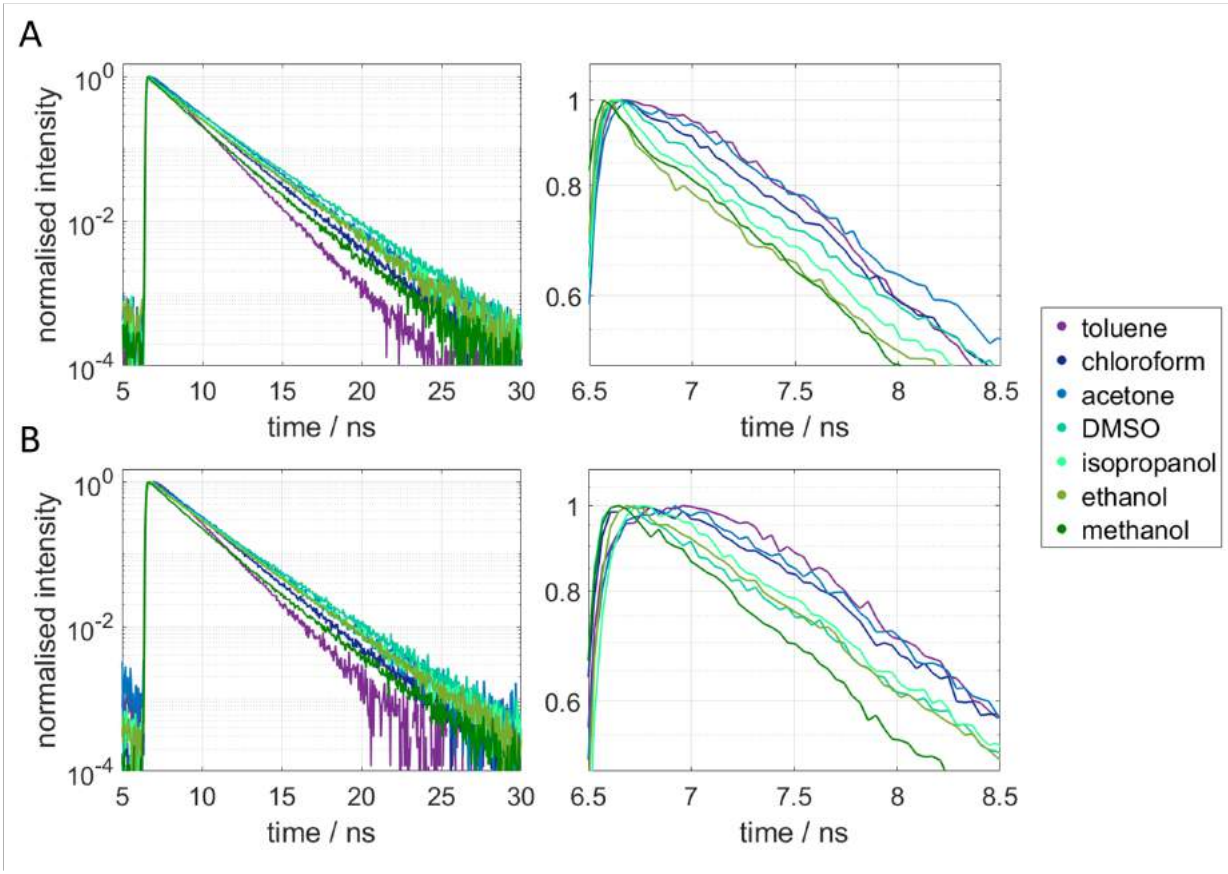

Figure 2.20: Intensity decays of laurdan acquired in the solvents from table 2.3. A.: Decays acquired in the blue spectral region (440-490 nm) and B.: in the green spectral region (500-530 nm). The panels on the right-hand side show the initial moments of the decay. Curves are representative of three decays per sample and emission filter.

Lifetime analysis Fluorescence intensity decays of laurdan in two spectral regions, 440-490 nm (blue channel) and 500-530 nm (green channel) were then acquired on the same samples using a 465/50 and a 514/30 emission filter, respectively, and representative decays are shown in Fig. 2.20. The use of two spectral windows allowed higher resolution of emission dynamics of laurdan.

Due to the wavelength-dependence of laurdan lifetimes and the large spectral windows used in the experiment, all the decays were multi-exponential with some curves displaying initial negative amplitudes (as visible by a shoulder in the initial slopes, on the right-hand side panels of Fig. 2.20). Negative amplitudes in the intensity decay are indicative of excited-state reactions, which has been suggested by others for laurdan. Indeed, using time-resolved spectroscopy, Viard et al. [188] have shown that laurdan may exist as two emissive excited states, with a "locally-excited" state (LE) populating a secondary "charge-transfer" species (CT), though both can be directly excited from the ground state. Moreover, laurdan displays a time-dependent emission spectrum, with the emission maximum shifting to the red at increasing times after excitation due to solvent relaxation effects [167]. As seen by comparison of panels A and B in Fig. 2.20, negative amplitudes are observed especially in the green channel, which may indicate that the CT undergoes stronger

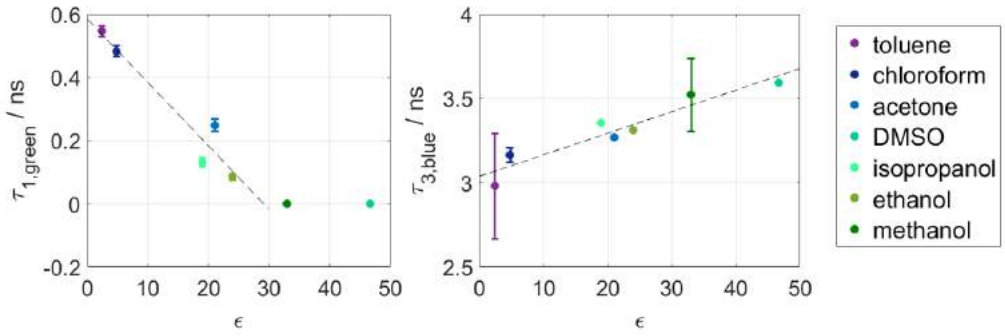

Figure 2.21: Graphs showing the relationships between the lifetime τ_1 associated with negative amplitude α_1 in the green channel (left), and the long lifetime τ_3 in the blue channel (right), with the dielectric constant ϵ. The dashed lines show the linear fits, with $R^2_{adj} = 0.9$ (left) and 0.88 (right), respectively. In the case of $\tau_{1,green}$, only the non-zero values were used for the linear fit (which excluded DMSO and methanol). Datapoints are average of n=3 repeats, with error bars representing the range of obtained values.

solvent relaxation than the LE state, an observation corroborated by the conclusions from in ref. [188].

The negative amplitudes are more present in solvents where laurdan emission wavelength is the shortest; this is linked to the choice of spectral windows: the blue channel is already in the long-wavelength tail of the emission spectrum of toluene and chloroform, whose emission maxima are at 426 and 442 nm, respectively. The summary of all the fits for the blue and green channels is shown in Appendix 1 of this Chapter. Correlations were sought between the fit parameters and indicators of solvent polarity as well as emission wavelength. The most significant correlations involved the dielectric constant ϵ and dipole moment μ, which showed negative trends with the negative amplitude α_1 and associated lifetime τ_1, as well as positive trends with the long lifetime component τ_3. Two significant linear relationships were found between $\tau_{1,\,green}$ and ϵ, and $\tau_{3,\,blue}$ and ϵ (Fig. 2.21).

This also resulted in overall positive trends between the average lifetime τ_{av} in both channels and these parameters, though a significant linear relationship was only established with the dipole moment μ (p_{value} of the fits below 0.05) (Fig. 2.22).

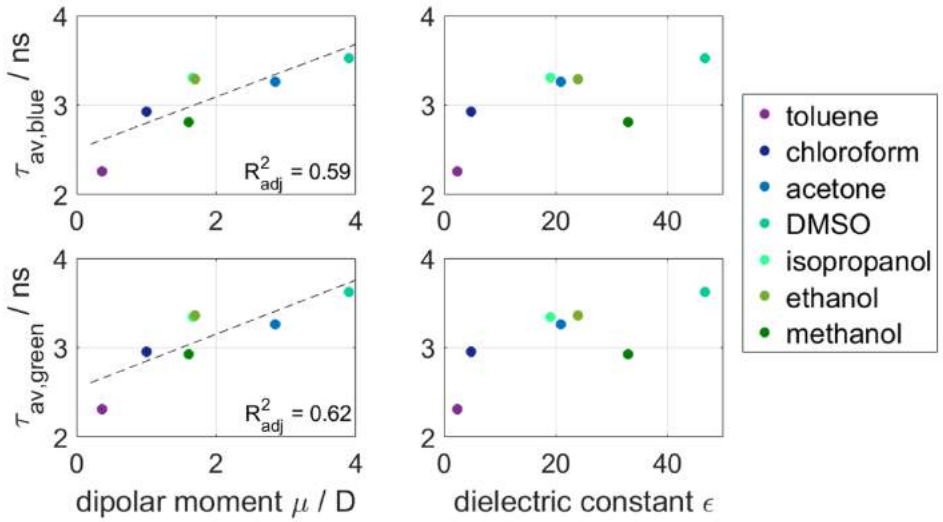

Figure 2.22: Relationship between the average lifetime in the blue (upper row) and green (lower row) channels, and the dipolar moment (left column) or dielectric constant (right). Error bars are smaller than the size of the data points .

Without attempting to elucidate the exact mathematical relationship between lifetime and indicators of solvent polarity, the important result here is that the emission lifetime parameters of laurdan, regardless of the detection wavelength, are more correlated to the dielectric constant and dipole moment than to the maximum emission wavelength or the relative polarity (see all plots in Appendix 1). This is strengthened by the fact that the only two solvents in which laurdan does not have a negative amplitude in the green channel are methanol and DMSO (Fig. 2.21, left), which have the highest dielectric constants of the range investigated, while having very different emission maxima. It is furthermore interesting to observe that once more, the polar, protic solvents deviate from an otherwise strong linear relationship between emission wavelength and average lifetimes, with overall lower τ_{av} values in these solvents, as seen in Fig. 2.23. This would suggest that while the establishment of hydrogen bonds decreases the energy of S1, it does not contribute to stabilising the excited state.

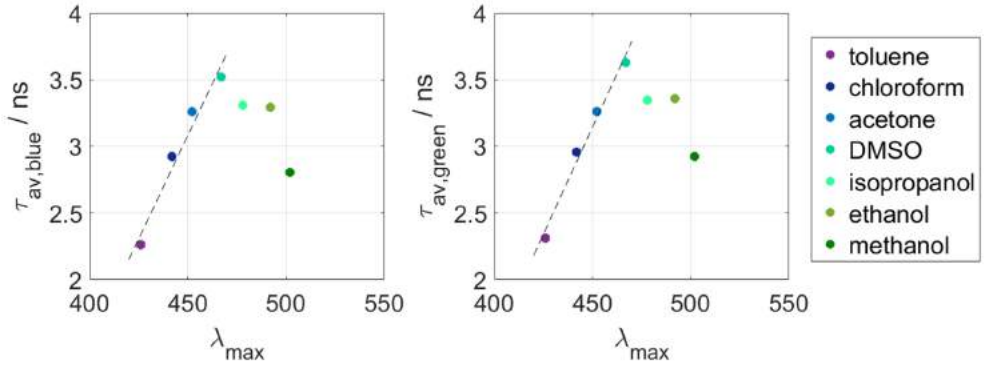

Figure 2.23: Plots of average lifetimes in the blue (left) and green (right) channels as a function the maximum emission wavelength. Linear fits involving the non-protic solvents are evidenced, with $R^2_{adj} = 0.94$ and 0.98, respectively.

What is surprising is that the overall relationship between emission wavelength, lifetime and polarity (longer lifetimes and longer wavelengths with higher solvent polarity, as shown in Figs. 2.19 and 2.22) in solvents does not follow what is observed in lipids. Indeed, laurdan has longer lifetimes and shorter wavelengths in packed bilayers, which are deemed to have lower polarity due to the exclusion of water molecules within. At the same time, the emission wavelengths and fluorescence lifetimes of laurdan in solvents and in bilayers are comparable: its emission maxima in bilayers are 440 nm in the gel phase and 490 nm in the liquid phase, as shown in Fig. 2.9, and the fluorescence lifetimes between 3 and 6 ns depending on the type of bilayer. This suggests results in solvents could realistically be used to understand the behaviour of laurdan in lipid environments. If such is the case, this data would point towards the fact that ordered bilayers have a higher dipolar strength than disordered ones, while having lower solvation abilities. One possible explanation is that in ordered bilayers, there are fewer water molecules, which therefore engage in fewer hydrogen bonds with laurdan. This contributes to shorter emission wavelengths. These water molecules are also less mobile and possibly less randomly oriented, hence causing an overall higher dipolar strength since they do not re-arrange upon excitation of laurdan, and explaining a longer emission lifetime.

From these results, two conclusions can be drawn to explain the photophysical behaviour of laurdan in solvents and bilayers:

- Laurdan emission wavelength is determined by the overall solvation ability of its environment, as quantified by E_T^N, which incorporates inherent properties of the solvent as well as solvent-solute interactions. Since GP values are directly related to the emission spectrum of laurdan, it is assumed that laurdan GP is a measure of the solvation ability of its environment. In a bilayer, this would correspond to the amount of water molecules in proximity of laurdan, with the ability to contract hydrogen bonds and re-orient upon its excitation, which can be

qualified as membrane hydration.

- Laurdan lifetime is sensitive to the dipolar strength of its environment, as defined by μ and ϵ, rather than to its overall solvation ability as defined by E_T^N.

To a certain extent, these experiments invalidate the commonly accepted assumption that the lifetime of laurdan reports on the same properties as its emission spectrum. This is useful, since it means that laurdan emission spectrum and lifetime can be used to quantify the hydration of the bilayer as well as its dipolar strength, independently.

2.3.2 Correlating membrane polarity and order parameters in homogeneous lipid mixtures

Using the results from previous section, which have established the environmental sensitivity of laurdan fluorescence, multiparameter imaging of this fluorophore in lipid bilayers was now carried out. GP, lifetime and anisotropy parameters were measured as a function of temperature in DOPC, POPC and DPPC GUVs. Results are presented in the following sections.

2.3.2.1 DOPC

The average lifetime as well as order parameters θ and Δ are shown as a function of temperature in boxplots Fig. 2.24:

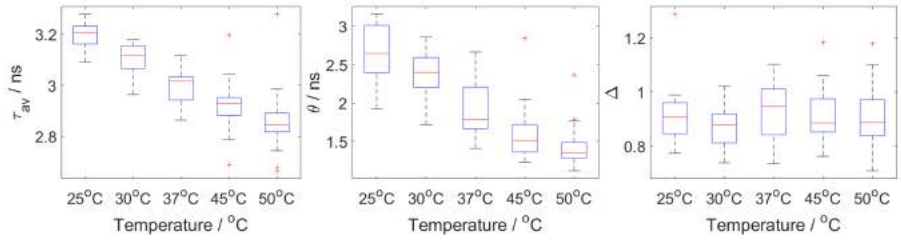

Figure 2.24: Boxplots showing average lifetime (left), rotational correlation time (centre) and order parameter Δ of laurdan in DOPC as a function of temperature. These results are from N=3 independent experiments, with a total of 109 GUVs in total.

The first observation is that the lifetime and rotational correlation time decrease with temperature, indicating a decrease in dipolar strength as well as an increase in the speed of rotational diffusion. Interestingly, the order parameter Δ is high (>80%) and stable with temperature, indicating that the rotational freedom of laurdan does not increase in DOPC in this temperature range. This suggests that in this type of disordered environment, rotational freedom is already maximal at room temperature. This is illustrated by Fig. 2.25, (right): the anisotropy decays faster at 50^{o}C compared to 25^{o}C, but the tail value r_∞ is similar at both temperatures. The fact that the anisotropy of laurdan decays to 0 in DOPC can be linked to high rotational mobility of the

probe; however, some restriction of the rotation is still expected in bilayers. The full depolarisation is therefore surprising. This can also be linked to the orientation of the fluorophore TDM with respect to the bilayer normal. Using molecular dynamics simulations, Osella et al. [189] have shown that the angle between the laurdan fluorochrome and the aliphatic tails is as high as 80^o. In such a situation, even restricted rotational motion of the probe such as rotation along its long axis leads to the fluorophore undergoing some angular displacement and contributing to depolarisation. The initial anisotropy value is consistent with steady-state anisotropy measurements from Harris et al. [91], who measured maximal anisotropy values of 0.26 - note that in any case the measured r_0 is affected by high-aperture depolarisation and so is not indicative of the fundamental anisotropy of laurdan.

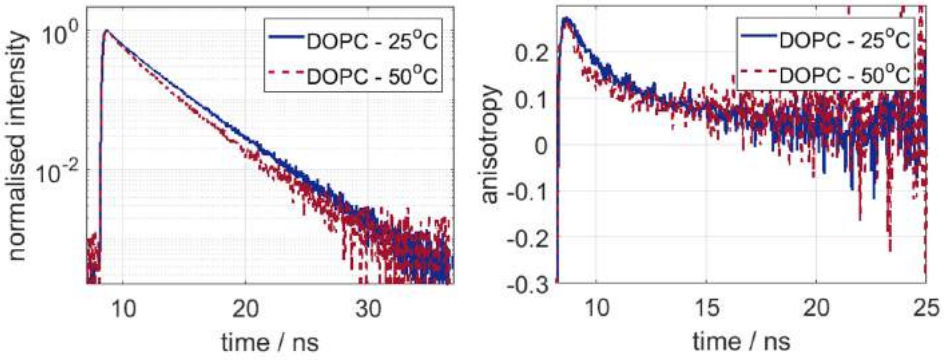

Figure 2.25: Examples of intensity (left) and anisotropy (right) decays of laurdan in DOPC at 25 and 50^oC.

τ_{av} can then be correlated with the order parameters θ and Δ to show the relationship between membrane polarity and membrane order, as shown in Fig. 2.26. τ_{av} and θ are bound by a linear relationship, with the following fit parameters:

Fit Parameter	Value
Intercept - y_{DOPC}, / ns	2.49 ± 0.02
Gradient - m_{DOPC}	0.26 ± 0.01
Goodness of fit - R^2_{adj}	0.99
p-value of the fit	1.10^{-4}

Table 2.4: Summary of parameters for the linear fit between τ_{av} and θ for DOPC.

This signifies that membrane polarity increases linearly with the dynamic order parameter θ. As expected, Δ shows no temperature evolution so no relationship with τ_{av} whatsoever.

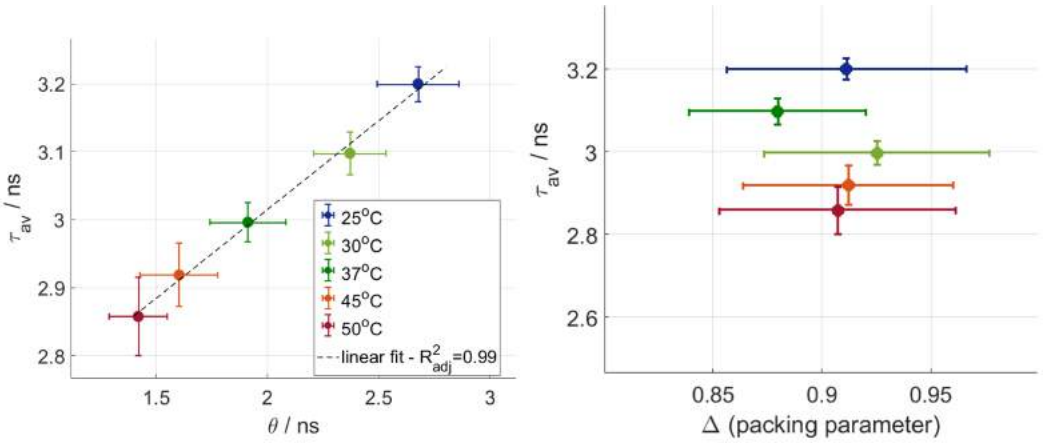

Figure 2.26: Relationship between laurdan lifetime and order parameters. Left: τ_{av} against θ the linear relationship is shown with the black dashed line. Right: τ_{av} against Δ. Span of error bars represent one standard deviation.

It is interesting to note that the order parameter θ is more sensitive to temperature than indicator of membrane polarity τ_{av}, as indicated by the 47% decrease between 25 and 50^{o}C for θ, against only 11% for τ_{av}, meaning that temperature affects membrane order more than its polarity.

From two confocal images acquired before the time-resolved data is taken, GP images can be computed for each GUV, allowing for a correlation between GP, τ, θ and Δ. GP analysis of DOPC vesicles as a function of temperature is presented in Fig. 2.27:

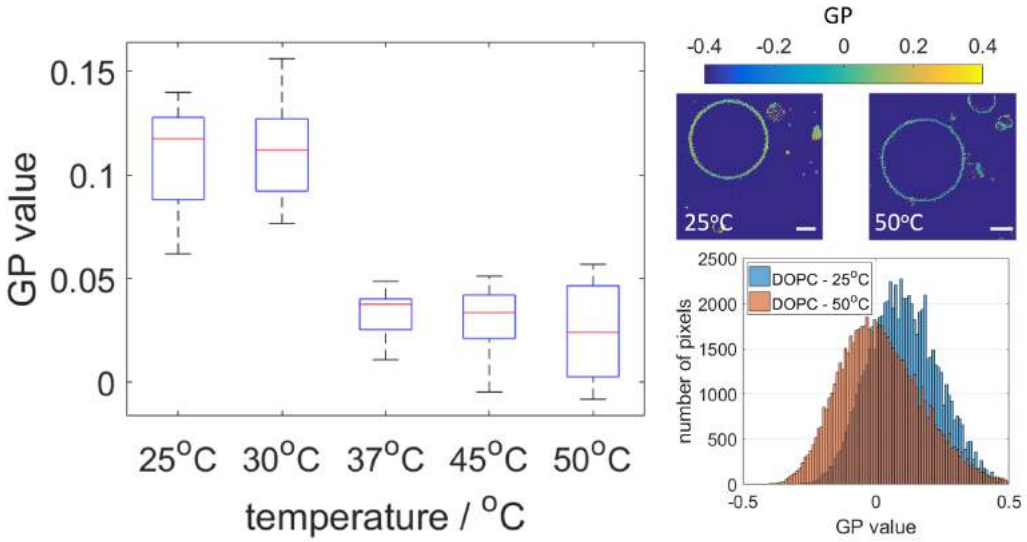

Figure 2.27: GP analysis of DOPC vesicles. Left: boxplot showing average GP values as a function of temperature. Right, above: GP images of representative GUVs at 25 and 50^{o}C. Right, below: histograms of GP values at 25 and 50^{o}C for all GP images at each respective temperature. Results were obtained on a minimum of n=7 GUVs per temperature.

GP values decrease with temperature, as expected; however the evolution does not appear to be continuous. This is unlikely to reflect a transition in the behaviour of DOPC at these temperatures, and is likely due to a random effect or an issue with the calibration of the confocal

PMTs - a quantitative correlation with the other parameters was therefore not established; however, GP follows the same evolution as lifetime and rotational correlation time, suggesting a positively correlated evolution of membrane hydration, polarity and fluidity in DOPC.

This first experiment shows the linear relationship between membrane polarity and the dynamic order parameter in DOPC, and shows little temperature sensitivity of the static order parameter Δ. GP values also show an overall negative trend with temperature, which needs to be confirmed with other types of lipids.

2.3.2.2 POPC

POPC presents a single unsaturation compared to DOPC, and therefore its melting temperature is higher (-2^{o}C for POPC against -17^{o}C for DOPC), though they are both in the L_d phase at room and physiological temperatures. The same parameters, τ_{av}, θ and Δ were computed for POPC as a function of temperature. The linear relationship between τ_{av} and θ is maintained, as seen in Fig 2.28 (diamonds), and with the following parameters:

Fit Parameter	Value
Intercept - y_{POPC}, / ns	2.55 ± 0.06
Gradient - m_{POPC}	0.27 ± 0.03
Goodness of fit - R^2_{adj}	0.96
p-value of the fit	2.10^{-3}

Table 2.5: Summary of parameters for the linear fit between τ_{av} and θ for POPC.

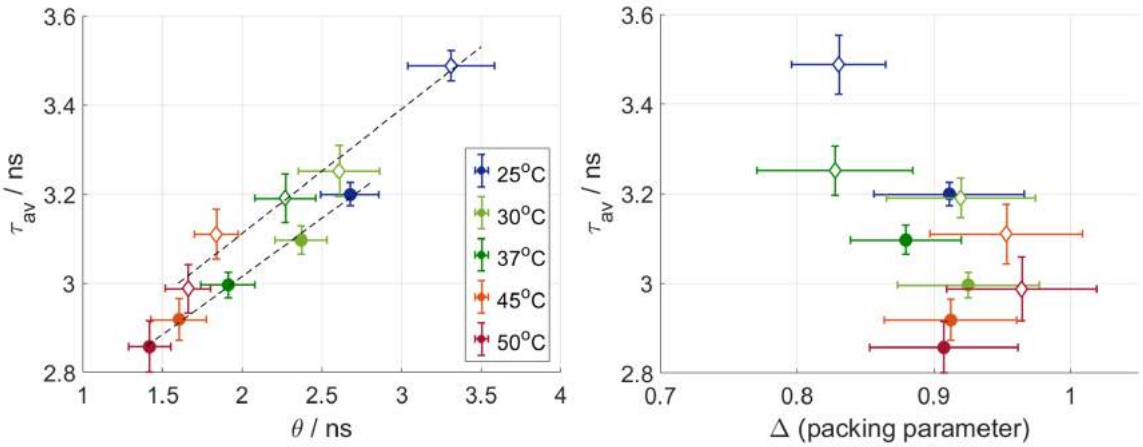

Figure 2.28: Relationship between τ_{av} and θ (left) and τ_{av} and Δ(right) for DOPC and POPC. Data for DOPC is the same as previous figure, data for POPC is shown as the white diamonds. The span of the error bars is one standard deviation. Data for POPC was acquired in N=3 independent experiments, for a total of 127 GUVs.

Data from POPC and DOPC were compared. Interestingly, the gradients m_{POPC} and m_{DOPC} are within the errors of each other, which means that the temperature sensitivity of membrane

polarity and order parameter θ is the same for both lipids. POPC is characterised by an overall higher dipolar strength, as evidenced by the longer lifetimes and the higher intercept than for DOPC (2.55 ± 0.06 against 2.49 ± 0.02 ns, respectively). The order parameter Δ is within a range similar to DOPC, but a slight increase with temperature can be detected, from lower rotational freedom than DOPC at room temperature, to higher values at 50^oC. It is tempting to conclude that a fully saturated tail increases the temperature sensitivity of bilayer order in POPC compared to DOPC; however, the large errors associated with the anisotropy parameters calls for caution for this type of interpretation. Examples of representative intensity and anisotropy decays for DOPC and POPC at matching temperatures are shown in Fig. 2.29 below:

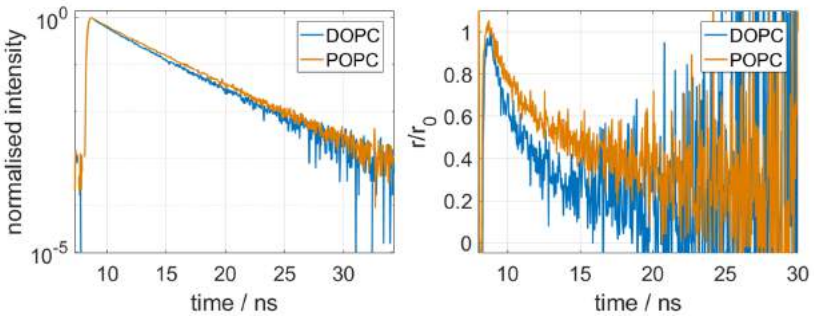

Figure 2.29: Representative normalised intensity (left) and anisotropy (right) decays for DOPC and POPC at 25^oC.

GP images and average GP values were computed for each temperature, as for DOPC. GP displayed a continuous decrease with temperature, as seen from the boxplots in Fig. 2.30 and example images.

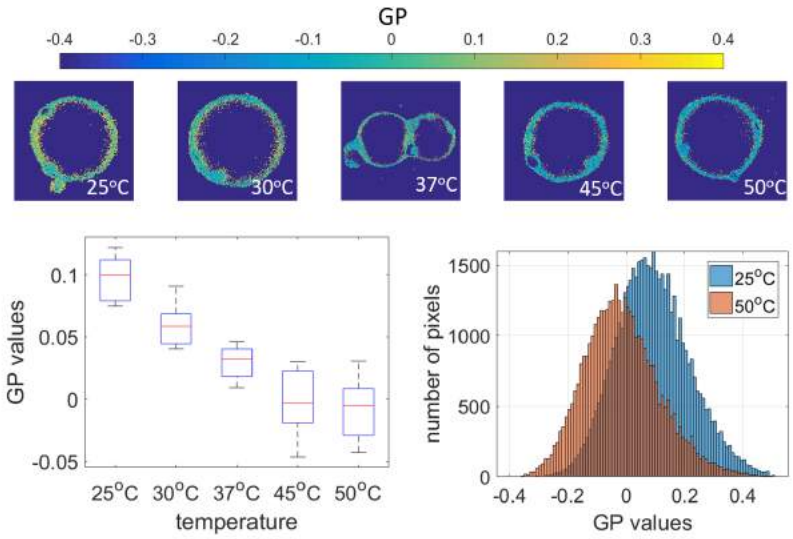

Figure 2.30: GP of laurdan in POPC as a function of temperature. Above: representative GP images of POPC GUVs at each temperature. Left: boxplots of average GP values for each temperature. Right: histograms of GP values at 25 and 50^{o}C, computed from all GP images at these temperatures. Only the 2 extreme temperatures are represented for clarity. Data is the results of a minimum of n=8 GUVs per temperature.

Since all parameters evolve continuously with temperature in these experiments, they are all correlated with each other. All linear fits between GP and these parameters are significant (p_{values} of the fits below 0.05); the most significant fit being between GP and θ, with $p_{value} = 2.10^{-4}$, and $R^2_{adj} = 0.99$.

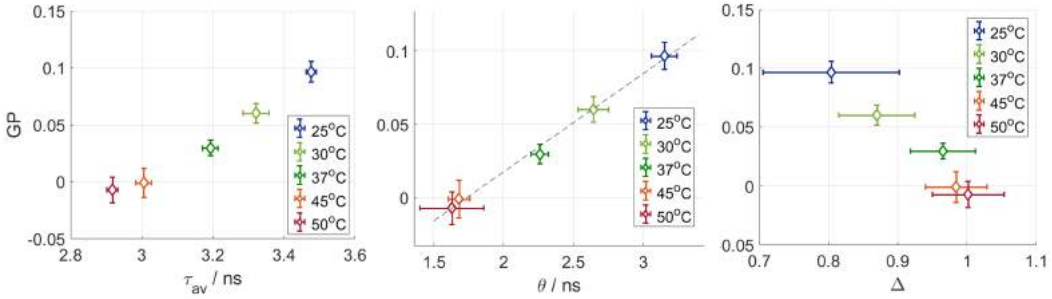

Figure 2.31: GP against polarity parameter τ_{av} (left) and against order parameters θ (centre) and Δ (right). The linear fit between GP and θ is shown with the black dashed line.

In POPC, the absolute variation in GP between 25^{o}C and 50^{o}C is of 0.1, which is slightly higher than in DOPC (0.08), which suggests that the increase in solvation of laurdan molecules which occurs in POPC when temperature increases is greater than that of DOPC.

In conclusion, the traditional Ld phase is characterised by a linear relationship between membrane hydration, polarity, and order parameters. The parameter that appears to have the strongest sensitivity is the rotational correlation time θ, while the temperature sensitivity of the other parameters was low, as summarised further in Table 2.6, signifying that these quantities have already

reached their maximal values in the range of temperatures investigated. The introduction of saturated chains within a Ld phase increases the dipolar strength of the membrane (longer lifetimes), but does not modify the relationship between membrane order and polarity. The data also suggests an increase in the temperature sensitivity of membrane hydration and packing. The variation in GP values is slightly higher in POPC; however, GP values are in the same range for both lipids and are not significantly different at 25^oC (p-value$>$0.05), suggesting that the presence of additional unsaturations does not greatly contribute to decreasing membrane hydration.

2.3.2.3 DPPC

With two fully saturated tails, the melting of DPPC is around 41^oC, and bilayers formed of DPPC are in the gel phase until that temperature. As seen in the methods section for temperature control, a sharp transition in GP values is obtained upon this transition (Fig 2.11), signifying an increase in the solvation of laurdan in the liquid phase. The objective is to investigate whether membrane polarity and order also follow the same pattern. Boxplots for τ_{av}, θ, GP and Δ as a function of temperature are presented in Fig. 2.32; τ_{av} and Δ visibly follow the same trend as GP, with a sharp transition in values between 41 and 45^oC. GP images and histograms for DPPC were already shown in Fig. 2.10.

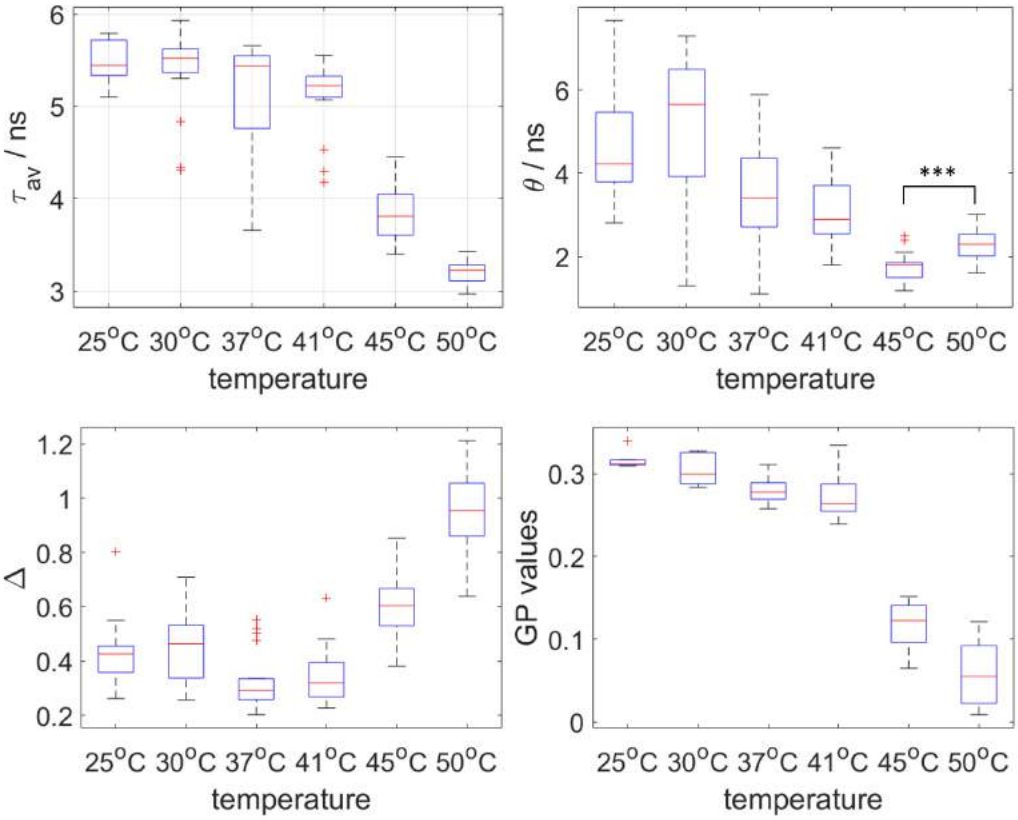

Figure 2.32: Boxplots for τ_{av} (upper - left), θ(upper - right) and Δ (lower - left) and GP (lower - right) as a function of temperature in DPPC. Data for τ_{av}, θ and Δ is the result of N=3 independent experiments, with a minimum of n=3 repeats per temperature and per experiment and a total of 123 measurements. Data for GP is taken from one of these experiments, with a minimum of n=6 repeats per temperature and a total of 43 GUVs.

The data for θ does not suggest a similar trend, though the error bars are large due to difficulties in fitting anisotropy decays for packed bilayers. While θ follows an overall negative evolution with temperature, it is not possible to identify a transition. There is also an anomalous and significant increase in the values of this parameter between 45 and 50^{o}C (2-tailed t-test, $p_{value} \ll 0.001$). These two observations may be due to the fact that θ depends on the rate of rotational diffusion as well as the width of the cone in which this diffusion takes place, as explained in the introduction. In this case, the width of the cone as reported by Δ increases markedly with temperature, going from 0.39$\pm$0.03 before 41^{o}C (average of all values between 25 and 41^{o}C) to 0.60$\pm$0.05 at 45^{o}C and finally 0.95$\pm$0.06 at 50^{o}C, yielding a 143% increase over the range investigated. This large increase in rotational freedom may contribute to the higher θ values at 50^{o}C than 45^{o}C, and the overall less structured evolution of this parameter. One should note that this effect was not observed in DOPC and POPC, since the sensitivity of Δ to temperature was low, and this parameter was already high at room temperature.

It is furthermore interesting to see that at 50^{o}C, after its transition temperature, DPPC behaves

as a Ld phase, in all aspects identical to DOPC. This is visible on the τ_{av} vs. θ and τ_{av} vs. Δ plots shown in Fig. 2.33, where the data for DPPC evolves from a parameter space clearly distinct from DOPC below transition temperature to the same parameter space as DOPC above this temperature. This is further illustrated in Fig. 2.34 showing intensity and anisotropy decays of laurdan in DOPC and DPPC.

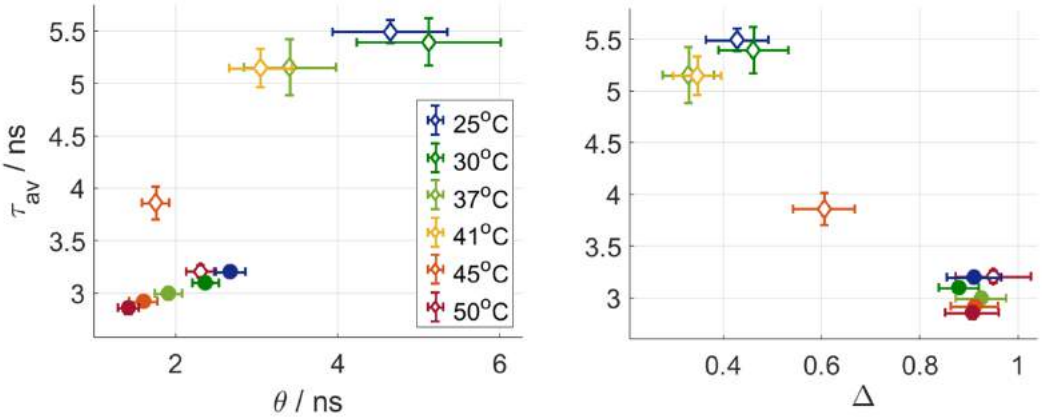

Figure 2.33: Plots of τ_{av} against θ (left) and τ_{av} against Δ (right), for DPPC (empty diamonds), compared to DOPC (full circles). Span of error bars is one standard deviation.

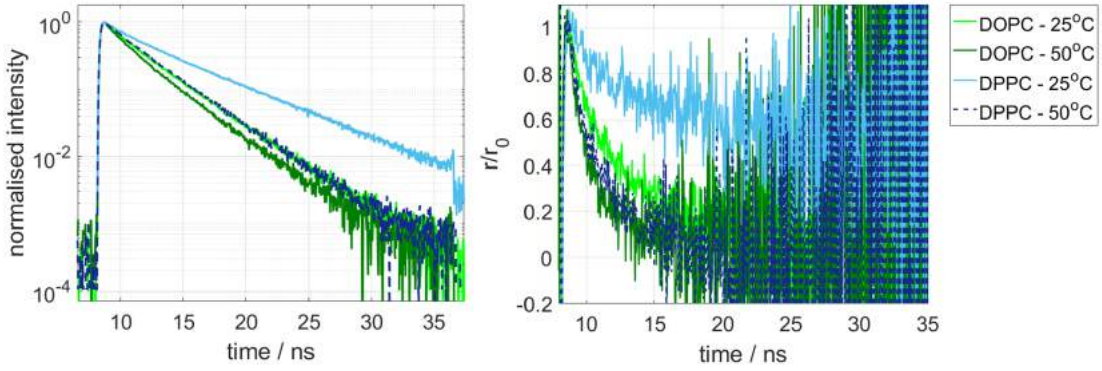

Figure 2.34: Representative intensity (left) and anisotropy (right) decays of laurdan in DOPC (green curves) and DPPC (blue curves) at 25^{o}C (light shades) and 50^{o}C (dark shades).

These results for DPPC and their comparison with those of DOPC and POPC yield the following conclusions:

- The main element affecting the solvation of laurdan in the bilayer as quantified by GP, the dipolar strength of the bilayer as quantified by τ_{av}, and the rotational freedom as quantified by Δ is the phase of the bilayer. Indeed, the difference between their values in DPPC below and above phase transition largely exceeds their range of evolution within the Ld phase in DOPC or POPC, as summarised in Table 2.6 below. Within the same phase, these parameters

are also sensitive to the nature of the bilayer to a lesser extent, as shown by the differences between POPC and DOPC and already discussed.

	$\delta GP = GP_{max} - GP_{min}$	$\delta\tau_{av} = \frac{\tau_{max}-\tau_{min}}{\tau_{max}}$	$\delta\theta = \frac{\theta_{max}-\theta_{min}}{\theta_{max}}$	$\delta\Delta = \frac{\lvert\Delta_{min}-\Delta_{max}\rvert}{\Delta_{min}}$
DOPC	0.08	11%	47%	0%
POPC	0.10	17%	50%	16%
DPPC	0.26	42%	62%	189%

Table 2.6: Summary of the variation in parameters over the temperature range investigated. The absolute difference in GP rather than a normalised one was computed, since the values cross 0, resulting in aberrant >100% variations.

- Membrane fluidity, as quantified by the dynamic order parameter θ, is sensitive to temperature regardless of the chemical composition of the bilayer or its phase, as seen by the similar $\delta\theta$ values between 25 and 50^{o}C in DOPC, POPC and DPPC. This is in line with the idea of a diffusion process determined principally by the temperature of the medium.

- Lastly, the concomitant increase in θ and decrease in Δ between 45 and 50^{o}C for DPPC confirms the model formulated by Kinosita et al [26], that the dynamic order parameter θ should depend on both the width of the cone in which laurdan rotates, and its rate of rotational diffusion.

2.3.3 The effect of cholesterol on the relationship between membrane hydration and membrane order

Next, DOPC and DPPC mixtures containing varying amounts of cholesterol were made, and the same experiments as with single lipid mixtures were carried out.

2.3.3.1 DOPC and cholesterol

DOPC:Cholesterol mixtures with 7:3 and 5:5 molar ratios were used to form GUVs. In such environments, the linear relationship between the lifetime and rotational correlation time of laurdan is preserved, as shown in Fig. 2.35. The gradient between these two parameters increases with cholesterol content, which means that the temperature sensitivity of the dipolar strength of the bilayer increases, while the range of variation of θ decreases slightly (from $\delta\theta = 50\%$ in pure DOPC, against $\delta\theta = 38\%$ with 30 and 50 mol% Chol.). The fit parameters are shown in table 2.7.

	τ_{av} against θ			τ_{av} against Δ			Range of variation			
XChol	m	p_{value}	R^2_{adj}	m/ns	p_{value}	R^2_{adj}	$\delta\tau_{av}$	$\delta\theta$	$\delta\Delta$	δGP
0%	0.26 ± 0.01	1.10^{-4}	0.99	NA	NA	NA	11%	47%	0%	0.08
30%	0.45 ± 0.07	8.10^{-3}	0.90	-3.2 ± 0.5	$9.5.10^{-3}$	0.90	17%	38%	24%	0.02
50%	0.85 ± 0.08	$1.5.10^{-3}$	0.97	-6.1 ± 0.2	1.10^{-4}	0.99	26%	38%	32%	0.04

Table 2.7: Summary of the linear fit results and ranges of variation for parameters τ_{av}, θ and Δ in DOPC-Chol GUVs. Note that results for pure DOPC are the same as shown in Table 2.4. The errors represent the standard errors of the linear fit parameters.

As visible on the right-hand panel of Fig 2.35, the order parameter Δ is lower than in pure DOPC, and becomes sensitive to temperature upon addition of cholesterol: Δ sees a 24% increase between 20 and 50^oC at 30 mol% cholesterol, and a 32% increase at 50 mol%. The relationship between Δ and τ_{av} is also linear, as shown by the summary of the fits in Table 2.7 (centre). The overall lower values of Δ indicate more restricted rotational motion in the presence of cholesterol, as expected. Compared to pure DOPC, the increase in Δ values with temperature may explain the smaller range of variation of θ in the presence of cholesterol: as the cone available to the laurdan molecule for diffusion widens with temperature, the dynamic order parameter decreases more slowly than if the cone is fixed in width, as is the case in pure DOPC. This is due, once more, to the fact that θ depends on both the rate and extent of rotational diffusion.

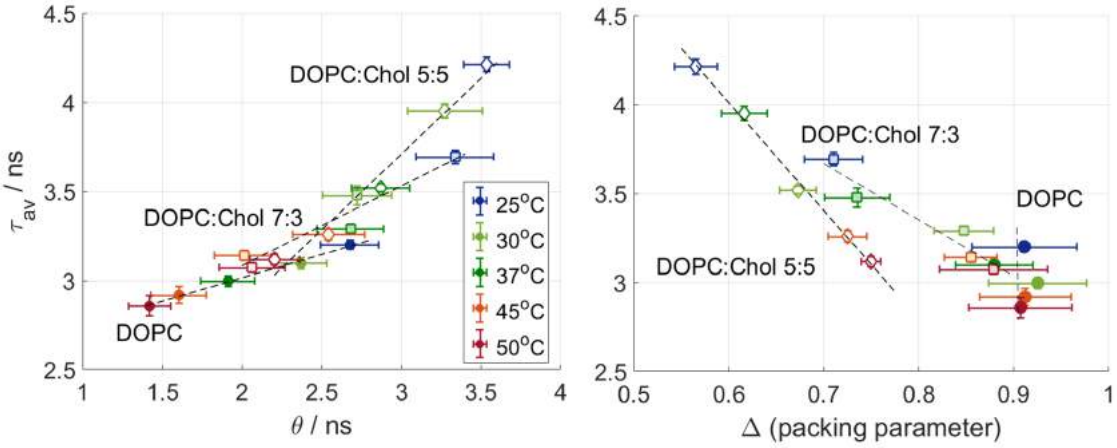

Figure 2.35: Plots of τ_{av} against θ and Δ in DOPC GUVs containing) 0% (full circles), 30% (light squares) or 50% (empty diamonds) cholesterol (mol%). Linear fits are represented with the black dashed lines. Data for DOPC is the same as shown before. Data for DOPC:Chol 7:3 is the result of N=2 independent experiments (61 GUVs in total). Data for DOPC:Chol 5:5 was from 1 experiment (41 GUVs in total).

The effect of cholesterol on the temperature sensitivity of parameters τ_{av}, θ and Δ is illustrated in Fig. 2.36, where examples of intensity and anisotropy decays of laurdan in DOPC:Chol 5:5 GUVs at 22, 37 and 50°C are shown. It is visible that at different temperatures, the anisotropy decays do not reach the same tail value, which indicates the temperature sensitivity of the static order

parameter Δ in the presence of cholesterol, which can be compared to the case of pure DOPC, Fig 2.25.

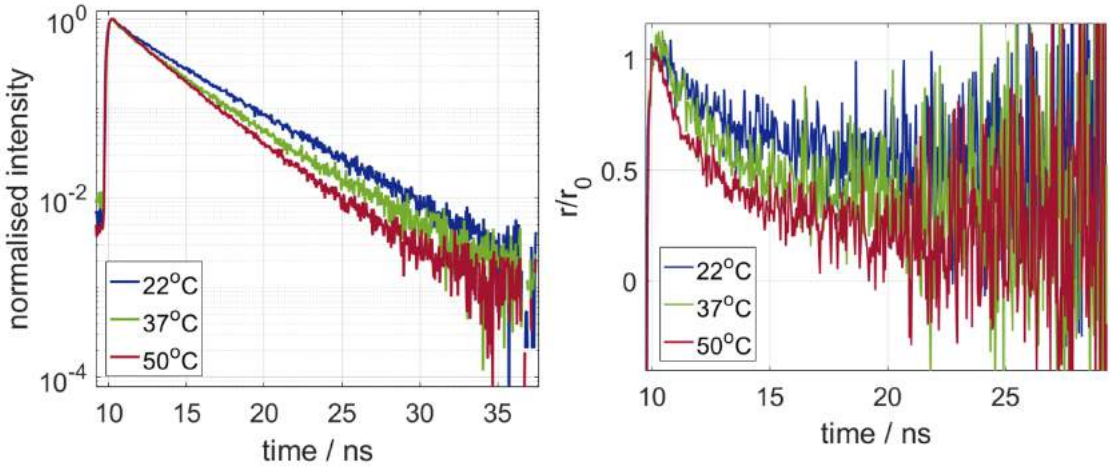

Figure 2.36: Examples of intensity (left) and anisotropy (right) decays of laurdan in DOPC:Chol 5:5 vesicles at 22 (blue), 37 (green) and 50^{o}C (red)

GP values were also computed for DOPC:Chol mixtures. GP increases with cholesterol content, with $GP_{30^oC} = 0.14 \pm 0.02$ at 30% Chol, and 0.24 ± 0.02 at 50% Chol. Though negative trends with temperature can be identified, the GP values appear more heterogeneous than the time-resolved parameters, and clear continuous decrease with temperature cannot be ascertained, as shown in the boxplot figures below (Fig. 2.37) and the unclear trend of δGP with cholesterol content (Table 2.7).

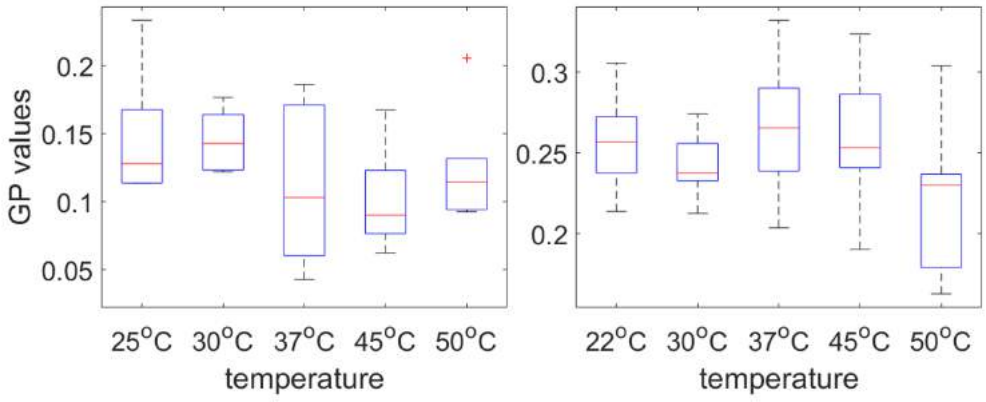

Figure 2.37: GP values for DOPC:Chol 7:3 (left) and 5:5 (right). Data is the result of a minimum n=6 repeats per temperature for DOPC:Chol 7:3 (30 GUVs), and n=8 for DOPC:Chol 5:5 (44 GUVs).

An interesting observation is that, unlike DPPC, DOPC:Chol mixtures do not behave like pure DOPC at high temperatures, and there is no transition from a solid to a liquid phase as was

observed in DPPC. Rather, the presence of cholesterol creates a new regime of membrane polarity and order parameters, with overall less solvation of laurdan as evidenced by the higher GP values, higher dipolar strength as evidenced by the longer lifetimes, and higher order parameters, with the introduction of a higher temperature sensitivity to these physical properties. This confirms the status of the "liquid-ordered" bilayer as a distinct environment altogether.

2.3.3.2 DPPC and Cholesterol

The effect of adding 10 or 30 mol% cholesterol to DPPC vesicles was studied. The evolution of the time-resolved parameters in such mixtures compared to that of pure DPPC is shown in Figs. 2.39-2.38. At 10% Cholesterol, a transition can still be clearly seen in the parameter values, while at 30% cholesterol this is no longer the case. In general, the range of variation of τ_{av} and θ is decreased, and below the transition temperature of DPPC, τ_{av} and θ are equivalent in pure DPPC and in DPPC:Chol mixtures. Above the transition temperature, this relationship is reversed, and these parameters are higher in DPPC:Chol. This shows that cholesterol "smoothens" the phase transitions of single lipid mixtures.

- In DPPC:Chol 9:1, θ values do not change between 37 and 50^{o}C, while Δ increases and τ_{av} decrease. More specifically, the increase in θ between 45 and 50^{o}C in DPPC is no longer visible. This is probably linked to the lower concomitant increase in Δ, and further validates the theory that the dynamic order parameter depends both on rate and extent of rotational motion.

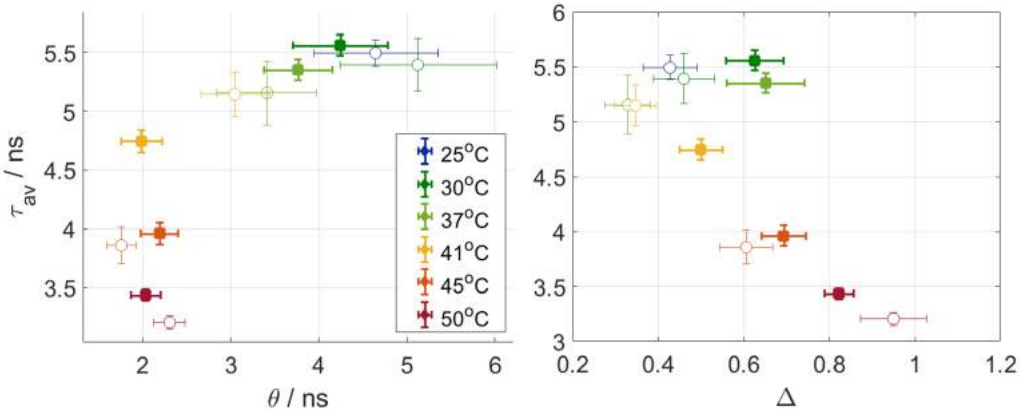

Figure 2.38: Plots of τ_{av} against θ and τ_{av} against Δ for DPPC (white circles) and DPPC:Chol 9:1 (full squares). The linear fit between θ and τ_{av} is shown by the black dashed line. DPPC data is the same as presented before; data for DPPC:Chol is the result of a minumum of n=8 repeats per temperature in total (40 GUVs).

- At 30% mol cholesterol the relationship between τ_{av} and θ appears to be linear, with the parameters shown in 2.8

Fit Parameter	Value
Intercept - $y_{DPPC-Chol}$, / ns	2.2 ± 0.3
Gradient - $m_{DPPC:Chol}$	0.85 ± 0.09
Goodness of fit - R^2_{adj}	0.94
p-value of the fit	9.10^{-4}

Table 2.8: Summary of parameters for the linear fit between τ_{av} and θ for DPPC:Chol 7:3.

The gradient of this fit is very close to that of DOPC:Chol 5:5 (see Table 2.7), with a higher intercept, showing that these two bilayers have the same correlation between polarity and membrane order, similarly to what was observed in the case of DOPC and POPC. The static order parameter Δ shows a similar evolution, with its range of variation dramatically reduced, and the absence of a transition, though a linear relationship between τ and Δ could not be statistically validated.

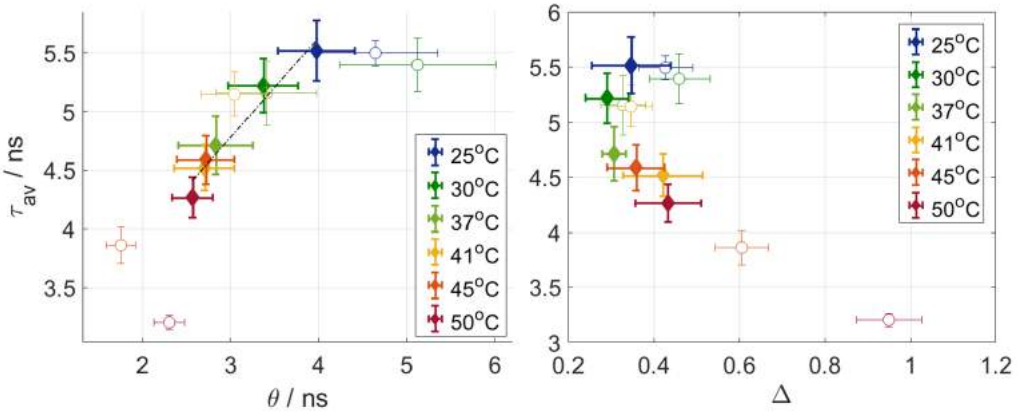

Figure 2.39: Plots of τ_{av} against θ and τ_{av} against Δ for DPPC (white circles) and DPPC:Chol 7:3 (full diamonds). The linear fit between θ and τ_{av} is shown by the black dashed line. DPPC data is the same as presented before; data for DPPC:Chol is the result of N=4 independent experiments, with a minumum of n=24 repeats per temperature in total (154 GUVs).

- It is difficult to interpret the higher Δ values at low temperatures for DPPC:Chol 9:1, and it is also not clear, why the static order parameter consistently decreases between 25 and 37^{o}C for all the samples containing saturated lipids. In spite of the large associated errors, this appears to be systematically the case and so must reflect the behaviour of laurdan in such bilayers; it is possible that in highly packed environments, the dye adopts a slightly different position in the bilayer, where more rotational freedom is available. The main piece of information which can be extracted from Δ is its reduced range of variation with cholesterol content.

The ranges of variation of the parameters for DPPC and DOPC:Chol mixtures are compared in Table. 2.9.

XChol	$\delta\tau_{av}$	$\delta\theta$	$\delta\Delta$	δGP
0	42%	62%	189%	0.26
10%*	38%	53%	64%	0.19
30%	23%	35%	49%	0.04

Table 2.9: Ranges of variation of the bilayer parameters for DPPC and DPPC:Chol 7:3. *DPPC-Chol 9:1 were not imaged at 25^{o}C so the ranges of variation were calculated from parameter values at 30^{o}C for these samples. This may reduce the range slightly.

GP values also display a negative trend with temperature, as seen in Figs. 2.41-2.40, similar to the time-resolved parameters. The transition is still clearly visible at 10% cholesterol. At 30% cholesterol, the decrease in GP values is much smaller than in pure DPPC, but consistent (p-values of 2-tailed t-test between 25 and and 37^{o}C 25 and 50^{o}C both below 0.001). Average GP stabilises after 41^{o}C, with no significant differences between the data points above this temperature.

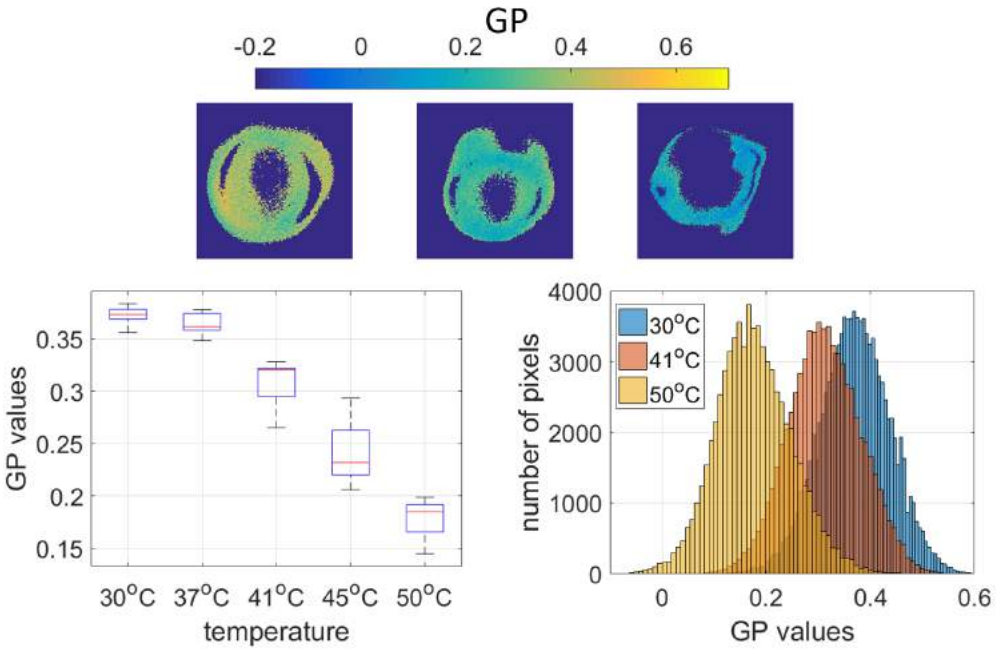

Figure 2.40: Laurdan GP analysis of DPPC:Chol 9:1 vesicles.

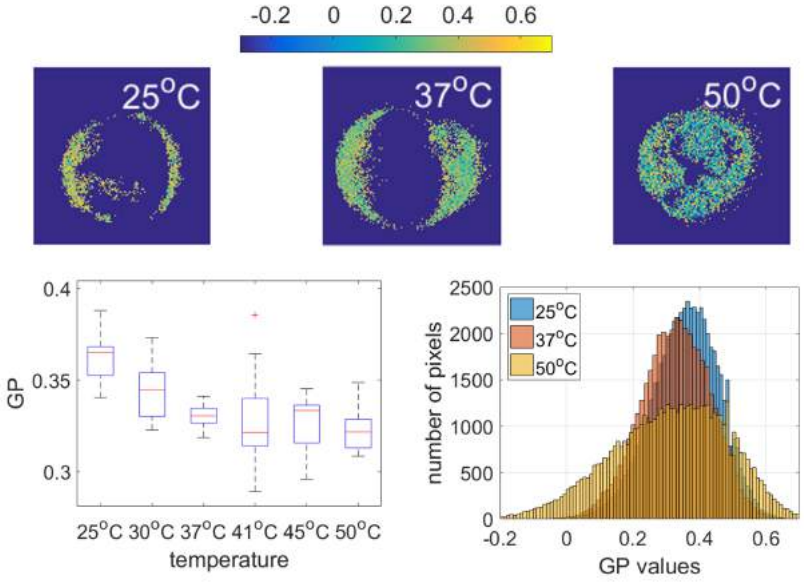

Figure 2.41: Laurdan GP analysis of DPPC:Chol 7:3 vesicles. Data is the result of a minimum of n=8 vesicles per temperature, with a total of 68 vesicles imaged.

In conclusion, these experiments show that the "liquid-ordered" phase which appears upon addition of cholesterol, is characterised by a higher temperature sensitivity of its polarity and order parameters than a Ld phase, all the while without undergoing a phase transition. It is also clear that the behaviour of a Lo phase varies strongly with its lipid composition and cholesterol content: DOPC:Chol 5:5 and DPPC:Chol 7:3 mixtures can be qualified as in the Lo phase, however they display very different ranges of variation for the parameters under study. From an evolutionary point of view, these properties of the Lo phase are interesting; indeed, by making slight changes to the composition of their lipid bilayers, organisms can control the physical properties of their membranes, while maintaining them in a "fluid" state which preserves the integrity of the membrane, and allows for diffusional processes to take place. This range of variation would not be possible with a Ld or gel phase alone.

2.3.4 Phase-separating lipid mixtures

Vesicles made from DPPC, DOPC and Cholesterol with 2:2:1 proportions were imaged, to examine the polarity, hydration and order parameters of such bilayers below and above phase separation temperature, which according to Veatch and Keller [134], is 34^{o}C. Below this temperature, (25 and 30^{o}C), clear domains are visible on the vesicles, as evidenced by areas of higher intensity. Fig. 2.42 shows an example of a phase-separated GUV, with all the types of images acquired: spectrally resolved confocal images to acquire GP information, and polarisation resolved FLIM images to acquire lifetime and anisotropy information.

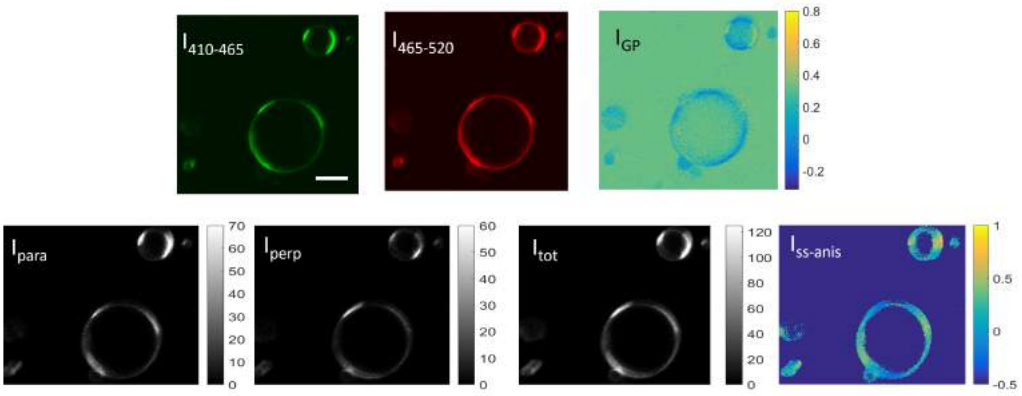

Figure 2.42: Example of series of images acquired for phase-separated GUV composed of DPPC:DOPC:Chol 2:2:1 at 25°C. First row shows confocal images at 410-465 and 465-520 nm, and the GP image computed from these images. Lower row shows the time-and polarisation-resolved images $I_{\parallel}$ and $I_{\perp}$, as well as the total intensity image I_{tot} and the steady state anisotropy image $I_{ss-anis}$. Scale bar is 10 μm.

ROIs around these domains were created manually using the 'roipoly' function in Matlab, and single intensity and anisotropy decays were computed for each ROI. GP histograms and average values were also calculated from the ROIs. Because the confocal-FLIM system did not have a pixel clock, the TCSPC image reconstruction did not have an exact pixel correspondence with the confocal system, since the scan parameters had to be set manually. This resulted in slight changes in aspect ratio and field of view of the images, which did not affect the analysis, but meant that ROIs had to be defined for GP and time-resolved data, separately. Fig. 2.43 below illustrates the procedure of ROI selection on a phase-separated vesicle and the resulting intensity, anisotropy and GP data.

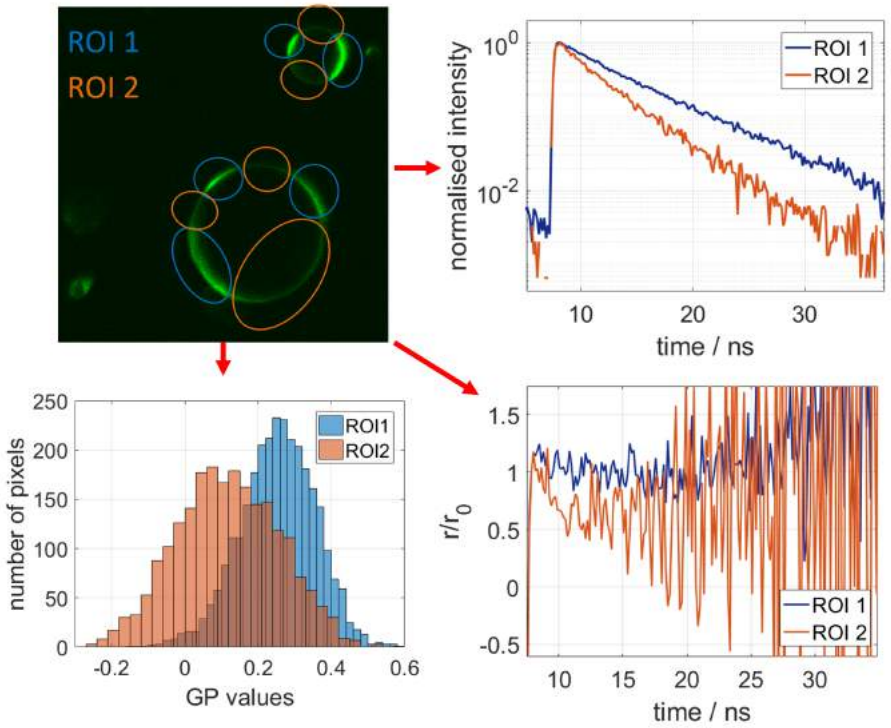

Figure 2.43: ROI selection on images of phase-separated GUVs. Domains are attributed to one of 2 ROIs, depending on their intensity (upper-left). Intensity decays (upper right), anisotropy decays (lower right) and GP values (lower left) are extracted from each ROI.

Further validation of the manual ROI selection is provided by inspection of the GP images. Domains with clearly different GP values are visible in the images below 34^{o}C, while the vesicles appear homogeneous above this temperature, as illustrated in the example images in Fig. 2.44:

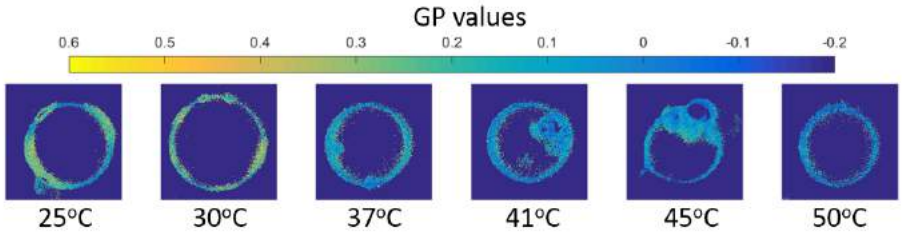

Figure 2.44: GP images of DPPC:DOPC:Chol 2:2:1 vesicles at varying temperatures.

The evolution of GP, θ, τ_{av} and Δ' in DPPC:DOPC:Chol 2:2:1 mixtures as a function of temperature is shown in the boxplots below (Fig. 2.45); at temperatures below 34^{o}C results are shown for each domain, while above 34^{o}C no domains were visible so data corresponded to the full GUVs. The unscaled order parameter Δ' was used here, for the reasons stated in the introduction of this chapter.

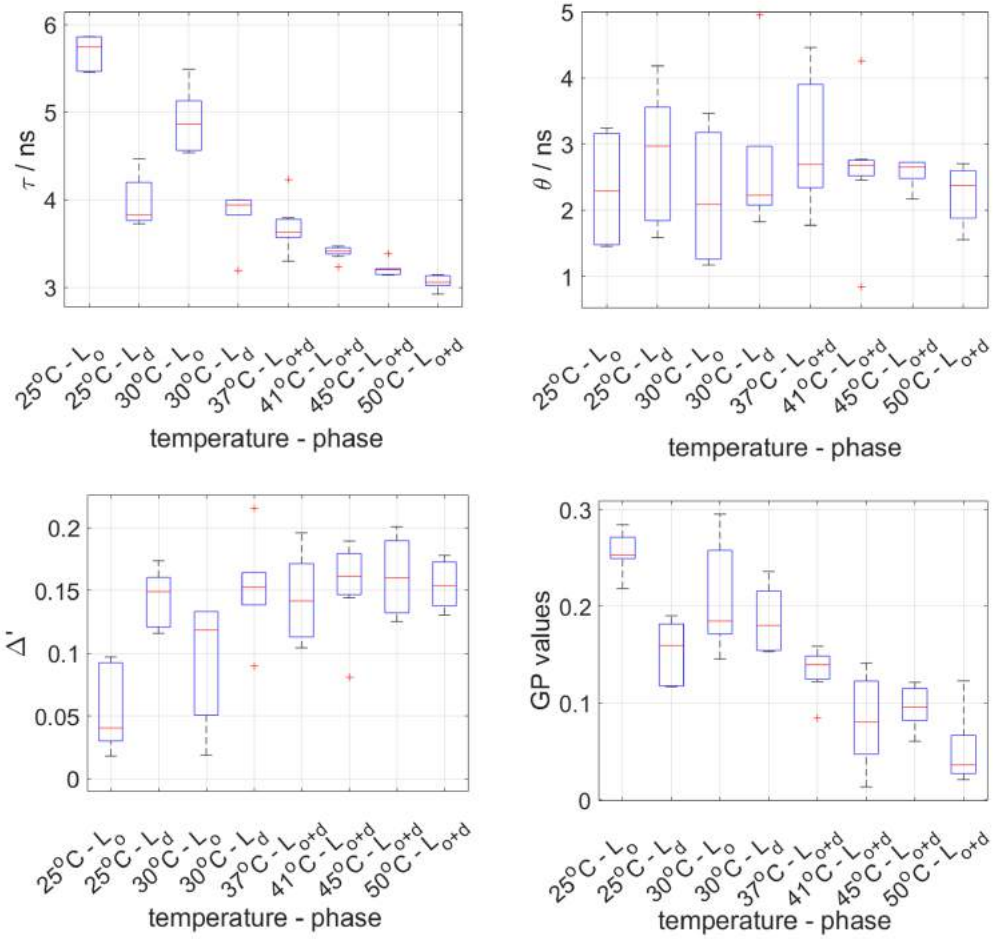

Figure 2.45: Boxplots of τ_{av} (upper-left), θ (upper-right), Δ' (lower left) and GP (lower left) values as a function of temperature for DPPC:DOPC:Chol vesicles. Data is the result of a minimum of n=6 vesicles per temperature.

As expected, below the phase mixing temperature, the domains present very different membrane order and polarity parameter values, with a more ordered domain (hereafter qualified as the "Lo" domain in a macroscopic sense) showing longer lifetimes, higher GP and lower static order parameter Δ' than a more disordered domain (Ld). The parameter θ does not show a particular trend, and the large variability of this parameter in this experiment prevents any quantitative analysis of its behaviour. This is unlikely to be due to the heterogeneity of the sample itself, since the other parameters are much more consistent within a group. The large spread of the θ values is probably linked to the difficulty of fitting anisotropy decays with lower resolution than previously.

To enable comparison between Lo and Ld domains with the binary lipid mixtures studied previously, values for the absolute order parameter Δ' were calculated for some of the previous lipid mixtures (Fig. 2.46, left). The relationships between τ_{av} and Δ established before also apply for τ_{av} and Δ': the presence of a transition in values for DPPC, and the reduction in the dynamic range for DPPC:Chol, are overall preserved. However, the relationship between τ_{av} and Δ' does

not appear to be linear (unlike τ_{av} and Δ'), with a saturation in values at higher temperatures. In the phase-separated GUVs, Δ' has consistent differences between the Lo and Ld domains: in the Lo domain its values are close to DPPC:Chol, while it is closer to DOPC:Chol in the Ld domain (Fig. 2.46, right). When the 2 phases are mixed, Δ' has an evolution similar to that of DOPC:Chol 5:5, albeit with lower values overall, probably linked to the presence of DPPC in the mixture.

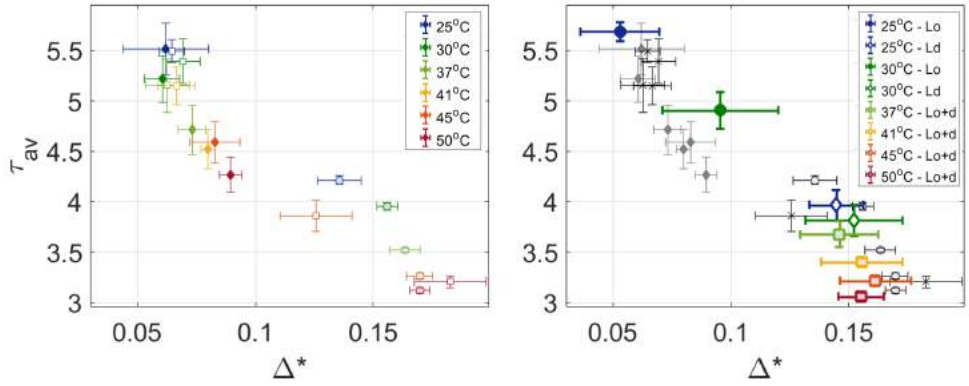

Figure 2.46: Relationship between lifetime and static order parameter Δ'. Left: Plot showing the relationship between τ_{av} and Δ' for the lipid mixtures presented in the previous paragraphs. □=DPPC ; ◇=DPPC:Chol 7:3 ; ○= DOPC:Chol 5:5. Right: The same data is overlaid with the values for the phase-separating GUVs.

τ_{av} and GP values appear to be correlated, before and after phase mixing as seen from Fig. 2.46 (right). This is in line with the idea that these two parameters sense different aspects of membrane polarity. Lifetime and GP values show continuous decrease with temperature, while the static order parameter appears to saturate after phase mixing, suggesting that while membrane polarity increases, membrane order as probed by the width of laurdan rotational cone angle has reached its minimal value after mixing of the two domains.

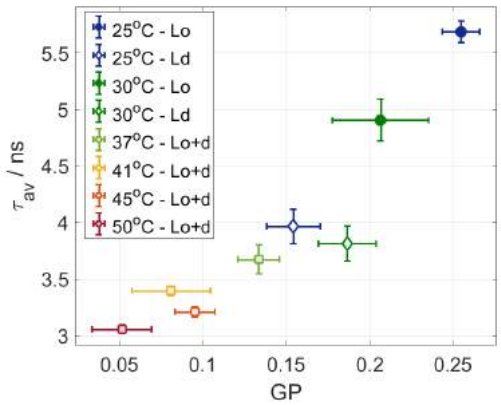

Figure 2.47: Correlation between lifetime and GP values in phase-separating mixtures.

It is interesting to compare the parameters of the two domains below mixing temperature, with those of the homogeneous phases containing DOPC or DPPC and cholesterol. Indeed, when phase

separation occurs, the Lo domain is composed of mainly cholesterol and saturated lipids, while the Ld domain is composed mainly of unsaturated lipids. Less is known about the more precise composition of these domains, and what exactly happens when they intermix. Here, this can be further investigated. At room temperature and 30^{o}C, the lifetime of the Lo domain is close to that of DPPC:Chol 7:3 presented in the previous sections (a 2-tailed t-test showed no statistically significant difference between these two scenarios). A stronger decrease in Δ' values in the ternary mixture than in DPPC:Chol 7:3 suggests that it may contain non-negligible amounts of DOPC as well. Similarly, the lifetime of the Ld domain is much closer to that of DOPC:Chol 7:3 than to pure DOPC, and even slightly higher (with a statistically significant difference between the two), showing that this phase contains non-negligible amounts of cholesterol and possibly DPPC as well. It cannot contain DPPC without cholesterol, since at these temperatures DOPC and DPPC are non-miscible.

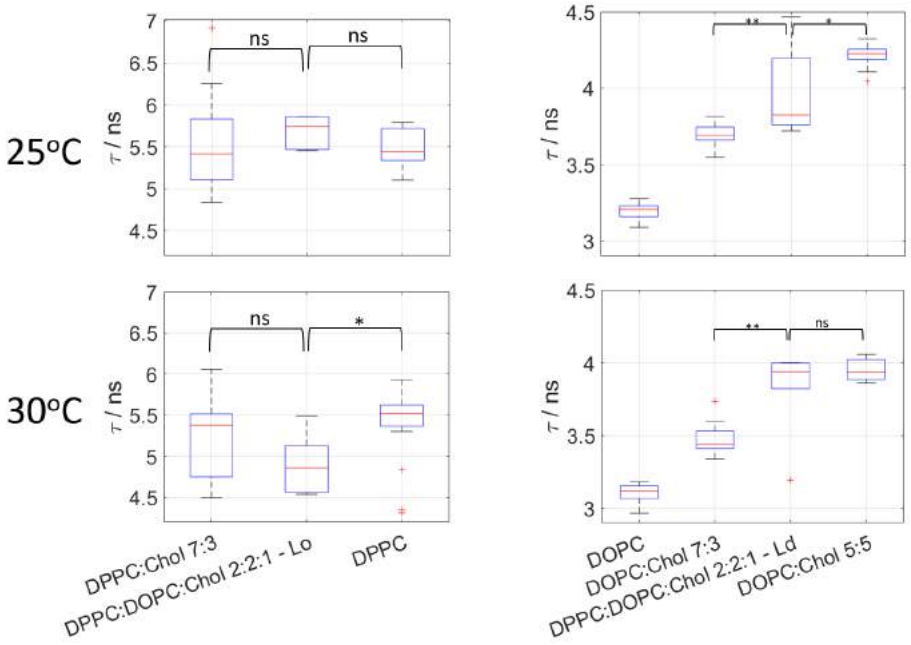

Figure 2.48: Analysis of the composition of the Lo-Ld domains using the results from homogeneous lipid bilayers. The lifetime of DPPC:Chol 7:3 and the Lo phase (left), and DOPC, DOPC:Chol 7:3 (right) and the Ld phase, are compared at 25^{o}C (above) and 30^{o}C (below). Results of 2-tailed t-tests are shown; *: p-values below 5.10^{-2}; **=p-values below 1.10^{-1}.

Another interesting aspect is that while the Lo domain sees large changes in parameter values between 25^{o}C and 30^{o}C, the parameters for the Ld domain are stable between these two temperatures (See boxplots for τ_{av} and Δ', as well as the plot of τ vs. Δ'). GP also shows a differential behaviour between the two domains: in the Lo domains, GP decreases by 13% between 25 and 30^{o}C, while in the Ld domains, GP increases by 18% (p-values$<$0.001), as shown in Fig. 2.49. In the Ld domain, the GP values increase from a level similar to that of DOPC:Chol 7:3 at 25^{o}C

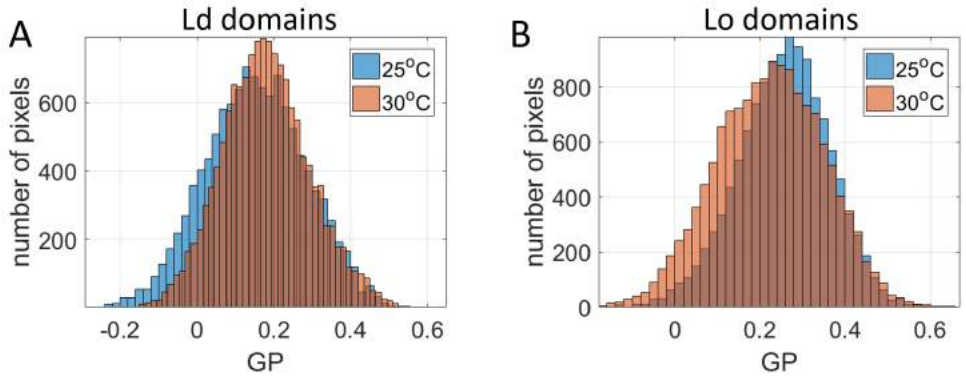

Figure 2.49: Evolution of GP values in the Ld (A) and Lo (B) domains between 25 and 30°C.

to values between DOPC:Chol 7:3 and DOPC:Chol 5:5 at 30°C. Note that statistical significance was found using pixel values rather than GP averages for each vesicle, due to the small number of vesicles imaged at each temperature.

These two observations indicate that between these two temperatures, the composition of the Ld domain changes, incorporating more cholesterol (and perhaps DPPC). Indeed, at 30°C, the lifetime of the Ld domain is closer to that of a DOPC:Chol 5:5 bilayer at the same temperature rather than a 7:3 bilayer, as seen on Fig. 2.48.

To conclude on whether or not the Ld domain incorporates significant amounts of DPPC as well as cholesterol, one can use the lifetime information from the Lo domain. Between 25 and 30°C, the lifetime of the Lo phase decreases consistently with that of a DPPC:Chol 7:3 binary mixture, as seen by the non-significant differences in lifetimes between these two experiments. This suggests that the composition of the Lo domain does not vary greatly between 25 and 30°C; specifically, the proportion between DPPC and Chol remains similar. Indeed, if more cholesterol than DPPC transitions to the Ld domain, then the proportion of cholesterol would decrease in the Lo phase. The lifetime would then be closer to that of pure DPPC at 30°C. On the contrary, the lifetime of the Lo domain is significantly lower than that of DPPC at 30°C, and closer to DPPC:Chol 7:3 mixtures (see Fig. 2.48, lower left). This suggests that between 25 and 30°C, lipids from the Lo domain mix in equal proportion with the Ld domain, while the Lo domain shrinks in size but keeps the same overall composition. It is also possible, as suggested by Haluska and colleagues, that the Lo domain contains a small amount of unsaturated lipids, though the data at hand does not allow to test this hypothesis. Of course, the nanoscale composition of theses phases cannot be resolved using this approach; however, this conclusion is in good agreement with the observation of nanoscale Lo domains within a Ld phase after phase separation, imaged by AFM by Bhatia and colleagues [123], and as shown in the introduction of this chapter; one can hypothesise that the macroscopic Ld domain would contain nanoscopic Lo domains, the quantity and size of these

domains being defined by temperature. These results show that our multi-dimensional approach is informative in resolving the relationship between membrane physical properties and membrane composition. A sketch of the mixing between the two domains as temperature is increased is proposed as a conclusion in Fig. 2.50.

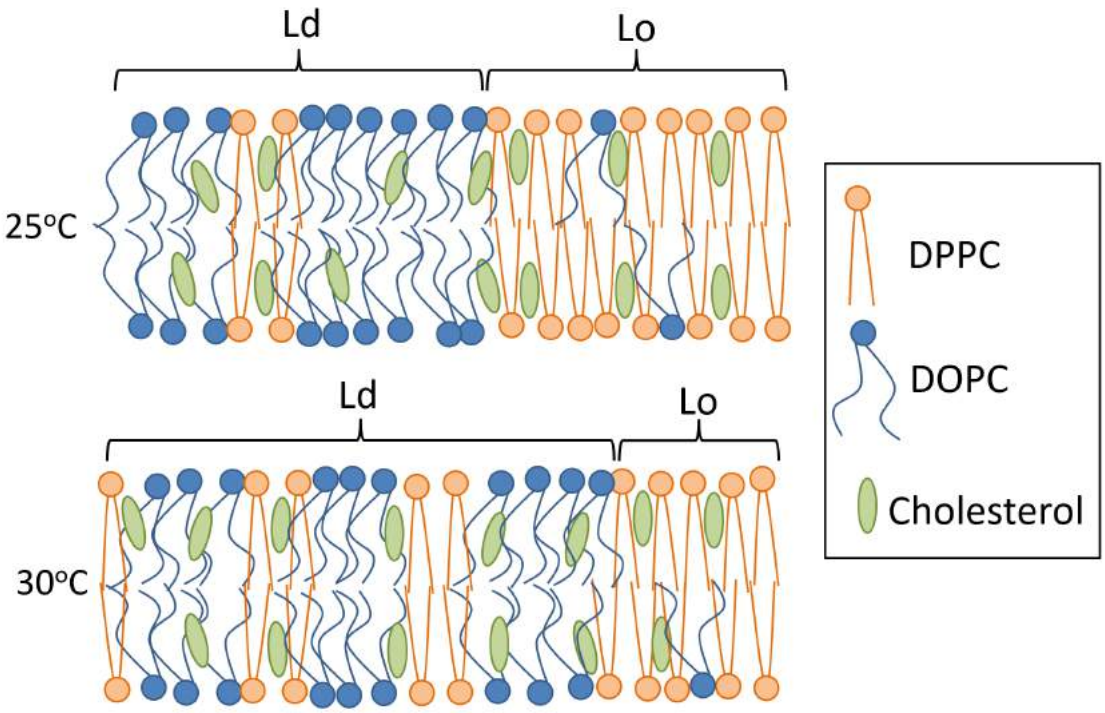

Figure 2.50: Proposed model of Lo-Ld domain mixing in ternary lipid mixtures. At low temperatures (in our case, 25°C), the two domains are composed of a majority of unsaturated lipids and cholesterol for the Ld domain, and saturated lipids and cholesterol for the Lo domain. Closer to the phase mixing temperature (in our case, 30°C), the Ld domain incorporates more elements of the Lo domain, in equal proportion. This changes the chemical composition of the Ld domain, conferring it the properties of a more ordered bilayer, while the Lo domain shrinks in size but maintains the same lipid composition. Note that the terms "Lo/Ld domains" are used for the macroscopic domains visible in ternary lipid mixtures, and are different from "Lo/Ld phases" which are used to describe the physical and chemical state of a specific lipid bilayer, region, whether observable with optical microscopy or not.

2.4 Conclusions and outlook

In this chapter, a multi-dimensional fluorescence imaging method was developed to image membrane microenvironment and order parameters simultaneously, and applied to artificial lipid bilayers. Simple experiments in solvents improved the understanding of the photophysical behaviour of environmentally-sensitive dyes di-4-ANEPPDHQ and laurdan. In particular, spectral and lifetime analysis of laurdan showed differential sensitivity of these two parameters to the polarity and hydration of the medium. Experiments with di-4-ANEPPDHQ showed some sensitivity to viscos-

ity, which is however unlikely to affect its fluorescence signal in lipid bilayers. Data in bilayers furthermore suggests limited insertion of this probe in highly packed bilayers such as DPPC.

From the data of laurdan in lipid bilayers, several conclusions were drawn about the relationship between these two concepts. Importantly, it was shown that within a traditional Lo or Ld phase, the behaviour of lipid bilayers varies significantly according to its chemical composition as well as its phase, as seen by the comparison between DOPC and POPC for the Ld phase, as well as between DOPC:Chol and DPPC:Chol mixtures for the Lo phase, and confirming the original hypothesis. The effect of lipid tail unsaturations and of cholesterol on membrane order and polarity was also discriminated using this method. Lastly, data from ternary mixtures displaying domain separation also yielded insight on the composition and dynamics of these domains. These experiments also validated the theoretical framework of the order parameters as formulated by Kinosita et al [26], and the angular distribution of laurdan TDM in bilayers from computational studies in ref. [189].

The results presented here also underline several limitations of this method, the main one being the large sensitivity of the anisotropy-derived parameters, in particular θ, to the quality of the data. Low intensities as caused by fast photobleaching of laurdan, or lower time resolution due to limitations in data size for images created a large spread of values for the fit parameters, and made some of the results difficult to analyse. The lifetime parameter allowed a consistent and absolute comparison of all lipid compositions and temperatures, and can therefore, for this type of system and setup, be identified as the most reliable parameter. In the next chapter, this method is extended to the investigation of biological membranes in cell-derived vesicles, as well as live cells.

Appendix 1 - fit results of laurdan lifetime in a range of solvents

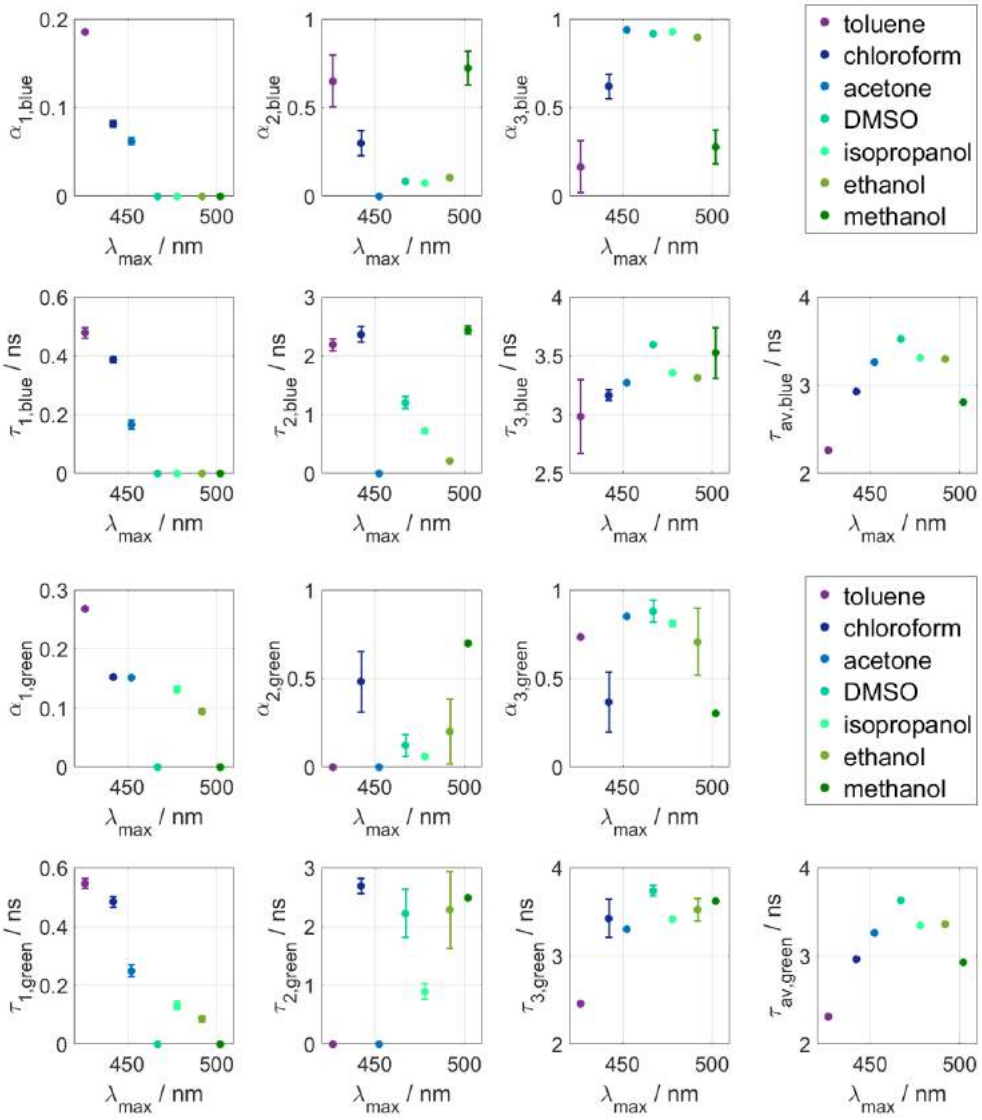

Figure 2.51: Lifetime parameters of laurdan in solution as a function of maximum emission wavelength λ_{max}. When decays were only fitted to 2 exponential components, the missing parameters were set to 0, with α_1 fixed as the absolute value of the negative amplitude, if present. Error bars represent the range of the obtained parameters (n=3 per condition).

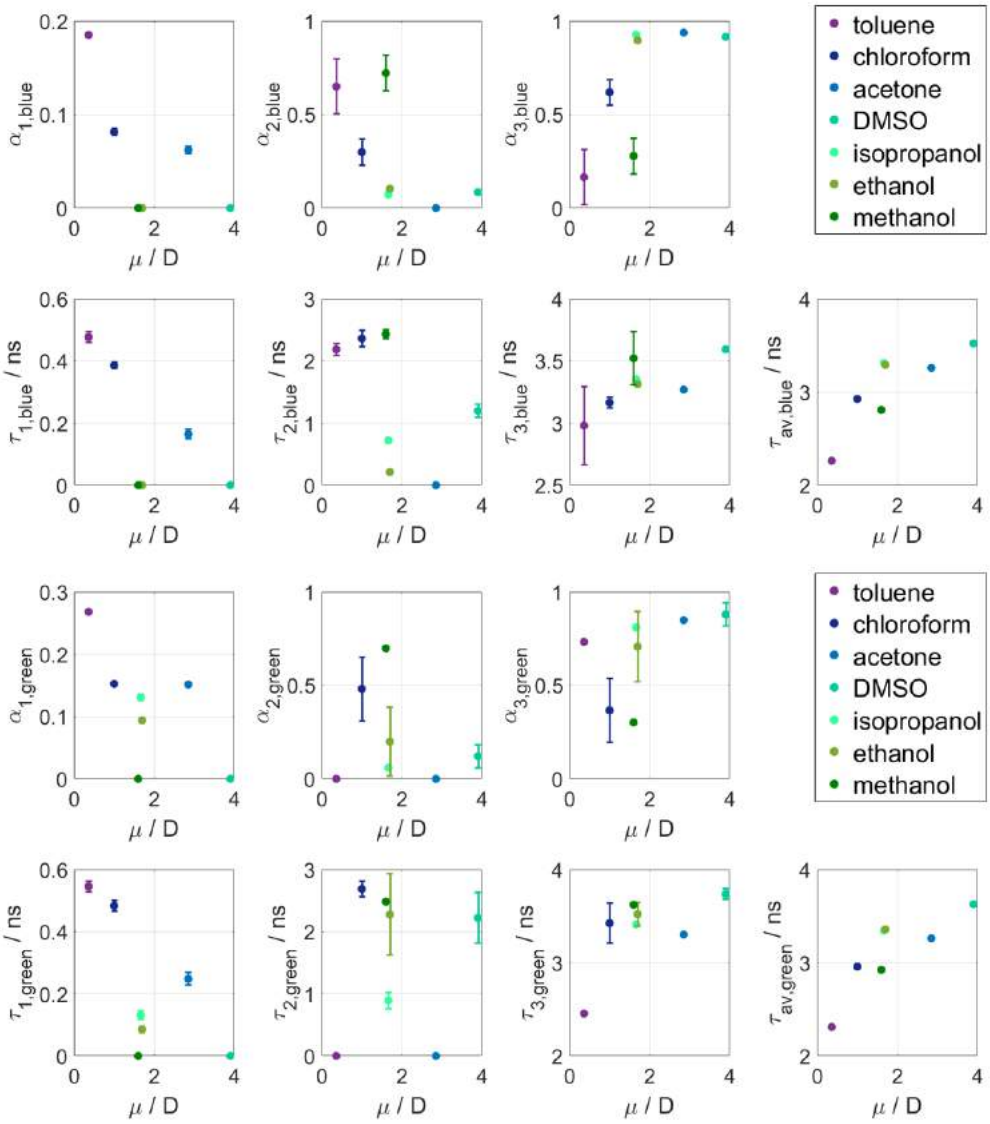

Figure 2.52: Lifetime parameters of laurdan in solution as a function of solvent dipole moment μ. When decays were only fitted to 2 exponential components, the missing parameters were set to 0, with α_1 fixed as the absolute value of the negative amplitude, if present. Error bars represent the range of the obtained parameters (n=3 per condition).

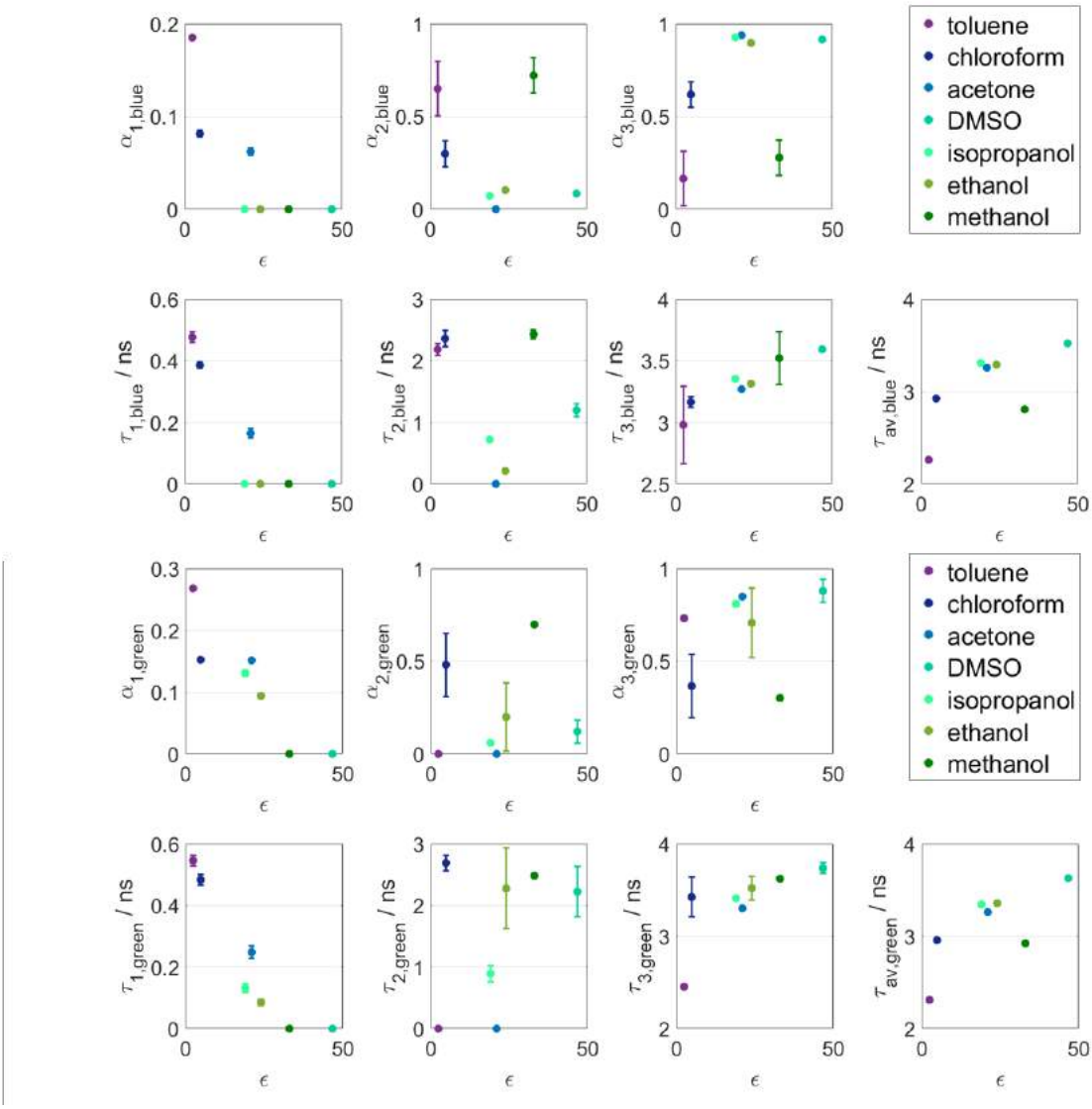

Figure 2.53: Lifetime parameters of laurdan in solution as a function of solvent dielectric constant ϵ. When decays were only fitted to 2 exponential components, the missing parameters were set to 0, with α_1 fixed as the absolute value of the negative amplitude, if present. Error bars represent the range of the obtained parameters (n=3 per condition).

	Blue Channel																							
	-α1	Δα1	τ1 / ns	Δτ1	α2	Δα2	τ2 / ns	Δτ2	α3	Δα3	τ3 / ns	Δτ3	τav / ns	Δτav	χ_r^2		Green Channel											
Toluene	0.185	0.002	0.48	0.04	0.6	0.3	2.2	0.2	0.2	0.3	3.0	0.6	2.26	0.03	1.227		-α1	Δα1	τ1 / ns	Δτ1	α2	Δα2	τ2 / ns	Δτ2	α3	Δα3	τ3 / ns	Δτ3	τav / ns	Δτav	χ_r^2
Chloroform	0.081	0.007	0.39	0.02	0.3	0.1	2.4	0.3	0.6	0.1	3.2	0.1	2.926	0.009	1.205	Toluene	0.268	0.006	0.55	0.03					0.7	0.0	2.5	0.0	2.31	0.03	1.072
Acetone	0.062	0.007	0.16	0.03					0.938	0.007	3.27	0.01	3.26	0.014	1.160	Chloroform	0.152	0.005	0.48	0.04	0.5	0.3	2.7	0.3	0.4	0.3	3.4	0.4	2.96	0.03	1.171
DMSO					0.084	0.004	1.2	0.2	0.916	0.004	3.593	0.005	3.52	0.010	1.166	Acetone	0.151	0.004	0.25	0.04					0.849	0.004	3.30	0.02	3.26	0.03	1.212
Isopropanol					0.072	0.003	0.72	0.06	0.928	0.003	3.354	0.007	3.311	0.009	1.114	DMSO					0.121	0.122	2.2	0.8	0.9	0.1	3.7	0.1	3.63	0.02	1.146
Ethanol					0.103	0.008	0.212	0.007	0.897	0.008	3.314	0.009	3.291	0.008	1.309	Isopropanol	0.131	0.010	0.132	0.03	0.060	0.019	0.9	0.3	0.81	0.03	3.41	0.01	3.35	0.02	1.150
Methanol					0.7	0.2	2.4	0.1	0.3	0.2	3.5	0.4	2.807	0.006	1.190	Ethanol	0.094	0.008	0.085	0.02	0.199	0.369	2	1	0.7	0.4	3.5	0.3	3.358	0.009	1.087
																Methanol					0.7	0.0	2.5	0.0	0.3	0.0	3.6	0.0	2.92	0.01	1.252

Figure 2.54: Summary of fit parameters for laurdan intensity decays in various solvents. The average value and range of each parameter is given.

Chapter 3

Application of multi-dimensional microscopy of laurdan to cell membranes

Research questions

The conclusions from the previous chapter indicate that the chemical nature of the bilayer strongly affects the relationship between membrane micro-environment and order parameters, as detected by multi-dimensional imaging of laurdan fluorescence. It was also shown that this method can inform on the chemical composition of a specific phase, as seen from the experiments in ternary mixtures. The objective in this section is to obtain information on the chemical nature and physical properties of cell membranes, by measuring the same parameters in a bilayer environment of now unknown chemical composition. Several objectives can be proposed:

- One of the interesting questions that this technique could contribute to answering is whether such parameters are determined solely by the chemical composition of the bilayer. In such a case, cell membranes would behave in a similar way to the lipid mixtures studied in the previous chapter, though the larger chemical diversity may elicit less obvious correlations. The other possibility is that extrinsic structural and chemical elements such as the submembrane actin cortex and membrane proteins affect the lipid micro-environment and order parameters, as the "picket-fence" model would suggest, and hence create a different relationship between these parameters than seen previously.

- It is known that different membrane compartments have different chemical compositions, in particular the plasma membrane is known to contain more cholesterol and sphingolipids

than the membranes of intracellular organelles and be generally more ordered. Organelle membranes have varied lipid compositions but are in general less rich in cholesterol and sphingomyelin than the plasma membrane [109]. Using the present method, biophysical differences in the behaviour of plasma and internal membrane material will be sought, and related to current knowledge about their chemical composition.

- The biological context mentioned in the previous chapter has underlined the defining roles of cholesterol and of membrane-cytoskeleton interactions for the lateral organisation of the cytoskeleton. The effect of these two actors of membrane organisation will therefore be studied by modulating their activity on cellular membranes.

3.1 General methods

3.1.1 Cell culture and staining

HeLa cells were seeded on sterile coverslips at the bottom of 6-well plates containing 5 mL of Dulbecco's Modified Eagle's Medium (DMEM) supplemented by 10% Fetal Bovine Serum (FBS) and Penicillin-Streptomycin-Glutamine (PSG), and incubated at 37°C – 5% CO_2 for 24-48 hours. The cells were then rinsed with and incubated for 45 minutes in serum free, high glucose imaging medium (FluoroBrite DMEM) containing 10µM laurdan. Cells were then washed 3 times and imaged in FluoroBrite DMEM in temperature-controlled chambers.

3.1.2 Cell-Derived Vesicles

Upon exposure to sulfhydryl blocking agents, production of vesicles containing plasma membrane material can be induced in many types of adherent cell cultures. This phenomenon and associated protocols were initially characterised in the '70s by Scott and Tank [190, 191, 192, 193], though the underlying mechanisms explaining such vesiculation remain unclear. These vesicles, or Giant Plasma Membrane Vesicles (GPMVs), have been shown to contain exclusively plasma membrane bilayer, and to be free of cytoskeleton [132], which makes them a promising system to isolate the plasma membrane for biophysical studies. GPMVs also display phase separation at low temperatures, an observation which supports the lipid raft hypothesis. In this project, GPMVs will be used as a comparative to live cell experiments, since they offer the possibility to investigate a larger temperature range and contain pure plasma membrane, bearing in mind that the chemical modification of the plasma membrane upon vesiculation may induce significant changes in the observed parameters.

GPMVs were prepared according to a protocol adapted from refs. [131, 133].

Initially, N-ethyl Maleimide was used as a vesiculation agent, since it does not contribute to crosslinking of biomolecules. However, the yield in GPMVs was extremely low using this compound, and it was not possible to perform microscopy reliably. The association of Dithiothreitol (DTT) and Paraformaldehyde (PFA) was therefore preferred. A stock solution of 1M DTT was prepared in pure ethanol. Stock solution of 4% PFA was prepared by adding 4g to 50 mL PBS, which was heated at 60^{o}C to produce a cloudy solution. NaOH drops were added until the solution became clear, and then the pH was adjusted to 7.4, and the volume completed to 100 mL. Both stock solutions were kept at -20^{o}C.

HeLa cells were seeded in 5 cm dishes containing DMEM supplemented with 10% FBS and PSG, and incubated at 37°C, 5% CO2 for 48h. The cells were then washed with PBS, stained with laurdan, washed with GPMV buffer (2 mM $CaCl_2$, 50 mM NaCl, 10 mM HEPES, pH 7.4), and incubated for with 2 mL GPMV buffer containing DTT and PFA at the concentration, temperature and duration stated when relevant.

At this point, GPMVs were visible under brightfield microscopy with a 10x objective (See Fig. 3.1).

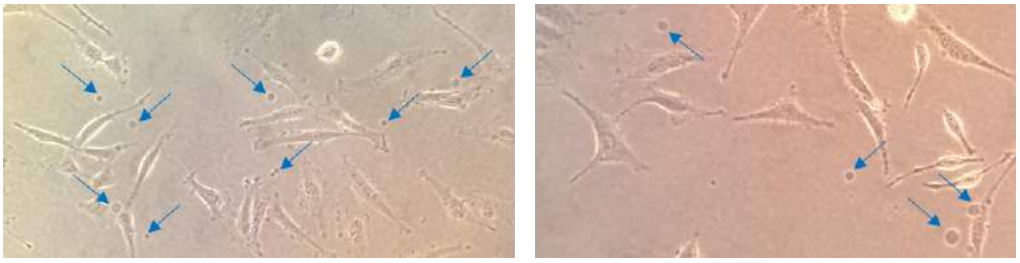

Figure 3.1: Brightfield images of HeLa cells after 1h incubation with vesiculation agents for GPMV extraction (10x phase contrast objective). The arrows point towards some visible GPMVs. The cells appear "grainy', which suggest the presence of many smaller vesicles at their surface. Note that the cells maintain their adherent character and elongated shapes, suggesting that this vesiculation is different from blebbing which occurs when cells become apoptotic.

The GPMV-rich suspension was then harvested and left in a 15 mL tube to sediment at 4°C overnight. The following day, 300 µL of suspension were taken from the bottom of the tube and inserted into the chamber of a temperature-controlled slide. The GPMVs were left to settle on the coverslip for 1h before imaging with confocal microscopy (Fig. 3.2). Unlike GUVs, GPMVs contain membrane glycoproteins and charged membrane-associated molecules, which ensured their immobilisation onto the coverslip surface without the need for suspension into an agarose gel.

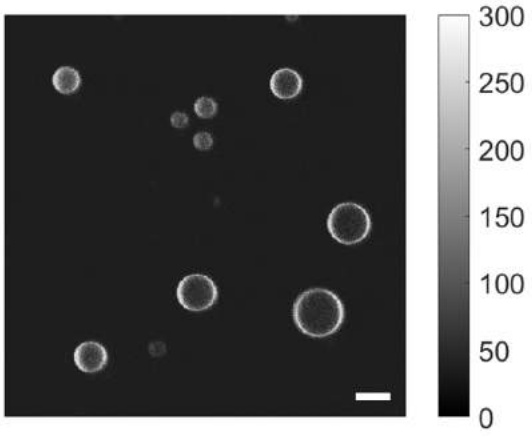

Figure 3.2: Confocal intensity image of GPMVs extracted from HeLa cells and stained with laurdan. Scale bar = $10\,\mu m$.

3.1.3 Imaging

Cells were imaged using the microscope setup described in the previous chapter, with image sizes of 512-by-512 pixels and an ADC resolution of 256 time bins. Image acquisition times were between 120 and 300s, and in general resulted in between 1 and 10 million photon events per image.

GPMVs were imaged in the same way as GUVs before: a single decay was accumulated for each vesicle, with a resolution of 1024 time bins, and temperature was varied from 20 to 50^oC.

3.1.4 Data analysis

3.1.4.1 ROI selection

For GP, fluorescence intensity and anisotropy decay analysis, ROIs were created around each cell, similarly to what was described for phase-separated GUVs, to select plasma membrane and internal membrane regions, as shown in Fig. 3.3. Typically, plasma membrane ROIs allowed intensities of approx. 1000-2000 photons in the maximum bin, while the internal membrane regions contained between 1000 and 10 000 photons. This was sufficient for double-exponential decay fitting.

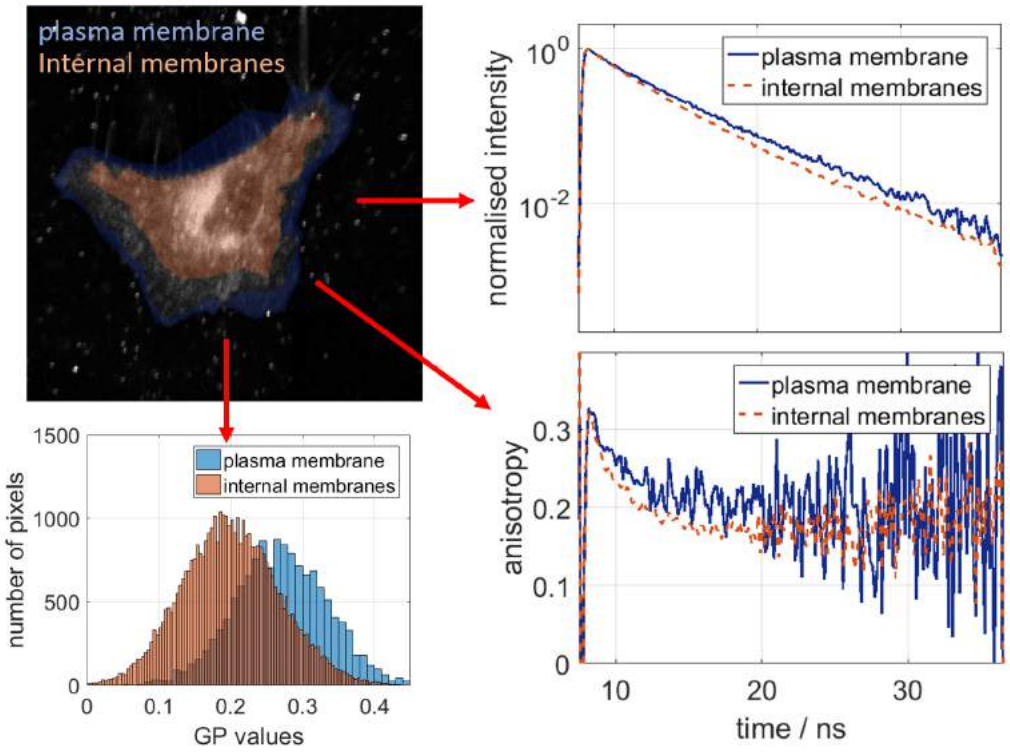

Figure 3.3: ROI selection for the analysis of cell membranes. ROIs are manually defined around plasma and internal membrane regions, and single anisotropy and intensity decays are computed for these regions. GP values are also calculated for all pixels in each ROI.

Single fluorescence decay data was analysed as explained in the previous section. GPMVs being smaller than HeLa cells, total intensities were lower and imaging times, shorter, (5-10 s) due to fast photobleaching of the samples. Total intensities usually did not exceed 1000 counts in the maximum bin.

3.1.4.2 Phasor analysis

Time-resolved fluorescence intensity image data was also analysed using the phasor method, which allowed resolution of the lifetime evolution in the experiments with a collective pixel-wise fashion, rather than binning all pixel information through ROI selection. The mathematical principle of phasor projection was mentioned in the introduction (See Equation 1.49). Here, phasor coordinates were calculated for pixels in all images. A convolution sum filter with a 5-by-5 kernel was applied to the data to reduce the noise of the dataset: each pixel is assigned as new value the sum of the intensities in the 5-by-5 pixel square centered around it. The phasor cloud was fitted to a straight line using a linear regression model ("fitlm" function in Matlab) intersecting the universal circle at two pure single-exponential positions, M1 and M2. The orthogonal projection of each datapoint $\mathcal{D}_i$ on this straight line was then computed; the distance $\mathcal{P}_i$ from M1 to the projection constitutes a single phasor coordinate for each pixel tailored to this particular dataset, which can be used as

a contrast range for phasor images and histograms. The origin was chosen at the long-lifetime intersection, such that low phasor coordinates are indicative of longer lifetimes, and high phasor coordinates, shorter lifetimes. The method is illustrated in Fig. 3.4.

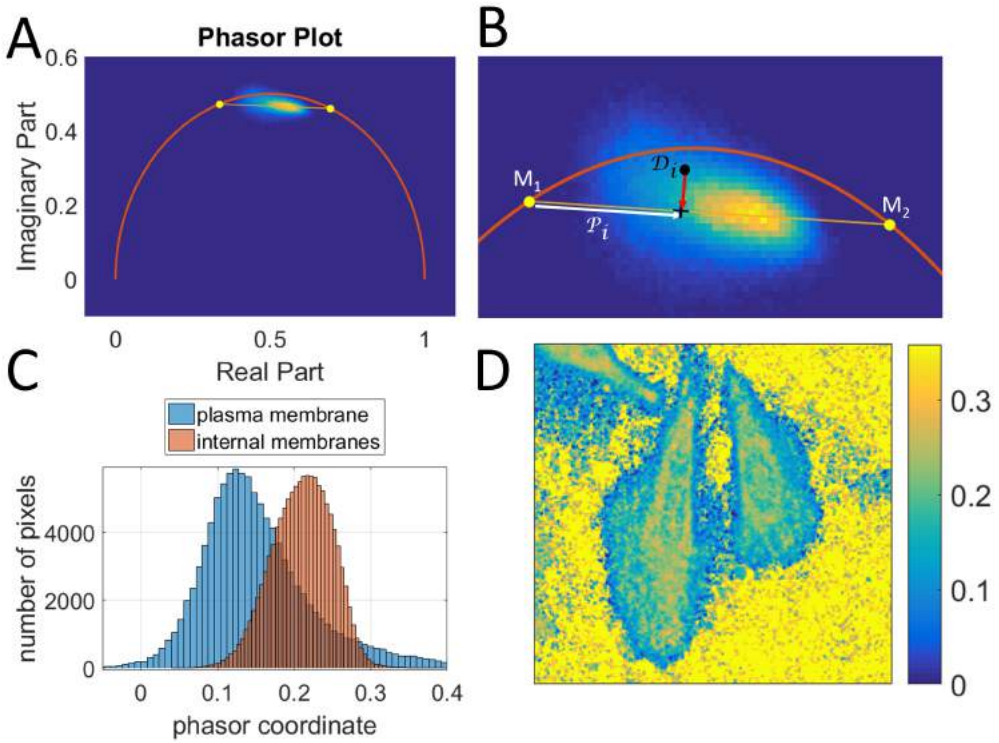

Figure 3.4: Illustration of the phasor analysis method. A: The phasor cloud of the control dataset at a particular temperature is fitted to a straight line. B: Each data point $\mathcal{D}_i$ in phasor space is projected on the segment M_1M_2, where M_1 and M_2 are the intersections between the fit line and the universal circle. The distance $\mathcal{P}_i$ between M_1 and the projection point is used as a single phasor coordinate to build histograms as shown in C, and as a contrast range for phasor images, as shown in D. Note that the background pixels seen in yellow in panel D were not included in the ROIs, and therefore did not contribute to the establishment of the phasor cloud and of the straight line.

Note that this global fitting method was not based on the position in phasor space of laurdan in model membranes as has been done by Owen et al, in ref. [138], which then provides more absolute information on the lifetime values and membrane microenvironment. Here, the idea was to generate the best possible one-dimensional basis on which to project a particular dataset. Phasor analysis includes a normalisation step, which attributes equal importance to all the pixels regardless of their brightness, and the lifetime contrast is resolved from the position of the entire population of pixels in phasor space, offering a fundamentally different approach compared to using ROI selection and decay fitting. Indeed, in low intensity regions such as the plasma membrane, fluorescence signal can easily be contaminated by background fluorescence from cell debris or laurdan particles attached to the coverslip, or by brighter pixels from internal membrane material contained in the ROI.

While great care was taken during ROI selection to avoid this, if such pixels are included in the ROI, this can constitute a significant contamination of the fluorescence signal. Phasor analysis therefore provides a good validation of results obtained through decay fitting. Phasor histograms were computed using the same ROIs as those used for decay fitting to select plasma and internal membrane pixels. Here, phasor fitting was performed in a non-weighted manner, where each pixel is given the same importance. Weighted fitting can be implemented, attributing increased weight to high-intensity pixels for example. Another possibility is to use the local density of data points in phasor space as a weighting factor. This yields a straight line which more closely follows the axis of the phasor cloud, as shown in Fig. 3.5 below. However, density-based weighting was more computationally intensive, and unweighted fits provided a reasonable basis spanning the spread of the data between conditions, and generated good contrast in the phasor images as seen in Fig. 3.4.D, so weights were not included the analysis presented here. If optimal contrast in the data is sought, for example to identify small regions of distinct decay profiles within an image, then such weighting procedures can improve the analysis.

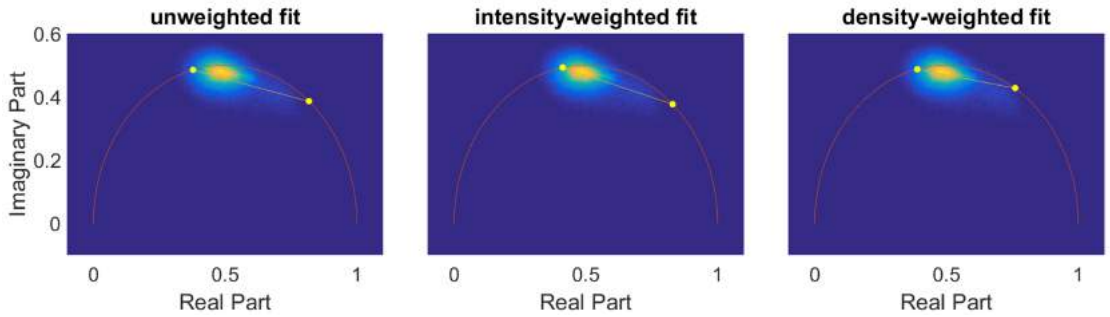

Figure 3.5: Effect of the weighting procedure in phasor fitting. Data represents plasma membrane pixels at room temperature. Left: unweighted fit. Centre: intensity-weighted fit: each data point in phasor space is given a weight equal to the integrated intensity in the corresponding pixel. Right: density-weighted fit: each data point in phasor space is given a weight equal to the number of datapoints within a distance of 0.025 (5% of the radius of the universal circle) in phasor space.

3.2 Correlating micro-environments and order parameters in HeLa cell membranes

3.2.1 Experiments on live cells

3.2.1.1 Relationship between membrane polarity and order parameters in live cell membranes

Boxplots for parameters τ_{av}, θ, Δ' and GP at room temperature (25 ± 1^{o}C) and 37^{o}C are shown in Fig. 3.7 for plasma membranes and in Fig. 3.8 for internal membranes. The range of variation of all parameters is shown in Table 3.1, and representative decays in Fig. 3.6. Temperature causes a

decrease in τ_{av} and GP values in all membranes as expected, as well as a decrease in θ values. The static order parameter Δ' shows more tenuous evolution, with a detectable small positive trend with temperature, though statistical significance was not established.

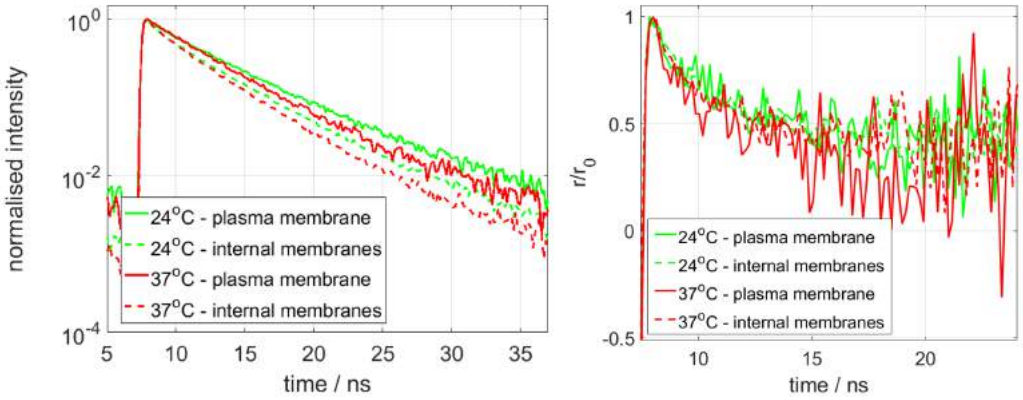

Figure 3.6: Representative normalised intensity (left) and anisotropy (right) decays of laurdan in HeLa cell membranes at 25 and 37°C.

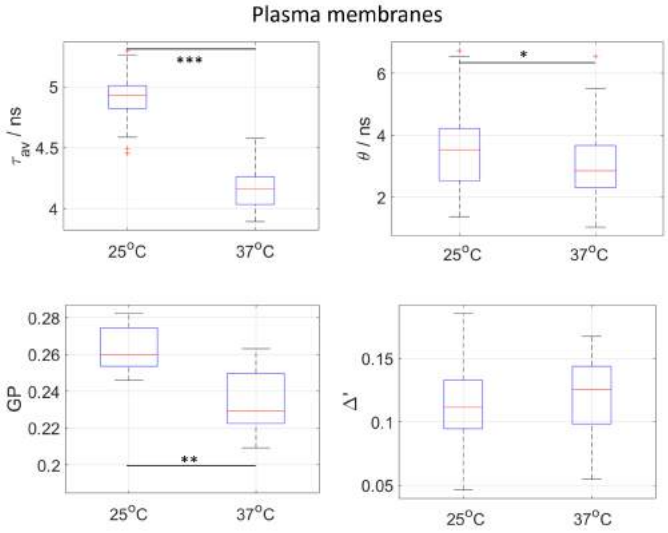

Figure 3.7: Boxplots of membrane parameters τ_{av}, θ, Δ, and GP in plasma membranes of HeLa cells at different temperatures. p-values of 2-tailed t-tests are shown; *: p-value$<$0.05; **: p-value$<$0.01; ***:p-value$<$0.001. Data is the result of a minimum of n=40 cells per temperature, from N=3 independent datasets. GP data is from one of these data sets, with a minimum of n=10.
.

	Plasma membrane	Internal membranes
$\delta\tau_{av}$	16%	14%
$\delta\theta$	15%	21%
$\delta\Delta'$	-6% (ns)	-6% (ns)
δGP	11%	35%

Table 3.1: Ranges of variation between 25 and 37^{o}C for the parameters in HeLa cells.

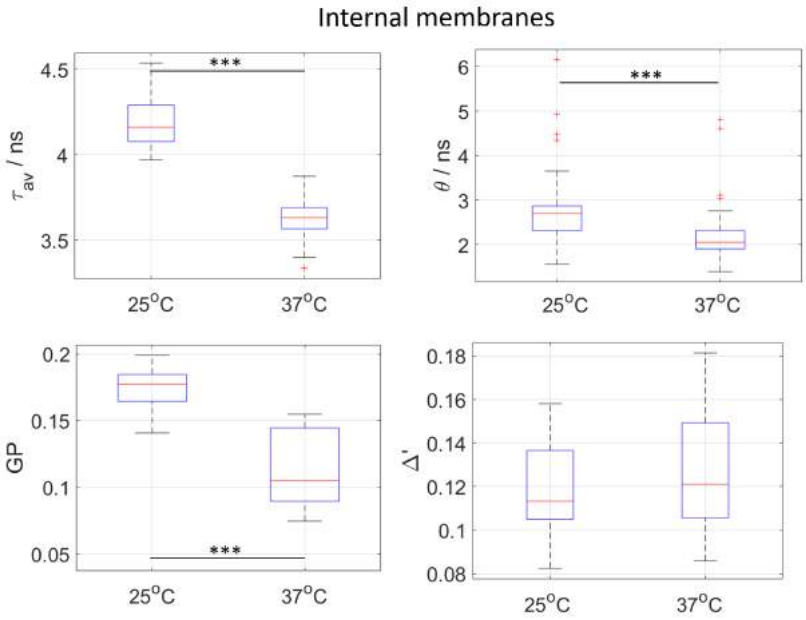

Figure 3.8: Boxplots of membrane parameters τ_{av}, θ, Δ, and GP in internal membranes of HeLa cells at different temperatures. p-values of 2-tailed t-tests are shown; *: p-value$<$0.05; **: p-value$<$0.01; ***: p-value$<$0.001.

While comparison with the behaviour of artificial membranes is of limited significance due to the complexity of the chemical composition of the cell membrane, the hydration and order parameters in cell membranes are within the same range as the systems studied previously, and more interestingly, their evolution with temperature as well, as can be seen in Fig. 3.9. The long lifetimes and high GP values in plasma membranes indicate low hydration, with values intermediate between DPPC:Chol 7:3 and DOPC:Chol 5:5. The order parameters θ and Δ show a similar trend. In internal membranes, the parameters indicate higher hydration and disorder than plasma membranes, as expected, with lower lifetimes, rotational times and GP values. The static order parameter Δ' on the other hand takes similar values in both types of membranes and is poorly sensitive to temperature, with only a 6% increase in internal membranes between 25 and 37^{o}C. This suggests that rotational freedom of fluorophores is not affected by temperature in cellular membranes and is high compared to model bilayers with the same degree of membrane polarity.

Another observation is that while having lower lifetimes, GP and θ values than the plasma

membrane, the internal membranes remain in a parameter space corresponding to a Lo phase in terms of the sensitivity of the τ_{av}-θ relationship. This shows a similar behaviour to that of the plasma membranes, with a shift towards lower lifetimes and rotational correlation times. This is interesting, since these two types of membranes have very different chemical compositions and in general different hydration and order parameters, though show similar temperature-dependent behaviour.

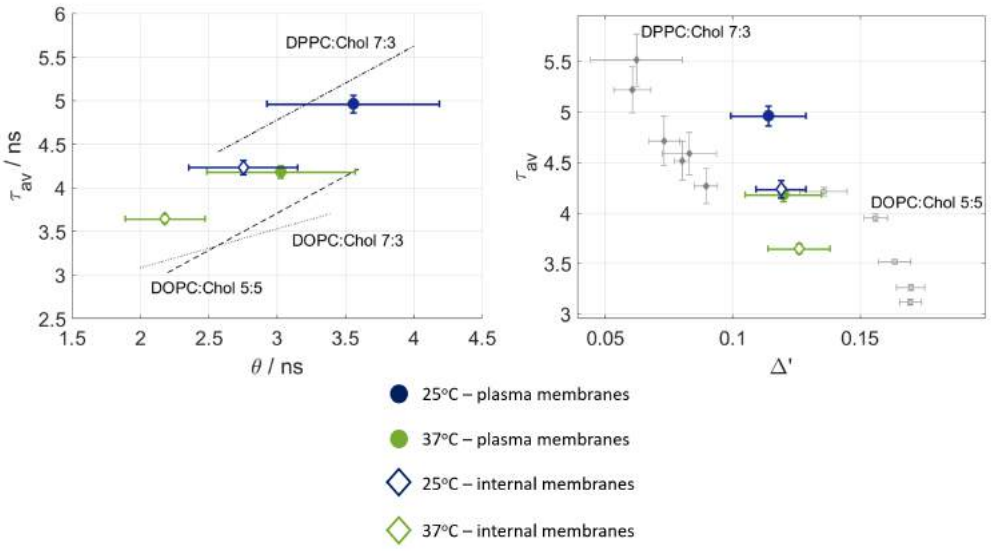

Figure 3.9: Plots showing the correlation between τ_{av} and θ (left) and τ_{av} and Δ (right) of laurdan in HeLa cell plasma (full symbols) and internal (empty symbols) membranes. The linear fits for PC:Chol mixtures from the previous chapters are also shown.

GP images are shown in Fig. 3.10, as well as histograms of all GP values from plasma and internal membrane ROIs as a function of temperature. What is visible here is that the range of variation in internal membranes is greater, with a continuous decrease in GP from 26 to 37^{o}C. GP in the plasma membrane shows a small decrease between 26 and 37^{o}C, suggesting a different temperature sensitivity of membrane hydration as probed by GP in the two membranes. This contrasts with the information from other parameters, which suggest a similar temperature sensitivity in the two types of membranes.

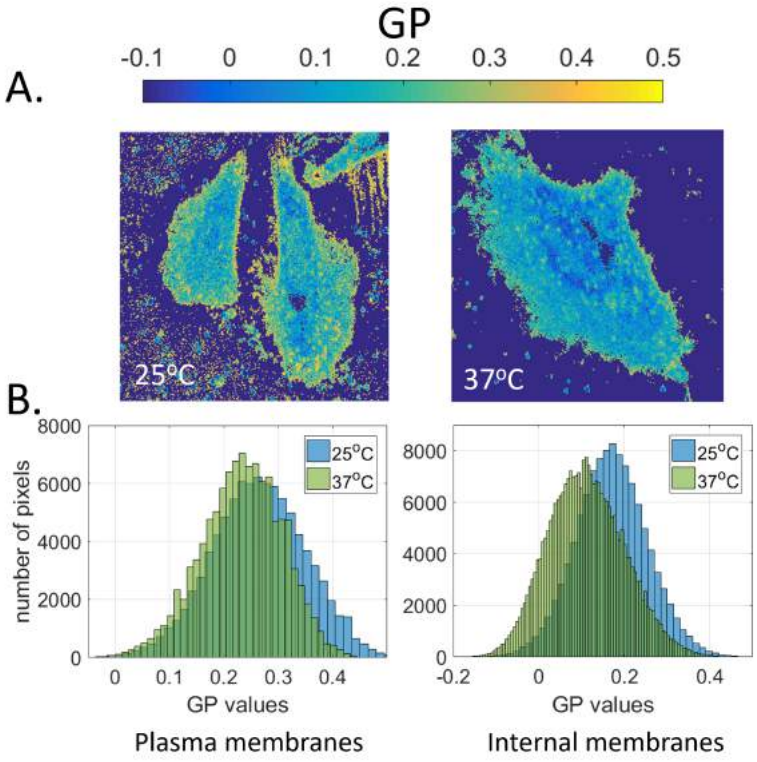

Figure 3.10: GP analysis of HeLa cell membranes as a function of temperature. A.: Examples of GP images at 26 (left) and 37^{o}C (right). Note that the bright background pixels emanating from cell debris were not included in the ROIs, and hence did not contribute to the calculation of average GP values or histograms shown in B (plasma and internal membranes, respectively).

This correlative approach has shown that cellular membranes have hydration and fluidity properties similar to those of a Lo phase, while maintaining lower packing; this may be linked to the greater variety of lipid molecules in plasma membranes and presence of inhomogeneities such as the presence of membrane proteins and the actin cytoskeleton. Membrane polarity and hydration also display differential behaviour, with a higher temperature sensitivity of membrane hydration in internal membranes compared to plasma membranes; this could be linked to the higher cholesterol content in the latter compartment. Meanwhile, membrane polarity shows the same temperature sensitivity in the two types of membranes.

3.2.2 Characterisation of cell-derived vesicles as a model system to study membrane microenvironments and order parameters

Next, membrane micro-environment and order parameters were investigated in GPMVs extracted from HeLa cells. These vesicles contain only plasma membrane material and are devoid of actin cytoskeleton; also, unlike live cells, they can be imaged at temperatures higher than 37^{o}C.

Below 30^{o}C, the vesicles showed two distinct phases on certain vesicles, with one domain dis-

playing lower intensities and lower GP values (see Fig. 3.11). However, the fluorescence intensities were too low to prompt a ROI selection procedure, and since the difference in GP values was small between these two domains, they were treated as single-phase. It is likely that to observe clearer phase separation, the GPMVs should have been cooled to lower temperatures, as also suggested in ref. [131], where GPMVs are cooled well below 20^oC to observe phase separation. GPMVs at low temperatures have been used in many studies to investigate phase behaviour in cell-derived membranes, as well as protein partitioning in the different phases [194, 133]. At higher temperatures, domains were not visible by eye.

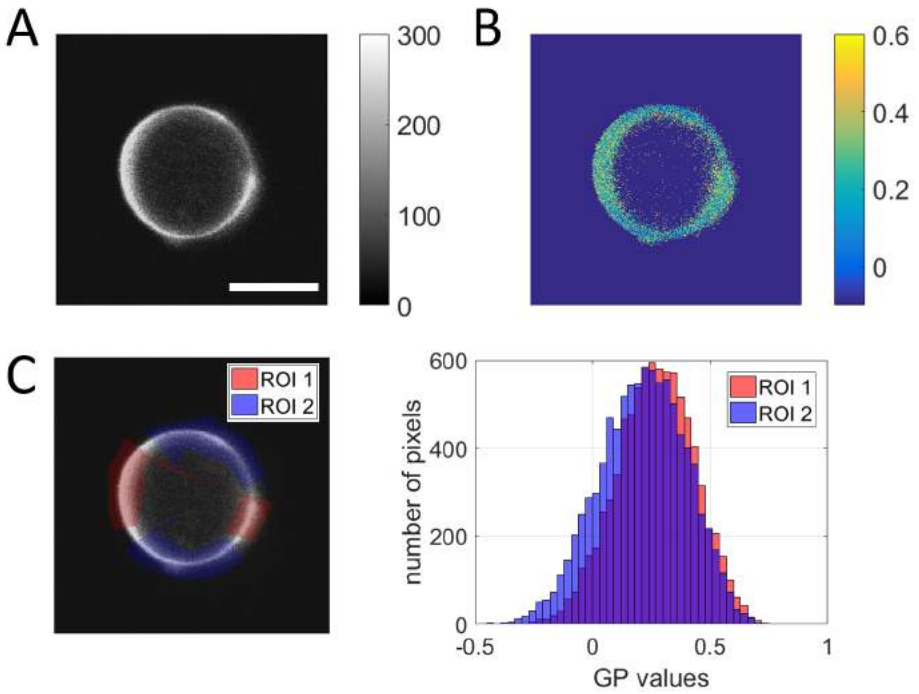

Figure 3.11: Domains at low temperature in GPMVs. A. Intensity image - two domains with different fluorescence intensities are distinguished. B: GP image. C. Manual ROI selection with corresponding GP histograms. Scale bar = $10\mu m$.

3.2.2.1 Studying the effect of vesiculating agent concentration on the characteristics of GPMV membranes

The concentration and type of vesiculating agents affects the characteristics of GPMVs. Indeed, the presence, size and phase mixing temperature in GPMVs have been shown to depend on the chemical compounds used to produce them [194, 133]. According to the literature [131, 133], concentrations in the range of 2-10 mM DTT are appropriate to obtain a high yield of GPMVs while maintaining the cells in a viable state during the vesiculation procedure. It was therefore investigated, whether the concentration of DTT/PFA within this range affected laurdan lifetime,

GP and order parameters. It was found that higher concentrations of vesiculating agents yield longer lifetimes (Fig. 3.12), and higher GP values (Fig. 3.13), which may be due to different membrane species having different susceptibility to vesiculation. Assuming that plasma membranes are heterogeneous at the nanoscale in terms of their lipid composition, it is possible that the more flexible, "fluid" domains of the bilayer containing more unsaturated lipids would more readily detach from the membrane and create GPMVs, and that the more ordered domains containing more cholesterol and saturated lipids would be less likely to vesiculate. Higher concentrations of vesiculating agents would then be required to yield a greater fraction of ordered domains in the GPMVs. This is further supported by the observation that the yield of GPMVs was greatly affected by temperature, with the vesiculating process considerably slowed down at temperatures below 25^{o}C. The present results support this hypothesis, and previous studies [131], also report that the proportion of phase-separated GPMVs was found to be positively correlated to the concentration in DTT.

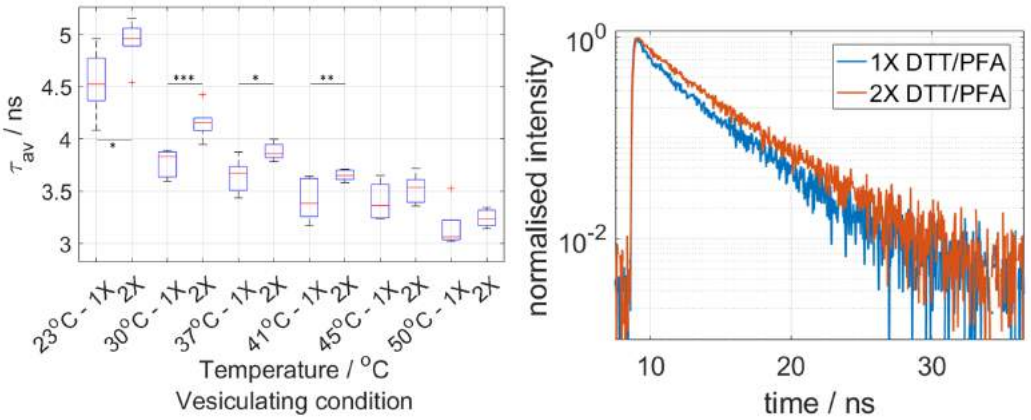

Figure 3.12: Effect of vesiculating agent concentration on laurdan lifetime in GPMVs. Left: Box-plots showing the lifetime of laurdan in GPMVs for two different concentrations of vesiculation agents: 1X = 2 mM DTT / 25 mM PFA, 2X = 4 mM DTT / 50 mM PFA. *: p-value$<$0.05; **: p-value$<$0.01; ***: p-value$<$0.001. Right: Examples of intensity decays at 30^{o}C for these two concentrations. Data is the result of a minimum of 5 GPMVs per condition with a minimum of 37 GPMVs per condition.

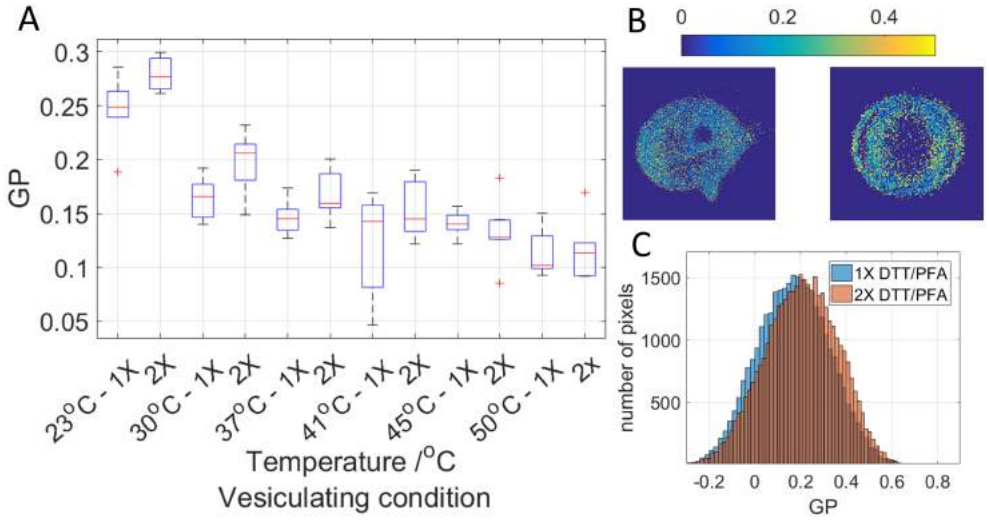

Figure 3.13: Effect of vesiculating agent concentration on laurdan GP in GPMVs. A: Boxplots showing the GP of laurdan in GPMVs for two different concentrations of vesiculation agents: 1X = 2 mM DTT / 25mM PFA, 2X = 4 mM DTT / 50 mM PFA. B: Examples of GPMV GP images at 30^{o}C for these two concentrations. C: Histograms of GP values for all images at 30^{o}C.

Order parameters θ and Δ' offer a less obvious relation with vesiculant concentration as shown in Fig. 3.14, with no statistical difference in behaviour between the two treatments. Lower resolution in these parameters is likely due to the lower intensities in GPMVs related to their small size and high photobleaching of laurdan. At 23^{o}C, the values of θ (significant) and Δ' (non-significant) are lower at the higher concentration of vesiculants. At low temperatures, the behaviour of the system is likely different due to the fact phase separation was observed in all vesicles. At higher temperatures, an overall trend could be identified with generally higher θ values at higher concentrations of vesiculating agents. However, the differences between the two conditions were only significant at 1 temperature point (37^{o}C), so in general the order parameters did not show a clear dependence to the vesiculating condition, unlike the membrane micro-environment parameters τ and GP.

In conclusion, these experiments shows that the concentration of vesiculating agents affects the fluorescence signal of laurdan in GPMVs. This could be linked to different chemical species in the membrane having different likelihood of partitioning into GPMV, or to the direct effect of the vesiculating agents themselves on the membrane.

3.2.2.2 Membrane microenvironment and order parameters in GPMVs

The temperature evolution of the membrane polarity and order parameters in GPMVs was investigated in comparison to live plasma membranes using a concentration of 4 mM DTT and 25 mM PFA, as shown in boxplots Fig. 3.15 and representative decays Fig. 3.16. These concentrations in vesiculants resulted in lifetime values close to those of live cell membranes (~5 ns at room tem-

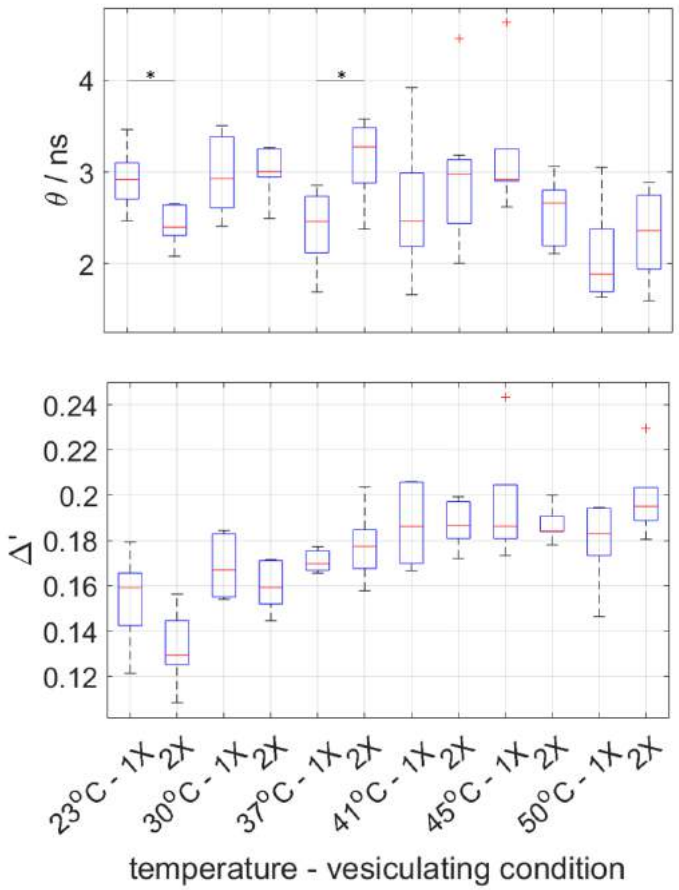

Figure 3.14: Boxplots showing the values of order parameters θ and Δ for two concentrations in vesiculating agents. 1X, 2X and p-values are as described previously.

perature), and so it was assumed that their lipid content was somewhat representative of the cell membrane. All parameters show the usual trend with temperature (as seen also in the previous subsection), suggesting higher hydration and lower order at higher temperatures. The dynamic order parameter θ increased at low temperatures between 22 and 30^{o}C, and then decreased again at higher temperatures. At the same time, the static order parameter Δ' increases strongly between 24 and 30^{o}C before showing a more moderate increase at higher temperatures. Here, it is possible that a large increase in Δ' may yield a simultaneous increase in θ, as was seen in DPPC at higher temperatures. This can be related to the fact that GPMVs are phase separated at low temperatures, and it is possible that at least part of the bilayer is in a highly ordered state, which would explain the present results. In general, the fluorescence intensity was higher in the more ordered regions of phase-separated vesicles; this was the case for GUVs as well as GPMVs (See Figs. 2.43 and 3.11) and also observed by Amaro et al. [121]. This would then cause laurdan fluorescence from the more ordered domains to dominate the signal, and therefore impact the lifetime and order parameters more significantly than that of the more disordered domain.

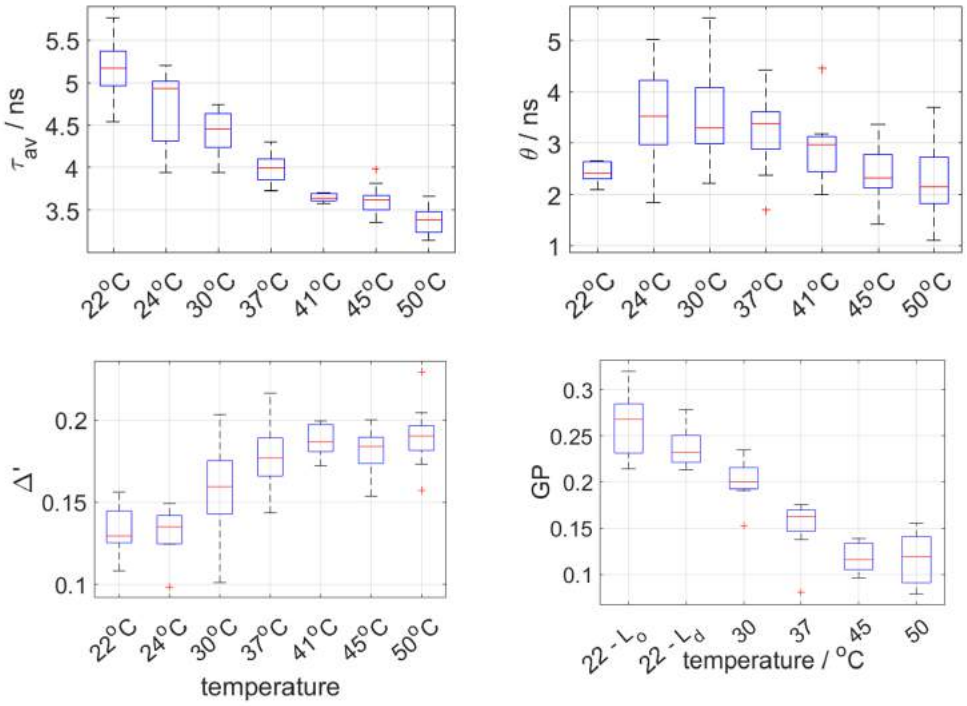

Figure 3.15: Boxplots showing the temperature evolution of parameters τ_{av}, θ, Δ, and GP in GPMVs. Data for time-resolved parameters is the result of N=2 independent experiments with a minimum of n=10 GPMVs per temperature. Data for GP is from one of these experiments.

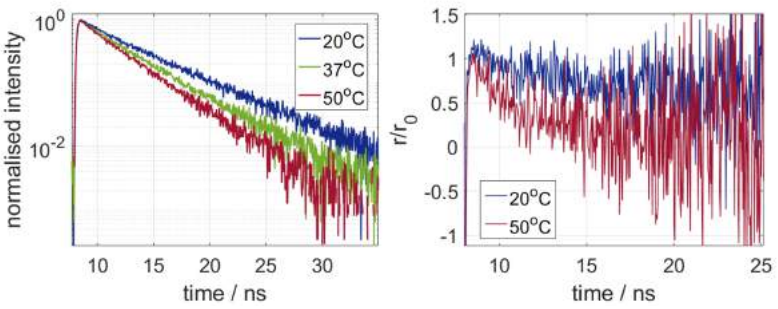

Figure 3.16: Examples of intensity (left) and normalised anisotropy (right) decays as a function of temperature in GPMVs. Only 2 temperatures are represented for clarity in the case of anisotropy decays.

The GP values show a large dynamic range, with continuous decrease and values situated between those of internal and plasma membranes. Examples of GP images and GP histograms are shown in Fig. 3.17.

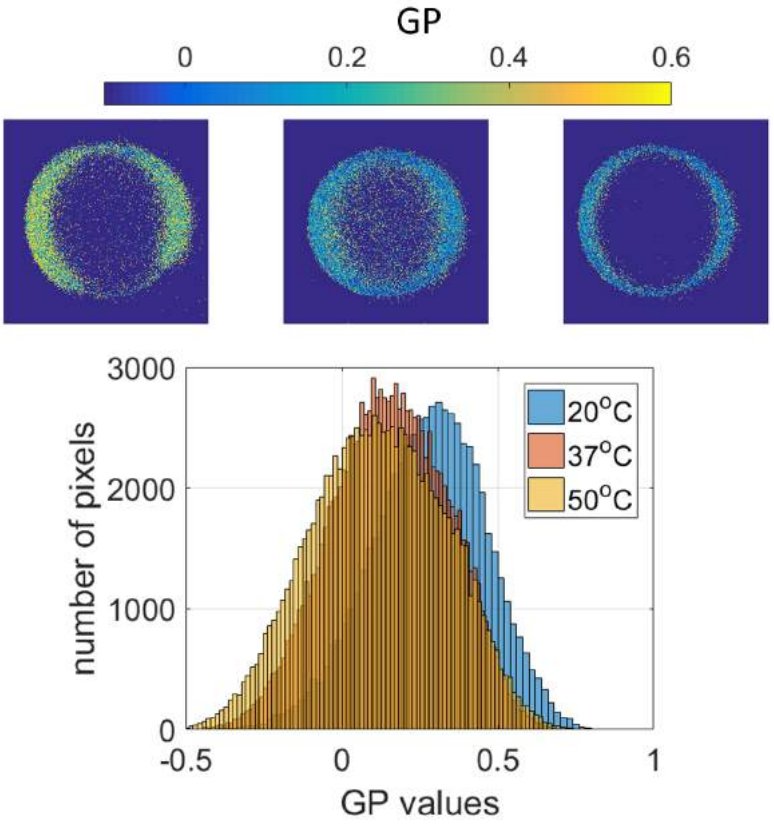

Figure 3.17: GP analysis of GPMVs. Images at 20 (left), 37 (middle) and 50^{o}C are shown, as well as the GP histograms at these temperatures. The histograms were computed from all images at each temperature.

3.2.2.3 Comparison of laurdan fluorescence in GPMVs and live cells

The correlations between the polarity and order parameters are shown in Fig. 3.18 and compared to those obtained in live cell membranes. It appears that the lifetime and dynamic order parameters

	τ_{av} against θ	τ_{av} against Δ'
Intercept	1.4 ± 0.6 ns	8.3 ± 0.5 ns
Gradient	0.8 ± 0.2	-25 ± 3 ns
p-value	*	***
R^2_{adj}	0.78	0.91

Table 3.2: Linear fit parameters for GPMVs. Note that for the fit of θ against τ, the data point at 20°C was not included.

are similar in both systems, while the static order parameter shows a clear linear positive evolution with temperature not observed in live cell membranes, with generally higher values.

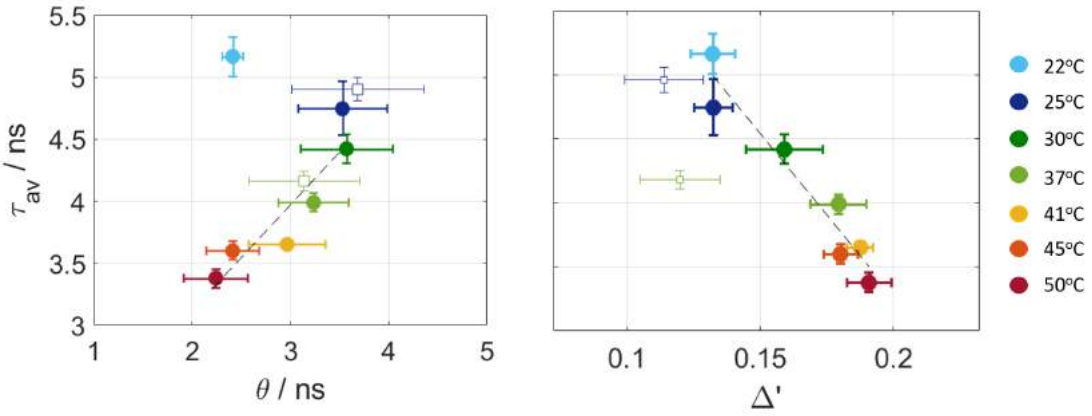

Figure 3.18: Correlation between lifetime τ and order parameters θ and Δ in GPMVs (circles) with corresponding linear fits. Results in cell plasma (squares) membranes from the previous section are also shown.

Overall, GPMV bilayers display a linear relationship between lifetime and order parameters, as illustrated in Fig. 3.18 with the fit parameters shown in Table 3.2.

These parameters are consistent with those of a Lo phase, with a gradient and intercept close to that of DPPC:Chol 7:3 mixtures for the relationship between τ and θ (see table 2.9 from the previous chapter).

These results support the data from live cell experiments showing that the plasma membrane overall behaves like a Lo phase in terms of membrane polarity and order parameters. However, the anomalously high static order parameter values points towards the fact that GPMVs are not fully representative of an unperturbed plasma membrane bilayer. This may be due to the absence of the actin cytoskeleton in GPMVs and reveal its role in controlling the properties of the plasma membrane, but a significant effect of vesiculating agent concentration on the chemical composition of GPMVs, and/or a direct effect of these compounds on the bilayer should not be excluded and prevents absolute conclusions on this point. This question will be further addressed by disrupting the cytoskeleton in live cells.

3.2.3 Effect of the actin cytoskeleton on membrane microenvironments and order parameters

As shown in the previous chapter, the actin cytoskeleton has a crucial role in organising the plasma membrane through its interaction with membrane associated proteins, and studies mentioned earlier have shown that actin networks interacting with membrane elements (lipids or proteins) maintain the lateral heterogeneity of membrane lipids at the nanoscale [125]. The hypothesis here is that since the cytoskeleton meshwork interacts with the membrane on a spatial scale largely exceeding the size of a single lipid molecule, its effect on our measured parameters (rotational diffusion of lipids and microenvironment) would be limited. To test this hypothesis, the experiments on GPMVs aimed to obtain cytoskeleton-free membrane fractions suitable for microscopy, however our results suggest that the modalities of GPMV production significantly affects their composition and behaviour. Therefore, live cells were treated with cytochalasin D, which inhibits actin polymerisation, to disrupt the effect of the submembrane actin cortex on the lateral organisation of the plasma membrane. This offered another way of quantifying the role of the cytoskeleton on the biophysical properties of the plasma membrane. In previous studies, Roess et al [195] have measured an increase in the rate of rotational diffusion of a membrane protein using phosphorescence anisotropy upon cytochalasin D treatment. Using FRAP, Kwik et al [196] have shown that there is an interplay between membrane cholesterol and actin cytoskeleton which controls the lateral diffusion of membrane proteins. Here, the objective is to determine whether the actin cytoskeleton also affects the polarity and order parameters of the cell membrane, at the scale of the lipid themselves.

Ref. [197] was used for the cytochalasin D treatment protocol. A 1 mg/mL stock solution of cytochalasin D was constituted in DMSO and kept at -20^{o}C. Cells were cultured and stained with laurdan as stated above, and imaged in a temperature-controlled slide which contained 300μL FluoroBrite DMEM complemented with 10 μM of cytochalasin D. Treatment with cytochalasin D causes changes in cell morphology (See Fig. 3.19), so it is important to image rapidly after treatment to ensure physiologically relevant data. Cells were incubated for 10 min in the presence of cytochalasin, and imaged immediately, at room temperature or 37^{o}C. Care was taken so that the imaging process would be finished within 45 minutes of the introduction of cytochalasin D.

Treatment with cytochalasin D was not found to affect the lifetime of laurdan in the plasma membranes at either of the temperatures probed (no significant differences to a 5% confidence between 10 μM cytochalasin D treatment and same-day control - see Fig. 3.20). GP values were not significantly different between the two treatments either (Fig. 3.21), though at both temperatures the GP is slightly higher on average. In internal membranes, the lifetime is also slightly higher at 37^{o}C, with a significant increase of 2.7% in lifetime upon exposure to cytochalasin

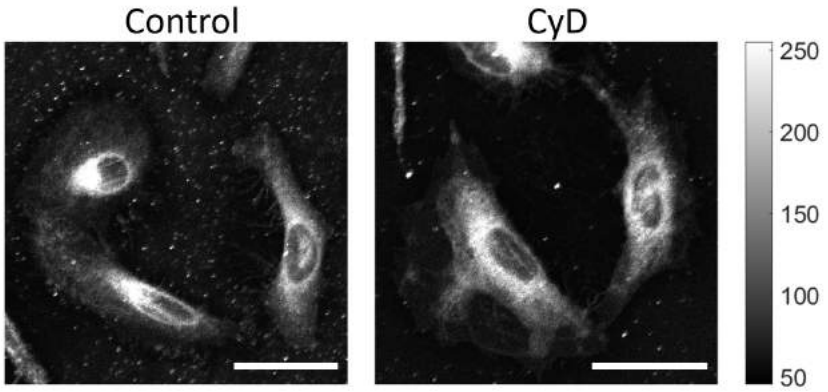

Figure 3.19: Images of HeLa cells stained with laurdan and treated with Cytochalasin D (right) compared to untreated cells (left). Scale bar is 50 μm.

D (p-value$<$0.001). Apart from this case, the absence of statistically significant differences between the control and cytoskeleton disrupted sample for GP and τ suggests that the actin cytoskeleton does not contribute significantly to maintaining membrane polarity, and that this is rather an intrinsic property of the lipid bilayer. It is possible that a larger dataset would enable the detection of slighter differences between the two conditions. However, the fact that this method was able to identify a 2.7% increase in lifetimes between the two conditions in the internal membrane material with high statistical significance provides some validation of the strength of the method.

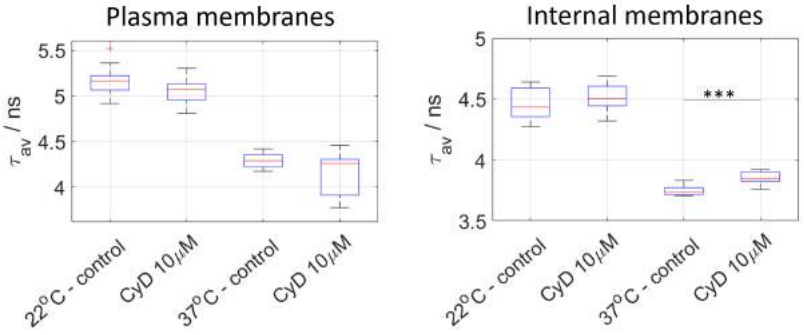

Figure 3.20: Lifetime analysis of laurdan upon cytoskeleton disruption. Left: lifetimes in plasma membranes. Right: in internal membranes. Data is the result of a minimum of n=10 cells per treatment, with a total of 55 cells imaged.

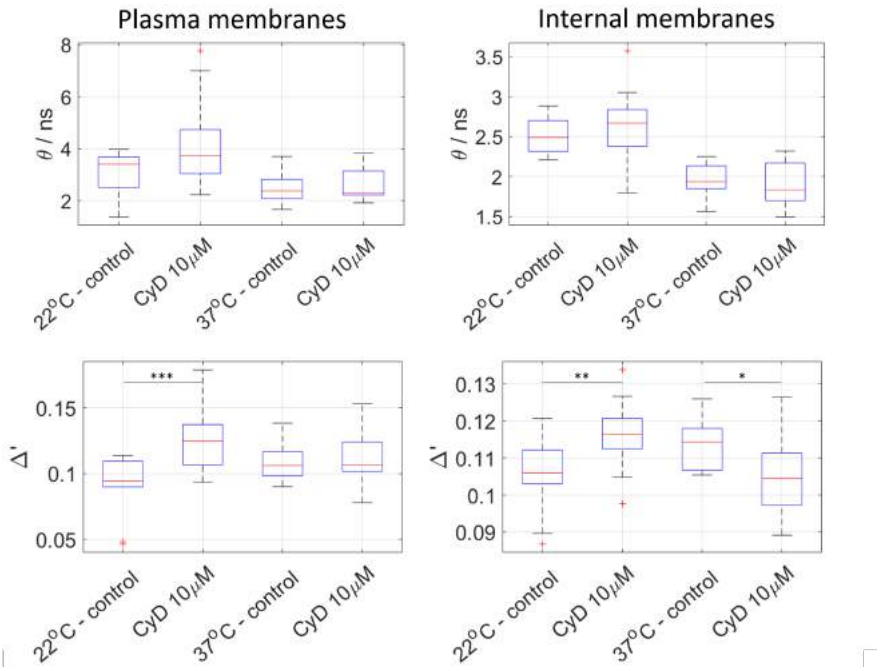

Figure 3.22: Boxplots showing the order parameters in plasma and internal membranes of HeLa cells treated with Cytochalasin D. ***: p-value<0.001; **: p-value<0.01; *: p-value<0.05.

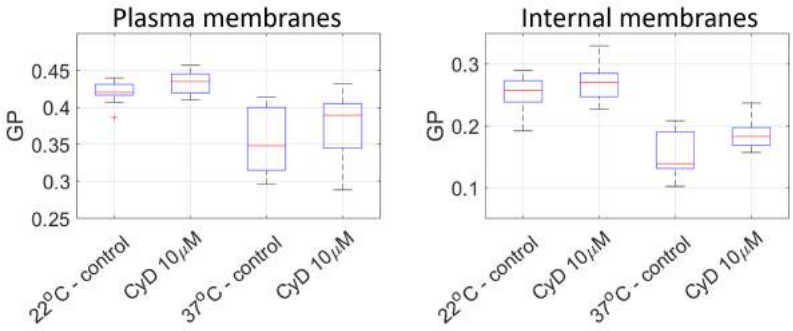

Figure 3.21: Boxplots showing GP values for plasma (left) and internal (right) membranes of control and cytochalasin D-treated cells.

The order parameters obtained upon cytochalasin D treatment are shown in Fig. 3.22. There was no statistical difference in the dynamic order parameter θ between the two situations in either plasma membranes or internal membranes at both temperatures; however, the static parameter Δ' increases significantly in both types of membranes at room temperature (37 and 10%, respectively). At 37^{o}C, no difference was observed in the plasma membranes, while a significant decrease in Δ' (8%) was observed in internal membranes.

The data from this section suggests that the actin cytoskeleton has little effect on membrane polarity, while it may contribute to reducing the rotational mobility of lipid molecules in cellular membranes, as seen by the increase in Δ' upon treatment with cytochalasin D. However, this effect is only seen at low temperatures, while at physiological temperature, no effect was de-

tected in the plasma membrane, and a small decrease in Δ' was detected in internal membranes. This last observation is consistent with the increase in lifetimes detected in the sample, indicating lower polarity and rotational freedom, respectively. The cytoskeleton does not interact with lipid molecules directly in the plasma membrane, but its interaction with membrane-associated proteins is thought to constitute diffusion barriers in the plasma membrane, and contribute to lower translational diffusion. Here, our results suggest that these diffusion barriers may also affect the rotational freedom of membrane molecules, possibly by maintaining lateral heterogeneity of the lipid the composition at nanoscale. This is consistent with the results obtained on GPMVs, where Δ' was higher than in the plasma membrane of live cells. Higher spatial resolution on the order parameters would be required to fully understand the intracellular effect of cytochalasin D treatment on organelle membranes, however, the fact that a correlated increase in τ and Δ' was observed at 37^{o}C suggests a modification of membrane microenvironments as well as its diffusion properties. In general, the small modification of the parameters studied here shows that temperature has a much stronger effect on plasma membrane hydration, polarity, and order parameters, than the cytoskeleton, confirming the hypothesis formulated earlier in this section. However, the observed increase in rotational diffusion corroborates previous observations of increased rotational motion of membrane proteins by Roess et al. [195], this time on the membrane lipids themselves.

3.3 Investigating the dynamics of cholesterol in cell membranes

Cholesterol is a major modulator of membrane microenvironments and order parameters, as the previous chapter has already underlined. Eukaryotic cells synthesize their own cholesterol and also receive it from the environment through Low Density Lipoprotein (LDL)-mediated transport uptake. Intracellular cholesterol trafficking is thought to take place via vesicular and non-vesicular trafficking, with possible involvement of membrane contacts in transferring cholesterol from one organelle to another [198, 199]. Cholesterol content was also shown to be regulated through a plasma membrane-bound transcription factor pathway by Brown and Goldstein [200, 201]. The turnover of cholesterol in membranes is high, and cells constantly lose and replenish the plasma membrane cholesterol. Using fluorescence microscopy, Hao et al. [151] observed macro-scale phase separation in the plasma membranes upon cholesterol depletion, which disappeared upon cholesterol repletion. Nishimura et al. also observe the establishment of gel phases in the plasma membrane upon cholesterol depletion, as evidenced by slower translational diffusion of membrane proteins [197]. In general, many biophysical studies have used cholesterol depletion as a convenient method to provoke changes in plasma membrane structure [169, 185, 138], and modification of the diffusional

properties of a membrane protein upon cholesterol depletion are interpreted as a sign of its localisation in rafts. However, the spatio-temporal dynamics of cholesterol localisation and production in the plasma membrane and within the cell remain less well elucidated. Using biochemical methods, Mahammad et al [202, 203] have established that cholesterol content is rapidly replenished (<1h) through intracellular production upon its depletion, pointing towards highly reactive pathways. The idea here is to resolve the effect of modulating cholesterol content in cells on membrane micro-environment and order parameters, at the cell membrane and in intracellular compartments. Cholesterol depletion experiments were therefore carried out, and the lifetime, GP and anisotropy parameters measured.

Cholesterol can be removed from cellular membranes using methyl-β-cyclodextrin, a water-soluble, ring-shaped oligosaccharide presenting a hydrophobic pocket into which lipids can enter. mβcd is large and does not penetrate into the cell, it therefore only depletes cholesterol through extraction from the plasma membrane, though since cholesterol trafficking in cells has been shown to be highly dynamic, intracellular compartments are rapidly depleted as well. The concentration and incubation times with mβcd used in other studies was reviewed, as summarised in the following table:

ref.	Incubation time	mβcd concentration
Nishimura et al. [197]	20-120 min	10 mM
Ilangumaran et al. [204]	30 min	2.5-20 mM
Kabouridis et al. [205]	5-120 min	10-15 mM
Hao et al. [151]	1h	10 mM

Table 3.3: Cholesterol depletion experiments in the literature.

For the present experiments, the objective is to study the biophysical properties of cell membranes in a physiological state, while modulating the cholesterol content, so the presence of distinct domains in the membrane was deemed undesirable. Moreover, the studies stated above where incubation times were varied showed strong variation of the studied physical and biochemical observables (decrease in diffusion coefficients [197], tyrosine kinase phosphorylation [205], release of membrane proteins in the supernatant [204]) already at short incubation times (below 30 minutes). Mahammad et al. also show that cholesterol extraction reaches a steady state before 30 minutes in Jurkat T Cells, with a stabilisation in the % extracted cholesterol [203, 202]. It was therefore assumed that if cells are depleted with cholesterol for short times, the integrity of the membrane would not be perturbed enough to cause large-scale phase separation, while provoking a significant enough modification to yield modifications of its physical properties.

After staining with laurdan as described above, cells were incubated with 7 mM cyclodextrin for 20 minutes. The cells were then rinsed 3 times and treated for GPMV extraction or imaged live immediately, as required.

3.3.1 Experiments on live cells

3.3.1.1 Plasma membranes

Fluorescence lifetime and anisotropy parameters were calculated for plasma and internal membrane regions for control and cholesterol-depleted cells. Boxplots for parameters τ_{av} of control and cholesterol-depleted cells in plasma and internal membranes are shown in Fig. 3.23. The first observation is that in plasma membranes, the lifetime of laurdan increases with cholesterol depletion, with high statistical significance at both temperatures (6 and 7.6% increases, respectively). Phasor analysis largely confirms the results obtained through parametric fitting, with the plasma membranes exhibiting lower phasor coordinates (i.e., longer lifetimes) when treated with mβcd. The displacement of the phasor cloud for plasma membrane pixels upon cholesterol depletion is illustrated in Fig. 3.24 (for room temperature only - similar cloud profiles were obtained at 37^{o}C). The histograms for phasor coordinates are shown in Fig. 3.25. Note that upon cholesterol depletion, the shape of the phasor cloud is also modified, and closely follows the universal circle. Since laurdan emission is multi-exponential even in homogeneous lipid mixtures, as seen from the previous chapter, this position on the universal circle is unlikely to reflect single-exponential behaviour. On the other hand, it is compatible with the presence of excited-state reactions leading to decay components with negative amplitudes, also discussed previously.

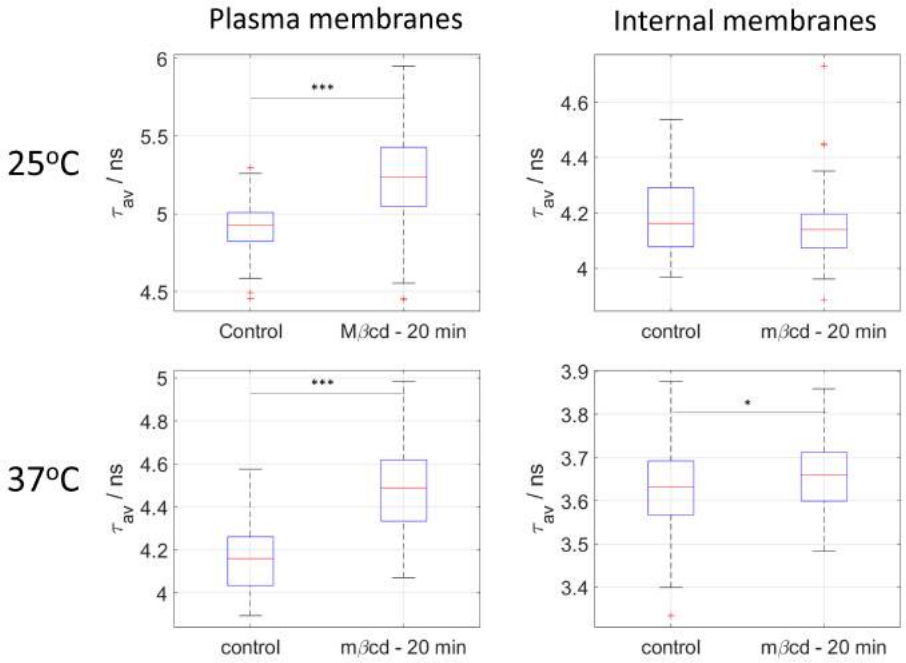

Figure 3.23: Boxplots showing the average lifetime of laurdan in plasma (left) and internal (right) membranes for control and cholesterol depleted cells at 25^{o}C (upper row) and 37^{o}C (lower row). Data is the result of N=2 independent experiments, with a minimum of n=31 cells imaged per condition. Results of 2-tailed t-tests are shown; *=p-value$<$0.05, **=p-value$<$0.01, ***=p-value$<$0.001. Analysis of each same-day dataset separately yields similar types of results.

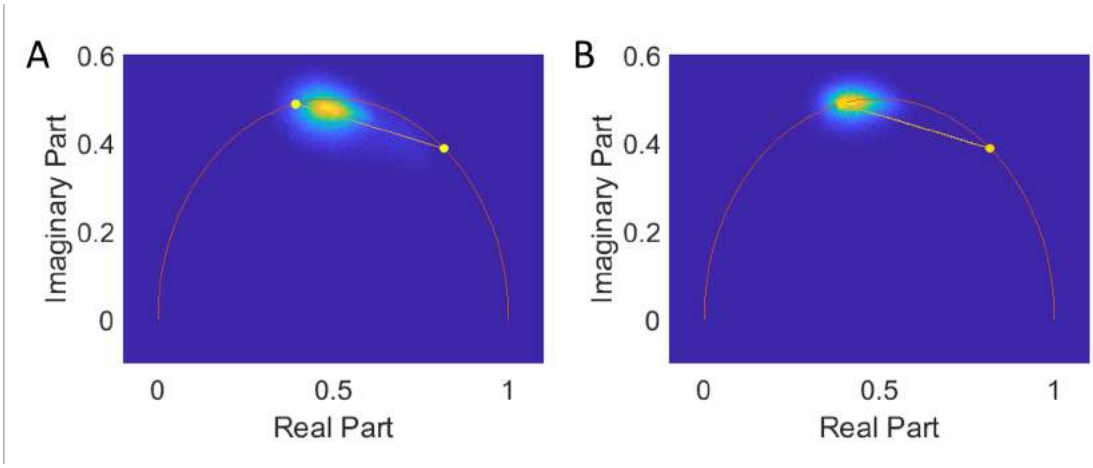

Figure 3.24: Phasor clouds of plasma membrane pixels in control (left) and cholesterol-depleted (right) cells, at 25°C. The yellow line was obtained by fitting all pixels (plasma and internal membranes) from the control dataset.

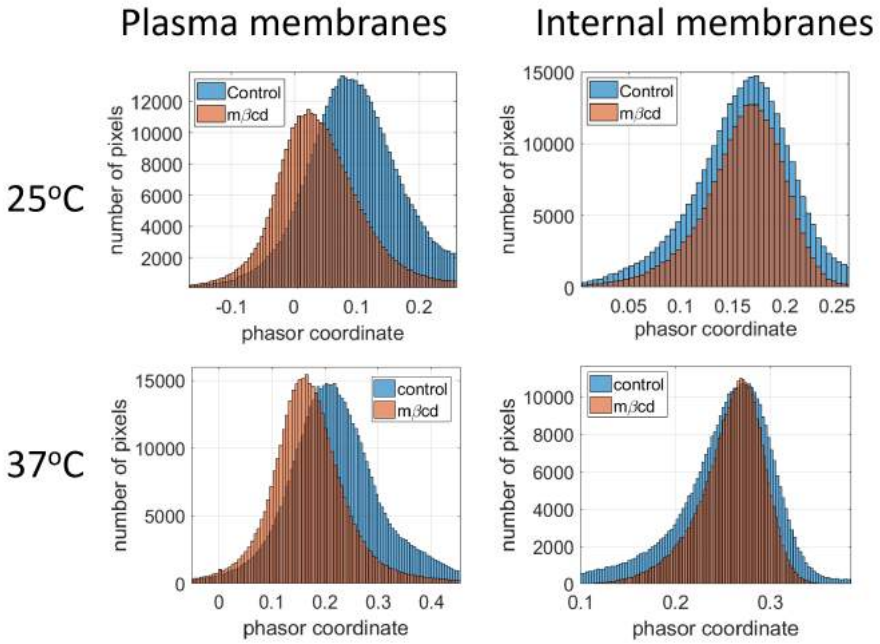

Figure 3.25: Phasor histograms of control and cholesterol-depleted cells at 26°C (above) and 37°C (below) in plasma (left) and internal (right) membranes. Phasor projection was done on same data as the one used for the fitting from Fig. 3.23: N=2 independent experiments, with a minimum of n=31 cells imaged per condition.

Simultaneously, there is little evolution of the GP values in plasma membranes upon cholesterol depletion, as seen from the GP histograms shown in Fig. 3.27. A small negative trend can be identified, with a 9% decrease at 25°C and 4.5% at 37°C. This would suggest that cholesterol depletion increases the hydration of the bilayer as probed by GP, as well as the dipolar strength of the membrane as probed by laurdan lifetime, though this effect is limited. In control cells and model membranes, longer lifetimes are correlated with higher GP values (see for example Fig. 2.46

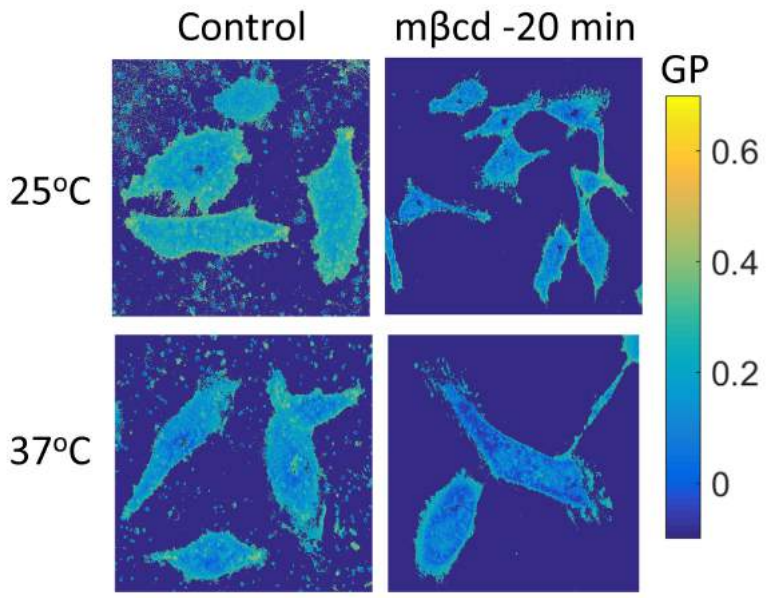

Figure 3.26: GP images of HeLa cells upon cholesterol depletion.

or 2.31), which is not observed here - which suggest that GP and lifetimes do not sense the same aspects of dipolar relaxation effects present in the lipid bilayer, as also suggested by Golfetto et al. [169]. It should also be noted that in GUV experiments, there was little difference between GP values in DPPC, DPPC:Chol 9:1 and DPPC:Chol 7:3 at room temperatures, suggesting that GP may not report on cholesterol content in highly ordered environments.

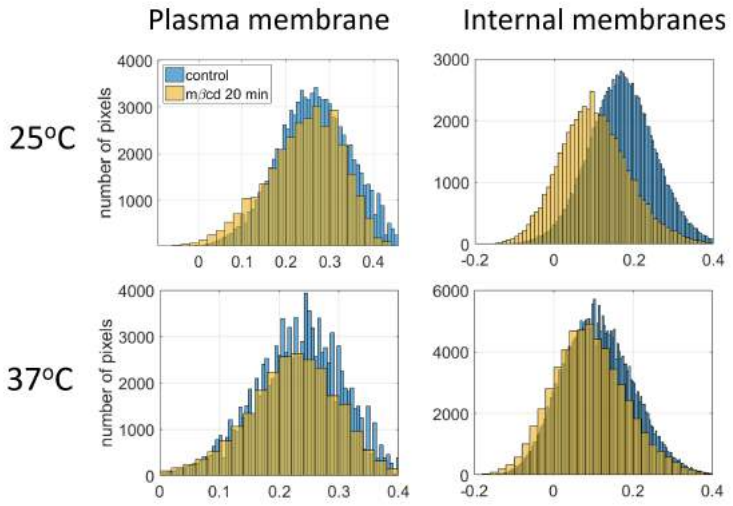

Figure 3.27: GP histograms of HeLa cell membranes upon cholesterol depletion at varying temperatures. Data is from one of the datasets used for lifetime analysis.

Meanwhile, the dynamic and static order parameters θ and Δ show little sensitivity to cholesterol depletion in plasma membranes, with only one significant difference in the datasets: a lower value of Δ' upon cholesterol depletion at room temperature suggests a decrease in membrane order

and lower rotational freedom.

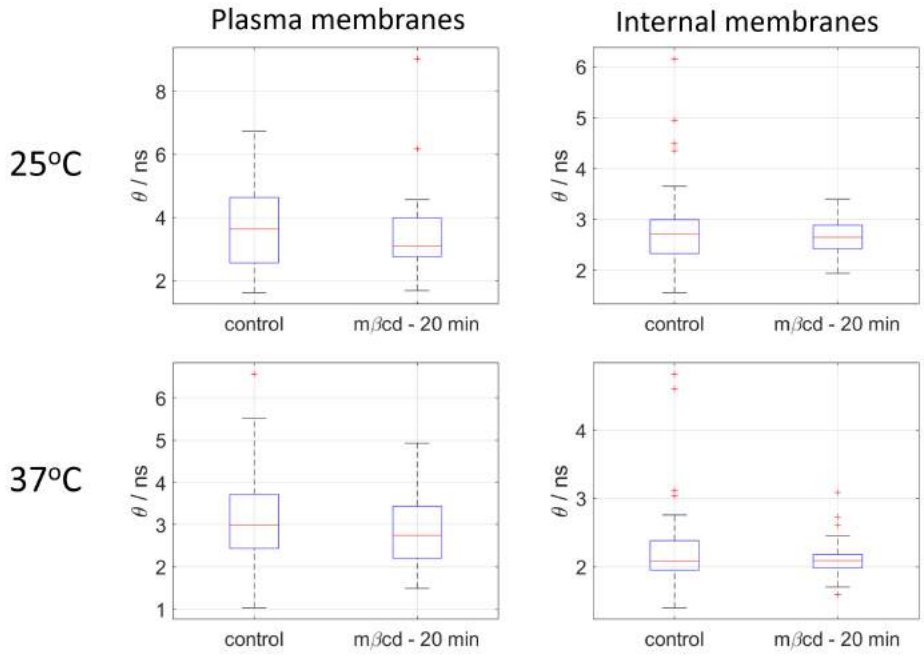

Figure 3.28: Boxplots showing the rotational correlation time θ of laurdan in plasma (left) and internal (right) membranes for control and cholesterol depleted cells at 25^{o}C and 37^{o}C.

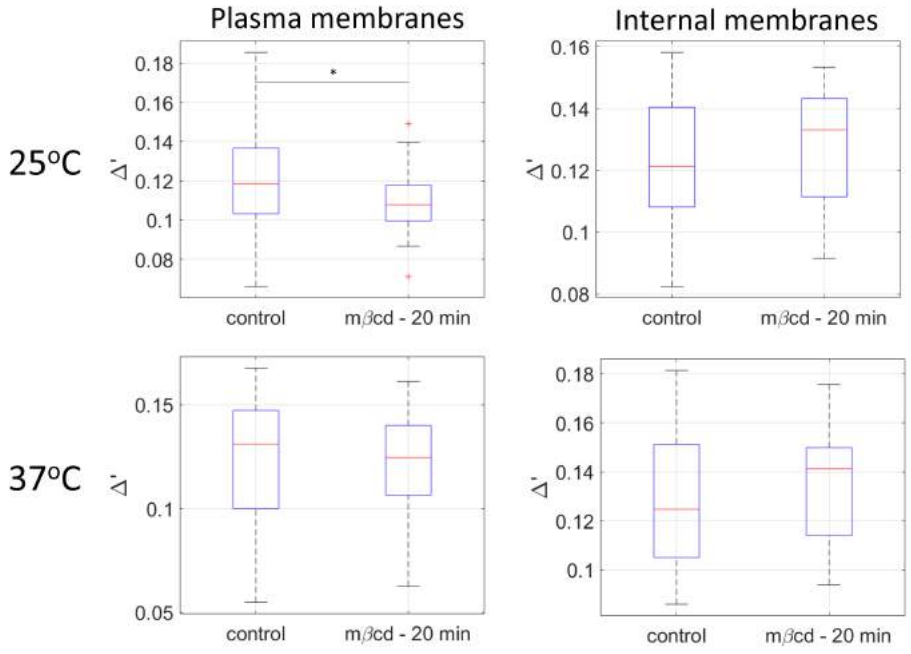

Figure 3.29: Boxplots showing the static order parameter of laurdan in plasma (left) and internal (right) membranes for control and cholesterol depleted cells at 25^{o}C and 37^{o}C.

Here, the lifetime information suggests that the plasma membrane generally behaves like a Lo phase, and depletion of cholesterol would push it towards the behaviour of a S phase. When cholesterol is removed, saturated lipids would separate from the unsaturated lipids to from gel

phase domains (however not observable at the macroscale in these experiments). This is in line with observations made by Nishimura et al. of a decreased lateral diffusion of membrane proteins upon cholesterol depletion [197]. Golfetto et al have also recorded an evolution towards longer lifetimes upon cholesterol depletion using phasor analysis of laurdan [169]. Finally, the lack of statistical difference in order parameters suggests that the plasma membrane retains a fluid state when cholesterol is removed. Results from the previous section suggest that the actin cytoskeleton restricts the rotational mobility of plasma membrane lipids; however, in ref. [196], the decrease in diffusion upon cholesterol depletion was reversed upon cytochalasin D treatment, evidencing an interaction between membrane cholesterol content and the action of the cytoskeleton on membrane diffusion properties.

3.3.1.2 Internal membranes

In the internal membranes, there is no statistical difference in laurdan lifetime at room temperature between the control and the treated sample, though the lifetime is shorter on average, and a small increase (1%) is detected at 37^{o}C (Fig. 3.23). Results from fitting are corroborated by phasor analysis, with no displacement of the phasor cloud and overlapping phasor coordinate histograms (see Fig. 3.25). Meanwhile, the GP values decrease in internal membranes upon cholesterol depletion, and the sensitivity to cholesterol depletion is higher than in plasma membranes, with 32 and 18% decreases at 25 and 37^{o}C, respectively. Similarly to what was observed in the plasma membrane, the order parameters show no significant evolution upon cholesterol depletion.

These results suggest more limited effect of cholesterol depletion on internal membranes; this is to be expected since cholesterol is depleted from the plasma membranes, and because internal membranes are less rich in cholesterol. Golfetto et al [169] have however recorded an evolution of internal membranes towards lower lifetimes in similar experimental conditions; this may be due to the different conditions used for mβcd in their experiments (1 mM mβcd added to the medium containing serum, for 1h). It is likely that the evolution of membrane microenvironment upon cholesterol depletion is highly dynamic, and that the changes observed in laurdan fluorescence depend highly on the experimental conditions. Monitoring the changes in cholesterol content upon cholesterol depletion in a time-resolved manner using GP and lifetime imaging of laurdan could be an interesting future subject of investigation to resolve intracellular cholesterol dynamics. The extent of cholesterol depletion could be related to the increases in lifetime, and external and internal flows of cholesterol could be quantified by measuring the recovery of the plasma membrane (subsequent decrease in lifetime) after cholesterol depletion when mβcd is removed, and replaced by a medium of controlled cholesterol content.

3.3.2 Experiments on cell-derived vesicles

In order to explore the effect of cholesterol depletion in a larger temperature range, GPMVs were extracted from cells stained with laurdan and depleted from cholesterol in the same conditions as the live cells presented above (in addition, a shorter incubation time with mβcd was probed). The results for the average lifetime parameter are shown below. Unexpectedly, the lifetime is sensibly shorter in cholesterol-depleted cells, and this is consistent at all temperatures. This result is opposite to what was observed in live cells. Each cell culture was treated with the same solution of vesiculating agents so this cannot be due to an effect of their concentration. Vesiculants were added after rinsing with the GPMV buffer so this should not be linked to the presence of cyclodextrin or cyclodextrin-cholesterol in the medium, either. It is possible that under conditions of depleted cholesterol the vesiculated fraction of the membrane is modified. As seen from the previous section, the plasma membrane becomes closer to a gel phase when depleted from cholesterol. It is possible that under low cholesterol conditions, the fraction of saturated lipids able to enter the vesicles is even lower. This would then yield a GPMV content overall richer in unsaturated lipids, compared to the ones obtained in higher cholesterol conditions.

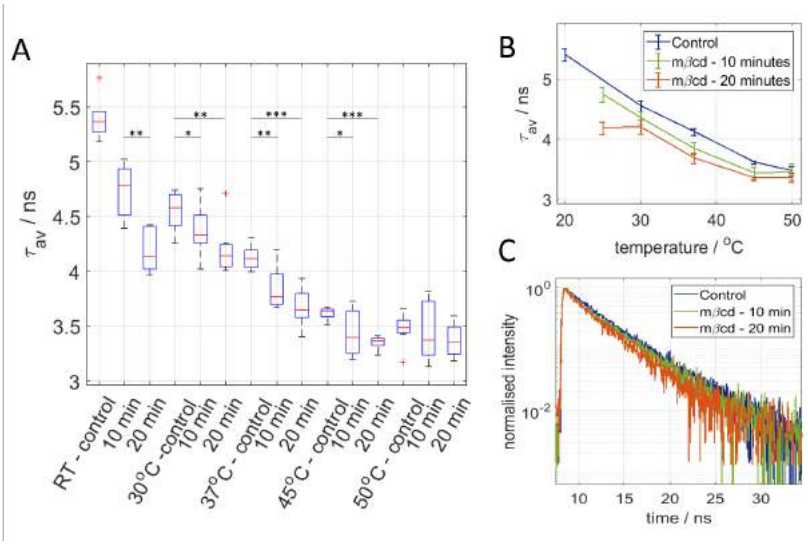

Figure 3.30: Lifetime analysis in GPMVs of cholesterol-depleted cells. A: Lifetime boxplots of the GPMVs at varying temperatures; room temperature was 20^{o}C for the control and 25^{o}C for the cholesterol depleted vesicles. p-values of t-tests are shown; *=p-value$<$0.05, **=p-value$<$0.01, ***=p-value$<$0.001. B: Plot showing the evolution of lifetime with temperature for each treatment. Error bars are one standard deviation. Results are from a minimum of n=6 vesicles per treatment and temperature, for at least 38 vesicles per treatment.

GP values from GPMVs are shown in the boxplots below (Fig. 3.30); results show less statistical significance than the lifetimes, and it appears that GP does not decrease with cholesterol depletion, as would be expected from the lifetime results and from the GP values in live cells. Indeed, at several temperature points the GP is clearly higher in the cholesterol-depleted samples.

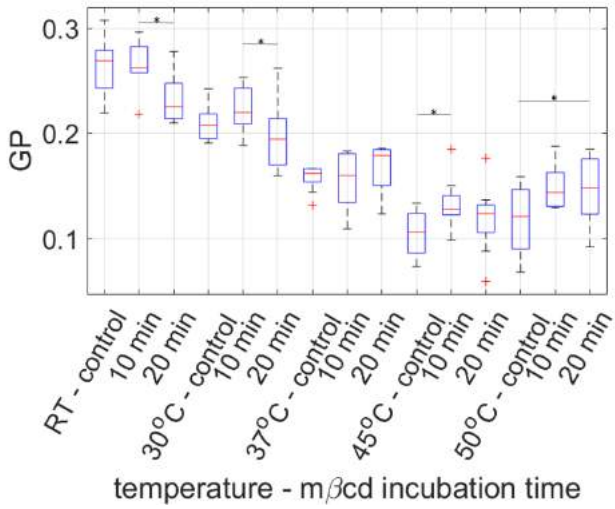

Figure 3.31: GP analysis in GPMVs from cholesterol-depleted cells - samples are the same as in Fig. 3.30.

The GPMVs produced from cholesterol-depleted cells were also much dimmer than the control cells, with average peak intensities of 650 counts for the two mβcd - treated cells, against 1150 for the control situation. This is likely due to the laurdan being scavenged from the membrane by the ring structure of mβcd. At these intensities, time-resolved anisotropy decays become extremely noisy, making exponential fitting less reliable. Binning of intensity decays in the time direction did not improve the quality of the fits; anisotropy data was therefore not exploited.

Overall these results on GPMVs are inconclusive in showing the role of cholesterol on membrane microenvironments and order parameters, since the parameter values do not correlate with those obtained in live cells. The reason for this is probably linked to the dynamics of GPMV formation and different partitioning of different lipid species into the vesicle phase. Moreover, the low intensities obtained in GPMVs precluded reliable extraction of the anisotropy parameters. These considerations along with the conclusions from section 3.2.2.1 point towards GPMVs being a limited model to study membrane microenvironments, due to the large number of factors affecting their characteristics.

3.4 Conclusions and discussion

In this chapter, multi-dimensional fluorescence imaging of laurdan was carried out in cellular membranes. Using this technique, it was shown that cell membranes display a relationship between membrane polarity and membrane order which is similar to the liquid ordered phase models in the previous chapter, while maintaining higher rotational freedom than such systems. The distinction between the plasma and internal membrane materials was possible, and showed that this relationship is similar in the two types of membranes, with internal membranes displaying higher

polarity and disorder, linked to a lower content in cholesterol and saturated lipids. This suggests that while plasma and internal membranes are located in different parameter spaces, highlighting their different chemical compositions, the relationship between membrane microenvironment and order parameters is conserved throughout the membrane material of the cell.

Treatment with cytochalasin D showed limited influence of the actin cytoskeleton on plasma membrane polarity, while rotational freedom was increased, suggesting an active role of the submembrane actin cortex in controlling the diffusional properties of the plasma membrane, which we hypothesise is linked to the establishment of lateral diffusion barriers within the lipid bilayer. The higher rotational freedom observed in GPMVs correlated with this observation, so both results are consistent in suggesting that the submembrane actin cortex determines in plasma membrane order at the level of the lipids themselves. Further validation could be provided by using anisotropy of another, more photostable dye, to give higher statistical confidence in the anisotropy parameters. It should be noted, that the effect of cytochalasin D was stronger at room temperature than at 37°C, so at physiological temperatures the influence of the cytoskeleton on lipid diffusion may be reduced.

On the other hand, cholesterol depletion yielded little influence on the order parameters, while membrane polarity and hydration were affected as measured by laurdan lifetime and GP. On this point, the present results validate previous studies: differential evolution of laurdan lifetimes in plasma and internal membranes (as also shown by Golfetto et al. [169]), with progression of plasma membrane material towards the gel phase [197] and stagnation or decrease of GP upon cholesterol depletion [206, 207]. Here, the present method allows measurement of GP and lifetime on the same field of view, which gives further confidence in these observations.

In internal membranes, the evolution of lifetime upon cholesterol depletion was lower than in plasma membranes, while there was a stronger decrease in GP values, highlighting that even though the plasma membrane is richer in cholesterol than the internal membranes, the intracellular membranes undergo strong and rapid modifications upon cholesterol depletion, suggesting fast dynamics of cholesterol transport and distribution in the cell. Together, these results show that the relationship between laurdan fluorescence lifetime and fluorescence emission is determined by many chemical and physical parameters, and that our multi-dimensional approach is informative in resolving the complex modification of membrane microenvironment in the plasma membranes of live cells.

A method to isolate actin-free plasma membrane fragments in the form of GPMVs was also used, and its suitability to study the biophysical properties of the membrane assessed. In summary, GPMVs showed significant differences compared to live cells and should therefore not be used as absolute measures of plasma membrane microenvironment and order parameters. This is postu-

lated to be linked to the unequal integration of different types of membrane lipids into GPMVs and possible direct influence of the vesiculating compounds, as evidenced by the dependence of laurdan fluorescence parameters on the concentration of DTT and PFA, and opposite evolution of laurdan lifetimes and GP in cholesterol-depleted cells and GPMVs. However, GPMVs are still a useful system to study the plasma membrane bilayer over a wide range of temperatures and conditions, and the linear relationships evidenced between membrane polarity and order parameters suggests a Lo-like phase behaviour of GPMV bilayers, which strengthened the results from live cell membranes.

In terms of image data analysis, the phasor approach was used here to confirm the results from decay fitting and to provide a more global picture of lifetime distribution in the image. The next chapter focuses on developing such global analysis techniques for FLIM and TR-FAIM data, which would support the ease of use and versatility of multi-dimensional fluorescence imaging techniques.

Chapter 4

Development of analysis techniques for time-resolved imaging data

Motivation and original idea

The previous chapters have focused on the simultaneous use of fluorescence lifetime and polarisation imaging to resolve membrane microenvironments and order parameters. While some useful conclusions were put forward using this method, the limitations linked to the difficulty of resolving lifetime and anisotropy parameters in imaging contexts where the signal-to-noise ratio is low became evident. Indeed, the accurate extraction of fluorescence intensity and anisotropy decay parameters is highly dependent on the quality of the data, and sometimes relies on assumptions on the number of decay components.

The phasor projection allow fit-free visualisation of the data, but suffers from certain ambiguities such as their sensitivity to instrumental factors, their limitation to a 2-dimensional projection of the data, and difficulty of their implementation on anisotropy decay data presenting a non-zero r_∞. Keeping the idea of the projection of decay data into a space of reduced dimensionality for ease of interpretation, we here work to develop an alternative global analysis technique which is robust to instrumental distortions of exponential decay data, and which would applicable to anisotropy data. The interest is also to analyse data with as little user knowledge as possible. Indeed, powerful FLIM analysis methods have been developed, which however rely on careful calibration using pre-determined reference samples [208], which are not always available. For anisotropy, the signal-to-noise requirements are even stronger than for FLIM, but unfortunately, fewer analysis options are available, since it is not as widespread a technique as FLIM. Warren et al. propose an anisotropy fitting module in the FLIMfit package [40], but the proposed model does not include an r_∞.

There is therefore interest in developing methods to improve the performance of time-resolved intensity and anisotropy analysis. In this chapter, a non-parametric method which can be used to resolve contrast in both time-resolved intensity and anisotropy is therefore developed.

One possible way of projecting data with optimal conservation of information and rejection of the noise is Principal Component Analysis (PCA). PCA is a well known statistical analysis method which identifies maximal and orthogonal directions of variance in the data (eigenvectors). Schematically, this is done by calculating the vector closest to all the data points in variable space, and then finding the second-closest vector, with a condition of orthogonality to the previous one, and so on. There are as many vectors as there are initial variables, and these vectors constitute an orthogonal basis for the dataset, onto which it can be projected. In practice, the eigenvectors are identified by Singular Value Decomposition (SVD) of the covariance matrix of the data.

It is usually possible to reduce significantly the number of dimensions in multivariate data, reflecting the fact that many original variables have a degree of correlation [209]. PCA has been used in many fields, including multi-channel scientific imaging [210, 211, 212], but has to the best of our knowledge never been applied to FLIM data. Figure 4.1 summarises an example of hyperspectral Raman images of HeLa cells analysed using PCA [213]. The results show that many features are identified within the cell, based on spectral differences between them.

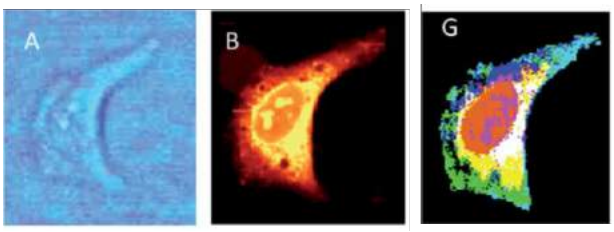

Figure 4.1: Hyperspectral Raman microscopy image of a HeLa cell imaged using PCA. A: Bright-field image of the cell. B: Integrated Raman C-H intensity image. G: PCA image resulting of the overlay of 3 PC abundance maps. Adapted from ref. [213] with permission from the Royal Society of Chemistry.

The idea here is to use arrival time bins in each pixel of a FLIM image in a similar fashion to spectral channel bins in a hyperspectral image. Each pixel constitutes an observation of the intensity at various time bins, each of which is a variable. This section shows the adaptation of PCA to TCSPC-FLIM images, and notably its tailoring to the Poisson-distributed character of single photon counting. Our PCA routine is validated on simulated data and compared to other non-fitting approaches such as the mean arrival time and phasor analysis. We then prove its performance to resolve membrane order on experimental data of HeLa cells stained with membrane dye di-4-ANEPPDHQ.

4.1 Application of PCA to TCSPC-FLIM

The principle is to use the varying abundances of respective decay components in each pixel of a FLIM image as contrast. For example, if there is only one decay component throughout the entire dataset (whether single-exponential or not), all pixels will decay at the same rate, and the only source of variance between pixels is the different intensities (due to fluorophore concentration or brightness). In this case, there is only one significant direction of variance in the data, and therefore a single eigenvector is expected. If there are two or more emitting species with different lifetimes, decay rates between pixels will also vary according to the abundances of these fluorescent species, and will constitute additional directions of variance. The objective of PCA-FLIM is to capture these directions of variance as eigenvectors, constituting an orthogonal basis into which the data can be newly projected.

As in phasor analysis, the TCSPC FLIM data set is treated as an array M of n pixels, in which the fluorescence intensity I is measured in q time bins. Principal component analysis relies on the singular value decomposition (SVD) of the covariance matrix (C) of this dataset. The covariance matrix is calculated as described in Eqs. (4.1) and (4.2):

$$C = \begin{bmatrix} cov_{1,1} & \dots & cov_{1,q} \\ \vdots & \ddots & \vdots \\ cov_{q,1} & \cdots & cov_{q,q} \end{bmatrix} \tag{4.1}$$

Where $cov_{i,j}$ is the covariance between noise-corrected intensity vectors at time bins i and j, which represents how the intensities at two time bins vary together:

$$cov_{i,j} = \frac{1}{n}\sum_{i=1}^{n}(I_{k,i} - \overline{I_i})(I_{k,j} - \overline{I_j}) \tag{4.2}$$

$I_{k,i}$ and $I_{k,j}$ represent the intensities in pixel k at time bins i and j respectively, and $\overline{I_i}$ and $\overline{I_j}$ are the average intensities in the image at time bins i, and j. Note that the diagonal terms correspond to the variances of the corresponding intensity vectors. The covariance matrix C is then subjected to singular value decomposition:

$$C = U.D.V^t \tag{4.3}$$

Where U is a matrix containing the left eigenvectors, D contains the eigenvalues, representing the variance carried by each of the new variables, and V^t is the transpose of V, containing the right eigenvectors, which are used as the new variables. SVD routines are available in most analytical software libraries. Once the eigenvectors are computed, the initial data can projected in this new

basis by writing each decay I_k as a linear combination of the eigenvectors:

$$s_{p,k} = \sum_{i=1}^{q} v_{p,i} I_{k,i} \tag{4.4}$$

Where $s_{p,k}$ is the score (projection) value of pixel k onto the p^{th} eigenvector, and $v_{p,i}$ is the value of this eigenvector at time bin i. $I_{k,i}$ is the intensity measured in pixel k, at time bin i. In matricial form, this equation can be written as:

$$S^t = V^t M^t \tag{4.5}$$

Where S contains the scores of all pixels on all principal components, V is the matrix defined in Eq. 4.3 and M is the data matrix. The contrast in the image is then visualised as a succession of score images and varying score values within each of them. What is expected is that there are as many eigenvectors as there are decay components, as therefore as many score images. The first score image is expected to reflect intensity variations in the data, since over an image the pixel-to-pixel variation in intensity usually constitute the largest source of variance. The ulterior score images show zones of varying decay profiles, if they exist. It is possible to remove the intensity variations in the data by a normalisation step; however this was not implemented, to preserve the Poisson-distributed character of the data, the importance of which will become apparent in section 4.1.2.

4.1.1 Searching for a performance metric adapted to global analysis methods

To test the performance of PCA on FLIM data and compare it to other analysis techniques, simulated FLIM datasets of selected decay rates and intensities were simulated by using a sample fluorescent cell image from ImageJ. The RGB channels were separated (see Figure 4.2), and each pixel of each channel was multiplied to a single-exponential decay in the third dimension. Note that the exponential decays are convolved with a short Gaussian centered at t=0 to mimic the effect of the laser pulse and detection rise time (IRF). The RGB channels were added, and finally the image was normalised so as to yield a specific average number of photons per pixel. Poisson noise was added using the "noise" function in the image analysis toolbox DIPimage. With this method, the fractional contribution $a_{I_{i,k}}$of each decay component k is defined in each pixel i by the intensity I of that pixel in the corresponding RGB channel.

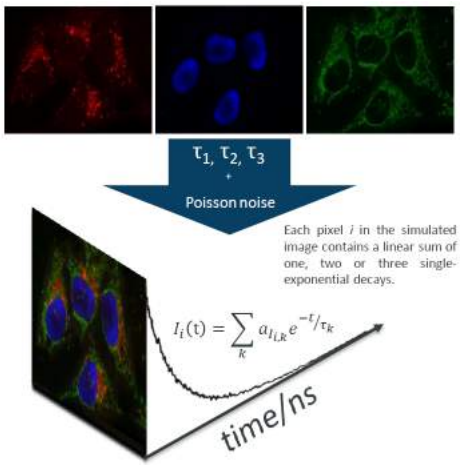

Figure 4.2: Multi-component HeLa cell images used for PCA-FLIM simulations. Upper left: lysosomes, centre: nuclei, right: mitochondria, Lower image: overlay - and schematic representation of a simulated decay pixel.

The first step in our evaluation of PCA is the establishment of a metric quantifying the success of information recovery from the initial simulated image. The main point is to determine whether the number and distribution of the recovered fluorescent components corresponds to those of the input components in the initial noise-free image. This metric should also be useful for the interpretation of PCA results on experimental data. For this, several methods are possible:

- One simple method is based on the eigenvectors: for all the dimensions from the new basis reporting on a direction of variance in the data, the time evolution of the corresponding eigenvectors should be structured, showing orthogonal directions of decaying intensity. Eigenvectors are structured when there is a clear time evolution in their values, rather than being dominated by noise (see examples in Fig. 4.12). The ulterior dimensions carry no information, and the resulting eigenvectors should have no structure, reflecting random noise in the data. Success of the PCA method for simulated data can therefore be assessed by comparison of the number of structured eigenvectors to the number of initial decay component inputs. In experimental data, the number of decay components can be deduced from the number of time-structured eigenvectors. Principal component analysis yields matrix D (Eq. 4.3) containing the eigenvalues associated to each principal component. They represent the "amount of total variance", or inertia, contained on their eigenvector. The sum of all eigenvalues yields the total variance of the initial dataset. The eigenvectors carry a decreasing proportion of the variance of the data, so the eigenvalues naturally represent the relevance of their associated eigenvector and could be used as figures of merit. However, eigenvalues and eigenvectors are absent in other methods such as phasor analysis, so are of limited use. Moreover, we have shown that with noisy data, presence of visible contrast in the score images does not necessarily translate into a clear step in the eigenvalues, as shown in Figure 4.4, blue data

points).

- In the case of simulated data, the goodness of the fit (coefficient of determination, R^2_{adj}) between the input data (intensities and abundances) and and the scores (or phasor values) can be calculated. An example is shown in Figure 4.3. Good recovery of input information yields high R^2_{adj} values, the maximum being 1. While R^2_{adj} represents an ideal metric in that it shows accuracy of information recovery, it is not useful for experimental data, where the original input abundances are not known.

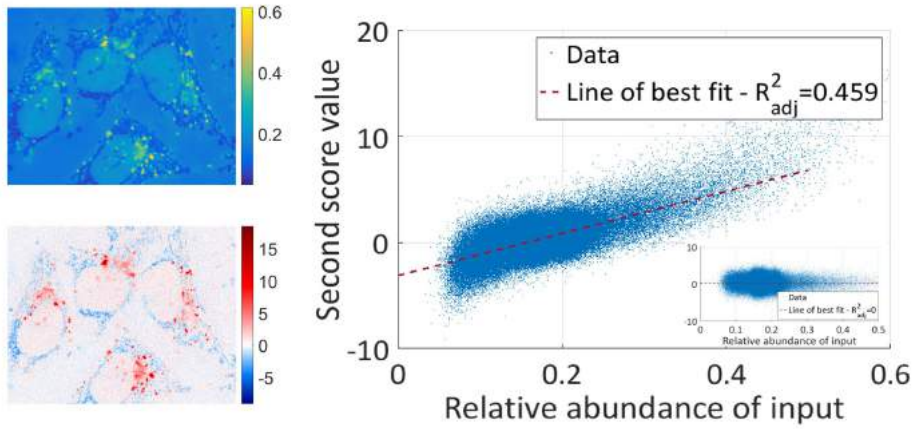

Figure 4.3: Example of the determination of goodness of fit between input information of a FLIM image and PCA results for 2-component simulated data (τ_1= 0.2 ns, τ_2=1 ns, 100 photons per pixel on average). The upper-left image shows relative abundance for the first lifetime component, A1τ_1/(A1τ_1+ A2τ_2). The lower-left image shows the second score image recovered by NC-PCA. The pixel values for both these images are correlated on the right-hand side panel (blue cloud). The cloud is fitted using a linear regression (dashed red line), and the determination coefficient R^2_{adj} displayed. The inset shows a cloud of randomly-generated points with same average and standard deviation as the second score image, plotted against the input abundance: the absence of any correlation yields a R^2_{adj} of 0.

- To satisfy compatibility with multiple methods and applicability to simulated or experimental data alike, a fully image-based evaluation metric would be desirable. For this, pixel autocorrelation can be used [214]: the image is correlated with itself in the x- and y- directions using Pearson's correlation coefficient (see Eq. 4.6), and the average of both coefficients is taken.

$$\begin{cases} \rho_x = \rho(I_{1:f-1,1:g},\, I_{2:f,1:g}) = \frac{cov(I_{1:f-1,1:g},\, I_{2:f,1:g})}{\sigma(I_{1:f-1,1:g})\sigma(I_{2:f,1:g})} \\ \rho_y = \rho(I_{1:f,1:g-1},\, I_{1:f,2:g}) = \frac{cov(I_{1:f,1:g-1},\, I_{1:f,2:g})}{\sigma(I_{1:f,1:g-1})\sigma(I_{1:f,2:g})} \\ \alpha = \frac{\rho_x+\rho_y}{2} \end{cases} \tag{4.6}$$

This autocorrelation at one pixel shift is named α. α values were found to be more indicative of visible contrast in the image than eigenvalue strengths, as visible in Figure 4.4. To further verify the relevance of this metric, α was compared to R^2_{adj} on simulated data of varying

lifetime and intensities. Both metrics were found to be highly correlated, with a Pearson's correlation coefficient of above 0.99 for 380 lifetime combinations simulated at 40 different intensities between 10 and 5000 photons per pixel on average. Results of this simulation are explained in more detail in the next section, and Figure 4.14 shows the parallel between α and R^2_{adj} on phasor and NC-PCA. This allows us to assume that the contrast-based metric α is a reliable measure of PCA and phasor alike.

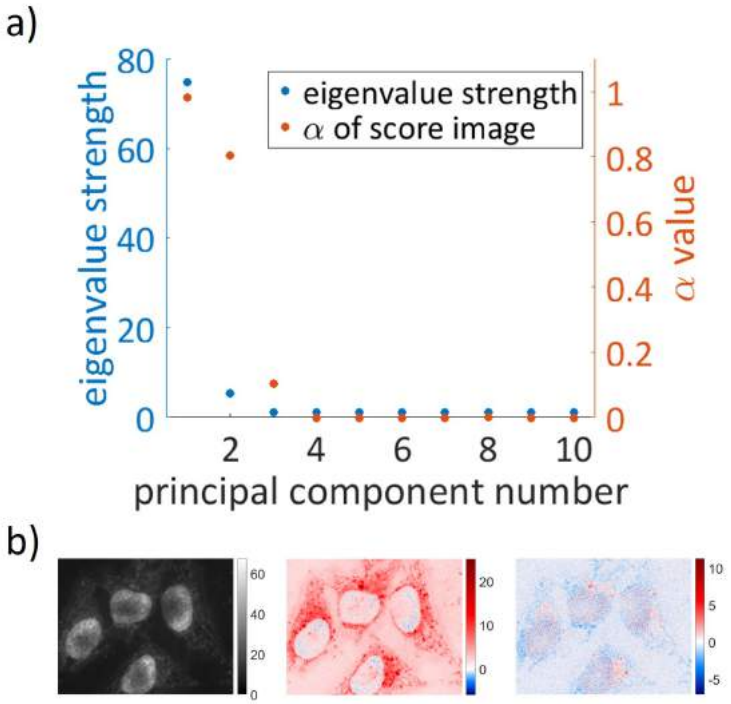

Figure 4.4: Eigenvalues and alpha metrics on a three-component simulation ($\tau_1 = 1$, $\tau_2 = 2.5$, $\tau_3 = 5$ ns, 200 photons per pixel on average). a) The third eigenvalue is only 5% higher than the 4th eigenvalue (λ_3=1.1442 and λ_4=1.0826), with the second and third eigenvalues significantly higher. The 3^{rd} alpha value, on the other hand, is clearly distinct from the 4^{th} alpha (α_3=0.1027 while α_4=-0.0006). b) Corresponding first (left), second (centre), and third (right) score images.

It is also interesting to use α as a measure of visible image contrast, drawing a parallel with the way a user assesses information contained in an image through visual inspection. If α values are correlated with our ability to identify features in an image, a threshold value for α could be established, to establish a binary "success/failure" decision of the PCA or phasor routine. This would allow us to run PCA on thousands of simulated images with varying intensities and lifetime combinations, and to decide for each of them - in an unsupervised fashion - whether the PCA was successful in assessing the number of components. This would probably depend on the image used, but can be done as a proof of concept on the specific image used for all our simulations. To identify the minimum α value corresponding to the appearance of visible contrast in a PCA score image, a 2-component FLIM image (τ_1=1 ns, τ_2=1.5 ns) was simulated at several low and

increasing intensities. At very low intensities, no contrast is visible in the score images and α values are very low (<0.05); features start appearing with a coinciding jump in α, to a value close to 0.1 (Figure 4.5). This was also found to be the case for other lifetime combinations (not shown), so the threshold value α_{min} to determine the success of the PCA routine was set to 0.1 in the simulated data presented here, hence linking the analysis to the visual inspection of experimental results.

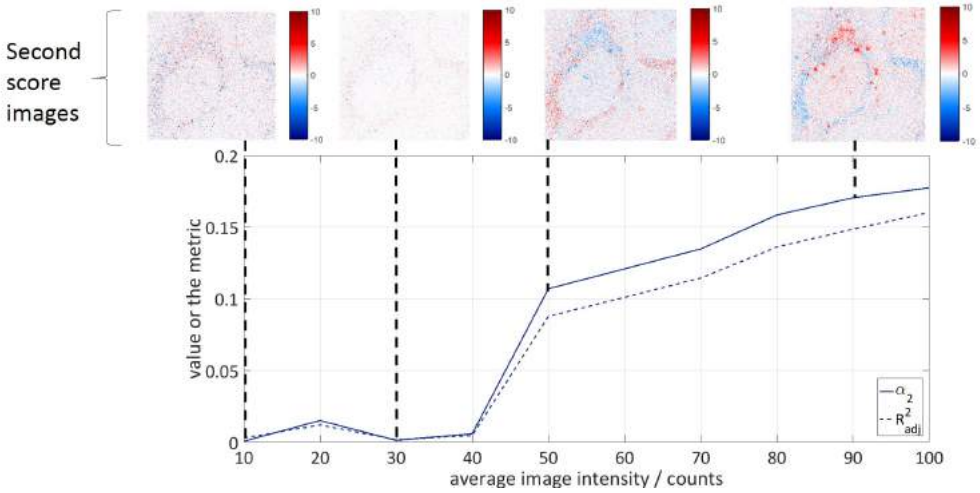

Figure 4.5: Determination of the lower threshold α_{min}. The image autocorrelation coefficient α_2 is calculated for second score images of simulated FLIM data (τ_1=1 ns, τ_2=1.5 ns) with varying intensities (photon counts). Visible contrast in lifetime between the organelles is visible with at least 50 photons per pixel on average, and this corresponds to the value of α_2 exceeding 0.1. R^2_{adj} is also shown (dashed blue line) to demonstrate the correlated evolution of both metrics.

4.1.2 The noise problem

Our first observation when applying PCA to simulated data was that while the contrast in lifetime was visible in the score images, an incorrect number of components was detected: for example, PCA of a 3-component FLIM image (τ_1=1.5 ns, τ_2= 3 ns, τ_3= 6 ns, 1000 photons per pixel on average) yields only two score images with visible contrast and $\alpha > 0.1$, while the last score image contains no visible features (Figure 4.6). Note that if there are 3 lifetime components, then the expected result is one score image representative of intensity variations, and then 2 more score images for showing regions of contrasting lifetimes.

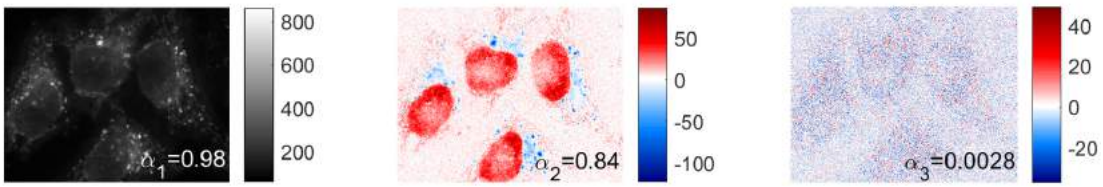

Figure 4.6: PCA score images from three-component simulated image (τ_1=1.5 ns, τ_2= 3 ns, τ_3= 6 ns, 1000 photons per pixel on average).

The reason for this failure could be linked to a signal-to-noise ratio too low for PCA sensitivity. This is however unlikely, given the very high α values for score images 1 and 2, comparatively to α_3. Another possible reason could be that the directions of variance identified by PCA do not correspond to the varying decay profiles. This can be due to non-orthogonality of the decay components and cannot be avoided; however, these features are the main sources of variance in FLIM data after pixel-wise intensity variations, and should coincide closely with the orthogonal vectors calculated by PCA. The following step was then to investigate the reason for this discrepancy, which likely lay in the structure of the data.

Frequently, variables in a dataset have different orders of magnitude and therefore different variances. Since PCA is based on the diagonalisation of the covariance matrix, the eigenvectors will inevitably be drawn towards the variables of high variance. For decaying TCSPC-FLIM data, this is very much the case since the initial moments of the decay have higher intensities than the later moments. The principal components therefore over-represent the weight of the initial time bins while the later ones are under-represented. It is possible that this effect contributes to the failure of PCA in our previous example.

To correct this heteroscedastic data structure, a pre-processing step consisting in dividing each intensity vector by its standard deviation can be performed, hence giving each a variance of 1. Matrix C (4.2) then becomes a correlation matrix:

$$C^v = \begin{bmatrix} 1 & \dots & corr_{1,q} \\ \vdots & \ddots & \vdots \\ corr_{q,1} & \cdots & 1 \end{bmatrix} \tag{4.7}$$

However, this method did not resolve our problem, as seen in Figure 4.7.

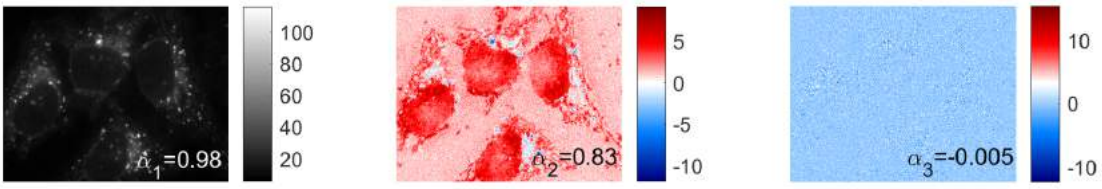

Figure 4.7: Variance-scaled PCA score images from three-component simulated image (τ_1=1.5 ns, τ_2= 3 ns, τ_3= 6 ns, 1000 photons per pixel on average).

It appears that the variance homogenisation did not correct for the unwanted principal components. We then sought other methods to pre-process the data for PCA, potentially more adapted to TCSPC-FLIM. One aspect yet unconsidered is the Poisson-distributed character of the noise in our data. The variance homogenisation as applied above corrects globally for variance differences

between time bins, but in fact there are 2 different sources for the variance of the data: firstly, the underlying data variance due to the differences in intensity and decay profiles between pixels, and secondly, the detection noise linked to single-photon counting. The idea for PCA would be to correct for the noise component of the variance, while resolving principal components according to the underlying data variance. In order to do this, normalisation of the variable vectors by their calculated standard deviations is probably not the best method since there is no distinction between these two components. Instead, a normalising factor closer to the estimation of the detection noise would be more appropriate: since single photon detection follows a Poisson law to a very good approximation, an estimate of the noise associated with an intensity measurement I is $\sqrt{I}$. In this case, at each time bin j the variable vector I_j could be scaled by a factor of $\sqrt{\overline{I_j}}$, where $\overline{I_j}$ is the average intensity in the image at time bin j, rather than $\sigma(I_j)$. This scaling yielded the expected effect, with three score images showing contrast according to lifetime information, as shown in Figure 4.8.

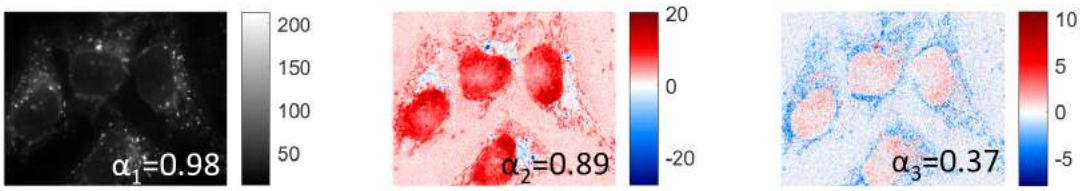

Figure 4.8: Poisson noise-scaled PCA score images from three-component simulated image (τ_1=1.5 ns, τ_2= 3 ns, τ_3= 6 ns, 1000 photons per pixel on average).

A more formal explanation to this observation was sought; to this effect, the data was simplified to an image with 128-by-128 pixels with 2 perfectly correlated time bins I_1 and I_2 ($I_1 \propto I_2$), as shown in Figure 4.9.a-b). Different types of noise were then applied to these vectors. The 3 types of PCA routines were used to recover the underlying correlations (the information is contained in the first eigenvector), and the result was compared to the initial, noise-free correlation. The black arrow in Figure 4.9.b) shows the noise-free correlation. If Gaussian noise of uniform variance (green cloud) is applied to the two time bins (4.9.c)), the principal component is accurately recovered by standard PCA (orange arrow). However, application of Poisson noise (Figure 4.9.e), blue cloud) on the same data prevents accurate recovery by standard PCA, as shown by the non-overlapping arrows. This could be explained by the creation of correlations between uncorrelated data upon application of signal-dependent, Poisson-distributed noise: indeed, as shown schematically in Figure 4.9.d), a clear principal component arises when Poisson noise is added to random data with no underlying correlation (orange arrow), while this is not the case with the uniform Gaussian alternative. The

variance scaling method (Figure 4.9.f)) seems to over-correct for the noise (the orange arrow is now above the black one, compared to panel e)). The scaling method based on the estimated Poisson standard deviation, allows accurate recovery of the underlying correlation in presence of Poisson noise, as shown in Figure 4.9.g).

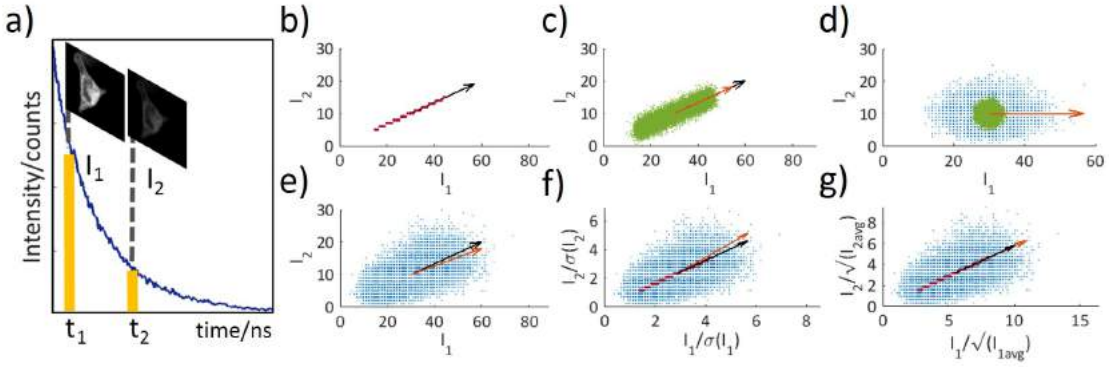

Figure 4.9: Effect of photon-counting variances on PCA. a) Representative decay and intensities of a time-resolved image at two time bins t_1 and t_2. b) Intensities in pixels of a noise-free image at two correlated time bins (correlation shown as the black arrow) are plotted against each other. c) Gaussian noise of uniform variance (green cloud) is applied to the data shown in b). d) Gaussian noise of uniform variance (green cloud) or Poisson noise (blue cloud) are added to two images of constant brightness (no source correlation). e) Poisson noise (blue cloud) is applied to the data shown in b). f) Normalising each image by its standard deviation does not allow recovery of the underlying data correlation. g) Normalising each image by the square-root of its average intensity recovers the underlying correlation, as seen by the overlapping orange and black arrows.

This simple 2-bin test was extended in a more quantitative way to a variety of intensity scenarios relevant to FLIM imaging, always preserving a perfect correlation in the noise-free data. The % difference between the slope coefficients in the noise-free correlation and the recovered one can be calculated to evaluate the performance of the PCA routines. The results from these simulations are shown in Figure 4.10. Panel a) shows the % error of the recovered correlation as contour plots, the yellow signifying large errors (only the lower-right triangle is represented, as the simulations with 2 time bins are symmetrical). It is clear from the results that Poisson noise correction (which we now call Noise-Corrected PCA, or NC-PCA) produces much smaller errors over the entire domain investigated, unlike unscaled and variance-scaled PCA, which both produce significant deviations in many cases. Three cases are illustrated in more detail :

- $I_1 \approx I_2$ (red dots on panel a), results shown in panel b)): The two bins have close average intensities, meaning both have the same noise intensity and the cloud is symmetrical. The recovery is good, whatever the type of scaling: all arrows are overlapped and the % error is low for all three types.

- $I_1 > I_2$ (yellow dots on panel a), results shown in panel c)): The high intensity bin has a greater variance so the unscaled PCA yields a principal component biased towards it (purple

arrow). Variance-based scaling improves the recovery but over-compensates (orange arrow).

- $I_1 \gg I_2$ (green dots on panel a), results shown in panel d)): The unscaled PCA performs better when there is a high mismatch between the two channel intensities rather than a moderate one, since the total variance of the sample can now be approximated to the variance of the high-intensity bin, yet it does not reach NC-PCA performance. The over-compensation of the variance-based scaling is aggravated, as seen by the high errors in this zone.

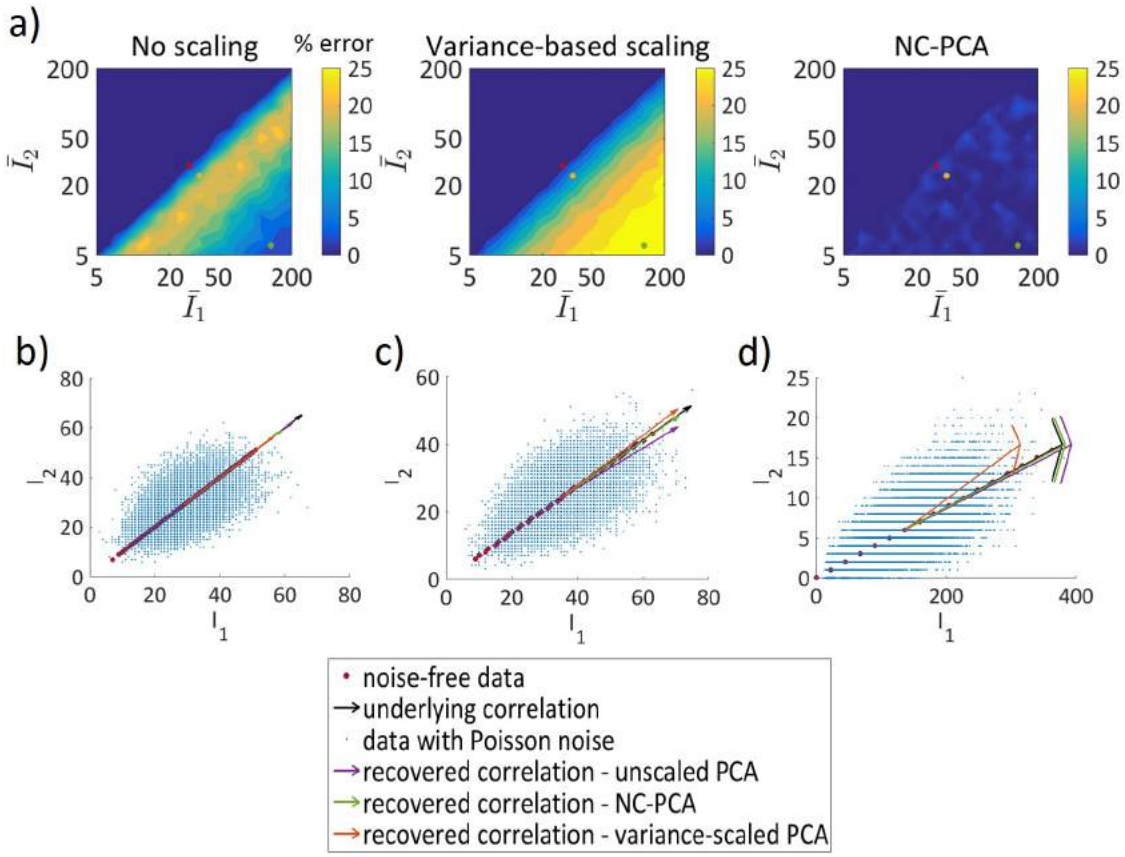

Figure 4.10: Evaluation of PCA performances on two bins for varying average bin intensities (see representative decay and bins in Figure 4.9.a)). a) Effect of the three scaling types on the % error between the coefficient of the principal direction (slope of the arrow) of the noise-free data and the one recovered through PCA from the noisy data. b) Scenario $I_1 \approx I_2$ (red dots on panels in a)). c) Scenario $I_1 > I_2$ (yellow dots); d) Scenario $I_1 \gg I_2$ (green dots).

While these simulations showed that NC-PCA was superior to unscaled and variance-scaled PCA, a mathematical confirmation that the eigenvectors recovered with Poisson-based noise correction are indeed equivalent to the underlying data correlation would further strengthen our case. For this, we considered once again the intensity vectors at two time bins i and j. The measured (noisy) intensity I_j^m can be written as:

$$I_j^m = I_j^t + \epsilon_j \tag{4.8}$$

Where I_j^t is the true intensity, and ϵ_j is the noise. The covariance between intensity vectors at two time bins is then written:

$$cov(I_i^m,\, I_j^m) = cov(I_i^t,\, I_j^t) + cov(I_i^t,\, \epsilon_j) + cov(I_j^t,\, \epsilon_i) + cov(\epsilon_i,\, \epsilon_j) \tag{4.9}$$

Writing the explicit form for term $cov(I_j^t,\, \epsilon_i)$ using the zero-mean distribution of the noise vectors yields:

$$\begin{aligned} cov(I_j^t,\, \epsilon_i) &= \tfrac{1}{n} \textstyle\sum_{k=1}^{n} (I_{k,j}^t - \overline{I_j^t}).\, \epsilon_{k,i} \\ &= \tfrac{1}{n} \textstyle\sum_{k=1}^{n} I_{k,j}^t.\, \epsilon_{k,i} \end{aligned} \tag{4.10}$$

The strength of the noise vectors ϵ_i are correlated, statistically, to the intensity vectors I_j^t. However, for a large number of observations (pixels) Equation 4.10 approaches zero, since the values $\epsilon_{k,i}$ fluctuate with zero mean around the predicted intensities. Symmetrically, this is also the case for term $cov(I_i^t,\, \epsilon_j)$ in Equation 4.9, and this argument holds for diagonal and non-diagonal terms of the matrices alike. Even though the strength of the noise depends on the intensity, these two terms vanish since their expected value is zero. Therefore, the covariance of the measured data $cov(I_i^m,\, I_j^m)$ can be simplified to the sum of covariances of the underlying "true" data $cov(I_i^t,\, I_j^t)$ and of the noise $cov(\epsilon_i,\, \epsilon_j)$:

$$cov(I_i^m,\, I_j^m) = cov(I_i^t,\, I_j^t) + cov(\epsilon_i,\, \epsilon_j) \tag{4.11}$$

Poisson-only noise dictates that the variances (i.e. the diagonal elements of the covariance matrix) of the noise are equal to the expected mean of the data $\langle I_i^t \rangle$. For a large number of observations (pixels), the mean $\overline{I_i^m}$ approaches the expected value $\langle I_i^t \rangle$. Moreover, we can also consider the noise vectors at different time bins (i.e., non-diagonal elements of the covariance matrix) to be statistically independent. Thus, we can write the covariance of the measured data from Equation 4.11 as:

$$cov(I_i^m,\, I_j^m) = cov(I_i^t,\, I_j^t) + \delta_{ij} \overline{I_i^m} \tag{4.12}$$

With δ_{ij} denoting Dirac's delta, i.e. only contributing on the diagonal.

On the other hand, the proposed noise correction can be applied to the measured data I^m at each time bin i:

$$\forall i \in [1, n],\, I_i^p = \frac{I_i^m}{\sqrt{\overline{I_i^m}}} \tag{4.13}$$

The covariance terms of this pre-processed data then become (from Equation 4.2):

$$\begin{aligned} cov^p_{i,j} &= \tfrac{1}{n}\sum_{k=1}^{n}\left(I^p_{k,i}-\overline{I^p_i}\right)\left(I^p_{k,j}-\overline{I^p_j}\right) \\ &= \frac{\frac{1}{n}\sum_{k=1}^{n}\left(I^m_{k,i}-\overline{I^m_i}\right)\left(I^m_{k,j}-\overline{I^m_j}\right)}{\sqrt{\overline{I^m_i}}\sqrt{\overline{I^m_j}}} \\ &= \frac{cov(I^m_i, I^m_j)}{\sqrt{\overline{I^m_i}}\sqrt{\overline{I^m_j}}} \end{aligned} \tag{4.14}$$

Using Equations 4.11 and 4.12, we see that this can now be written as:

$$cov^p_{i,j} = \frac{cov(I^t_i,\, I^t_j)}{\sqrt{\overline{I^m_i}}\sqrt{\overline{I^m_j}}} + \delta_{i,j} \tag{4.15}$$

As is seen in the last step, we use the fact that the mean approximates the expectancy for a large number of observations (pixels). By scaling the measured covariance by the measured Poisson scaling factors estimated from the mean over all pixels, we can approximate a scaled true covariance, with a uniform noise contribution. In matricial syntax, this yields:

$$C^p = D_{\overline{I}} C^t D_{\overline{I}} + \mathbb{I}_q \tag{4.16}$$

Where $\mathbb{I}_q$ is the identity matrix of dimension q and $D_{\overline{I}}$ is a diagonal matrix containing the average intensity scaling factors:

$$D_{\overline{I}} = \begin{bmatrix} 1/\sqrt{\overline{I^m_1}} & 0 & \cdots & \cdots & 0 \\ 0 & \ddots & & & \vdots \\ \vdots & & 1/\sqrt{\overline{I^m_i}} & & \vdots \\ \vdots & & & \ddots & 0 \\ 0 & \cdots & \cdots & 0 & 1/\sqrt{\overline{I^m_q}} \end{bmatrix} \tag{4.17}$$

Lastly, we show that eigenvectors of a matrix M_q are unchanged by addition of identity matrix $\mathbb{I}_q$:

By definition, if v is eigenvector to matrix M, $\lambda \in \mathbb{R}$ exists such that:

$$\begin{aligned} & Mv = \lambda v \\ \implies & (M + \mathbb{I}_q)v = \lambda v + \mathbb{I}_q v \\ \implies & (M + \mathbb{I}_q)v = (\lambda + 1)v \end{aligned} \tag{4.18}$$

The eigenvalue is changed to $\lambda + 1$, but the eigenvector v remains unchanged. Thus, the eigenvectors of the rescaled measured covariance approximate the eigenvectors of the rescaled true underlying covariance.

4.1.3 Validation of NC-PCA on simulated data

Now that we have tailored PCA to TCSPC-FLIM data and its noise characteristics and found an appropriate evaluation method, NC-PCA can be tested on simulated data and its performance compared to that of phasor analysis and mean lifetime determination. A visual workflow of NC-PCA is proposed in Fig. 4.11.

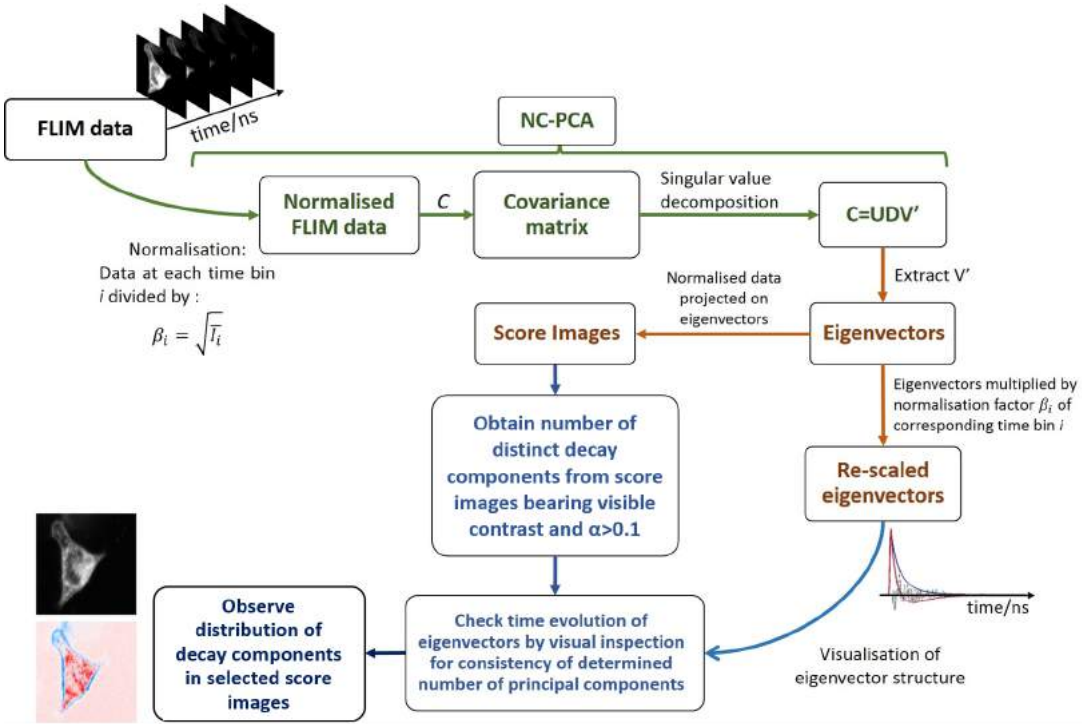

Figure 4.11: Visual representation of the NC-PCA procedure.

4.1.3.1 Comparison between NC-PCA and phasor analysis

Performance of NC-PCA was benchmarked against the existing global analysis method, phasor projection. Phasor analysis was performed using Eq. 1.49, and the phasor cloud was fitted to a straight line to generate a contrast range between the pixels, as shown in Section 3.1.4. As mentioned in the previous chapter, phasor fitting can be performed with or without weights. Weighted phasor fitting using pixel intensities or density of datapoints in phasor space improves the quality of phasor analysis, as shown in Fig. 3.5. The question therefore arises, against which phasor fitting routine NC-PCA should be compared. Weighted fitting could also be implemented in NC-PCA, which also relies on a least-squares approach for the determination of Principal Components [209]. Comparing both routines without weighting therefore allows for a ground comparison of the quality of both projections, with the understanding that the presented results might underestimate the resolution capability of either method, if such weighting was to be introduced. Note that this weighting is different from the Poisson noise correction presented in the previous section,

which consists in pre-processing the data for subsequent projection.

4.1.3.2 Visual examples

As explained in the previous paragraphs, NC-PCA on a FLIM image yields a series of score images and of eigenvectors. We expect as many eigenvectors with a structured time evolution and corresponding score images with visible contrast as there are real input component images in the simulation. Figure 4.12 shows the results for simulated FLIM images with one, two or three decay components where the fractional contribution of each decay component is determined by the intensities in the corresponding RGB channel, to generate a realistic distribution of relative abundances of lifetimes. The ground truth corresponds to the image shown in Fig. 4.2. It is clear that the expected results are confirmed, with respectively 1, 2, and 3 structured eigenvectors and score images: the ulterior eigenvectors (shown in grey) and corresponding score images (rightmost image) show no identifiable structure contrast. The cellular features may still be visible in the images, but the corresponding α values are very low ($\ll$0.1), which means they do not bear any information.

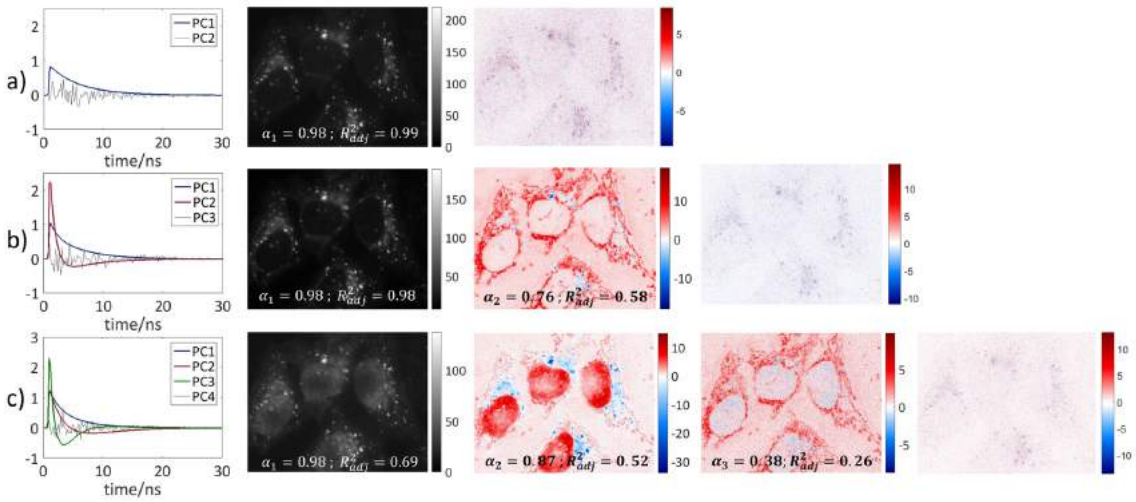

Figure 4.12: Examples of NC-PCA results for simulated FLIM images containing one (a), two (b) or three (c) fluorescence decay components. On the left, the time evolution of the dataset is shown by the eigenvectors; the images in the central panels correspond to the score image. α and R^2_{adj} values are given for the images showing contrast; the following images show no significant contrast in lifetime and all have α well below 0.1. Note that the three-component simulation contains the channel image with nuclear fluorescence, which appears clearly in the score images.

4.1.3.3 Parameter sweep

A lifetime and intensity parameter sweep covering a wide range of relevant values was now performed:

- The repetition rate was fixed at 20 MHz (50ns period) with 256 time bins and an IRF of 235

ps FWHM were used to represent typical measuring conditions.

- The lifetimes were varied from 0.2 ns to 8.25 ns, using 20 values, spaced evenly in log-scale. This spacing was chosen to represent a reasonable range of short lifetimes.
- The intensities were varied from 10 to 10000 photons per pixel on average, with 40 values, spaced evenly in log-scale, to represent a reasonable range of low intensities.
- The fractional contributions of each decay component were determined by the pixel intensities in the RGB channels, as before.

Two-component FLIM images were simulated with all possible combinations of these parameters, representing $20 \times 20 \times 40 = 16000$ simulations, as shown in the parameter volumes Figure 4.13.

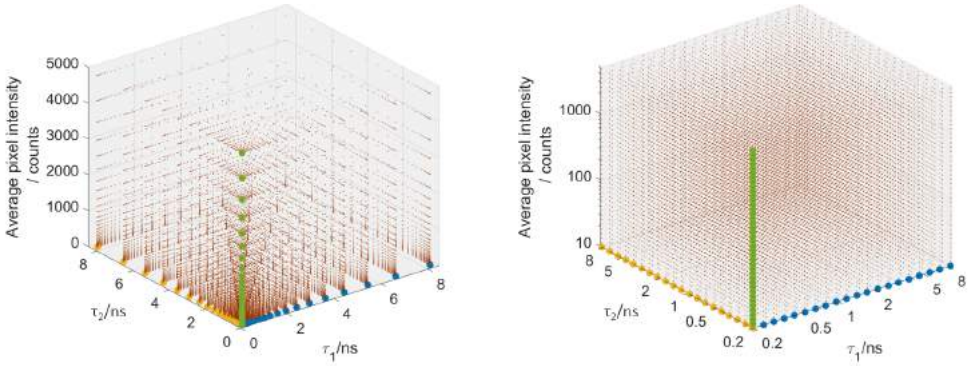

Figure 4.13: FLIM image parameter sweep: each simulation is represented by a point in the (τ_1, τ_2, I) parameter space; the values taken by variables τ_1, τ_2 and I are shown in bold blue, yellow and green dots on the axes, respectively. The space is represented in linear (left) and logarithmic (right) scales, showing the even spacing of lifetime and intensity parameter values in the log scale.

NC-PCA and phasor analysis were performed on each of them; the α values of the last expected score image (e.g., α_2, second score image for a 2-component simulation) for NC-PCA and of the phasor projection image for phasor analysis. R^2_{adj} was also calculated for each of them, using the initial noise-free abundance map as the reference data. This enabled analysis of PCA and phasor results of this large dataset in a systematic, computational manner. Figure 4.14 shows the values for both metrics in the form of contour plots at 50, 100 and 500 photons per average. Each contour plot is to be visualised as a slice of the cube of simulations from Fig. 4.13, seen from above.

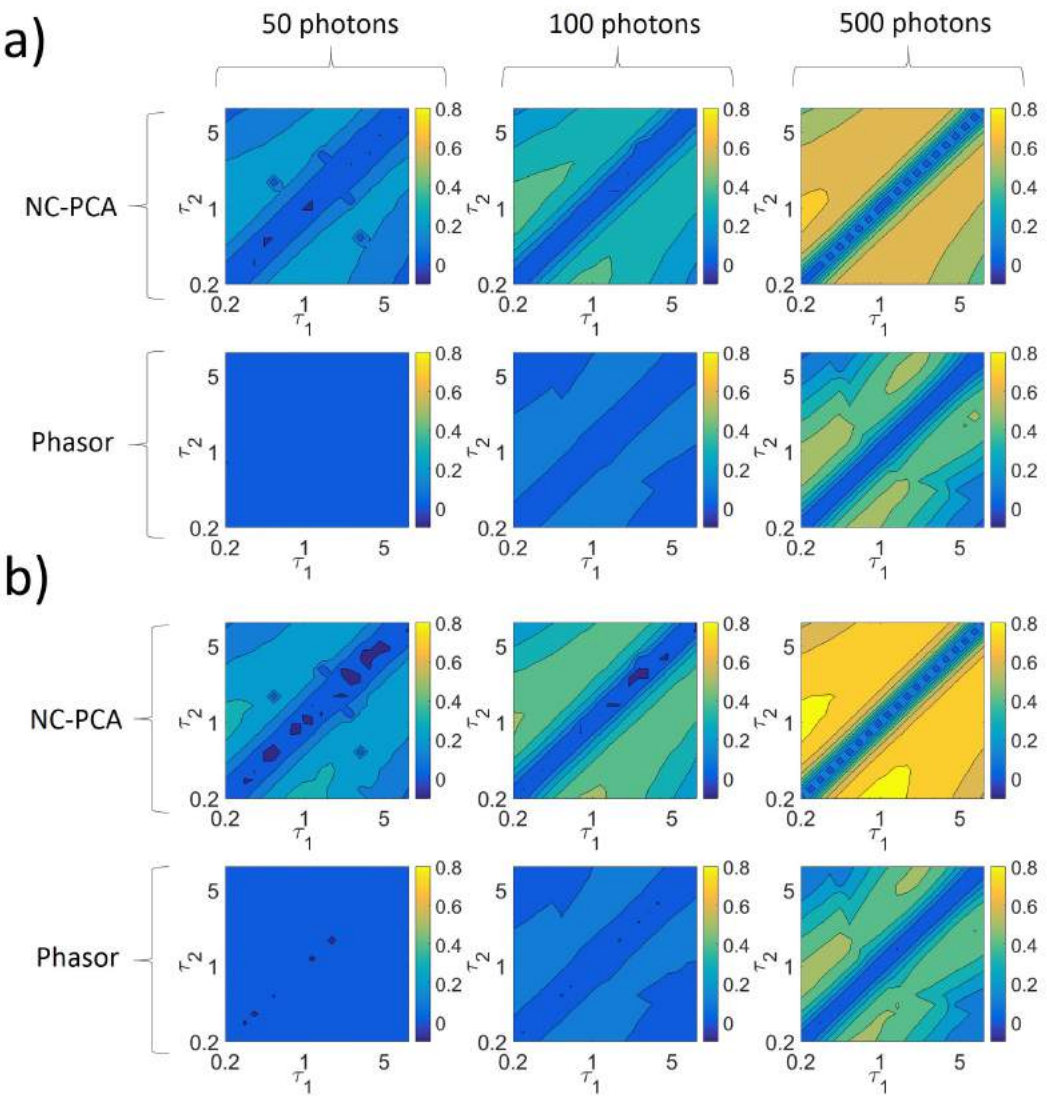

Figure 4.14: Comparison of α and R^2_{adj} metrics on 2-component simulated data with varying intensities and lifetime values. a) Contour plots represent the R^2_{adj} as a function of the input lifetime values for NC-PCA (above) and phasor (below) procedures, with 50 (left), 100 (middle) and 500 (right) photons per pixel on average. b) The α_2 coefficient is represented for the same data.

The first obvious conclusion is the confirmation of the proximity between these two metrics, as shown by their correlated evolution. Secondly, NC-PCA seems to perform better than phasor, with consistently higher α and R^2_{adj} values for the PCA routine. NC-PCA is successful in identifying two components with very low intensities (from 100 photons per pixel on average) for a large combination of lifetimes, which appears promising. The results can also be shown by representing the minimum intensity required for each lifetime combination to reach the threshold value of $\alpha_{min} = 0.1$ (Figure 4.15). Two components were detected with fewer than 100 photons per pixel on average for a large range of lifetimes using NC-PCA, representing 84.5% of all images. Phasor analysis of the same data shows comparable profiles, though higher intensities were necessary for success with phasor than with NC-PCA: only 40.5% of all phasor images reached $\alpha > \alpha_{min}$ below

100 photons.

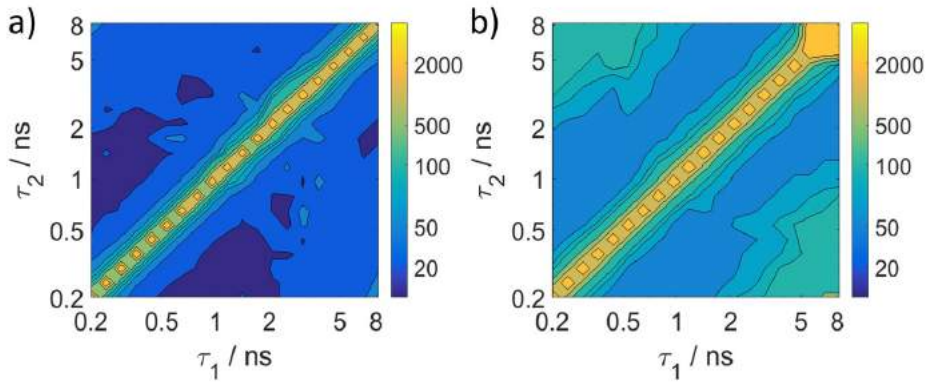

Figure 4.15: Contour plots showing the minimum intensity (average number of photons per pixel as indicated by the scale bar on the right) necessary for the accurate number of decay components to be detected in two-component simulated data for varying lifetime combinations. a) NC-PCA on two-component mixtures (see values in main text); b) Phasor analysis on the same data. The diagonal streaks in both panels correspond to the images where $\tau_1 = \tau_2$. .

These results are encouraging, since with such low photon counts, multi-exponential decay fitting cannot be soundly attempted, as shown in the first chapter, and NC-PCA seems to offer better sensitivity than the state-of-the art global analysis method, i.e. phasor analysis.

The same method was used to probe the performance in the case of three decay species (Fig. 4.16). Parameters τ_1 and τ_2 were varied in the same manner, while τ_3 was fixed to 2.5 ns. The intensity range was increased to a maximum of 10 000 photons per pixel on average. NC-PCA yielded the accurate number of components under 1000 photons for 60% of all images, which include most combinations of lifetimes between 1 ns and 8.25 ns. Three components were detected under 5000 photons for 78.25% of all images.

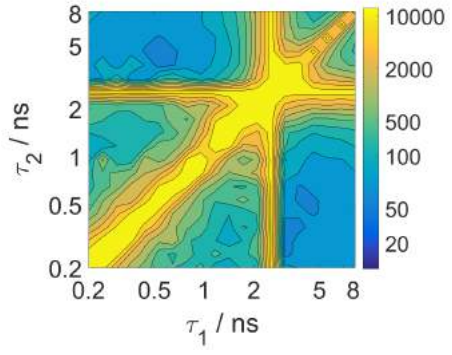

Figure 4.16: Contour plot showing the minimum intensity (average number of photons per pixel as indicated by the scale bar on the right) necessary for the accurate number of decay components to be detected in three-component simulated data for varying lifetime combinations. The diagonal streaks correspond to the images where $\tau_1 = \tau_2$, while the horizontal and vertical streaks correspond to the cases where $\tau_2 = \tau_3$ and $\tau_1 = \tau_3$, respectively.

4.1.3.4 Simulating a FRET situation

One of the most attractive uses of FLIM is the detection and quantification of FRET, which occurs when fluorescent molecules are in close proximity. It is therefore interesting to test our analysis method on such data. Typically, FRET results in an additional decay component in the donor intensity decay, corresponding to the non-radiative energy transfer of excitation energy from the donor to the neighbouring acceptor.

A FRET between GFP and an acceptor was simulated: the non-fretting regions hence have a lifetime $\tau_r = {}^1/_{k_r}$, while the fretting regions have a lifetime equal to:

$$\tau_{et} = \frac{1}{k_r + k_{et}} \tag{4.19}$$

Where k_{et} is the rate of energy transfer defined in Eq. 1.56 (Chapter 1). FRET efficiencies as defined in Eq. *1.58* rarely exceed 50% in the majority of cases in physiological conditions, and is usually much lower than this [105, 215, 30]. This is especially the case for FRET of GFP-like fluorescent proteins, where the β-barrels impose a lower limit on inter-fluorophore distance [30]. FRET efficiencies between organic fluorophores can take much higher values. This is the cause of the main difficulty in detecting FRET: low FRET efficiencies and a small fraction of interacting fluorophores in a pool of non-interacting ones produces a small change in lifetime only, with low photon contributions. We started by setting E to 25%. Using $\tau_r = 2.2$ ns for GFP, this yields $k_{et} = 0.1515.10^{-9}$ s for the rate of energy transfer, and a lifetime for the fretting regions of $\tau_{et} = 1.65$ ns. τ_r and τ_{et} were used as input lifetimes of two-component simulations, both components being given equal brightness (i.e, the same number of photons). The pixels then display a superposition of these two states, mimicking a mixture of interacting and non-interacting GFP molecules. The images were simulated with 200, 500, 1000 and 5000 photons per pixel on average, and then analysed with NC-PCA, phasor analysis or mf_d, a technique based on mean photon arrival time analysis.

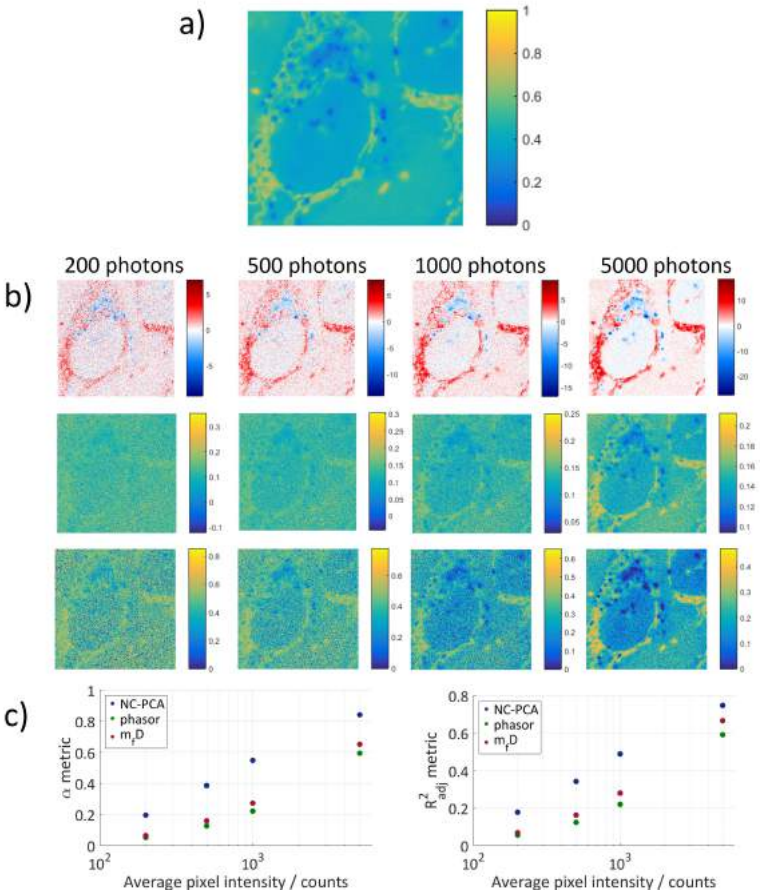

Figure 4.17: Comparison of NC-PCA with minimal fraction of donor and phasor methods on a simulated FLIM FRET dataset with τ_r= 2.2 ns and τ_{et}= 1.65 ns, using a 1:1 stoichiometry model. a) Input relative abundance of interacting species. b) Recovered images after NC-PCA (top row), phasor (middle row) and minimum fraction of donor (bottom row), for 200, 500, 1000 and 5000 photons. c) Metrics calculated for the images: α (left) and R^2_{adj} (right).

α and R^2_{adj} metrics are both unequivocal at showing that NC-PCA performs better than both methods: the interacting regions are differentiated from the non-interacting ones for as little as 200 photons per pixel on average with NC-PCA, which is not the case for the other methods.

4.1.3.5 Testing for the robustness of NC-PCA to experimental conditions

Non-fluorescent background Dark counts or room light can often create a constant background offset in the decays. Our expectation is that NC-PCA should be unperturbed by it, since background affects all pixels in the same way it should not be a source of variance in the image. This was tested in a two-component simulation ($\tau_1 = 1$ ns, $\tau_2 = 5$ ns, 1000 photons per pixel on average) by adding 0, 1 or 5 counts per bin before application of Poisson noise. NC-PCA correctly identified 2 components on all three datasets, with only a slight decrease in α_2 values, and small modification in the eigenvector profiles. The background effect is visible in the score values, where the background areas of the image (where there is no fluorescence from the cells) take non-zero values, as seen from the shift to blue or red colours in the corresponding images of Figure 4.18.

The contrast between the fluorescent parts of the cells however, remains unchanged.

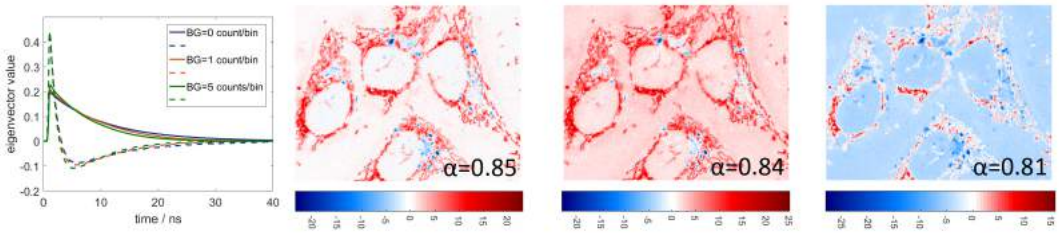

Figure 4.18: Effect of non-fluorescent background offset on NC-PCA results. Left: first (full lines) and second (dashed lines) eigenvectors for 0 (blue), 1 (orange) and 5 (green) counts per bin. Centre and right: Second score images for each of these respective cases, with corresponding α values.

In phasor analysis, background subtraction is vital prior to calculation of phasor coordinates, since the presence of a non-zero offset amounts to an additional decay component with infinite lifetime. The results is a dramatic modification of the position of the phasor cloud, as illustrated in Figure 4.19.

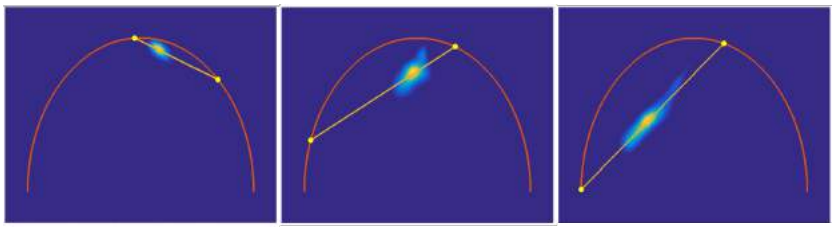

Figure 4.19: Phasor clouds for 0 (left), 1 (centre) and 5 (right) counts per bin, on the same data as in Figure 4.18.

Background subtraction, even correctly performed, yields noisier data clouds in phasor analysis, so poorer recovery of decay information. It seems that NC-PCA is a more robust alternative in this case.

Effect of the instrument response function The measured fluorescence decay is always the convolution of the "perfect" fluorescence exponential decay and of the instrument response function, itself a combination of laser pulse width and detector transit time spread. This creates a distortion of the decay which can be substantial. IRFs can be measured or estimated for better extraction of decay parameters through fitting using iterative deconvolution (the decays are fit knowing they are convolutions) [31]. In phasor analysis, the effect of the IRF can be accounted for [216], so that a single-exponential decay indeed lands on the semi-circle. We tested the effect of IRFs of various widths (FWHMs) on simulated FLIM data, using the same parameters as for the background effect simulation. This time, IRFs of 0.235, 1.18 and 2.35 ns were convolved with the exponential decays prior to NC-PCA. Results show that the eigenvectors are visibly affected (Figure 4.20), reflecting the widened shape of the decay when the IRF is large. However, the two components were still

accurately determined, with no or very little modification in the score image contrast, as seen from the high α values and similarity in the images.

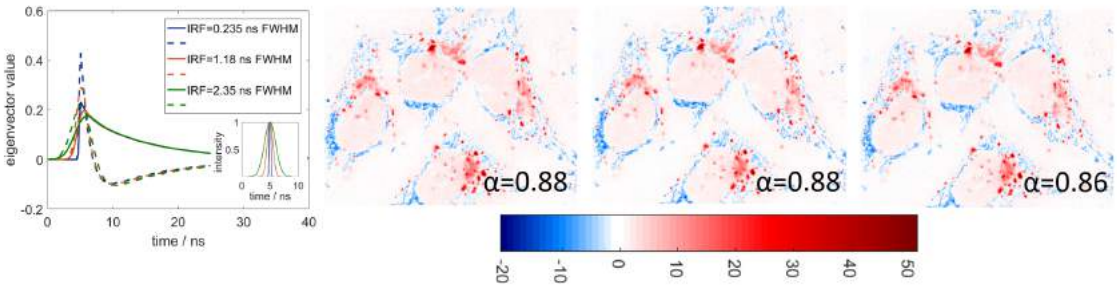

Figure 4.20: Effect of the IRF width on NC-PCA results for simulated 2-component data (see parameters in previous paragraph). Left: first and second eigenvectors for IRF with 0.235 (blue), 1.18 (orange) and 2.35 (green) ns FWHMs. Inset: The normalised pulses are shown, centered at 5 ns. Centre and right: second score images for each of these respective cases, with corresponding alpha values.

Conclusion from NC-PCA validation on simulated data NC-PCA has proved to be at least as performing as other global analysis methods such as phasor and mf_d, while offering greater sensitivity and robustness to experimental conditions such as non-fluorescent background, large IRF or incomplete decays. NC-PCA can now be tested as a proof of concept on experimental data.

4.1.4 Application of NC-PCA to experimental data

4.1.4.1 Detection of fine lifetime variations at an interface

Large fluorescent beads made of polymer encapsulating a fluorophore were imaged in glycerol using confocal TCSPC-FLIM with 467 nm excitation (Fig. 4.21. A). No particular lifetime contrast was expected on this sample; however when using NC-PCA it was clear that two different regions were identified on the beads (Fig. 4.21.D-F). Upon fitting the data using non-linear least squares and a single-exponential model, the lifetime on the edges of the bead was slightly ($<$5%) shorter, going from 2.9 to around 2.8 ns (Fig. 4.21.B).

We postulate that this may be due to a refractive index mismatch between the inside and the outside of the bead, yielding shorter lifetimes at the interface, as established by Strickler and Berg [22]. This is is confirmed by the fact that the effect was reversed when the beads were imaged in water: the lifetime was slightly longer in the inside. This also indicated that lifetime variation was not due to a correlation between lifetime and intensities, which were lower at the edges of the bead. Results suggest that this effect was detected by PCA, as evidenced by two score images with α values above 0.1 (1 and 0.13, respectively) and visible contrast. The first score image is correlated to the integrated intensity (see panels A, D and G - the correlation between the two

images is above 99%), while the second image displays higher positive scores at the interface and negative scores inside the bead (see panels B and E), with small but significant correlation with lifetime values obtained from fitting (ρ=0.25). The structure in the second eigenvector is visible but less obvious than in the data simulations (Panel F). This may be due to the proximity of the decay profiles in the two regions identified.

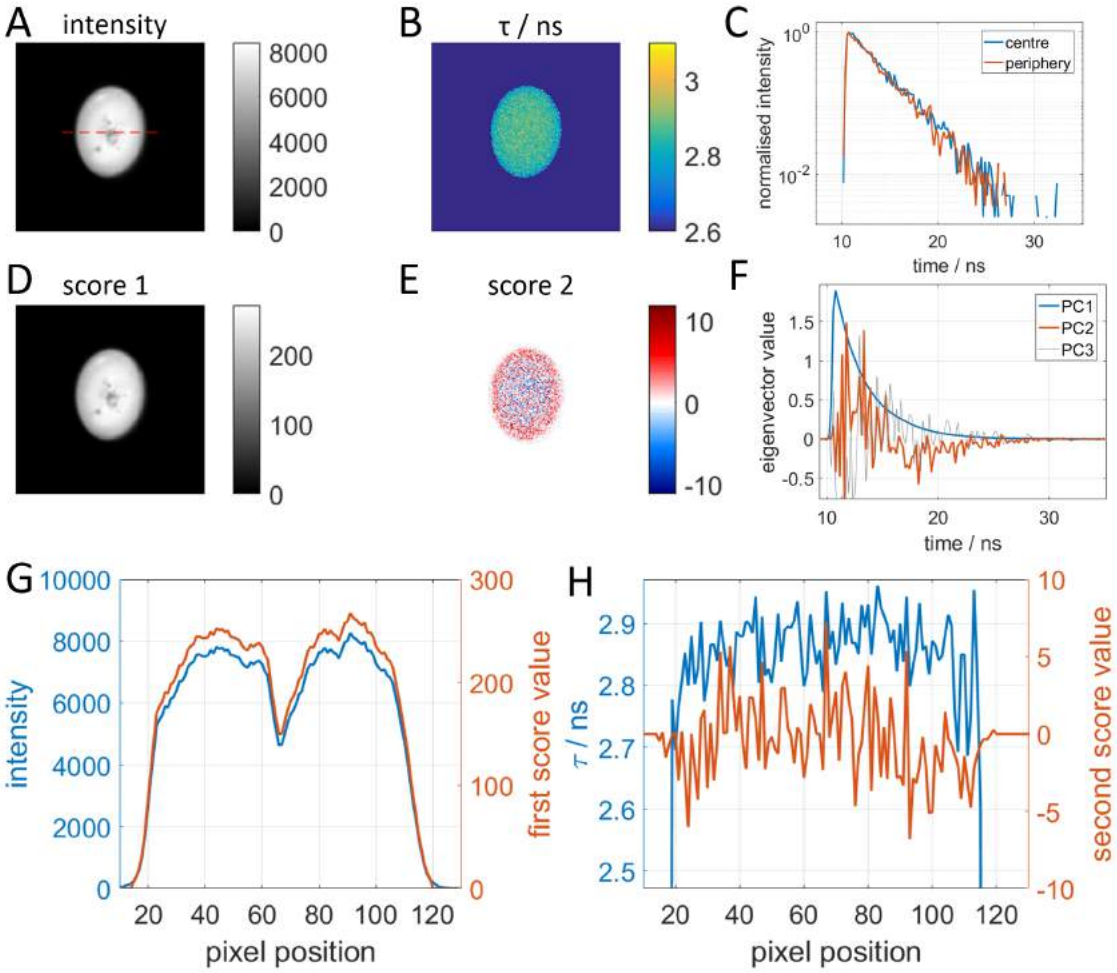

Figure 4.21: NC-PCA results on a fluorescent bead in glycerol. Initial image was 512-by-512 pixels; a bin factor of 2 (real binning - reducing the number of pixels) was applied to the data so that lifetimes could be more accurately fitted. A: Integrated intensity image. B: Single-exponential lifetime fit C: Representative decays in the centre and periphery of the bead. D: First Score image, E: Second Score image, F: NC-PCA eigenvectors, G: Pixel values along the profile shown by the red dashed line on panel A for intensity and score values. H: Pixel values along the same profile for lifetime and second score values (note that the negative score values were taken so that the evolution of score values was in the same direction as τ values).

Phasor analysis of the same data showed a very uniform lifetime distribution and overlapped the universal circle, confirming mono-exponentiality (Fig. 4.22).

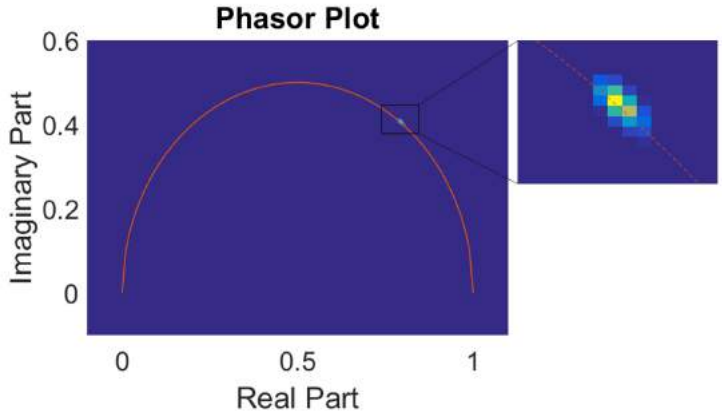

Figure 4.22: Phasor analysis of the FLIM image of a fluorescent microbead in glycerol. Note that an offset phase of -0.5 time bins was applied to correct for the effect of the instrument response and obtain a cloud of points on the universal circle. The inset shows a zoom on the cloud of points.

This experimental application shows the efficiency of NC-PCA in resolving small lifetime changes in the image. It also shows the complimentary information provided by phasor and NC-PCA, where phasor projection gives reliable information on the number of exponential components, while NC-PCA sensitively identifies contrast in the image according to lifetimes regardless of exponentiality of the data.

4.1.4.2 Detection of membrane microenvironments and effect of cholesterol depletion using NC-PCA on HeLa cells stained with di-4-ANEPPDHQ

Di-4-ANEPPDHQ was used in initial experiments since it was more photostable and allowed higher intensities, to validate the performance of NC-PCA on experimental data relevant to our investigation. NC-PCA on HeLa cells stained with Di-4-ANEPPDHQ yielded 2 structured principal components (Fig. 4.23). The first score image (Fig. 4.23. c) is closely related to the integrated intensity image (Fig. 4.23. a), with a Pearson correlation coefficient above 0.99 between the two images. The second score image (Fig. 4.23. d) shows clear contrast between the plasma membrane (negative scores, in blue) and internal membranes (positive scores, in red), highlighting the spatial distribution of two distinct microenvironments, in agreement with previous experimental results [138].

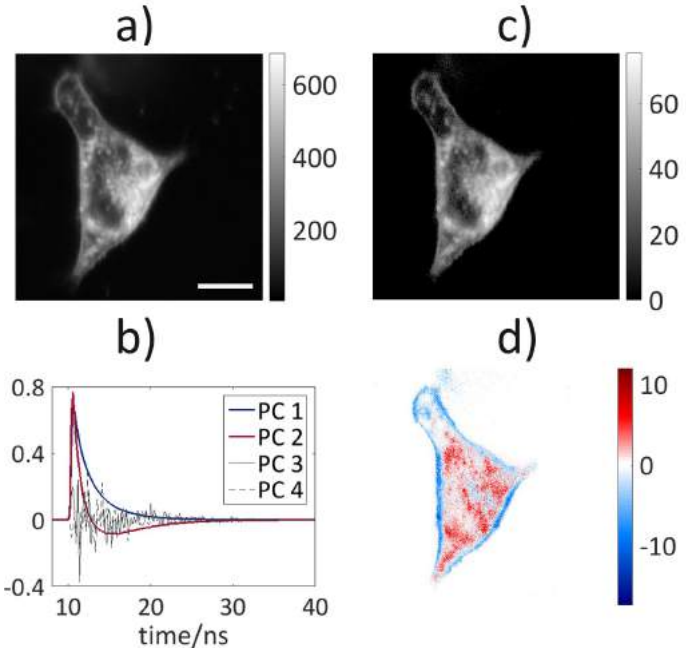

Figure 4.23: HeLa cells stained with di-4-ANEPPDHQ and analyzed with NC-PCA (representative results from n = 13 cells). a) Integrated intensity image. The average pixel contains 82 photons. b) Four first eigenvectors obtained with NC-PCA. c) First and d) second score images corresponding to the two first principal components. Scale bar = 10 μm.

NC-PCA was compared to phasor projection for the same experimental data, as visible in Fig. 4.24. The phasor cloud lies within the universal circle, indicating multi-exponential decays. The phasor image and the second score image from the NC-PCA results were rescaled so as to appear on a color scale ranging from 0 to 1, to allow direct comparison. Both show similar performances, with α values above 0.8 and contrast essentially between the plasma and internal membranes. It is worth noting that NC-PCA projection is robust to the threshold value, due to conservation of intensity information during the analysis. This is not the case for phasor projection, which operates on normalised data, hence assigning equal importance to pixels with different intensities. NC-PCA therefore does not require this thresholding as a pre-processing step which simplifies the analysis.

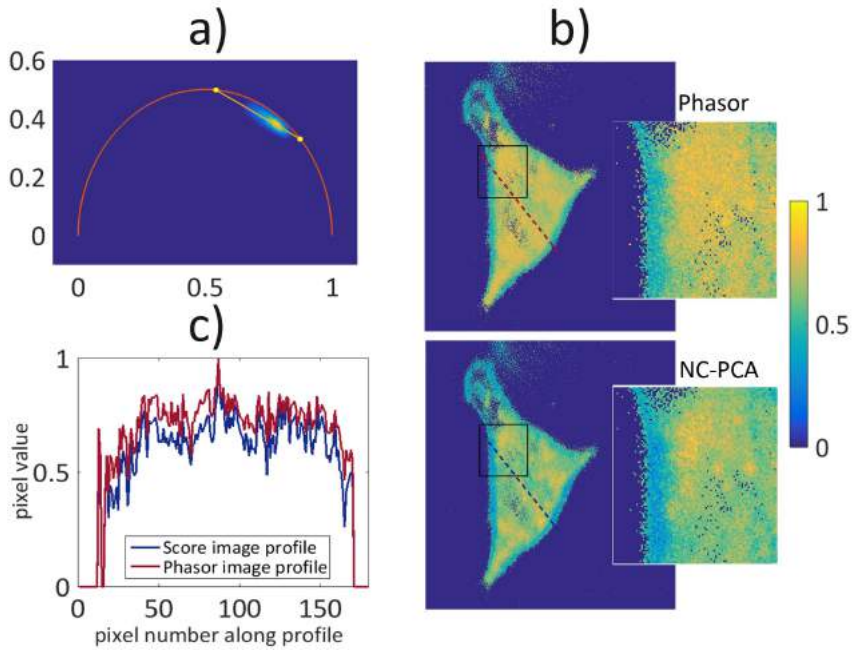

Figure 4.24: Comparison of NC-PCA and phasor projections on FLIM images of HeLa cells stained with di-4-ANEPPDHQ. (a) Phasor plot of the data; under a 2-component assumption the cloud was fitted to a straight line and intersection points with the universal circle found. b) The phasor image (above) and second score image from NC-PCA (below) are represented in the same colour scale. The zoomed section corresponds to a 100 × 100 pixel square. c) The pixel values along the dashed lines in b) are plotted as profiles.

The modification of plasma membrane order during cholesterol depletion was investigated similarly to what was done in the previous chapter. Data from membrane regions (highlighted in Fig. 4.25. a) in control and cholesterol-depleted cells was projected in the basis created by the control cell shown in Fig. 4.23. b. Whilst there is no significant change in the first score values (which indicates similar intensities), the scores on the second eigenvector are shifted towards the positive values (4.25. b), closer to those of the intracellular membranes. This suggests that the lifetime of di-4-ANEPPDHQ decreases upon cholesterol depletion, which is the opposite of what was observed with laurdan. These results are however consistent with previous work from Owen et al. [185] on lifetime of di-4-ANEPPDHQ upon cholesterol depletion, and highlight once more that laurdan and di-4-ANEPPDHQ exhibit distinct environmental sensitivity.

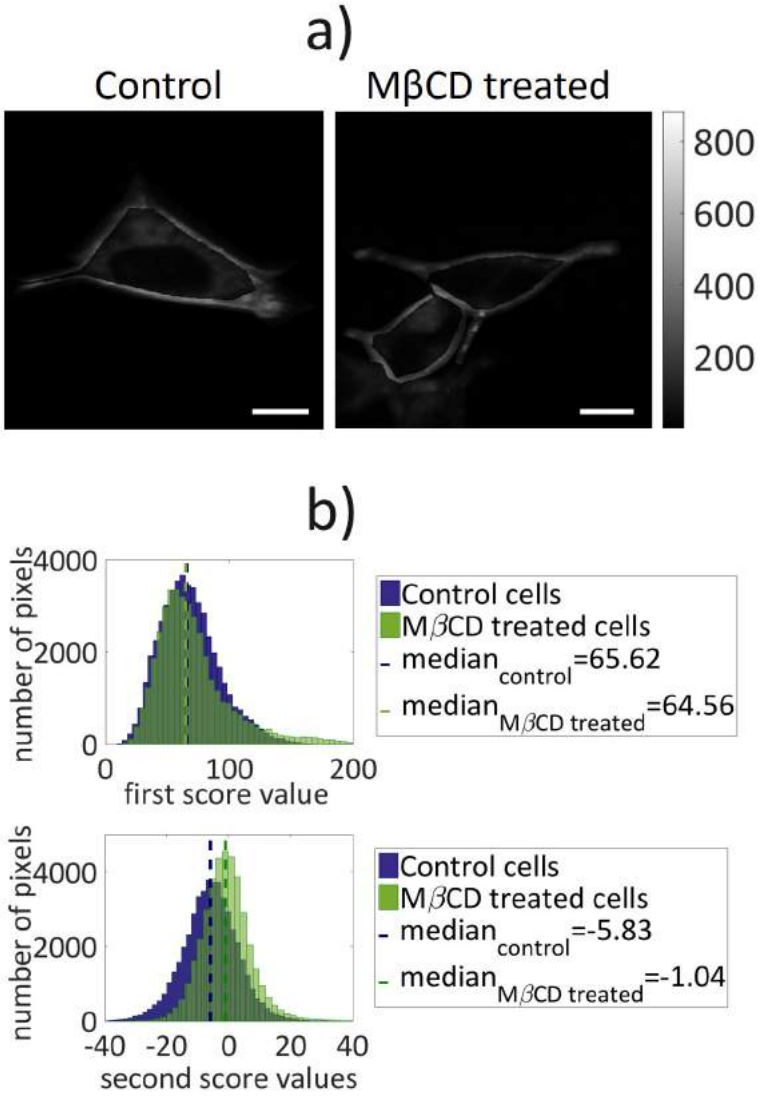

Figure 4.25: The effect of cholesterol depletion on cell plasma membranes. a) Cholesterol-depleted and control cells with selected membrane ROI highlighted. The average intensity of the images in the dataset was 74 photons per pixel. b) Histograms of NC-PCA scores on first (above) and second (below) eigenvectors of membrane regions in control (blue, n = 13) and cholesterol-depleted (green, n = 10) cells. Scale bars = 10 μm.

4.1.5 NC-PCA for de-noising

PCA is often used as a de-noising step in signal processing and has been applied to various fields of scientific imaging [217, 213, 218]. To de-noise data using PCA, the first significant principal components are selected while the ones containing no structure are discarded in the projection. For each individual data point, a linear sum of the selected eigenvectors weighed by the corresponding score of the data point yields the de-noised result (See Eq. 4.4). An example of the effect of NC-PCA based filtering is shown on a representative pixel of the HeLa cell in Fig. 4.26, a procedure which could also be used for pre-processing in phasor analysis or decay fitting approaches or other component recovery strategies.

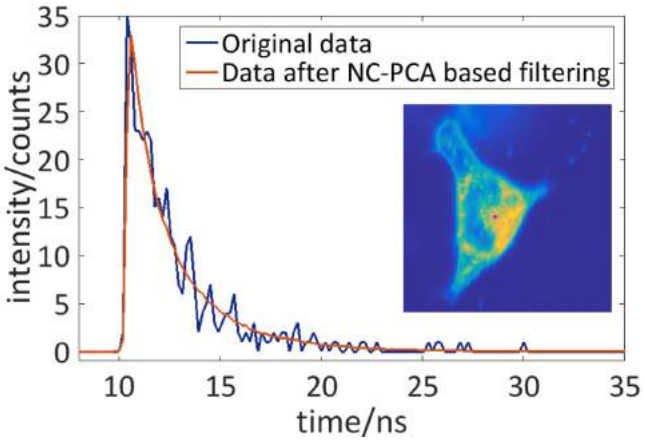

Figure 4.26: The decay in the pixel shown in purple on the inset image (integrated intensity) is plotted before (blue) and after (orange) NC-PCA based filtering.

4.2 NC-PCA and time-resolved anisotropy data

While it is useful to develop novel image analysis methods for FLIM data, it is even more profitable to implement such routines for time-resolved fluorescence anisotropy imaging data. Indeed, with TR-FAIM it is rare that contrast according to anisotropy decay parameters can be displayed on a pixel-wise basis in samples such as cells or tissues. This is due to the limitations on the signal-to-noise ratio, as explained in section 1.6.5.1. Typically, anisotropy decays are computed by binning polarisation-resolved intensity decays in pixels from specific regions of interest (ROI). This precludes the observation of fine contrast, as well as many image analysis procedures such as the correlation between anisotropy and lifetime or spectral parameters, etc. The analysis procedures described in the first section are unsatisfactory because of their dependence on high intensities in parallel and perpendicular channels, or not being applicable in case of multi-exponential intensity decays and presence of an r_∞.

The idea here is to apply NC-PCA to TR-FAIM images, much in the same was as was done for FLIM. The first part describes adapting the NC-PCA procedure to TR-FAIM, while the second section shows the results on simulated data. In the last part, NC-PCA is used on experimental data, and NC-PCA is used to correlate anisotropy and intensity decay information in images acquired on the polarisation-resolved TCSPC FLIM system.

4.2.1 Adaptation of NC-PCA to TR-FAIM

The principle of PCA on TCSPC data shown in the previous section applies here, with the following relationship between anisotropy in pixel i, $r_{k,i}$, score value on principal component p, $s^r_{p,k}$, and p^{th} principal component value, $v_{p,i}$ (adapted from Eq. 4.4):

$$s^r_{p,k} = \sum_{i=1}^{q} v_{p,i} r_{k,i} \tag{4.20}$$

The main modification concerns the nature of the noise correction. While FLIM displays well-characterised Poisson noise, the noise distribution of TR-FAIM data is not analytically defined. Several options are therefore possible to operate a noise correction before applying PCA: applying no noise correction whatsoever (unscaled PCA), using the classic normalisation with the standard deviation of the anisotropy at each time bin (variance-scaled PCA), and lastly, using the uncertainty associated with any anisotropy reading, as calculated in equation 1.52 (uncertainty-scaled PCA). These three types of noise correction were tested on simulated data. Noisy anisotropy images were simulated according to the procedure described in section 1.6.5.2 and as illustrated in Fig. 4.27.

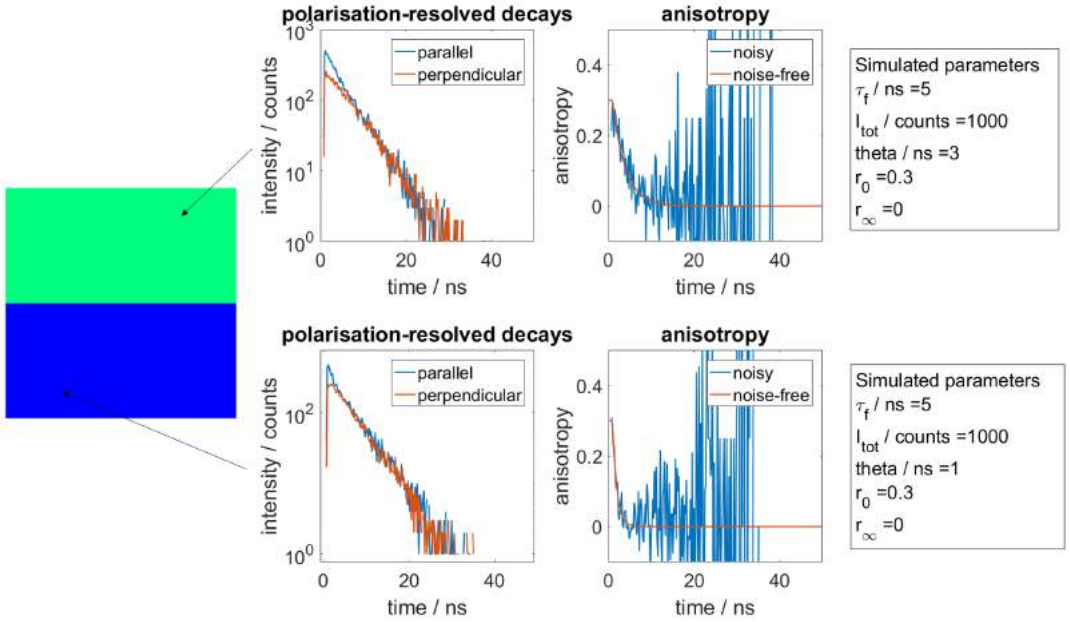

Figure 4.27: Simulation of simple anisotropy image data for validation of PCA method and noise correction. The image consisted in 2 rectangles of 50-by-25 pixels each (as shown on the left). Each rectangle was attributed distinct intensity and/or decay parameters as required. An example of simulated polarised intensity decays and corresponding anisotropy decays is shown on the central panels, with the corresponding input parameters shown in the boxes on the right. Here, all parameters are kept identical, except for $\theta = 3$ ns on the upper rectangle, and $\theta = 1$ ns on the lower one.

PCA with all three scalings was performed. Uncertainty and variance-based noise correction produced similar results: a single score image bearing contrast (Fig. 4.28.A), and similar eigenvector profiles (Fig. 4.28.B-C). Uncertainty and variance scaling also show differential noise patterns in the second principal component, highlighting the effect of these two scaling strategies. Unscaled PCA showed no contrast in the first principal component, suggesting that the data was dominated by noise without noise correction (Fig. 4.28.D - score image not shown). If the noisy tail end of the data was removed, then unscaled PCA showed similar results to the two other types of scalings,

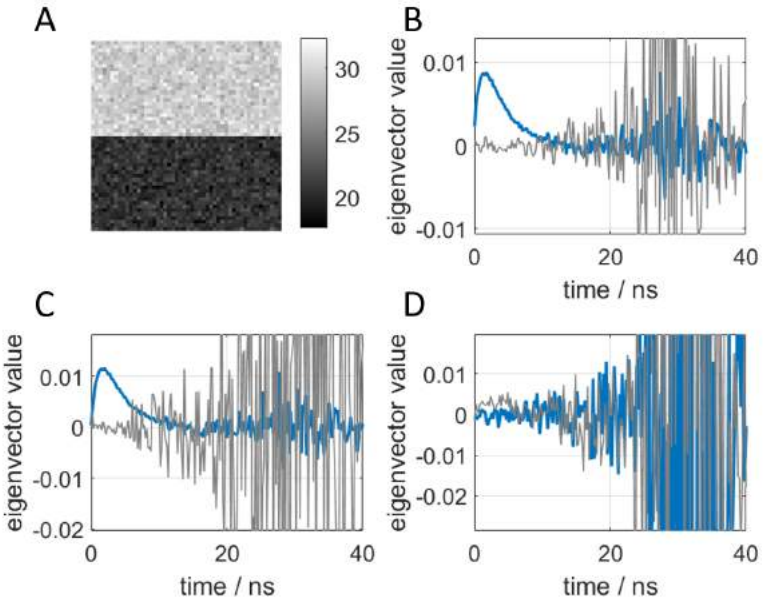

Figure 4.28: PCA results with 3 different scalings applied to the simulated anisotropy image data shown in Fig. 4.27. A: Score 1 image from the anisotropy-scaled PCA. This image was identical for all variance and uncertainty-based scalings. B: eigenvectors for uncertainty-scaled PCA. C: eigenvectors for variance-scaled PCA. D: eigenvectors for unscaled PCA.

suggesting that the highly noisy end of the anisotropy decays was the main contributor to the failure of unscaled PCA.

Since it is not obvious from this example whether uncertainty or variance-based scaling is more appropriate, some limiting conditions were sought to identify the effect of these corrections on the success of the procedure. In particular, it was verified, whether the intensity decay parameters I_0 and τ were reflected in the PCA results. Indeed, fluorescence intensities at any time bin will affect the noise level in the anisotropy decay, and this in itself can constitute a source of contrast in the data which is undesirable. To test for this effect, simulated data with identical anisotropy decay parameters, but different intensity parameters I_{tot} and τ was created, and PCA results analysed for each type of scaling. Parameters were chosen to reflect values of typical experimental data obtained in the lab. Input parameters and results are summarised in Fig. 4.29.

	Zone	I_{tot}	τ / ns	r_o	θ / ns	r_∞	NC-PCA results		
							$\alpha_{\delta(r)}$	$\alpha_{\sigma(r)}$	$\alpha_{n.s.}$
A	1	2.6x10^3	3	0.3	3	0.1	0.06±0.03	0.65±0.01	0.58±0.02
	2		5						
B	1	3.4.x10^3	4				0.2 ± 2.10^{-2}	6 ± 9.10^{-3}	0.4 ± 1.10^{-2}
	2	2.1x10^3							

(a)

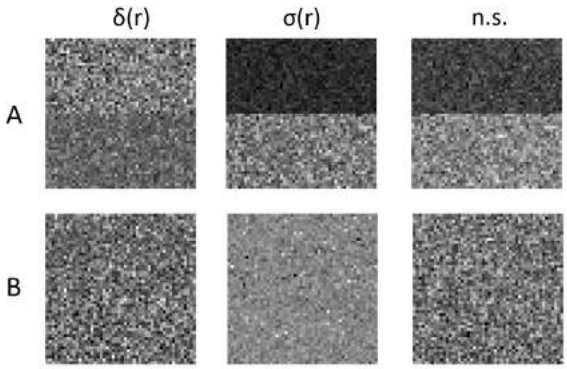

(b)

Figure 4.29: Testing the effect of intensity parameters on NC-PCA of anisotropy data. (a) table showing the input parameters and NC-PCA results for simulations A and B. Note that for simulation A, the initial intensity was different for zones 1 and 2, in order to obtain identical total intensities. Simulations with identical initial intensities (and therefore different total intensities, due to different lifetimes) yielded similar results. In simulation B, I_0=165 counts in zone 1 and 100 counts in zone 2 (on average). Each simulation was carried out 10 times with identical noise-free input and random Poisson noise on the polarisation-resolved intensity decays - average α values are given with their standard deviation. (b) First score images for each type of scaling in simulations A (above) and B (below).

Results from simulation A show that uncertainty-based scaling yields significantly lower α values than variance-based and unscaled PCA, with the two other types producing significant contrast in the first principal component (α>0.1). This suggests that this type of noise correction more accurately discards noise originating from the structure of the intensity decays. At higher intensities, $\alpha_{\delta(r)}$ increased and took values above 0.1, but was always lower than the two other types of scalings. It is also interesting to see that unscaled PCA is sensitive to changes in lifetimes, while it did not detect changes in rotational correlation times, highlighting the strong effect of fluorescence intensity on the noise levels in anisotropy decays. Results from simulation B show that all types of scalings accurately discard the effect of intensity variations in the data for a fixed lifetime, as seen from the low α values and absence of contrast in the score images. Uncertainty-based scaling showed even lower α values again than the two other types of scaling.

From these observations, it was determined that uncertainty-based and variance-based scalings enable extraction of anisotropy decay information, but that the uncertainty-based scaling was more efficient in discarding the noise originating from intensity differences in the data. Therefore, this type of scaling was selected for further investigation of the efficiency of NC-PCA on anisotropy data

	Zone	τ / ns	r_∞
A	'mitochondria'	4	0.10
	'lysosomes'		
B	'mitochondria'	4	0.1
	'lysosomes'		0.05
C	'mitochondria'	5	0.1
	'lysosomes'	4	0.05

(a)

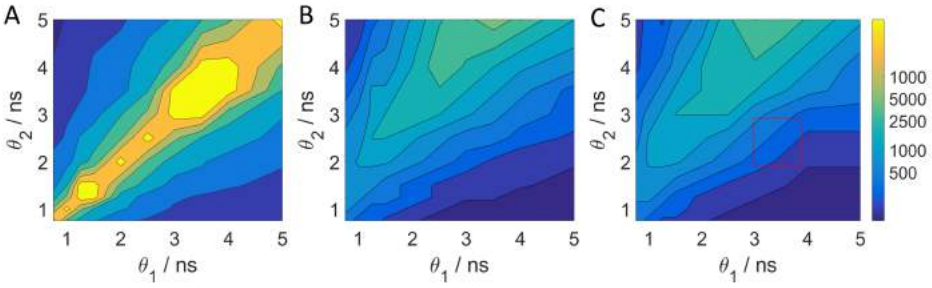

(b)

Figure 4.30: Effect of intensity and anisotropy parameters on NC-PCA success. (a) Table summarising the changes in parameter values for simulations A, B and C. For all three simulations, θ_1 and θ_2 were varied between 0.75 and 5 ns (10 values), and total intensities were varied between 10^3 and 3.10^5 photons per decay on average (14 values). (b) Minimum peak intensities necessary to resolve two anisotropy decay components in an image as a function of θ_1 and θ_2 values, for each of the cases described in (a). Note that the colour scale is in peak intensity, not total intensity, for easier readability. The red square in panel C represents the parameter space relevant to the data of laurdan in HeLa cell membranes from the previous chapter.

with varying decay parameters and noise levels. These results also show that the noise in anisotropy data is in general more dependent on variations in lifetime, than variations in fluorescence intensity.

4.2.2 Assessing NC-PCA performance as a function of decay parameters θ, r_0, r_∞, I_0 and τ

Parameter sweeps were performed to establish the minimum intensities necessary to detect contrast in the first score image (corresponding to the criterium $\alpha_1 > 0.1$, as established in the previous section) in different situations. Since anisotropy decay profiles depend on many more parameters than intensity decay profiles, there are potentially an infinity of cases to simulate. The investigation was therefore limited to cases relevant to experimental data obtained on HeLa cells from the previous chapter, where a correlation between τ, θ and r_∞ was observed. The input images used were the reduced "HeLa Cells" image, to reproduce experimental data more faithfully.

First, parameters τ and r_∞ were fixed to $\tau = 4$ ns and $r_\infty = 0.1$ while θ_1 and θ_2 were varied (Fig. 4.30.A). Then, the same simulations were carried out with a situation where $r^1_\infty = 0.1$ and $r^2_\infty = 0.05$ Fig. 4.30.B). Lastly, two decay times $\tau_1 = 5$ ns and $\tau_2 = 4$ ns were used.

Results from these simulations show that minimal intensities required to resolve two anisotropy

decay components are approximately an order of magnitude higher than for NC-PCA of FLIM, reflecting the fact that anisotropy data is noisier. When r_∞ is varied, the two decay components are resolved for lower intensities overall (comparison of panels A and B); however, the profiles of NC-PCA performance with respect to θ_1 and θ_2 become asymmetric. Indeed, in B, the parameters are better resolved than in case A when θ_1 (coupled with $r_\infty = 0.1$) is longer than θ_2 (coupled with $r_\infty = 0.05$), and less well resolved than in case A when θ_1 is shorter than θ_2. This asymmetry is further increased when the lifetime associated with θ_2 is shorter than the one associated with θ_1. This illustrates the fact that in the presence of noise, it is difficult to discriminate between a combination of long θ - low r_∞ and short θ - high r_∞, and that this difficulty may not be just limited to fitting. However, in the case of our experimental data, short θ values are correlated with lower r_∞ values and also shorter lifetimes, which means that the parameter area of interest would be located in the lower-right of panel C (highlighted by the rectangle in red), and that two anisotropy components could potentially be resolved with initial intensities lower than 500 photons on average. This is better than what was obtained through decay fitting, where a minimum of 1000 photons is in general necessary to confidently fit an anisotropy decay. For a case where $\theta_1 = 3$ ns and $\theta_2 = 2$ ns, we obtain a minimal intensity of 330 photons on average in the maximum bin.

4.2.3 Application of NC-PCA on experimental time-resolved anisotropy and intensity data

4.2.3.1 Case of free rotation: resolving lifetime and rotational correlation time changes in water-glycerol mixtures.

A simple test of the performance of NC-PCA on anisotropy data can be carried out using fluorescein in water-glycerol mixtures. The rotation of the dye in high glycerol content mixtures is slower, while the fluorescence intensity remains similar. The objective is to determine whether information recovered by NC-PCA was a good predictor of rotational correlation times in the image. Interestingly, higher glycerol contents also yield higher refractive indices, which produce slightly shorter lifetimes, linked to the Strickler-Berg relationship (Eq. 1.7). This is therefore also a good system to test the simultaneous resolution of contrast in lifetime and anisotropy parameters using NC-PCA.

In practice, 80:20 and 60:40 glycerol:water mixtures were prepared, and fluorescein was dissolved in each of them to a micromolar amount. They were then placed in adjacent wells of an 8-well plate and imaged with a low-magnification objective on the setup described previously, so that the two wells would appear in the field of view. A 128-by-128 pixel image size was chosen to optimise intensity in each pixel. Intensity and steady-state anisotropy images are shown in Figs.

4.31. A and D. The intensity decays in each pixel were fitted to a mono-exponential model to yield the fluorescence lifetime τ, shown in Fig. 4.31. B, with representative decays shown in panel C. The rotational correlation time was also computed from the Perrin equation (Eq. 1.30) using the lifetimes τ, steady state anisotropy values, and $r_0 = 0.38$ taken for the fundamental anisotropy of fluorescein. Note that this value was lower on our setup due to depolarisation through the objective, so the values of θ may be slightly under-estimated; however, the range of value remains unchanged. Representative anisotropy decays are shown in panel F, corresponding to the same pixels as panel C. Note that while there is a clear difference between the two pixels in terms of anisotropy decay, these decays are too noisy to be fitted.

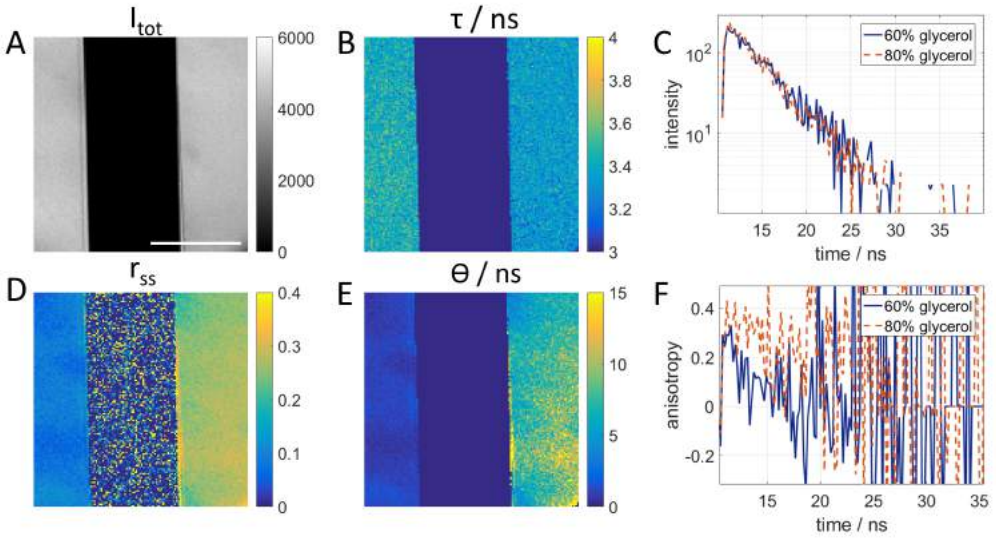

Figure 4.31: Fluorescein in 60:40 and 80:20 glycerol:water mixtures. A. Total intensity image. B. Lifetime image. C. Representative intensity decays from one pixel in each well. D. Steady-state anisotropy image. E. Rotational correlation time image. F. Representative anisotropy decays from one pixel in each well.

NC-PCA was performed on the time-resolved intensity and anisotropy images calculated from the Perrin equation. Results on the anisotropy data show one principal component, and the corresponding score values were highly correlated to rotational correlation time ($\rho = 0.95$), and to the fluorescence lifetime to a lesser extent ($\rho = -0.5$), as shown in Fig. 4.32.

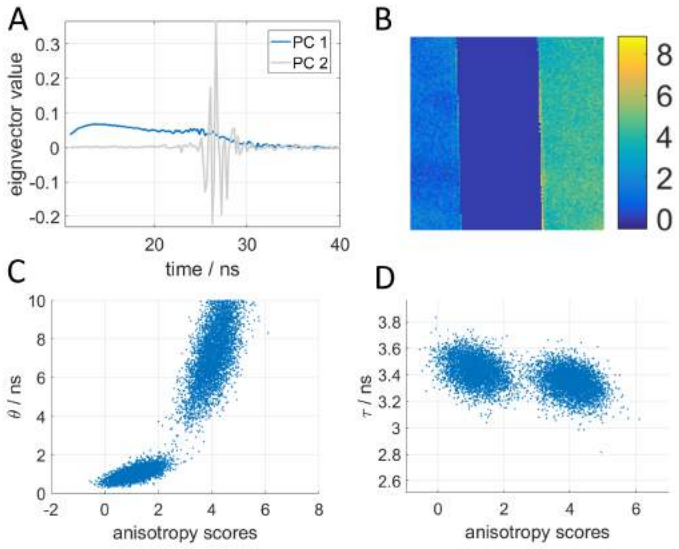

Figure 4.32: NC-PCA on anisotropy data of fluorescein in water-glycerol mixtures. A. Principal components. B. First score image. C. Scatter plot of anisotropy score against theta pixel values. D. Scatter plot of anisotropy score against lifetime pixel values.

Results on the intensity data show two principal components, as expected, with the first principal component representative of pixel intensity ($\rho = 1$), while the second principal component was correlated to the fluorescence lifetime ($\rho = -0.75$). There was also a correlation with θ and the second principal component ($\rho = 0.54$) though this correlation was lower.

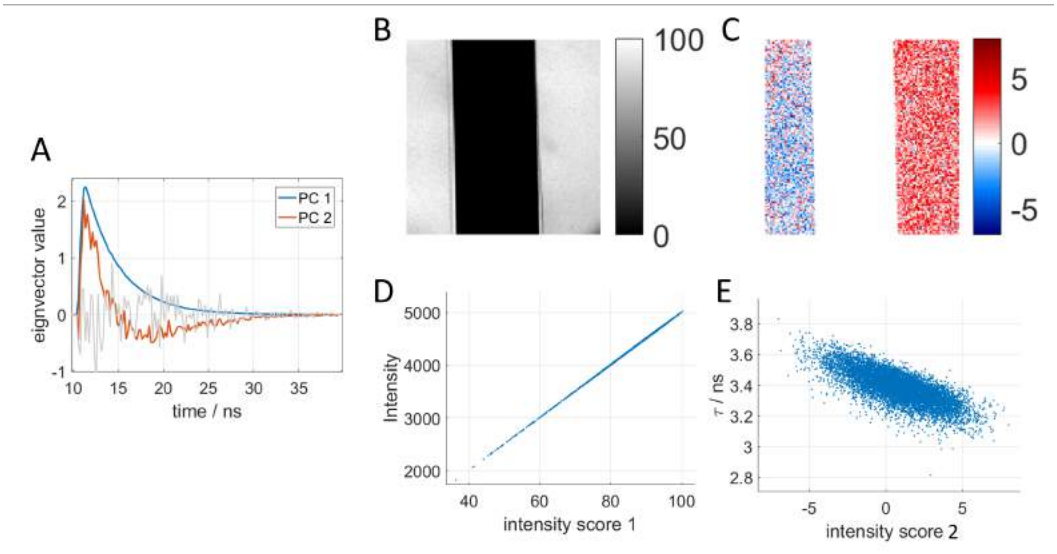

Figure 4.33: NC-PCA results on the intensity decays of fluorescein in glycerol. A. Principal components. B. First score image. C. Second score image (Vive la France!). D. Scatter plot of score 1 against intensity pixel values. E. Scatter plot of score 2 against lifetime pixel values.

The main result here is that the NC-PCA procedure on anisotropy was successful in resolving contrast according to rotational correlation times. The first NC-PCA anisotropy component was the best predictor of the rotational correlation time, and conversely, the first principal component

was mainly determined by rotational correlation times (as opposed to lifetimes). The residual correlation between intensity NC-PCA principal components and θ, and anisotropy principal components and τ, is inevitable due to the underlying correlation between τ and θ. Score values for the two NC-PCA routines can now be used to represent the contrast in the data in terms of anisotropy and lifetimes as 2-D histograms, shown in Fig. 4.34.

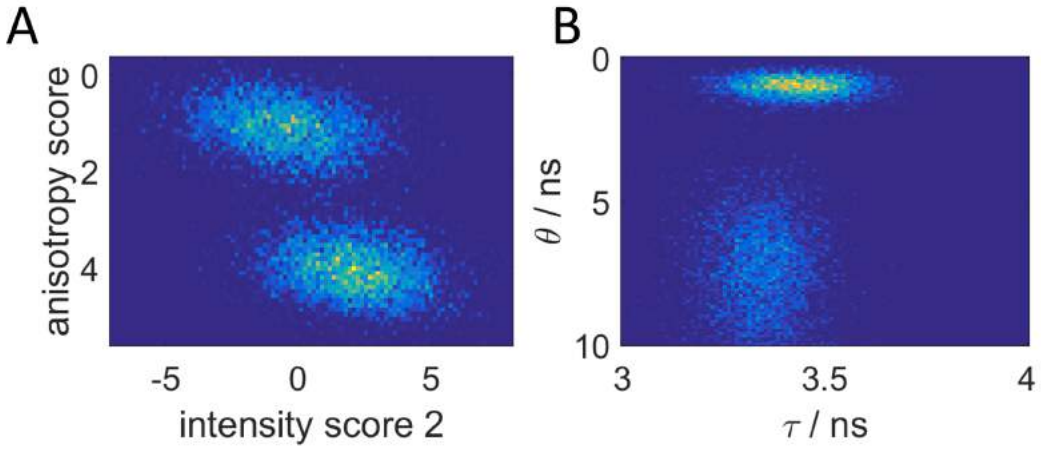

Figure 4.34: 2-D histograms displaying contrast in the data according to anisotropy and lifetime. A. Contrast resolved using NC-PCA. B. Contrast resolved using the input parameters.

From this, the effect of PCA on projecting a cloud of data into a new space with optimisation of the contrast is clearly visible. It is also clear that NC-PCA modifies the spread of data compared to the initial parameter values, as shown by the parallel between panels A and B in Fig. 4.34.

This application shows that NC-PCA is feasible on experimental anisotropy data, and can be combined with NC-PCA of FLIM to resolve contrast determined by lifetime and anisotropy simultaneously. On this relatively simple system, it was possible to compute rotational correlation times from the Perrin equation since pixel-wise fitting of lifetimes was feasible due to the mono-exponential character of fluorescein decay, and the absence of a r_∞. In essence NC-PCA provides similar information to the parametric analysis, albeit less noisy. In most relevant cases however, intensity decays are more complex, and in our specific case, the additional presence of an r_∞ prevents pixel-wise resolution of decay parameters, hence the usefulness of this approach.

4.2.3.2 Application of NC-PCA to TR-FAIM of di-4-ANEPPDHQ in model membranes

NC-PCA was now used to resolve anisotropy contrast in lipid bilayers. Here di-4-ANEPPDHQ was used instead of laurdan since it was more photostable and yielded brighter images. In the case of anisotropy in membrane environments, rotation is hindered and fluorophore distribution is locally

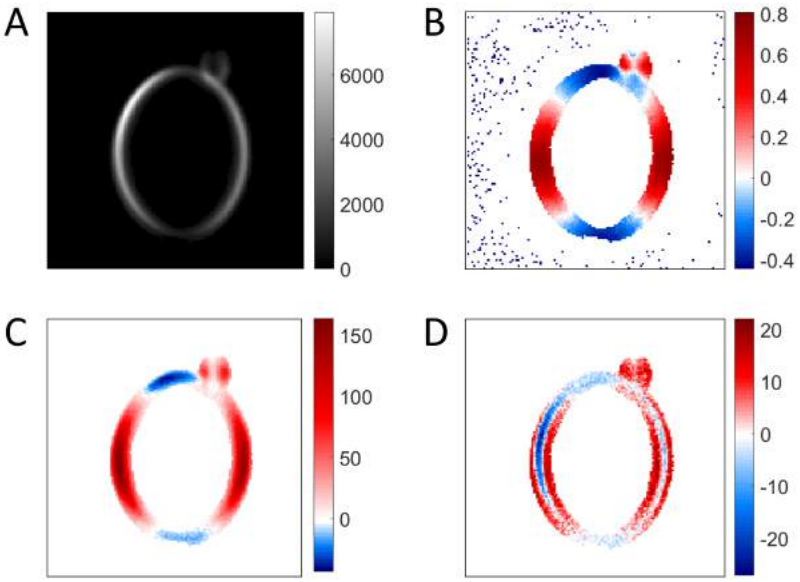

Figure 4.35: NC-PCA on time-resolved anisotropy image of a SM-Chol 7:3 vesicle stained with di-4-ANEPPDHQ. A. Intensity image. B. Steady-state anisotropy image. The 'blue-white-red' colourmap is used here to highlight the distribution of anisotropy values. C. First score image. D. Second score image.

non-random; this yields heterogeneous r_0 and r_∞ values and can potentially constitute directions of variance in a time-resolved anisotropy image. To test for this effect, NC-PCA was applied to single-phase GUVs stained with di-4-ANEPPDHQ, where r_0 and r_∞ vary with angular position relative to the excitation polarisation, but the rate of rotational diffusion does not change, so what is expected is a single principal component reflecting the angular dependence of anisotropy levels. In essence, the situation is not dissimilar to that of an intensity image with a single decay component from the previous section. However, NC-PCA of such data yielded 2 principal components. The first score image (Fig. 4.35.C) was highly correlated with steady-state anisotropy (Fig. 4.35.B) (ρ=0.89), and also to pixel intensity (Fig. 4.35. A), to a lesser extent (ρ=0.45). The opposite trend was observed on the second score values (Fig. 4.35.D), with higher correlation with intensity (ρ=-0.65), than with anisotropy values (ρ=0.35). Correlations between NC-PCA results and input data is further illustrated by the line profiles in Fig. 4.36. C and D. The correlation between steady-state anisotropy and intensity was in itself low (ρ=0.17). NC-PCA on the intensity image yielded one principal component which was as usual strongly correlated to total intensity (not shown). No other principal components indicate that the lifetimes are homogeneous within the vesicle.

These results mean that NC-PCA of TR-FAIM data accurately resolves local variation in fluorophore orientation. However, intensity variations within the image are also reflected in the PCA results. This is illustrated by the comparison of pixel values along a section of the GUV

bilayer (Fig. 4.36.B). The steady-state anisotropy values are stable along the profile, showing that the orientation of fluorophores along this section (which actually is a projection of the bilayer at all altitudes within the confocal volume, explaining its thickness) does not vary. The intensity values however show a Gaussian profile. The score values along this profile vary strongly and are correlated with the intensity (ρ=0.95 and -0.97 for scores 1 and 2, respectively) more than with steady-state anisotropy (ρ=0.59 and -0.48, respectively). Increasing the threshold value to select pixels of higher intensities only did not improve the situation - the bilayer cross-sections became narrower, but the intensity variation was still reflected in a second principal component.

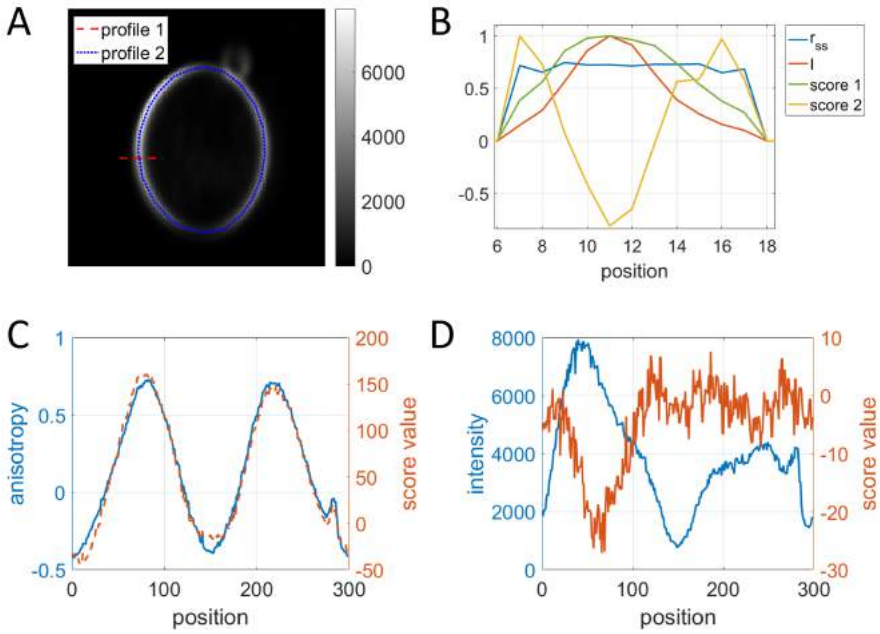

Figure 4.36: Analysis of pixel values for intensity, steady-state anisotropy and NC-PCA anisotropy results on two line profiles shown in A. B. pixel values for steady-state anisotropy, intensity, score 1 and score 2 along line profile 1. C. pixel values for steady-state anisotropy and score 1 along line profile 2. D. pixel values for intensity and score 1 along line profile 2.

This shows that the PCA results are a combination of anisotropy and intensity information, probably due to the change in noise levels caused by changes in intensities. This would suggest that the noise correction applied is not sufficient to reject variations in intensity from PCA on anisotropy data, and that this could potentially hinder the resolution of contrast in rotational correlation times when intensity fluctuations in the image are large. This result differs from NC-PCA on FLIM data, where the intensity fluctuations were always easily distinguished from lifetime fluctuations. This may reflect the larger impact of the noise on the contrast between two pixels in anisotropy data. This last point precludes further application of NC-PCA on TR-FAIM with the present noise correction strategy. Indeed, in complex images such as live cells or phase-separating GUVs, different regions of interest (plasma membranes vs. internal membranes, or ordered vs.

disordered domains) have very different intensity levels, and therefore noise levels in the anisotropy decays. This is then expected to correlate with changes in anisotropy parameters, which makes discrimination between the two effects difficult.

To correct for this effect, one possible solution is the implementation of a pixel-specific noise correction. This type of scaling is commonly performed on datasets prior to PCA before, for example in ref. [210]. The Anscombe transform is another example of such a procedure [219]. Indeed, our type of noise correction is currently based on image-wide averaging of the noise estimates at each time bin and therefore does not incorporate pixel-by-pixel intensity contrast. This is especially suited for NC-PCA of intensity decay data, and enabled preservation of the linearity of the relationships between pixels in the image. However, in anisotropy data a pixel-by-pixel noise correction procedure may be justified. The appropriate reverse-scaling procedure would then be required to restore the relationship between pixel values.

Conclusions and outlook

In this section, the development and first application of Noise-Corrected Principal Component Analysis (NC-PCA) to TCSPC-FLIM was presented. We show that this approach, which takes into account the Poisson-distributed noise inherent to single-photon detection, accurately resolves the number of emitting components and their distribution in FLIM data without requiring prior knowledge of their individual decay profiles. NC-PCA is a useful novel technique for FLIM processing, due to its robustness in unfavourable conditions such as low intensity, presence of non-fluorescent background and poor component separation. Simulations show that NC-PCA requires fewer photons to identify the components compared to phasor analysis (Fig. 4.15). Poorly separated emitting species are resolved with as few as 200 photons on average per pixel as shown by the simulated FRET example, and performances were superior to the mfd technique (Fig. 4.17). Considering the limited photon budget available from fluorophores [220], performance at low signal to noise levels is an important aspect of our method, which is also relevant for STED-FLIM, where point spread function engineering reduces the available fluorescence signal. Applying our method to experimental data, distinct microenvironments were separated in di-4-ANEPPDHQ stained HeLa cells, showing contrast in lipid microenvironment the plasma and internal membranes. Modification of plasma membrane polarity due to cholesterol depletion was shown by a shift of the second score values.

The eigenvectors of PCA are mutually orthogonal and thus do not offer direct representation of the underlying fluorescence decay components, which are not orthogonal and decay exponentially. However, although component determination is a fundamentally underdetermined problem, sta-

tistical means and model-based optimization can be used to recover individual decay components (such as Independent Component Analysis, Non-negative Matrix Factorisation or End Member Analysis), the discussion of which is outside the scope of this work. NC-PCA is not based on nonlinear fitting, and it only requires a few seconds to perform. The present study shows the feasibility of our NC-PCA approach for experimental TCSPC FLIM data, and highlights key advantages such as compatibility with low photon counts, independence of thresholds and uniform background, and no prior knowledge of fluorescence decay kinetics is required. However, NC-PCA is by no means limited to FLIM analysis and may prove very useful for the analysis of data from various imaging- or non-imaging-modalities such as multispectral fluorescence imaging, positron emission tomography (PET), Raman or CARS imaging. The noise-correction approach can also be generalized to encompass other types of noise, further expanding the range of applicability of NC-PCA.

To this effect, NC-PCA was extended to time-resolved anisotropy data, with a noise correction based on the error propagation of the Poissonian uncertainties into anisotropy values. Results on simulated data show that this approach resolved contrast in anisotropy parameters with approximately 3 times fewer photons than necessary for anisotropy decay fitting. Applied to mixtures of fluorescein in solutions of different viscosity, combined NC-PCA of anisotropy and intensity data efficiently discriminated regions of distinct rotational correlation time and lifetimes. On more complex anisotropy image data, a significant contribution of intensity variations was detected in NC-PCA results, signifying that the variation in noise levels had a significant impact on anisotropy profiles. One possible solution to this issue is the establishment of another type of noise correction, taking the pixel-by-pixel variations in intensity into account, which will be the object of future work.

Chapter 5

Conclusions and future directions

Photophysical characterisation of laurdan and di-4-ANEPPDHQ

By characterising the photophysical behaviour of laurdan and di-4-ANEPPDHQ in solution, some clarifications were brought onto the environmental sensitivity of these fluorophores, which allowed to reduce the set of assumptions related to the true meaning of their fluorescence lifetime and emission spectrum. This will contribute to the conversation about the use of these dyes to sense micro-environments. On this topic, the main findings of this work include:

- Laurdan spectral emission and fluorescence lifetime report on related, but different, aspects of solvent polarity. Laurdan lifetime was correlated with solvent polarity as defined by dielectric constant and dipole moment, while its emission wavelength was strongly correlated with the overall solvation ability of the medium, which is influenced by H-bonding. The relationship between these two observables is reversed in bilayers compared to that of solvents, pointing towards a less obvious correlation between them than previously assumed (Chapter 2).

- The lifetime of di-4-ANEPPDHQ in the S phase suggests an incomplete insertion of the dye in the bilayer. These results offer many subjects for further investigation. This is the object of ongoing work: to address this question, the parallel study of di-4-ANEPPDHQ fluorescence signatures with molecular dynamics simulations will bring useful insight of the localisation and dynamics of this molecule in lipid bilayers of different compositions.

- It also appears that di-4-ANEPPDHQ and laurdan sense different properties of the lipid bilayer, as recently suggested by Amaro et al. [121]. Indeed, di-4-ANEPPDHQ was shown to exhibit significant sensitivity to solvent viscosity (Chapter 2), a property that laurdan does not have (laurdan is highly fluorescent in non-viscous solvents). While this property is likely less relevant in hindered environments such as the lipid bilayer, it suggests that these dyes have clearly distinct photophysical behaviours and environmental sensitivities. This

is further strengthened by the fact that upon cholesterol depletion, the lifetime of laurdan increases, while the lifetime of di-4-ANEPPDHQ decreases, as shown in our experiments here and previously demonstrated by Dr Dylan Owen in his doctoral thesis and published in ref. [185]. Further characterisation of di-4-ANEPPDHQ using spectroscopy and MD simulations will likely inform this question.

Simultaneous probing of membrane microenvironment and order parameters in bilayers and cell membranes

This project has established the theoretical, experimental and analytical framework to perform truly independent but simultaneous quantification of membrane polarity, hydration and order parameters in lipid bilayers and cell membranes using fluorescence microscopy of environmentally-sensitive dye laurdan. The efficient measurement of time-resolved anisotropy in addition to lifetime and emission spectrum on the same field of view constitutes progress in the field of fluorescence imaging in general, as it offers 3 dimensions with which to probe a biological system. Here, 3 parameters were independently measured in a single measuring step, with an additional parameter acquired using 2-colour confocal imaging. This yields data with high information density.

In Chapter 2, this method was applied to the extensive characterisation of the correlations between these parameters in artificial lipid bilayers. Interesting findings include the fact that order parameters and membrane polarity are linearly related as temperature was varied within a lipid phase, and that modifications of the chemical nature of the bilayer preserved this linearity. It was also shown that addition of cholesterol or presence of saturated chains yielded different modifications of the relationship between these parameters. Furthermore, this data supports the theoretical findings of Kinosita et al. [26] regarding the establishment of order parameters θ and Δ. This method was used to inform on the modality of domain mixing in phase-separated lipid vesicles, a subject which can be further investigated by measuring a wider variety of phase-separating binary or ternary lipid compositions. Extensions of this study also include the investigation of the effect of the polar headgroup on membrane polarity and order parameters, as well as the presence of membrane proteins.

This method was then extended to cellular membranes, which showed that the relationship between membrane polarity and membrane order is similar in plasma and intracellular membrane contents, and is consistent with a bilayer in the Lo phase, while maintaining lower packing than artificial membranes. Disruption of the actin cytoskeleton led to a decrease in membrane order, while the membrane hydration and polarity were not affected, suggesting a role of the submembrane actin cortex in controlling plasma membrane fluidity.

On the other hand, depletion of cholesterol led to modifications in membrane hydration and

polarity, while the order parameters were less affected. Differential results from lifetime and GP data suggest that cholesterol depletion has contrasting effects on membrane polarity and hydration, and that these effects are different in plasma and internal membranes.

Further research is therefore needed to truly understand the relationship between laurdan lifetime and emission wavelength in physiologically relevant contexts. For example, fluorescence imaging experiments could be coupled with biochemical assays to determine the % of extracted cholesterol. This could easily be done by extraction of plasma membrane material, using GPMV isolation or membrane fragmentation protocols. The specific extraction of different intracellular membrane compartments is less straightforward. For this, counter-staining experiments with cholesterol-binding dye filipin or fluorophore-bound cholesterol could also be carried out, to correlate the spatio-temporal dynamics of membrane microenvironment and cholesterol localisation. An appropriate multiplexed imaging configuration would need to be devised, with a lifetime detection capacity for laurdan or di-4-ANEPPDHQ, and a fluorescence intensity quantification capacity for cholesterol density and localisation.

Secondly, GPMVs were characterised as a model to study order and microenvironments in cell-derived lipid bilayers. Results confirm conclusions obtained on live cells as to the "Lo" behaviour of the plasma membrane, while displaying significantly different parameter values, suggesting differential integration of lipid components during the vesiculation process, and possible direct effect of the vesiculating agents themselves.

Future work on this topic also includes the use of other environmentally-sensitive dyes, to probe different types of micro-environments with order parameters, such as membrane charge, curvature, etc. Dyes developed by the lab of Profs. Mely and Dr. Klymchenko would be good candidates for such projects, with for example dye F2N12SM probing membrane charge [162].

Analysis strategies for FLIM and TR-FAIM

In Chapter 1, existing methods for the analysis of time-resolved anisotropy data were discussed and compared, with a quantification of their success using simulated data. A weighted fitting procedure was introduced, using the propagation of the uncertainties from the polarisation intensity decays, which showed more accurate recovery of anisotropy parameters than unweighted fits. This constitutes a significant improvement to anisotropy analysis.

In Chapter 4, methods to analyse FLIM and TR-FAIM data in low-intensity image data were explored, with the objective to perform simultaneous resolution of lifetime and anisotropy parameters. A global analysis method based on PCA was developed, and a noise correction step based on the Poissonian character of TCSPC noise was necessary for the accurate resolution of lifetime parameters. NC-PCA was shown to offer sensitive and robust detection of contrast in noisy TC-

SPC images. An additional advantage is the possibility to tailor the procedure to the type of data by adapting the noise correction, as shown by the application of NC-PCA to FLIM and TR-FAIM data. Resolution of contrast according to rotational correlation time was possible when intensity variations within the image were limited, enabling combined NC-PCA of lifetime and anisotropy data. Future work includes finer adaptation of the noise correction in time-resolved anisotropy to eliminate the influence of signal-dependent intensity in the image, for example by introducing pixel-specific corrections. This will allow more extensive application of this new tool to other biological questions where lifetime and anisotropy can be used simultaneously. NC-PCA could for example be applied to FRET imaging, where the lifetime of the donor decreases upon energy transfer, while the anisotropy of the acceptor decreases compared to when it is excited directly [75, 221]. Note that this technique requires direct excitation of the acceptor, using for example an alternative excitation microscope setup, (ALEX).

Building a graphical user interface for NC-PCA

The use and popularity of any novel analysis routine is greatly promoted by the development of user-friendly software that does not require expertise in a specific programming language. Therefore, a Graphical User Interface (GUI) for NC-PCA running on Matlab was created and is still under construction. Users can upload FLIM images from the Matlab work environment and run NC-PCA and phasor analysis on them, with a choice of expected number of decay components, threshold, etc, and possibility of ROI selection in image space and projected space. The capability to analyse larger datasets will be implemented, with the possibility of projecting new data into a PCA basis determined from another dataset, as shown in the case of cholesterol depletion in this chapter.

As a final word, this thesis has demonstrated the possibility of simultaneous recording of all the parameters of the fluorescence signal on the same sample, and this approach has proved relevant to the multi-dimensional imaging of lipid bilayers and cell membranes. Contributions were made to the current knowledge in bilayer micro-environment and membrane dye photophysics, and new methodological tools to analyse time-resolved fluorescence intensity and anisotropy image data were introduced.

Appendix

Appendix 1: Code for NC-PCA of TCSPC data

Note: full code and user guide for NC-PCA, data simulation and phasor analysis were published along with publication 1. (**Le Marois, A.**, Labouesse, S., Suhling, K., Heintzmann, R., Noise-Corrected Principal Component Analysis of fluorescence lifetime imaging data (2016). Journal of Biophotonics 10, 1124-1133, 2017. doi:10.1002/jbio.201600160), and available on request.

```
function [mybasis, Eigenvectors, Scores, mask_ncpca, FiltImg,
NoiseCorrection,alphas]=NCPCA(mydata, MaxDims, NormType, threshold, selectROI,
addpar)
```

```
if nargin < 1
    mydata=format_raw_data;
end
if nargin < 2
MaxDims=4;  % Subspace dimension to project to or one more to see if the next
component is "just" noise
end
if nargin < 3
    NormType='Poisson';
end
if nargin<4
    threshold=0.1;
end
if nargin<5
    selectROI=0;
end
if nargin<6
    addpar=0;
end
%arrange data in 3-D dip_image dataset
if ndims(mydata)==2;
    mydata=reshape(mydata,sqrt(size(mydata,1)),sqrt(size(mydata,1)),size(mydata,2));
end

if selectROI==0
    roi=ones(size(mydata,1),size(mydata,2));
else,
    figure
    imshow(double(sum(mydata,[],3)))
    caxis([0 max(max(double(sum(mydata,[],3))))])
    colormap jet
    roi=roipoly;
end
mydata=mydata.*roi;
mydata=dip_image(mydata);
%background estimation
[out,Bg,bg_im]=backgroundoffset(squeeze(mean(mydata(:,:,round(size(mydata,3)/2):size(
mydata,3)-1),[],3)));
switch NormType
    case ''
    %No correction
        NoiseCorrection=1;
        int=mydata;
    case 'Poisson'
    %Scaling factor = square root of average intensity at each time
    %bin.
        NoiseCorrection=sqrt(mean(mydata,[],[1 2])+eps);
        size(NoiseCorrection)
        int=mydata
    case 'Variance'
    %Scaling factor = standard deviation at each time bin
        NoiseCorrection=std(mydata,[],[1 2])+eps;
        int=mydata;
```

```
    case 'Anis'
        % Scaling factor = calculated uncertainty of anisotropy

NoiseCorrection=(3.*sqrt(addpar{1}.*addpar{1}.*addpar{2}+addpar{2}.*addpar{2}.*addpar
{1}).//((addpar{1}+2.*addpar{2}).*(addpar{1}+2.*addpar{2})));
        NoiseCorrection(isnan(NoiseCorrection))=1;
        NoiseCorrection=mean(dip_image(NoiseCorrection),[],[1 2]);
        %optimise range on which to perform PCA
            [~,range_start]=min(NoiseCorrection);

range_end=find(NoiseCorrection(:,:,range_start(3):size(NoiseCorrection,3)-
1)==1,1,'first')+range_start(3)-2;
            if isempty(range_end);
                range_end=size(mydata,3)
            end
            NoiseCorrection=dip_image(NoiseCorrection(:,:,range_start(3):range_end-
1));
            mydata=mydata(:,:,range_start(3):range_end-1);
        %Use intensity for threshold
        int=dip_image(addpar{1}+2.*addpar{2});
        %set bg to 0 (anisotropy)
        Bg=0;
    otherwise
        help
        error('unknown NormType');
end

%find peak - set all pixels below threshold to 0
[maxv,peak_ind]=max(squeeze(mean(int,[],[1 2])));
mask_ncpca=(int(:,:,peak_ind))>threshold;
mask_ncpca=mask_ncpca.*roi;
% The background is removed before the normalization, however, the norm is estimated
including the background
mydata=(mydata-round(Bg))*mask_ncpca;

%Image is normalised by scaling factor
mydata_norm = mydata ./ NoiseCorrection;

%image arranged as vectors containing each a decay.
allvecs=transpose(double(reshape(mydata_norm,[size(mydata_norm,1)*size(mydata_norm,2)
size(mydata_norm,3)])));
allvecs_selected=allvecs(transpose(any(transpose(allvecs))),:);
%Data is centered around the mean
allvecs_cent=bsxfun(@minus, allvecs_selected,mean(allvecs_selected,1));

%covariance matrix of dataset
myc = (allvecs_cent'*allvecs_cent)/(size(allvecs_cent,1)-1);

%SVD of covariance matrix
[U D V] = svd(transpose(myc));

%Extraction of first desired eigenvectors
mybasis=V(:,1:MaxDims);

%Optional : force positive maximum of Eigenvectors
for i=1:MaxDims;
   if abs(min(mybasis(:,i)))>abs(max(mybasis(:,i)));
```

```
        mybasis(:,i)=-mybasis(:,i);
    end
end

%calculate orthogonal projection of pixel data on the selected eigenvectors
%= pixel scores
projected=transpose(transpose(mybasis)*transpose(allvecs));
Scores=reshape(dip_image(transpose(projected)),[size(mydata_norm,1)
size(mydata_norm,2) MaxDims]);
% Apply reverse scaling to eigenvectors
if prod(size(NoiseCorrection)) > 1
    Eigenvectors=mybasis .* repmat(transpose(double(squeeze(NoiseCorrection))),[1
size(mybasis,2)]);
else
    Eigenvectors=mybasis .* NoiseCorrection;
end
alphas=round(alpha(Scores),3)
colorder=[0.08,0.17,0.55;0.47,0.67,0.19;0.85,0.33,0.1;0.93,0.69,0.13;0.64,0.08,0.18];
%Display NC-PCA results
figure
for i=1:MaxDims
plot(Eigenvectors(:,i),'LineWidth',1.5,'Color',colorder(i,:))
title('Principal Components')
hold on
end
xlabel('time / ns')
ylabel('eigenvector value')
legend({'PC1','PC2','PC3','PC4'})
set(gca,'FontSize',20,'XGrid','on','YGrid','on')

figure
for i=1:MaxDims
subplot(1,MaxDims,i)
sc(i)=imshow(double(Scores(:,:,i-1)));
caxis([min(Scores(:,:,i-1)) max(Scores(:,:,i-1))])
title({strcat('score
image',num2str(i));strcat('\alpha',num2str(i),'=',num2str(alphas(i)))})
 end

% %Filtering
DF=D;
DF(MaxDims+1:end,MaxDims+1:end)=0;
% Forces all "unwanted" Eigenvalues to be zero and the others to be one.
%Thus only a projection onto the subspace is performed.
for n=1:MaxDims
    DF(n,n)=1;
end
Filtered = (U*(DF*(transpose(V)*transpose(allvecs))));
FiltImg=reshape(dip_image(Filtered),[size(mydata_norm,1) size(mydata_norm,2)
size(Filtered,1)]).* NoiseCorrection;
```

Published with MATLAB® R2016b

Appendix 2: Copyright Clearances

Table 5.1 below lists the figures subject to Copyright, along with the license to re-use obtained from the Copyright Clearance Centre for this thesis.

Figure number	Reference number	Publisher	License number	License date
Figs. 1.3 & 1.2	Kubitscheck (ed.) [8]	John Wiley and Sons	3984910741599	Nov 09, 2016
Fig 2.2	Veatch et al. [134]	Elsevier	4287621421760	Feb 14, 2018
Fig 2.4	Haluska et al. [173]	Elsevier	4287101509097	Feb 13, 2018
Fig 4.1	Milijkovic et al. [213]	Royal Society of Chemistry	4287630592345	Feb 14, 2018

Table 5.1: Summary of figures subject to copyright in this thesis. License to re-use was obtained for print and electronic formats.

Colophon

This thesis was written using free software: the text was written in LyX/LaTeX, some figures made using ImageJ, and some analyses were made using DIPImage and OME bioformats toolboxes. The author thanks the developers of these projects for their invaluable contributions to the scientific community.

Bibliography

[1] A. H. Fischer, K. A. Jacobson, J. Rose, and R. Zeller, "Hematoxylin and Eosin Staining of Tissue and Cell Sections," *Cold Spring Harbor Protocols*, vol. 2008, p. pdb.prot4986, Jan. 2008.

[2] F. Zernike, "How I Discovered Phase Contrast," *Science*, vol. 121, pp. 345–349, Nov. 1955.

[3] F. Zernike, "Phase contrast, a new method for the microscopic observation of transparent objects," *Physica*, vol. 9, pp. 686–698, July 1942.

[4] "Method of the Year 2008," *Nature Methods*, vol. 6, pp. 1–1, Jan. 2009.

[5] K. Suhling, L. M. Hirvonen, J. A. Levitt, P.-H. Chung, C. Tregidgo, A. Le Marois, D. A. Rusakov, K. Zheng, S. Ameer-Beg, S. Poland, S. Coelho, R. Henderson, and N. Krstajic, "Fluorescence lifetime imaging (FLIM): Basic concepts and some recent developments," *Medical Photonics*, vol. 27, pp. 3–40, May 2015.

[6] B. Valeur and M. N. Berberan-Santos, *Molecular Fluorescence: Principles and Applications*. John Wiley & Sons, May 2012.

[7] T. J. Zielinski, E. Harvey, R. Sweeney, and D. M. Hanson, "Quantum States of Atoms and Molecules," *Journal of Chemical Education*, vol. 82, p. 1880, Dec. 2005.

[8] R. Heintzmann, "Introduction to Optics and Photophysics," in *Fluorescence Microscopy* (U. Kubitscheck, ed.), pp. 1–31, Wiley-VCH Verlag GmbH & Co. KGaA, 2013.

[9] J. Franck and E. G. Dymond, "Elementary processes of photochemical reactions," *Transactions of the Faraday Society*, vol. 21, pp. 536–542, Jan. 1926.

[10] E. U. Condon, "Nuclear Motions Associated with Electron Transitions in Diatomic Molecules," *Physical Review*, vol. 32, pp. 858–872, Dec. 1928.

[11] M. Kasha, "Characterization of electronic transitions in complex molecules," *Discussions of the Faraday Society*, vol. 9, pp. 14–19, Jan. 1950.

[12] K. Suhling, P. M. W. French, and D. Phillips, "Time-resolved fluorescence microscopy," *Photochemical & Photobiological Sciences*, vol. 4, no. 1, p. 13, 2005.

[13] E. Fort and S. Gresillon, "Surface enhanced fluorescence," *Journal of Physics D: Applied Physics*, vol. 41, p. 013001, Jan. 2008.

[14] K. Suhling, L. M. Hirvonen, J. A. Levitt, P.-H. Chung, C. Tregidgo, A. Le Marois, D. A. Rusakov, K. Zheng, S. Ameer-Beg, S. Poland, S. Coelho, R. Henderson, and N. Krstajic, "Fluorescence lifetime imaging (FLIM): Basic concepts and some recent developments," *Medical Photonics*, vol. 27, pp. 3–40, May 2015.

[15] A. Chmyrov, T. Sanden, and J. Widengren, "Iodide as a Fluorescence Quencher and PromoterâMechanisms and Possible Implications," *The Journal of Physical Chemistry B*, vol. 114, pp. 11282–11291, Sept. 2010.

[16] A. S. Klymchenko and R. Kreder, "Fluorescent Probes for Lipid Rafts: From Model Membranes to Living Cells," *Chemistry & Biology*, vol. 21, pp. 97–113, Jan. 2014.

[17] M. Chalfie, Y. Tu, G. Euskirchen, W. W. Ward, and D. C. Prasher, "Green fluorescent protein as a marker for gene expression," *Science (New York, N.Y.)*, vol. 263, pp. 802–805, Feb. 1994.

[18] G. V. Los, L. P. Encell, M. G. McDougall, D. D. Hartzell, N. Karassina, C. Zimprich, M. G. Wood, R. Learish, R. F. Ohana, M. Urh, D. Simpson, J. Mendez, K. Zimmerman, P. Otto, G. Vidugiris, J. Zhu, A. Darzins, D. H. Klaubert, R. F. Bulleit, and K. V. Wood, "HaloTag: A Novel Protein Labeling Technology for Cell Imaging and Protein Analysis," *ACS Chemical Biology*, vol. 3, pp. 373–382, June 2008.

[19] C. Hoffmann, G. Gaietta, A. Zuern, S. R. Adams, S. Terrillon, M. H. Ellisman, R. Y. Tsien, and M. J. Lohse, "Fluorescent labeling of tetracysteine-tagged proteins in intact cells," *Nature Protocols*, vol. 5, pp. 1666–1677, Oct. 2010.

[20] M. C. Skala, J. M. Squirrell, K. M. Vrotsos, J. C. Eickhoff, A. Gendron-Fitzpatrick, K. W. Eliceiri, and N. Ramanujam, "Multiphoton microscopy of endogenous fluorescence differentiates normal, precancerous, and cancerous squamous epithelial tissues," *Cancer Research*, vol. 65, pp. 1180–1186, Feb. 2005.

[21] M. C. Skala, K. M. Riching, D. K. Bird, A. Gendron-Fitzpatrick, J. Eickhoff, K. W. Eliceiri, P. J. Keely, and N. Ramanujam, "In vivo Multiphoton Fluorescence Lifetime Imaging of Protein-bound and Free NADH in Normal and Pre-cancerous Epithelia," *Journal of biomedical optics*, vol. 12, no. 2, p. 024014, 2007.

[22] S. J. Strickler and R. A. Berg, "Relationship between Absorption Intensity and Fluorescence Lifetime of Molecules," *The Journal of Chemical Physics*, July 2004.

[23] J. R. Lakowicz, *Principles of Fluorescence Spectroscopy*. Springer Science & Business Media, Apr. 2013.

[24] S. E. Temple, V. Pignatelli, T. Cook, M. J. How, T.-H. Chiou, N. W. Roberts, and N. J. Marshall, "High-resolution polarisation vision in a cuttlefish," *Current Biology*, vol. 22, pp. R121–R122, Feb. 2012.

[25] C. Thaler, P. Blank, S. Koushik, and S. Vogel, "Time-Resolved Fluorescence Anisotropy," in *FLIM Microscopy in Biology and Medicine* (R. Clegg and A. Periasamy, eds.), pp. 245–320, Chapman and Hall/CRC, July 2009.

[26] K. Kinosita, S. Kawato, and A. Ikegami, "A theory of fluorescence polarization decay in membranes.," *Biophysical Journal*, vol. 20, pp. 289–305, Dec. 1977.

[27] G. Arfken, "12 - Legendre Functions," in *Mathematical Methods for Physicists (Third Edition)*, pp. 637–711, Academic Press, 1985.

[28] K. Bahlmann and S. W. Hell, "Depolarization by high aperture focusing," *Applied Physics Letters*, vol. 77, pp. 612–614, July 2000.

[29] D. O'Connor and D. Phillips, *Time-correlated single photon counting*. Academic Press, Dec. 1984.

[30] A. C. Hoepker, A. Wang, A. L. Marois, K. Suhling, Y. Yan, and G. Marriott, "Genetically encoded sensors of protein hydrodynamics and molecular proximity," *Proceedings of the National Academy of Sciences*, p. E2569âE2574, Apr. 2015.

[31] Wolfgang Becker, *The bh TCSPC Handbook*. 5th ed., 2012.

[32] G. R. Haugen, B. W. Wallin, and F. E. Lytle, "Optimization of data acquistion rates in time correlated single photon fluorimetry," *Review of Scientific Instruments*, vol. 50, pp. 64–72, Jan. 1979.

[33] W. Becker, "HPM 100-40 : High Speed Hybrid Detector for TCSPC."

[34] W. Becker, B. Su, O. Holub, and K. Weisshart, "FLIM and FCS detection in laser-scanning microscopes: increased efficiency by GaAsP hybrid detectors," *Microscopy Research and Technique*, vol. 74, pp. 804–811, Sept. 2011.

[35] W. Becker, A. Bergmann, M. A. Hink, K. Koenig, K. Benndorf, and C. Biskup, "Fluorescence lifetime imaging by time-correlated single-photon counting," *Microscopy Research and Technique*, vol. 63, no. 1, pp. 58–66, 2004.

[36] P. Peronio, G. Acconcia, I. Rech, and M. Ghioni, "Improving the counting efficiency in time-correlated single photon counting experiments by dead-time optimization," *The Review of Scientific Instruments*, vol. 86, p. 113101, Nov. 2015.

[37] J. L. Rinnenthal, C. Boernchen, H. Radbruch, V. Andresen, A. Mossakowski, V. Siffrin, T. Seelemann, H. Spiecker, I. Moll, J. Herz, A. E. Hauser, F. Zipp, M. J. Behne, and R. Niesner, "Parallelized TCSPC for Dynamic Intravital Fluorescence Lifetime Imaging: Quantifying Neuronal Dysfunction in Neuroinflammation," *PLOS ONE*, vol. 8, p. e60100, Apr. 2013.

[38] W. Becker, *Advanced Time-Correlated Single Photon Counting Techniques*, vol. 81 of *Springer Series in Chemical Physics*. Berlin, Heidelberg: Springer Berlin Heidelberg, 2005.

[39] M. J. Cole, J. Siegel, S. E. D. Webb, R. Jones, K. Dowling, M. J. Dayel, D. Parsons-Karavassilis, P. M. W. French, M. J. Lever, L. O. D. Sucharov, M. A. A. Neil, R. Juskaitis, and T. Wilson, "Time-domain whole-field fluorescence lifetime imaging with optical sectioning," *Journal of Microscopy*, vol. 203, pp. 246–257, Sept. 2001.

[40] S. C. Warren, A. Margineanu, D. Alibhai, D. J. Kelly, C. Talbot, Y. Alexandrov, I. Munro, M. Katan, C. Dunsby, and P. M. W. French, "Rapid global fitting of large fluorescence lifetime imaging microscopy datasets," *PloS One*, vol. 8, no. 8, p. e70687, 2013.

[41] Sytsma, J, Vroom, J.M., De Grauw, C. J, and Gerritsen, H. C., "Time-gated fluorescence lifetime imaging and microvolume spectroscopy using two-photon excitation," *Journal of Microscopy*, vol. 191, pp. 39–51, July 1998.

[42] V. Y. Soloviev, K. B. Tahir, J. McGinty, D. S. Elson, M. A. A. Neil, P. M. W. French, and S. R. Arridge, "Fluorescence lifetime imaging by using time-gated data acquisition," *Applied Optics*, vol. 46, pp. 7384–7391, Oct. 2007.

[43] V. Devauges, C. Marquer, S. Lecart, J.-C. Cossec, M.-C. Potier, E. Fort, K. Suhling, and S. Leveque-Fort, "Homodimerization of Amyloid Precursor Protein at the Plasma Membrane: A homoFRET Study by Time-Resolved Fluorescence Anisotropy Imaging," *PLOS ONE*, vol. 7, p. e44434, Sept. 2012.

[44] T. Hinsdale, C. Olsovsky, J. J. Rico-Jimenez, K. C. Maitland, J. A. Jo, and B. H. Malik, "Optically sectioned wide-field fluorescence lifetime imaging microscopy enabled by structured illumination," *Biomedical Optics Express*, vol. 8, pp. 1455–1465, Mar. 2017.

[45] S. E. D. Webb, Y. Gu, S. Leveque-Fort, J. Siegel, M. J. Cole, K. Dowling, R. Jones, P. M. W. French, M. A. A. Neil, R. Juskaitis, L. O. D. Sucharov, T. Wilson, and M. J. Lever, "A wide-field time-domain fluorescence lifetime imaging microscope with optical sectioning," *Review of Scientific Instruments*, vol. 73, Mar. 2002.

[46] D. M. Grant, J. McGinty, E. J. McGhee, T. D. Bunney, D. M. Owen, C. B. Talbot, W. Zhang, S. Kumar, I. Munro, P. M. P. Lanigan, G. T. Kennedy, C. Dunsby, A. I. Magee, P. Courtney, M. Katan, M. a. A. Neil, and P. M. W. French, "High speed optically sectioned fluorescence lifetime imaging permits study of live cell signaling events," *Optics Express*, vol. 15, pp. 15656–15673, Nov. 2007.

[47] D. M. Grant, D. S. Elson, D. Schimpf, C. Dunsby, J. Requejo-Isidro, E. Auksorius, I. Munro, M. a. A. Neil, P. M. W. French, E. Nye, G. Stamp, and P. Courtney, "Optically sectioned fluorescence lifetime imaging using a Nipkow disk microscope and a tunable ultrafast continuum excitation source," *Optics Letters*, vol. 30, pp. 3353–3355, Dec. 2005.

[48] A. Esposito, H. C. Gerritsen, and F. S. Wouters, "Optimizing frequency-domain fluorescence lifetime sensing for high-throughput applications: photon economy and acquisition speed," *Journal of the Optical Society of America. A, Optics, Image Science, and Vision*, vol. 24, pp. 3261–3273, Oct. 2007.

[49] C. J. d. Grauw and H. C. Gerritsen, "Multiple Time-Gate Module for Fluorescence Lifetime Imaging," *Applied Spectroscopy*, vol. 55, pp. 670–678, June 2001.

[50] A. N. Bader, E. G. Hofman, J. Voortman, P. M. P. van Bergen en Henegouwen, and H. C. Gerritsen, "Homo-FRET Imaging Enables Quantification of Protein Cluster Sizes with Subcellular Resolution," *Biophysical Journal*, vol. 97, pp. 2613–2622, Nov. 2009.

[51] A. N. Bader, E. G. Hofman, P. M. P. van Bergen en Henegouwen, and H. C. Gerritsen, "Imaging of protein cluster sizes by means of confocal time-gated fluorescence anisotropy microscopy," *Optics Express*, vol. 15, pp. 6934–6945, May 2007.

[52] P. J. Verveer and Q. S. Hanley, "Frequency domain FLIM theory, instrumentation, and data analysis," in *Laboratory Techniques in Biochemistry and Molecular Biology*, vol. 33 of *Fret and Flim Techniques*, pp. 59–94, Elsevier, 2009.

[53] M. Zhao, X. Wan, Y. Li, W. Zhou, and L. Peng, "Multiplexed 3d FRET imaging in deep tissue of live embryos," *Scientific Reports*, vol. 5, p. 13991, Sept. 2015.

[54] S. Shrestha, M. J. Serafino, J. Rico-Jimenez, J. Park, X. Chen, S. Zhaorigetu, B. L. Walton, J. A. Jo, and B. E. Applegate, "Multimodal optical coherence tomography and fluorescence

lifetime imaging with interleaved excitation sources for simultaneous endogenous and exogenous fluorescence," *Biomedical Optics Express*, vol. 7, pp. 3184–3197, Sept. 2016.

[55] A. H. A. Clayton, Q. S. Hanley, D. J. Arndt-Jovin, V. Subramaniam, and T. M. Jovin, "Dynamic Fluorescence Anisotropy Imaging Microscopy inthe Frequency Domain (rFLIM)," *Biophysical Journal*, vol. 83, pp. 1631–1649, Sept. 2002.

[56] M. A. Digman, V. R. Caiolfa, M. Zamai, and E. Gratton, "The Phasor Approach to Fluorescence Lifetime Imaging Analysis," *Biophysical Journal*, vol. 94, pp. L14–L16, Jan. 2008.

[57] N. KrstajiÄ, S. Poland, J. Levitt, R. Walker, A. Erdogan, S. Ameer-Beg, and R. K. Henderson, "0.5 billion events per second time correlated single photon counting using CMOS SPAD arrays," *Optics Letters*, vol. 40, pp. 4305–4308, Sept. 2015.

[58] N. KrstajiÄ, J. Levitt, S. Poland, S. Ameer-Beg, and R. Henderson, "256 Ã 2 SPAD line sensor for time resolved fluorescence spectroscopy," *Optics Express*, vol. 23, pp. 5653–5669, Mar. 2015.

[59] S. P. Poland, N. Krstajic, J. Monypenny, S. Coelho, D. Tyndall, R. J. Walker, V. Devauges, J. Richardson, N. Dutton, P. Barber, D. D.-U. Li, K. Suhling, T. Ng, R. K. Henderson, and S. M. Ameer-Beg, "A high speed multifocal multiphoton fluorescence lifetime imaging microscope for live-cell FRET imaging," *Biomedical Optics Express*, vol. 6, pp. 277–296, Jan. 2015.

[60] L. M. Hirvonen, W. Becker, J. Milnes, T. Conneely, S. Smietana, A. L. Marois, O. Jagutzki, and K. Suhling, "Picosecond wide-field time-correlated single photon counting fluorescence microscopy with a delay line anode detector," *Applied Physics Letters*, vol. 109, p. 071101, Aug. 2016.

[61] L. M. Hirvonen and K. Suhling, "Wide-field TCSPC: methods and applications," *Measurement Science and Technology*, vol. 28, no. 1, p. 012003, 2017.

[62] "Introduction to Microscopy | Duke Light Microscopy Core Facility."

[63] L. M. Hirvonen, W. Becker, J. Milnes, T. Conneely, S. Smietana, A. L. Marois, O. Jagutzki, and K. Suhling, "Picosecond wide-field time-correlated single photon counting fluorescence microscopy with a delay line anode detector," *Applied Physics Letters*, vol. 109, p. 071101, Aug. 2016.

[64] K. Suhling, L. M. Hirvonen, W. Becker, S. Smietana, H. Netz, J. Milnes, T. Conneely, A. Le Marois, and O. Jagutzki, "Wide-field TCSPC-based fluorescence lifetime imaging (FLIM) microscopy," vol. 9858, pp. 98580J–98580J–10, 2016.

[65] P. T. C. So, C. Y. Dong, B. R. Masters, and K. M. Berland, "Two-Photon Excitation Fluorescence Microscopy," *Annual Review of Biomedical Engineering*, vol. 2, no. 1, pp. 399–429, 2000.

[66] E. E. Hoover and J. A. Squier, "Advances in multiphoton microscopy technology," *Nature Photonics*, vol. 7, pp. 93–101, Feb. 2013.

[67] M. Goeppert-Mayer, "Ueber Elementarakte mit zwei Quantenspruengen," *Annalen der Physik*, vol. 401, pp. 273–294, Jan. 1931.

[68] A. Hopt and E. Neher, "Highly nonlinear photodamage in two-photon fluorescence microscopy.," *Biophysical Journal*, vol. 80, pp. 2029–2036, Apr. 2001.

[69] K. Suhling, J. Levitt, and P.-H. Chung, "Time-Resolved Fluorescence Anisotropy Imaging," in *Fluorescence Spectroscopy and Microscopy* (Y. Engelborghs and A. J. Visser, eds.), vol. 1076, pp. 503–519, Totowa, NJ: Humana Press, 2014.

[70] K. Zheng, T. P. Jensen, L. P. Savtchenko, J. A. Levitt, K. Suhling, and D. A. Rusakov, "Nanoscale diffusion in the synaptic cleft and beyond measured with time-resolved fluorescence anisotropy imaging," *Scientific Reports*, vol. 7, Feb. 2017.

[71] S. W. Hell and M. Kroug, "Ground-state-depletion fluorscence microscopy: A concept for breaking the diffraction resolution limit," *Applied Physics B*, vol. 60, no. 5, pp. 495–497, 2005.

[72] S. W. Hell and J. Wichmann, "Breaking the diffraction resolution limit by stimulated emission: stimulated-emission-depletion fluorescence microscopy," *Optics Letters*, vol. 19, pp. 780–782, June 1994.

[73] M. J. Rust, M. Bates, and X. Zhuang, "Sub-diffraction-limit imaging by stochastic optical reconstruction microscopy (STORM)," *Nature Methods*, vol. 3, pp. 793–796, Oct. 2006.

[74] L. Novotny and B. Hecht, "Principles of Nano-Optics by Lukas Novotny," June 2006.

[75] V. Devauges, D. R. Matthews, J. Aluko, J. Nedbal, J. A. Levitt, S. P. Poland, O. Coban, G. Weitsman, J. Monypenny, T. Ng, and S. M. Ameer-Beg, "Steady-State Acceptor Fluorescence Anisotropy Imaging under Evanescent Excitation for Visualisation of FRET at the Plasma Membrane," *PLOS ONE*, vol. 9, p. e110695, Oct. 2014.

[76] H. Kang, B. Jia, and M. Gu, "Polarization characterization in the focal volume of high numerical aperture objectives," *Optics Express*, vol. 18, pp. 10813–10821, May 2010.

[77] D. A. Smith, G. McKenzie, A. C. Jones, and T. A. Smith, "Analysis of time-correlated single photon counting data: a comparative evaluation of deterministic and probabilistic approaches," *Methods and Applications in Fluorescence*, vol. 5, no. 4, p. 042001, 2017.

[78] J. Kim and J. Seok, "Statistical properties of amplitude and decay parameter estimators for fluorescence lifetime imaging," *Optics Express*, vol. 21, pp. 6061–6075, Mar. 2013.

[79] T. Hauschild and M. Jentschel, "Comparison of maximum likelihood estimation and chi-square statistics applied to counting experiments," *Nuclear Instruments and Methods in Physics Research Section A: Accelerators, Spectrometers, Detectors and Associated Equipment*, vol. 457, pp. 384–401, Jan. 2001.

[80] S. Baker and R. D. Cousins, "Clarification of the use of CHI-square and likelihood functions in fits to histograms," *Nuclear Instruments and Methods in Physics Research*, vol. 221, pp. 437–442, Apr. 1984.

[81] T. A. Laurence and B. A. Chromy, "Efficient maximum likelihood estimator fitting of histograms," *Nature Methods*, vol. 7, pp. 338–339, May 2010.

[82] M. I. Rowley, A. C. C. Coolen, B. Vojnovic, and P. R. Barber, "Robust Bayesian Fluorescence Lifetime Estimation, Decay Model Selection and Instrument Response Determination for Low-Intensity FLIM Imaging," *PLOS ONE*, vol. 11, p. e0158404, June 2016.

[83] M. I. Rowley, P. R. Barber, A. C. C. Coolen, and B. Vojnovic, "Bayesian analysis of fluorescence lifetime imaging data," in *Proc. SPIE 7903, Multiphoton Microscopy in the Biomedical Sciences XI, 790325*, vol. 7903, pp. 790325–790325–12, 2011.

[84] M. Köllner and J. Wolfrum, "How many photons are necessary for fluorescence-lifetime measurements?," *Chemical Physics Letters*, vol. 200, pp. 199–204, Nov. 1992.

[85] P. J. Verveer, A. Squire, and P. I. H. Bastiaens, "Global Analysis of Fluorescence Lifetime Imaging Microscopy Data," *Biophysical Journal*, vol. 78, pp. 2127–2137, Apr. 2000.

[86] G. Golub and V. Pereyra, "Separable nonlinear least squares: the variable projection method and its applications," *Inverse Problems*, vol. 19, no. 2, p. R1, 2003.

[87] S. Padilla-Parra, N. Audugé, M. Coppey-Moisan, and M. Tramier, "Quantitative FRET Analysis by Fast Acquisition Time Domain FLIM at High Spatial Resolution in Living Cells," *Biophysical Journal*, vol. 95, pp. 2976–2988, Sept. 2008.

[88] C. Stringari, A. Cinquin, O. Cinquin, M. A. Digman, P. J. Donovan, and E. Gratton, "Phasor approach to fluorescence lifetime microscopy distinguishes different metabolic states of germ

cells in a live tissue," *Proceedings of the National Academy of Sciences of the United States of America*, vol. 108, pp. 13582–13587, Aug. 2011.

[89] F. S. Wouters and A. Esposito, "Quantitative analysis of fluorescence lifetime imaging made easy," *HFSP Journal*, vol. 2, pp. 7–11, Feb. 2008.

[90] K. Lidke, B. Rieger, D. Lidke, and T. Jovin, "The role of photon statistics in fluorescence anisotropy imaging," *IEEE Transactions on Image Processing*, vol. 14, pp. 1237–1245, Sept. 2005.

[91] F. M. Harris, K. B. Best, and J. D. Bell, "Use of laurdan fluorescence intensity and polarization to distinguish between changes in membrane fluidity and phospholipid order," *Biochimica et Biophysica Acta (BBA) - Biomembranes*, vol. 1565, pp. 123–128, Sept. 2002.

[92] E. G. Novikov, V. V. Skakun, J. W. Borst, and A. J. W. G. Visser, "Maximum entropy analysis of polarized fluorescence decay of (E)GFP in aqueous solution," *Methods and Applications in Fluorescence*, vol. 6, Aug. 2017.

[93] P. Kapusta, R. Erdmann, U. Ortmann, and M. Wahl, "Time-Resolved Fluorescence Anisotropy Measurements Made Simple," *Journal of Fluorescence*, vol. 13, pp. 179–183, Mar. 2003.

[94] A. J. Cross and G. R. Fleming, "Analysis of time-resolved fluorescence anisotropy decays.," *Biophysical Journal*, vol. 46, pp. 45–56, July 1984.

[95] "Primer: fluorescence imaging under the diffraction limit : Article : Nature Methods."

[96] S. S. Vogel, C. Thaler, and S. V. Koushik, "Fanciful FRET," *Sci. STKE*, vol. 2006, pp. re2–re2, Apr. 2006.

[97] T. Foerster, "Energiewanderung und Fluoreszenz," *Naturwissenschaften*, vol. 33, pp. 166–175, June 1946.

[98] T. Foerster, "Zwischenmolekulare Energiewanderung und Fluoreszenz," *Annalen der Physik*, vol. 437, no. 1-2, pp. 55–75, 1948.

[99] G. N. M. v. d. Krogt, J. Ogink, B. Ponsioen, and K. Jalink, "A Comparison of Donor-Acceptor Pairs for Genetically Encoded FRET Sensors: Application to the Epac cAMP Sensor as an Example," *PLOS ONE*, vol. 3, p. e1916, Apr. 2008.

[100] A. Shivalingam, M. A. Izquierdo, A. Le Marois, A. Vysniauskas, K. Suhling, M. K. Kuimova, and R. Vilar, "The interactions between a small molecule and G-quadruplexes are visualized

by fluorescence lifetime imaging microscopy," *Nature Communications*, vol. 6, p. 6:8178, Sept. 2015.

[101] H. D. Vishwasrao, A. A. Heikal, K. A. Kasischke, and W. W. Webb, "Conformational Dependence of Intracellular NADH on Metabolic State Revealed by Associated Fluorescence Anisotropy," *Journal of Biological Chemistry*, vol. 280, pp. 25119–25126, Jan. 2005.

[102] F. Tanaka and N. Mataga, "Theory of Time-Dependent Photo-Selection in Interacting Fixed Systems," *Photochemistry and Photobiology*, vol. 29, pp. 1091–1097, June 1979.

[103] M. Tramier, T. Piolot, I. Gautier, V. Mignotte, J. Coppey, K. Kemnitz, C. Durieux, and M. Coppey-Moisan, "Homo-FRET versus hetero-FRET to probe homodimers in living cells," vol. 360 of *Biophotonics, Part A*, pp. 580–597, Academic Press, 2003.

[104] A. Ivetic, "Signals regulating L-selectin-dependent leucocyte adhesion and transmigration," *The International Journal of Biochemistry & Cell Biology*, vol. 45, pp. 550–555, Mar. 2013.

[105] K. Rzeniewicz, A. Newe, A. Rey Gallardo, J. Davies, M. R. Holt, A. Patel, G. T. Charras, B. Stramer, C. Molenaar, T. F. Tedder, M. Parsons, and A. Ivetic, "L-selectin shedding is activated specifically within transmigrating pseudopods of monocytes to regulate cell polarity in vitro," *Proceedings of the National Academy of Sciences of the United States of America*, vol. 112, pp. E1461–E1470, Mar. 2015.

[106] M. J. Sarmento, A. Coutinho, A. Fedorov, M. Prieto, and F. Fernandes, "Ca2 + induces PI(4,5)P2 clusters on lipid bilayers at physiological PI(4,5)P2 and Ca2 + concentrations," *Biochimica et Biophysica Acta (BBA) - Biomembranes*, vol. 1838, pp. 822–830, Mar. 2014.

[107] E. G. Hofman, A. N. Bader, J. Voortman, D. J. v. d. Heuvel, S. Sigismund, A. J. Verkleij, H. C. Gerritsen, and P. M. P. van Bergen en Henegouwen, "Ligand-induced EGF Receptor Oligomerization Is Kinase-dependent and Enhances Internalization," *Journal of Biological Chemistry*, vol. 285, pp. 39481–39489, Oct. 2010.

[108] W. D. Cameron, C. V. Bui, A. Hutchinson, P. Loppnau, S. Graeslund, and J. V. Rocheleau, "Apollo-NADP$^+$: a spectrally tunable family of genetically encoded sensors for NADP$^+$," *Nature Methods*, vol. 13, p. 352, Feb. 2016.

[109] R. M. Epand, "Introduction to membrane lipids," *Methods in Molecular Biology (Clifton, N.J.)*, vol. 1232, pp. 1–6, 2015.

[110] K. Simons and E. Ikonen, "Functional rafts in cell membranes," *Nature*, vol. 387, p. 569, June 1997.

[111] P. A. Janmey, "The Cytoskeleton and Cell Signaling: Component Localization and Mechanical Coupling," *Physiological Reviews*, vol. 78, pp. 763–781, Jan. 1998.

[112] P. C. Hu and N. Malmstadt, "Asymmetric giant lipid vesicle fabrication," *Methods in Molecular Biology (Clifton, N.J.)*, vol. 1232, pp. 79–90, 2015.

[113] G. van Meer, D. R. Voelker, and G. W. Feigenson, "Membrane lipids: where they are and how they behave," *Nature reviews. Molecular cell biology*, vol. 9, pp. 112–124, Feb. 2008.

[114] M. Denz, S. Chiantia, A. Herrmann, P. Mueller, T. Korte, and R. Schwarzer, "Cell cycle dependent changes in the plasma membrane organization of mammalian cells," *Biochimica et Biophysica Acta (BBA) - Biomembranes*, vol. 1859, pp. 350–359, Mar. 2017.

[115] G. E. Atilla-Gokcumen, E. Muro, J. Relat-Goberna, S. Sasse, A. Bedigian, M. L. Coughlin, S. Garcia-Manyes, and U. S. Eggert, "Dividing cells regulate their lipid composition and localization," *Cell*, vol. 156, pp. 428–439, Jan. 2014.

[116] E. A. Forssen, D. M. Coulter, and R. T. Proffitt, "Selective in vivo localization of daunorubicin small unilamellar vesicles in solid tumors," *Cancer Research*, vol. 52, pp. 3255–3261, June 1992.

[117] R. T. Proffitt, L. E. Williams, C. A. Presant, G. W. Tin, J. A. Uliana, R. C. Gamble, and J. D. Baldeschwieler, "Liposomal blockade of the reticuloendothelial system: improved tumor imaging with small unilamellar vesicles," *Science*, vol. 220, pp. 502–505, Apr. 1983.

[118] R. T. Proffitt, L. E. Williams, C. A. Presant, G. W. Tin, J. A. Uliana, R. C. Gamble, and J. D. Baldeschwieler, "Tumor-imaging potential of liposomes loaded with In-111-NTA: biodistribution in mice," *Journal of Nuclear Medicine: Official Publication, Society of Nuclear Medicine*, vol. 24, pp. 45–51, Jan. 1983.

[119] S.-T. Yang, V. Kiessling, J. A. Simmons, J. M. White, and L. K. Tamm, "HIV gp41-mediated membrane fusion occurs at edges of cholesterol-rich lipid domains," *Nature Chemical Biology*, vol. 11, pp. 424–431, June 2015.

[120] L. F. Aguilar, J. A. Pino, M. A. Soto-Arriaza, F. J. Cuevas, S. Sanchez, and C. P. Sotomayor, "Differential Dynamic and Structural Behavior of Lipid-Cholesterol Domains in Model Membranes," *PLOS ONE*, vol. 7, p. e40254, June 2012.

[121] M. Amaro, F. Reina, M. Hof, C. Eggeling, and E. Sezgin, "Laurdan and Di-4-ANEPPDHQ probe different properties of the membrane," *Journal of Physics D: Applied Physics*, vol. 50, no. 13, p. 134004, 2017.

[122] R. B. Lira, J. Steinkuehler, R. L. Knorr, R. Dimova, and K. A. Riske, "Posing for a picture: vesicle immobilization in agarose gel," *Scientific Reports*, vol. 6, p. 25254, May 2016.

[123] T. Bhatia, P. Husen, J. H. Ipsen, L. A. Bagatolli, and A. C. Simonsen, "Fluid domain patterns in free-standing membranes captured on a solid support," *Biochimica Et Biophysica Acta*, vol. 1838, pp. 2503–2510, Oct. 2014.

[124] A. Honigmann, C. Walter, F. Erdmann, C. Eggeling, and R. Wagner, "Characterization of horizontal lipid bilayers as a model system to study lipid phase separation," *Biophysical Journal*, vol. 98, pp. 2886–2894, June 2010.

[125] A. Honigmann, S. Sadeghi, J. Keller, S. W. Hell, C. Eggeling, and R. Vink, "A lipid bound actin meshwork organizes liquid phase separation in model membranes," *eLife*, vol. 3, p. e01671, Mar. 2014.

[126] K. Yokota and T. Ogino, "Phase separation in lipid bilayer membranes induced by intermixing at a boundary of two phases with different components," *Chemistry and Physics of Lipids*, vol. 191, pp. 147–152, Oct. 2015.

[127] J. Brewer, H. S. Thoke, R. P. Stock, and L. A. Bagatolli, "Enzymatic studies on planar supported membranes using a widefield fluorescence LAURDAN Generalized Polarization imaging approach," *Biochimica Et Biophysica Acta*, vol. 1859, no. 5, pp. 888–895, 2017.

[128] J. Brewer, J. Bernardino de la Serna, K. Wagner, and L. A. Bagatolli, "Multiphoton excitation fluorescence microscopy in planar membrane systems," *Biochimica Et Biophysica Acta*, vol. 1798, pp. 1301–1308, July 2010.

[129] M. I. Angelova, S. Soleau, P. Meleard, F. Faucon, and P. Bothorel, "Preparation of giant vesicles by external AC electric fields. Kinetics and applications," in *Trends in Colloid and Interface Science VI* (C. Helm, M. Loesche, and H. Moehwald, eds.), no. 89 in Progress in Colloid & Polymer Science, pp. 127–131, Steinkopff, 1992.

[130] K. R. Levental and I. Levental, "Giant plasma membrane vesicles: models for understanding membrane organization," *Current Topics in Membranes*, vol. 75, pp. 25–57, 2015.

[131] K. R. Levental and I. Levental, "Isolation of giant plasma membrane vesicles for evaluation of plasma membrane structure and protein partitioning," *Methods in Molecular Biology (Clifton, N.J.)*, vol. 1232, pp. 65–77, 2015.

[132] F. Schneider, D. Waithe, M. P. Clausen, S. Galiani, T. Koller, G. Ozhan, C. Eggeling, and E. Sezgin, "Diffusion of lipids and GPI-anchored proteins in actin-free plasma membrane

vesicles measured by STED-FCS," *Molecular Biology of the Cell*, vol. 28, pp. 1507–1518, June 2017.

[133] E. Sezgin, H.-J. Kaiser, T. Baumgart, P. Schwille, K. Simons, and I. Levental, "Elucidating membrane structure and protein behavior using giant plasma membrane vesicles," *Nature Protocols*, vol. 7, pp. 1042–1051, June 2012.

[134] S. L. Veatch and S. L. Keller, "Separation of Liquid Phases in Giant Vesicles of Ternary Mixtures of Phospholipids and Cholesterol," *Biophysical Journal*, vol. 85, pp. 3074–3083, Nov. 2003.

[135] S. J. Singer and G. L. Nicolson, "The fluid mosaic model of the structure of cell membranes," *Science (New York, N.Y.)*, vol. 175, pp. 720–731, Feb. 1972.

[136] J. Bernardino de la Serna, G. J. Schuetz, C. Eggeling, and M. Cebecauer, "There Is No Simple Model of the Plasma Membrane Organization," *Frontiers in Cell and Developmental Biology*, vol. 4, Sept. 2016.

[137] A. I. Magee and I. Parmryd, "Detergent-resistant membranes and the protein composition of lipid rafts," *Genome Biology*, vol. 4, p. 234, Oct. 2003.

[138] D. M. Owen, D. J. Williamson, A. Magenau, and K. Gaus, "Sub-resolution lipid domains exist in the plasma membrane and regulate protein diffusion and distribution," *Nature Communications*, vol. 3, p. 1256, 2012.

[139] A. Honigmann, V. Mueller, H. Ta, A. Schoenle, E. Sezgin, S. W. Hell, and C. Eggeling, "Scanning STED-FCS reveals spatiotemporal heterogeneity of lipid interaction in the plasma membrane of living cells," *Nature Communications*, vol. 5, p. 5412, Nov. 2014.

[140] T. Fujiwara, K. Ritchie, H. Murakoshi, K. Jacobson, and A. Kusumi, "Phospholipids undergo hop diffusion in compartmentalized cell membrane," *The Journal of Cell Biology*, vol. 157, pp. 1071–1082, June 2002.

[141] B. Winckler, P. Forscher, and I. Mellman, "A diffusion barrier maintains distribution of membrane proteins in polarized neurons," *Nature*, vol. 397, pp. 698–701, Feb. 1999.

[142] W. S. Trimble and S. Grinstein, "Barriers to the free diffusion of proteins and lipids in the plasma membrane," *The Journal of Cell Biology*, vol. 208, p. 259, Feb. 2015.

[143] K. Jacobson, O. G. Mouritsen, and R. G. W. Anderson, "Lipid rafts: at a crossroad between cell biology and physics," *Nature Cell Biology*, vol. 9, pp. 7–14, Jan. 2007.

[144] K. Gaus, E. Chklovskaia, B. Fazekas de St. Groth, W. Jessup, and T. Harder, "Condensation of the plasma membrane at the site of T lymphocyte activation," *The Journal of Cell Biology*, vol. 171, pp. 121–131, Oct. 2005.

[145] O. G. Mouritsen, "Model Answers to Lipid Membrane Questions," *Cold Spring Harbor Perspectives in Biology*, vol. 3, p. a004622, Jan. 2011.

[146] G. E. Atilla-Gokcumen and U. S. Eggert, "A comparative LC-MS based profiling approach to analyze lipid composition in tissue culture systems," *Methods in Molecular Biology (Clifton, N.J.)*, vol. 1232, pp. 103–113, 2015.

[147] A. Grelard, C. Loudet, A. Diller, and E. J. Dufourc, "NMR Spectroscopy of Lipid Bilayers," in *Membrane Protein Structure Determination*, Methods in Molecular Biology, pp. 341–359, Humana Press, Totowa, NJ, 2010.

[148] A. Ramamoorthy, D.-K. Lee, J. S. Santos, and K. A. Henzler-Wildman, "Nitrogen-14 solid-state NMR spectroscopy of aligned phospholipid bilayers to probe peptide-lipid interaction and oligomerization of membrane associated peptides," *Journal of the American Chemical Society*, vol. 130, pp. 11023–11029, Aug. 2008.

[149] T. T. Mills, S. Tristram-Nagle, F. A. Heberle, N. F. Morales, J. Zhao, J. Wu, G. E. S. Toombes, J. F. Nagle, and G. W. Feigenson, "Liquid-Liquid Domains in Bilayers Detected by Wide Angle X-Ray Scattering," *Biophysical Journal*, vol. 95, pp. 682–690, July 2008.

[150] J. Relat-Goberna and S. Garcia-Manyes, "Direct Observation of the Dynamics of Self-Assembly of Individual Solvation Layers in Molecularly Confined Liquids," *Physical Review Letters*, vol. 114, p. 258303, June 2015.

[151] M. Hao, S. Mukherjee, and F. R. Maxfield, "Cholesterol depletion induces large scale domain segregation in living cell membranes," *Proceedings of the National Academy of Sciences*, vol. 98, pp. 13072–13077, June 2001.

[152] J. S. Goodwin, K. R. Drake, C. L. Remmert, and A. K. Kenworthy, "Ras diffusion is sensitive to plasma membrane viscosity," *Biophysical Journal*, vol. 89, pp. 1398–1410, Aug. 2005.

[153] M. P. Clausen, E. Sezgin, J. Bernardino de la Serna, D. Waithe, B. C. Lagerholm, and C. Eggeling, "A straightforward approach for gated STED-FCS to investigate lipid membrane dynamics," *Methods (San Diego, Calif.)*, vol. 88, pp. 67–75, Oct. 2015.

[154] N. Bag, D. H. X. Yap, and T. Wohland, "Temperature dependence of diffusion in model and live cell membranes characterized by imaging fluorescence correlation spectroscopy," *Biochimica et Biophysica Acta (BBA) - Biomembranes*, vol. 1838, pp. 802–813, Mar. 2014.

[155] B. Hebert, S. Costantino, and P. W. Wiseman, "Spatiotemporal Image Correlation Spectroscopy (STICS) Theory, Verification, and Application to Protein Velocity Mapping in Living CHO Cells," *Biophysical Journal*, vol. 88, pp. 3601–3614, May 2005.

[156] D. Axelrod, "Carbocyanine dye orientation in red cell membrane studied by microscopic fluorescence polarization.," *Biophysical Journal*, vol. 26, pp. 557–573, June 1979.

[157] J. V. Rocheleau, M. Edidin, and D. W. Piston, "Intrasequence GFP in Class I MHC Molecules, a Rigid Probe for Fluorescence Anisotropy Measurements of the Membrane Environment," *Biophysical Journal*, vol. 84, pp. 4078–4086, June 2003.

[158] R. K. P. Benninger, B. Vanherberghen, S. Young, S. B. Taner, F. J. Culley, T. Schnyder, M. A. A. Neil, D. Wustner, P. M. W. French, D. M. Davis, and B. Onfelt, "Live cell linear dichroism imaging reveals extensive membrane ruffling within the docking structure of natural killer cell immune synapses," *Biophysical Journal*, vol. 96, pp. L13–15, Jan. 2009.

[159] R. Machan, Y. H. Foo, and T. Wohland, "On the Equivalence of FCS and FRAP: Simultaneous Lipid Membrane Measurements," *Biophysical Journal*, vol. 111, pp. 152–161, July 2016.

[160] J. A. Levitt, P. E. Morton, G. O. Fruhwirth, G. Santis, P.-H. Chung, M. Parsons, and K. Suhling, "Simultaneous FRAP, FLIM and FAIM for measurements of protein mobility and interaction in living cells," *Biomedical Optics Express*, vol. 6, pp. 3842–3854, Oct. 2015.

[161] M. R. Dent, I. Lopez-Duarte, C. J. Dickson, N. D. Geoghegan, J. M. Cooper, I. R. Gould, R. Krams, J. A. Bull, N. J. Brooks, and M. K. Kuimova, "Imaging phase separation in model lipid membranes through the use of BODIPY based molecular rotors," *Physical Chemistry Chemical Physics*, vol. 17, pp. 18393–18402, July 2015.

[162] R. Kreder, S. Oncul, O. A. Kucherak, K. A. Pyrshev, E. Real, Y. Mely, and A. S. Klymchenko, "Blue fluorogenic probes for cell plasma membranes fill the gap in multicolour imaging," *RSC Advances*, vol. 5, no. 29, pp. 22899–22905, 2015.

[163] V. Kilin, Z. Darwich, L. Richert, P. Didier, A. Klymchenko, and Y. Mely, "Two photon fluorescence imaging of lipid membrane domains and potentials using advanced fluorescent probes," in *Multiphoton Microscopy in the Biomedical Sciences XIII; 85880S* (S. Proceedings, ed.), vol. 8588, pp. 85880S–85880S–13, 2013.

[164] Y. Niko, P. Didier, Y. Mely, G.-i. Konishi, and A. S. Klymchenko, "Bright and photostable push-pull pyrene dye visualizes lipid order variation between plasma and intracellular membranes," *Scientific Reports*, vol. 6, p. 18870, Jan. 2016.

[165] T. Parasassi, G. De Stasio, G. Ravagnan, R. M. Rusch, and E. Gratton, "Quantitation of lipid phases in phospholipid vesicles by the generalized polarization of Laurdan fluorescence.," *Biophysical Journal*, vol. 60, pp. 179–189, July 1991.

[166] T. Parasassi, G. Ravagnan, R. M. Rusch, and E. Gratton, "Modulation and Dynamics of Phase Properties in Phospholipid Mixtures Detected by Laurdan Fluorescence," *Photochemistry and Photobiology*, vol. 57, pp. 403–410, Mar. 1993.

[167] T. Parasassi, E. K. Krasnowska, L. Bagatolli, and E. Gratton, "Laurdan and Prodan as Polarity-Sensitive Fluorescent Membrane Probes," *Journal of Fluorescence*, vol. 8, pp. 365–373, Dec. 1998.

[168] K. Gaus, T. Zech, and T. Harder, "Visualizing membrane microdomains by Laurdan 2-photon microscopy," *Molecular Membrane Biology*, vol. 23, pp. 41–48, Feb. 2006.

[169] O. Golfetto, E. Hinde, and E. Gratton, "Laurdan Fluorescence Lifetime Discriminates Cholesterol Content from Changes in Fluidity in Living Cell Membranes," *Biophysical Journal*, vol. 104, pp. 1238–1247, Mar. 2013.

[170] E. K. Krasnowska, L. A. Bagatolli, E. Gratton, and T. Parasassi, "Surface properties of cholesterol-containing membranes detected by Prodan fluorescence," *Biochimica Et Biophysica Acta*, vol. 1511, pp. 330–340, Apr. 2001.

[171] L. Malacrida, D. M. Jameson, and E. Gratton, "A multidimensional phasor approach reveals LAURDAN photophysics in NIH-3t3 cell membranes," *Scientific Reports*, vol. 7, Aug. 2017.

[172] D. M. Owen, C. Rentero, A. Magenau, A. Abu-Siniyeh, and K. Gaus, "Quantitative imaging of membrane lipid order in cells and organisms," *Nature Protocols*, vol. 7, pp. 24–35, Jan. 2012.

[173] C. K. Haluska, A. P. Schroeder, P. Didier, D. Heissler, G. Duportail, Y. Mely, and C. M. Marques, "Combining Fluorescence Lifetime and Polarization Microscopy to Discriminate Phase Separated Domains in Giant Unilamellar Vesicles," *Biophysical Journal*, vol. 95, pp. 5737–5747, Dec. 2008.

[174] S. A. Sanchez, M. A. Tricerri, and E. Gratton, "Laurdan generalized polarization fluctuations measures membrane packing micro-heterogeneity in vivo," *Proceedings of the National Academy of Sciences of the United States of America*, vol. 109, pp. 7314–7319, May 2012.

[175] S. Mazeres, E. Joly, A. Lopez, and C. Tardin, "Characterization of M-laurdan, a versatile probe to explore order in lipid membranes," *F1000Research*, July 2014.

[176] T. Parasassi, A. M. Giusti, M. Raimondi, and E. Gratton, "Abrupt modifications of phospholipid bilayer properties at critical cholesterol concentrations.," *Biophysical Journal*, vol. 68, pp. 1895–1902, May 1995.

[177] Thermo Fischer Scientific, "Avidin-Biotin Interaction."

[178] M. J. Sarmento, M. Prieto, and F. Fernandes, "Reorganization of lipid domain distribution in giant unilamellar vesicles upon immobilization with different membrane tethers," *Biochimica et Biophysica Acta (BBA) - Biomembranes*, vol. 1818, pp. 2605–2615, Nov. 2012.

[179] S. W. Botchway, A. M. Lewis, and C. D. Stubbs, "Development of fluorophore dynamics imaging as a probe for lipid domains in model vesicles and cell membranes," *European Biophysics Journal*, vol. 40, pp. 131–141, Feb. 2011.

[180] "Phase Transition Temperatures for Glycerophospholipids | Avanti Polar Lipids."

[181] K. Lidke, B. Rieger, D. Lidke, and T. Jovin, "The role of photon statistics in fluorescence anisotropy imaging," *IEEE Transactions on Image Processing*, vol. 14, pp. 1237–1245, Sept. 2005.

[182] T. Foerster and G. Hoffmann, "Die Viskositaetsabhaengigkeit der Fluoreszenzquantenausbeuten einiger Farbstoffsysteme," *Zeitschrift fuer Physikalische Chemie*, vol. 75, no. 1_2, pp. 63–76, 1971.

[183] M. K. Kuimova, G. Yahioglu, J. A. Levitt, and K. Suhling, "Molecular Rotor Measures Viscosity of Live Cells via Fluorescence Lifetime Imaging," *Journal of the American Chemical Society*, vol. 130, pp. 6672–6673, May 2008.

[184] P. Jurkiewicz, L. Cwiklik, P. Jungwirth, and M. Hof, "Lipid hydration and mobility: An interplay between fluorescence solvent relaxation experiments and molecular dynamics simulations," *Biochimie*, vol. 94, pp. 26–32, Jan. 2012.

[185] D. M. Owen, P. M. P. Lanigan, C. Dunsby, I. Munro, D. Grant, M. A. A. Neil, P. M. W. French, and A. I. Magee, "Fluorescence lifetime imaging provides enhanced contrast when imaging the phase-sensitive dye di-4-ANEPPDHQ in model membranes and live cells," *Biophysical Journal*, vol. 90, pp. L80–82, June 2006.

[186] C. Reichardt, "Solvatochromic Dyes as Solvent Polarity Indicators," *Chemical Reviews*, vol. 94, pp. 2319–2358, Dec. 1994.

[187] C. Reichardt and T. Welton, *Solvents and Solvent Effects in Organic Chemistry*. John Wiley & Sons, Aug. 2011.

[188] M. Viard, J. Gallay, M. Vincent, O. Meyer, B. Robert, and M. Paternostre, "Laurdan solvatochromism: solvent dielectric relaxation and intramolecular excited-state reaction," *Biophysical Journal*, vol. 73, pp. 2221–2234, Oct. 1997.

[189] S. Osella, N. A. Murugan, N. K. Jena, and S. Knippenberg, "Investigation into Biological Environments through (Non)linear Optics: A Multiscale Study of Laurdan Derivatives," *Journal of Chemical Theory and Computation*, vol. 12, pp. 6169–6181, Dec. 2016.

[190] R. E. Scott, "Plasma membrane vesiculation: a new technique for isolation of plasma membranes," *Science*, vol. 194, pp. 743–745, Nov. 1976.

[191] R. E. Scott, R. G. Perkins, M. A. Zschunke, B. J. Hoerl, and P. B. Maercklein, "Plasma membrane vesiculation in 3t3 and SV3t3 cells. I. Morphological and biochemical characterization," *Journal of Cell Science*, vol. 35, pp. 229–243, Feb. 1979.

[192] R. E. Scott, "Undifferentiated and differentiated L6 myoblast plasma membranes. I: Comparison of the morphology of plasma membrane vesiculation and the factors influencing the vesiculation process," *Cell Differentiation*, vol. 7, pp. 325–334, Dec. 1978.

[193] D. W. Tank, E. S. Wu, and W. W. Webb, "Enhanced molecular diffusibility in muscle membrane blebs: release of lateral constraints.," *The Journal of Cell Biology*, vol. 92, pp. 207–212, Jan. 1982.

[194] T. Baumgart, A. T. Hammond, P. Sengupta, S. T. Hess, D. A. Holowka, B. A. Baird, and W. W. Webb, "Large-scale fluid/fluid phase separation of proteins and lipids in giant plasma membrane vesicles," *Proceedings of the National Academy of Sciences*, vol. 104, pp. 3165–3170, Feb. 2007.

[195] D. A. Roess, M. A. Jewell, C. J. Philpott, and B. G. Barisas, "The rotational diffusion of LH receptors differs when receptors are occupied by hCG versus LH and is increased by cytochalasin D," *Biochimica Et Biophysica Acta*, vol. 1357, pp. 98–106, June 1997.

[196] J. Kwik, S. Boyle, D. Fooksman, L. Margolis, M. P. Sheetz, and M. Edidin, "Membrane cholesterol, lateral mobility, and the phosphatidylinositol 4,5-bisphosphate-dependent organization of cell actin," *Proceedings of the National Academy of Sciences*, vol. 100, pp. 13964–13969, Nov. 2003.

[197] S. Y. Nishimura, M. Vrljic, L. O. Klein, H. M. McConnell, and W. E. Moerner, "Cholesterol Depletion Induces Solid-like Regions in the Plasma Membrane," *Biophysical Journal*, vol. 90, pp. 927–938, Feb. 2006.

[198] E. Ikonen, "Cellular cholesterol trafficking and compartmentalization," *Nature Reviews Molecular Cell Biology*, vol. 9, p. 125, Feb. 2008.

[199] K. Simons and E. Ikonen, "How cells handle cholesterol," *Science (New York, N.Y.)*, vol. 290, pp. 1721–1726, Dec. 2000.

[200] M. S. Brown and J. L. Goldstein, "A proteolytic pathway that controls the cholesterol content of membranes, cells, and blood," *Proceedings of the National Academy of Sciences of the United States of America*, vol. 96, pp. 11041–11048, Sept. 1999.

[201] M. S. Brown, J. Ye, R. B. Rawson, and J. L. Goldstein, "Regulated Intramembrane Proteolysis: A Control Mechanism Conserved from Bacteria to Humans," *Cell*, vol. 100, pp. 391–398, Feb. 2000.

[202] S. Mahammad and I. Parmryd, "Cholesterol homeostasis in T cells. Methyl-beta-cyclodextrin treatment results in equal loss of cholesterol from Triton X-100 soluble and insoluble fractions," *Biochimica Et Biophysica Acta*, vol. 1778, pp. 1251–1258, May 2008.

[203] S. Mahammad and I. Parmryd, "Cholesterol Depletion Using Methyl-beta-cyclodextrin," in *Methods in Membrane Lipids*, Methods in Molecular Biology, pp. 91–102, Humana Press, New York, NY, 2015.

[204] S. Ilangumaran and D. C. Hoessli, "Effects of cholesterol depletion by cyclodextrin on the sphingolipid microdomains of the plasma membrane," *The Biochemical Journal*, vol. 335 (Pt 2), pp. 433–440, Oct. 1998.

[205] P. S. Kabouridis, J. Janzen, A. L. Magee, and S. C. Ley, "Cholesterol depletion disrupts lipid rafts and modulates the activity of multiple signaling pathways in T lymphocytes," *European Journal of Immunology*, vol. 30, pp. 954–963, Mar. 2000.

[206] B. M. Stott, M. P. Vu, C. O. McLemore, M. S. Lund, E. Gibbons, T. J. Brueseke, H. A. Wilson-Ashworth, and J. D. Bell, "Use of fluorescence to determine the effects of cholesterol on lipid behavior in sphingomyelin liposomes and erythrocyte membranes," *Journal of Lipid Research*, vol. 49, pp. 1202–1215, Jan. 2008.

[207] S. Mukherjee and A. Chattopadhyay, "Monitoring the organization and dynamics of bovine hippocampal membranes utilizing Laurdan generalized polarization," *Biochimica et Biophysica Acta (BBA) - Biomembranes*, vol. 1714, pp. 43–55, Aug. 2005.

[208] T. Niehoerster, A. Loeschberger, I. Gregor, B. Kraemer, H.-J. Rahn, M. Patting, F. Koberling, J. Enderlein, and M. Sauer, "Multi-target spectrally resolved fluorescence lifetime imaging microscopy," *Nature Methods*, vol. 13, pp. 257–262, Mar. 2016.

[209] I. T. Jolliffe, *Principal Component Analysis*. New York: Springer, 2 edition ed., Oct. 2002.

[210] M. R. Keenan and P. G. Kotula, "Accounting for Poisson noise in the multivariate analysis of ToF-SIMS spectrum images," *Surface and Interface Analysis*, vol. 36, pp. 203–212, Mar. 2004.

[211] X. Liu, B. Zhang, J. Luo, and J. Bai, "4-D Reconstruction for Dynamic Fluorescence Diffuse Optical Tomography," *IEEE Transactions on Medical Imaging*, vol. 31, pp. 2120–2132, Nov. 2012.

[212] F. Pedersen, M. Bergström, E. Bengtsson, and B. Långström, "Principal component analysis of dynamic positron emission tomography images," *European Journal of Nuclear Medicine*, vol. 21, pp. 1285–1292, Dec. 1994.

[213] M. Miljković, T. Chernenko, M. J. Romeo, B. Bird, C. Matthäus, and M. Diem, "Label-free imaging of human cells: algorithms for image reconstruction of Raman hyperspectral datasets," *The Analyst*, vol. 135, pp. 2002–2013, Aug. 2010.

[214] C. Robertson and S. C. George, "Theory and practical recommendations for autocorrelation-based image correlation spectroscopy," *Journal of Biomedical Optics*, vol. 17, Aug. 2012.

[215] M. Peter, S. M. Ameer-Beg, M. K. Y. Hughes, M. D. Keppler, S. Prag, M. Marsh, B. Vojnovic, and T. Ng, "Multiphoton-FLIM Quantification of the EGFP-mRFP1 FRET Pair for Localization of Membrane Receptor-Kinase Interactions," *Biophysical Journal*, vol. 88, pp. 1224–1237, Feb. 2005.

[216] L. Martelo, A. Fedorov, and M. N. Berberan-Santos, "Fluorescence Phasor Plots Using Time Domain Data: Effect of the Instrument Response Function," vol. 119, pp. 10267–10274, Aug. 2015.

[217] J. Salmon, C.-A. Deledalle, R. Willett, and Z. Harmany, "Poisson noise reduction with non-local PCA," in *2012 IEEE International Conference on Acoustics, Speech and Signal Processing (ICASSP)*, pp. 1109–1112, Mar. 2012.

[218] J. Y. Qu, H. Chang, and S. Xiong, "Fluorescence spectral imaging for characterization of tissue based on multivariate statistical analysis," *Journal of the Optical Society of America A*, vol. 19, no. 9, p. 1823, 2002.

[219] M. Makitalo and A. Foi, "Optimal Inversion of the Anscombe Transformation in Low-Count Poisson Image Denoising," *IEEE Transactions on Image Processing*, vol. 20, pp. 99–109, Jan. 2011.

[220] Q. Zhao, I. T. Young, and J. G. S. de Jong, "Photon budget analysis for fluorescence lifetime imaging microscopy," *Journal of Biomedical Optics*, vol. 16, no. 8, p. 086007, 2011.

[221] A. Esposito, A. N. Bader, S. C. Schlachter, D. J. v. d. Heuvel, G. S. K. Schierle, A. R. Venkitaraman, C. F. Kaminski, and H. C. Gerritsen, "Design and application of a confocal microscope for spectrally resolved anisotropy imaging," *Optics Express*, vol. 19, pp. 2546–2555, Jan. 2011.